Detecting Cosmological Reionization on Large Scales Through the 21 cm H I Line

A thesis submitted for the degree
of Doctor of Philosophy of
the University of Sydney

A. P. Chippendale

1 September 2009

This thesis contains no material that has been accepted for the award of any other degree or diploma by any university. To the best of the author's knowledge and belief, it contains no material previously published or written by another person, except where due reference is made in the text.

A. P. Chippendale
1 September 2009

For my family

ABSTRACT

This thesis presents the development of new techniques for measuring the mean redshifted 21 cm line of neutral hydrogen during reionization. This is called the 21 cm cosmological reionization monopole. Successful observations could identify the nature of the first stars and test theories of galaxy and large-scale structure formation.

The goal was to specify, construct and calibrate a portable radio telescope to measure the 21 cm monopole in the frequency range 114 MHz to 228 MHz, which corresponds to the redshift range $11.5 > z > 5.2$. The chosen approach combined a frequency independent antenna with a digital correlation spectrometer to form a correlation radiometer. The system was calibrated against injected noise and against a modelled galactic foreground.

Components were specified for calibration of the sky spectrum to 1 mK/MHz relative accuracy. Comparing simulated and measured spectra showed that bandpass calibration is limited to 11 K, that is 1% of the foreground emission, due to larger than expected frequency dependence of the antenna pattern. Overall calibration, including additive contributions from the system and the radio foreground, is limited to 60 K. This is 160 times larger than the maximum possible monopole amplitude at redshift eight. Future work will refine and extend the system known as the Cosmological Reionization Experiment Mark I (CoRE Mk I).

PUBLICATIONS AND PRESENTATIONS

A number of publications and presentations based on the work in this thesis were made over the course of this project. They are listed here for reference.

1. **A. P. Chippendale, R. Subrahmanyan,** "Measuring the Metre-Wave Sky Spectrum with Milli-Kelvin Accuracy: Engineering Challenges and Australian Opportunities", in *Proceedings of the Workshop on Applications of Radio Science*, Hobart, February 2004.

2. **R. Subrahmanyan, A. P. Chippendale, R. D. Ekers,** "Cosmological Re-ionization Experiment," *ATNF News*, No. 56, June 2005.

3. **R. Subrahmanyan, R. D. Ekers, A. P. Chippendale,** "ATNF Cosmological Reionization Experiment," presented at Reionizing the Universe, Groningen, 27 June - 1 July 2005.

4. **A. P. Chippendale, R. Subrahmanyan, R. D. Ekers,** "Effects of Interference on the ATNF Cosmological Reionization Experiment at Mileura", in *Proceedings of the XXIXth General Assembly of the International Union of Radio Science*, Delhi, 23-29 October 2005.

5. **A. P. Chippendale, R. Subrahmanyan, R. D. Ekers,** "The Cosmological Reionization Experiment," presented at New Techniques and Results in Low Frequency Astronomy, Hobart, 7-10 December 2005.

6. **A. P. Chippendale, R. Subrahmanyan, R. D. Ekers,** "The Cosmological Reionization Experiment," presented at the TEXAS Symposium on Relativistic Astrophysics, Melbourne, 11-15 December 2006.

7. **R. D. Ekers, R. Subrahmanyan, A. P. Chippendale** "Progress in Measuring the Global Spectrum," presented at the Fifth Harvard-Smithsonian Conference on Theoretical Astrophysics: 21 cm Cosmology, Harvard, 12-15 May 2008.

ACKNOWLEDGEMENTS

First, I would like to acknowledge my supervisors:

- Prof. Ravi Subrahmanyan, Director of the Raman Research Institute (formerly of the CSIRO Australia Telescope National Facility); and
- Prof. Anne Green, Head of the School of Physics at the University of Sydney.

Ravi continually challenges me to be more precise and more empirical. I can only aspire to his breadth of scientific and engineering knowledge. I would benefit greatly by following his example of solving problems as fast as possible whilst learning as much as possible from them. Ravi led the design of the antenna for this project and wrote the initial code for convolving antenna pattern models with the radio sky. Ravi also reviewed my drafts with contradictory depth and speed. I would also like to thank Ravi for a memorable tour of the Ooty Radio Telescope.

Anne is an outstanding mentor and motivator. She continually pressed me to make this thesis relevant and to make it complete. Anne leads the School of Physics with a passion and never lets a good opportunity pass by a student without reminding them that they should be assertive.

I thank the Golden Key International Honour Society for awarding me their US$10,000 Graduate Scholar Award to support my postgraduate study.

The University of Sydney provided financial support through the Postgraduate Research Support Scheme for me to present work relating to this thesis at the International Union of Radio Science (URSI) General Assembly in Delhi, 2005. I also thank URSI for providing financial travel support to attend the same meeting.

I would like to acknowledge the Australia Telescope National Facility (ATNF) which is a division of Australia's Commonwealth Scientific and Industrial Research Organisation (CSIRO). The ATNF allowed me to participate in their graduate student program whilst maintaining my working role as an engineer for them. My colleagues have been generous in creating time and space for me to complete this work. In particular I thank Prof. Ron Ekers for championing this project as part of his Federation Fellowship research programme. He drew together the necessary people to make this project possible.

Also at the ATNF, Barry Parsons carried out the structural design of the antenna and supervised its construction. Mick McDonald professionally constructed the unique antenna out of the non-standard styrofoam that we supplied to his carpentry workshop. Mick also built exquisite foam lined pine boxes to safely ship the antenna across Australia. George Graves provided expert advice on component selection for the front-end. Mark Leach designed the power supplies and the optocouplers for switching the noise sources under computer control. Raji Chekkala and Troy Elton

integrated and packaged the front-end components, power supplies, and samplers in a form useful for field work. I also thank the kind ATNF staff at Narrabri who gave daily practical assistance during the integration and testing of the system at their site.

Still at the ATNF, Ron Beresford assisted me with the logistics of getting the antenna to the Murchison Radioastronomy Observatory (MRO) on the other side of the continent. He saw the equipment safely there and pitched in with the daily work required to set-up and run the antenna at the MRO. I also thank Peter Axtens for giving useful comments on the front-end chapter, and Dr. John O'Sullivan for participating in one of the early test measurements at Narrabri where he provided many useful suggestions for diagnosing system performance. Dr. Mike Kesteven pressed me to make the correlator designed for this thesis more generally useful and has since applied it to antenna holography and interferometry. He has written a significant amount of software to make the correlator useful for these tasks and I have benefited directly from this in my work at the ATNF.

Prof. Frank Briggs of the Australian National University kindly participated in one of the system integration runs at Narrabri. Frank also invited me to present a review of this project at the Murchison Widefield Array International Project Meeting in Canberra, 2009. I thoroughly enjoyed this opportunity to trade stories with other groups attempting to constrain reionization through 21 cm measurements. I was impressed by their creativity and perseverance.

Dr. Dan Werthimer at the University of California, Berkeley supplied the SERENDIP V spectrometer board used to implement the correlator for this thesis. Not only did he supply the board, but he welcomed me to visit his exciting group at the UC Berkeley Space Sciences Laboratory. Dan and his team spared time to train me in the use of the board when they were busy delivering a new back-end to Arecibo that probably required more attention.

Finally, I would like to thank my family: Imma, Robbie, Paul, Susan, Jason, David, Inge, Mim, Nicky, Ebba and Muriel. In addition to making everything worthwhile and accommodating my narrow focus on this task, a number of you spent hard hours weeding out even more poor spilling and grammer than remain in this final work.

CONTENTS

LIST OF FIGURES

LIST OF TABLES

Chapter 1

INTRODUCTION

This chapter provides an overview of the Cosmological Reionization Experiment Mark I (CoRE Mk I) to detect the mean redshifted 21 cm line of neutral hydrogen, hereafter called the 21 cm cosmological reionization monopole. The goal was to develop a system capable of measuring the sky spectrum with 1 mK accuracy over the 114 MHz to 228 MHz band. This is extremely challenging due to galactic foreground emission that is 10^5 to 10^6 times stronger than the 21 cm monopole. The chosen method combined a frequency independent antenna with a digital correlation spectrometer to form a correlation radiometer.

1.1 Science Goals

The principal goal was to constrain the 21 cm cosmological reionization monopole by measuring the sky spectrum over the frequency range 114 MHz to 228 MHz, which corresponds to the redshift range $11.5 > z > 5.2$.

Measuring the 21 cm monopole would constrain:

- the large-scale average temperature and ionization histories of the intergalactic medium (IGM);
- the luminosity and spectrum of the first radiating sources; and
- the cosmological parameters.

Much less work has been done on the 21 cm monopole than on the 21 cm fluctuation statistics and imaging targeted by the 1.5 billion euro Square Kilometre Array. This is peculiar considering that the 21 cm monopole may be measured with a single low-cost antenna.

A first effort to detect the 21 cm monopole was made by the Experiment to Detect the Global EOR Signature (Bowman et al., 2007). Early results placed an upper limit of 450 mK on the 21 cm monopole assuming a rapid transition to a fully ionized IGM at a redshift of eight. Theory presented in this thesis shows that the maximum possible monopole amplitude at a redshift of eight is 370 mK assuming instantaneous reionization and reheating, Lyman-alpha line coupling of the neutral hydrogen spin temperature to the matter temperature, and no significant preheating.

This thesis aims for a direct measurement of the monopole rather than a filtered detection. This more general approach requires no assumptions about the expected signal, but generates stricter requirements for the measurement system.

Calibration accuracy and a sensitivity of 1 mK are aimed for, so that the ionization fraction and cosmological parameters may be extracted from the 21 cm monopole emission signal. Emission will have an amplitude of approximately 30 mK that can only be wiped out by spectrally complex foreground emission or by variations of reionization history over different lines of sight. The swing from absorption to emission can have an amplitude of up to approximately 300 mK. Calibration accuracy and sensitivity of 0.1 mK are therefore sufficient to begin constraining models of reionization. However, the larger absorption signal may not be present due to preheating or the lack of a Lyman-alpha background.

1.2 Method

This thesis aims for direct measurement of the reionization spectrum. A lot of useful information can be extracted from a direct measurement, including the temperature and ionization history of hydrogen, and the spectrum and luminosity of the sources that reionize hydrogen. Direct measurement will therefore remain an important goal beyond likely initial detection by filtering techniques.

Filtered detection assumes a template reionization spectrum and reports the probability that measured data are consistent with this template. This can increase the signal to noise ratio of detection. It can also reduce the sensitivity to calibration residuals to the extent that the residuals are orthogonal to the template spectrum.

Bowman et al. (2007) successfully applied a filtering technique that subtracts a polynomial from the measured spectrum and compares residuals to those predicted for a template 21 cm monopole spectrum. This generated a limit on the 21 cm monopole amplitude for scenarios where it has sharp features that cannot be accurately fitted by the polynomial.

Direct measurement requires full calibration of: the system bandpass; additive contributions from the system; and additive contributions from the radio foreground. This thesis designs, implements, and tests a system that can be calibrated to a level sufficient for measuring the reionization monopole spectrum.

Measurements are made with the antenna directed at the zenith and bandpass calibrated using the position dependent component of the galactic foreground. This requires the antenna pattern to be significantly frequency independent so that the spatial structure of the foreground does not cause erroneous frequency structure in the measured spectrum. A pyramidal log-spiral antenna was designed with a near frequency independent antenna pattern that can be bandpass calibrated to within 1 mK/MHz.

Additive contributions were reduced by implementing the system as a correlation radiometer as shown in figure 1.1. The signal is split directly after the antenna by

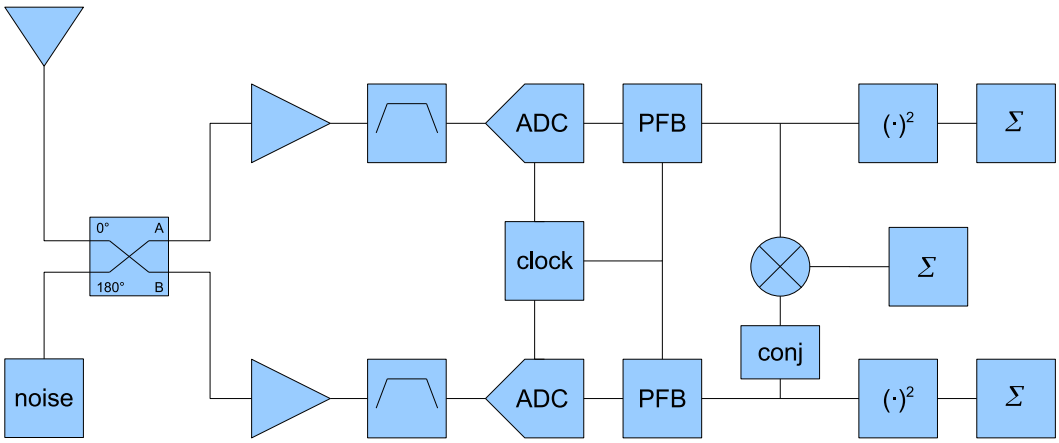

Fig. 1.1: Correlation radiometer - splitting the signal directly after the antenna with a 180° hybrid.

a 180° hybrid. Each half of the signal is amplified and filtered by an analogue front-end, and then channelised and correlated by a digital back-end. Additive noise contributions from each half are independent and do not correlate so long as coupling between the two receiver halves is low.

Components were specified for calibration of the sky spectrum to 1 mK/MHz relative accuracy. This required special attention to the linearity of the front-end and to quantisation distortion in the back-end. The final system was deployed to the Murchison Radioastronomy Observatory (MRO).

The observation band of 114 MHz to 228 MHz ($11.5 > z > 5.2$) was chosen at the commencement of this thesis to avoid stronger galactic foreground at lower frequencies; to include a control band above 203 MHz ($z < 6$) where the cosmological reionization monopole should be zero (quasar observations indicate that reionization is mostly complete at $z \approx 6$, Fan et al. 2006b); to allow the use of a smaller, more manageable antenna; and to avoid the 87.5 MHz to 108 MHz FM broadcast band for initial testing.

Subsequent modelling of the cosmological reionization monopole showed that a 282 mK swing from absorption to emission in the cosmological reionization monopole is possible between 101 MHz and 131 MHz. The observation band was not lowered as the above reasons make it an easier band in which to learn about calibration. In addition, the monopole's swing from absorption to emission is not present if neutral hydrogen is reheated before its spin temperature is coupled to its kinetic temperature. The model prediction for the weaker (30 mK) emission signal does fall in the 114 MHz to 228 MHz band and its presence is inevitable if reionization is reasonably coherent along different lines of sight.

1.3 Thesis Outline

Chapter 2 provides the scientific context for this experiment. It reviews structure formation theory and prospects for advancing it by observing the cosmological reionization monopole. Observing the reionization monopole can strongly constrain structure formation theories as reionization is coeval with formation of the first gravitationally bound objects. The first objects cause feedback that complicates structure formation. Observing the reionization monopole can provide much needed measures of this feedback: the spectrum and amount of radiation emitted by the first objects; the temperature history of the intergalactic medium (IGM); and the ionization history of the IGM. The state of the IGM is important as it is both the material source and energy sink for structure formation.

Chapter 3 predicts the 21 cm reionization monopole spectrum using a model that is consistent with contemporary observations. The expectation is for a 282 mK swing from absorption at 101 MHz to emission at 131 MHz. Emission commences with an amplitude of 28 mK and decays gradually to zero at 193 MHz. Although the sharp swing from absorption is not centred in the observing band of the current experiment, its location is sensitive to model parameters such as the ionizing luminosity and the X-ray spectral index of the first sources. The large swing from absorption to emission assumes a Lyman-alpha line radiation background that cou-

ples the neutral hydrogen spin temperature to the matter temperature before rapid reionization and reheating. Models of this class may be constrained with 0.1 K sensitivity. However, the absorption signal can be completely wiped out by pre-heating of the IGM or by the lack of a Lyman-alpha background. The conservative design target of 1 mK sensitivity would allow constraint of cosmological parameters and the ionized fraction from the weaker emission signal which is expected to be inevitable.

Chapter 4 describes the requirements and implementation of an antenna for measuring the reionization monopole. Confusion of spatial and spectral structure of the sky brightness due to frequency dependence of the antenna pattern is a significant issue. It is shown that an antenna with a power pattern that varies by 4% peak-to-peak at its half-power points can measure the sky spectrum with 1 mK accuracy at 1 MHz resolution. This leads to an investigation of frequency independent and log-periodic antennas. A two-arm pyramidal log-spiral antenna that can meet the power pattern requirement is designed, simulated, and constructed.

Chapter 5 presents the design and implementation of the front-end. Keeping distortion and unwanted additive contributions less than 1 mK requires careful attention to the selectivity and linearity of the front-end. A model is presented for estimating nonlinear distortion of broadband noise plus narrowband interference using parameters commonly found on component data sheets. This model is applied to the final amplifier in the front-end that operates the furthest out of its linear range. It is shown that distortion due to amplifier nonlinearity should be less than 1 mK for interference power levels typical of the MRO where the system was deployed.

Chapter 6 discusses the specification and implementation of the back-end. Distortions due to quantisation of noise and interference are analysed for a reionization experiment at the MRO. Numerical simulations show that 1-bit quantisation is adequate at the MRO so long as a renormalised van Vleck correction is made to the measured spectrum. The back-end is, however, implemented with 8-bit quantisation and no correction. Provided the input noise power level is optimised, distortion due to 8-bit quantisation is less than 1 mK for even the strongest interference observed at the MRO. A theoretical analysis is made of distortion due to multi-bit quantisation of noise and interference. This results in a guide for selecting an appropriate bit resolution and input noise power level for an analogue to digital converter (ADC) operating in a given interference environment. The correlator is implemented in a field programmable gate array (FPGA). It uses a 1,024 point polyphase filter bank to channelise two 114 MHz inputs that are then correlated and accumulated.

Chapter 7 presents the calibration of drift-scan measurements made with the completed system at the MRO. Antenna bandpass calibration left 11 K peak-to-peak residuals, that is 1% of the radio foreground, with a peak spectral slope of 5 K/MHz on 1 MHz scales. The antenna's half-power beamwidth and pointing both varied with frequency by one degree. Antenna pattern frequency dependence was evaluated using difference spectra where additive contributions cancel along with the reionization spectrum. Overall calibration was limited to 60 K when a model for the additive contributions was subtracted before bandpass calibration. Peak-

to-peak calibration residuals were 160 times larger than the maximum possible monopole amplitude at a redshift of eight.

Chapter 8 concludes by reiterating the contributions made by this thesis and outlining future work to improve the Cosmological Reionization Experiment.

Part I

SCIENTIFIC CONTEXT

Chapter 2

REIONIZATION AND STRUCTURE FORMATION

This chapter reviews structure formation theory and prospects for advancing it by observing the redshifted 21 cm line of neutral hydrogen (H I). This provides the scientific context for this thesis which develops practical techniques for observing the mean redshifted 21 cm line on the largest spatial scales. This signal is referred to as the 21 cm cosmic reionization monopole.

Cosmology and large-scale structure formation are well covered by a number of texts (Peebles, 1993; Peacock, 1999; Padmanabhan, 1993). This chapter summarises key points required to understand the the significance of the reionization monopole and to predict its spectrum in the next chapter.

2.1 Introduction

A primary goal of cosmologists today is to constrain[1] structure formation theory by observing cosmological reionization. The prospects for achieving this through 21 cm observations were reviewed by Furlanetto et al. (2006).

Significant quantities of H I formed for the first time after the big bang during the epoch of recombination at a redshift of $z_{rec} \approx 1{,}100$. At this time, the Universe had expanded, reduced in density, and cooled to a point where the redshifted thermal background radiation was insufficient to keep matter ionized. Much later, at a redshift of about eleven, the first sources of ultraviolet and X-ray radiation formed and began to reheat and reionize the intervening intergalactic medium (IGM). This process is called cosmological reionization.

Observing cosmological reionization can strongly constrain structure formation theories as reionization is coeval with formation of the first gravitationally bound objects. Observing the redshifted 21 cm line of H I throughout reionization could yield the temperature, ionization state, density field, and velocity field of the IGM as functions of position and time. This information is significant as the IGM is both the material source and energy sink for structure formation. Observing the redshifted 21 cm line can also determine the nature of the first radiating sources and their effect on structure formation.

Current structure formation models are poorly constrained as there is approximately a 1.6 billion year gap in observations of large-scale structure corresponding to redshifts $1{,}100 \gtrapprox z \gtrapprox 4$. Anisotropy in the cosmic microwave background radiation (CMBR) shows that the early Universe was very smooth with fractional temperature variations of order one part in 10^5 at $z_{rec} \approx 1{,}100$. Observations of the clustering of galaxies to $z \approx 0.3$ and the clustering of Lyman-alpha line (Ly-α) absorbers in quasar spectra to $z \approx 4$ reveal a very structured modern Universe[2] with galaxies that exceed the mean density by up to a million times. Gravitational instability successfully explains the broad evolution of these density fluctuations but does not explain the details of galaxy formation.

Models of galaxy formation are complicated by numerous feedback mechanisms.

[1] Constraining a theory or model means to test its predictions against observations and therefore identify the valid range of model parameters that are consistent with reality.

[2] Capital-U Universe is the observed one that we live in whereas small-u universe refers to any number of model universes.

The first sources affect the formation of future sources by injecting radiative and mechanical energy into the IGM and by synthesising new elements. Cosmological reionization coincides with the formation of the first stars or galaxies and may therefore trace their feedback contributions.

Many initiatives are underway to tackle this 21 cm cosmology. Several large arrays of radio telescopes are being built to measure spatial and spectral statistics of the redshifted 21 cm line during reionization. This thesis constitutes one of a handful of smaller efforts to measure the 21 cm reionization monopole with a single antenna. The 21 cm monopole would indicate the mean ionized fraction and temperature of the hydrogen component of the IGM on the largest scales as a function of time. This information can be used to deduce the nature of the first sources of radiation and their impact upon structure formation.

2.2 Structure Formation in the Early Universe

2.2.1 Cosmology

A host of observations indicate that the Universe is flat and presently dominated by vacuum energy in the form of a cosmological constant (Spergel et al., 2003, 2007). This vacuum energy causes empty space-time to give rise to a repulsive gravitational pressure that counteracts the attraction of normal matter and drives the present accelerated expansion of the Universe.

It is thought that the vacuum energy density drove an exponential expansion of the very early Universe known as cosmological inflation. This amplified quantum fluctuations into macroscopic density fluctuations that seeded structure formation at later times. The initial fluctuations of gravitational potential were nearly scale invariant with a power spectrum that is nearly a power law.

The ΛCDM, or concordance, model of big bang cosmology is the simplest model that agrees with current observations. Its main elements are a near power law spectrum of initial density fluctuations, initial inflation and later accelerated expansion due to the cosmological constant Λ, and a significant quantity of cold dark matter (CDM). This non-baryonic matter is termed cold as it becomes non-relativistic at early times and dark as it cannot be observed via absorption or emission of electromagnetic radiation. This model is therefore often referred to as the power law ΛCDM cosmological model. The next chapter predicts the expected 21 cm cosmic reionization monopole spectrum assuming power law ΛCDM.

Current observations fit a power law ΛCDM model with matter density parameter $\Omega_m \approx 0.28$ and vacuum energy density parameter $\Omega_\Lambda \approx 0.72$. The Universe appears flat with $\Omega_\Lambda + \Omega_m = 1$ to the limit of observation. The baryonic density parameter $\Omega_b \approx 0.046$ suggests that about 83% of the present total matter density is constituted by cold dark matter.

The power law ΛCDM model with the above parameters agrees with measurements of anisotropy in the CMBR (Hinshaw et al., 2009, 2007; MacTavish et al., 2006), light element abundances (Coc et al., 2004), large-scale structure observations (Percival et al., 2007; Tegmark et al., 2004; Cole et al., 2005), the supernova

Tab. 2.1: Power law ΛCDM cosmological parameters for WMAP5+BAO+SN (Komatsu et al., 2009) with 68% confidence intervals.

Parameter	Symbol	Value
Hubble constant	H_0	$70.1 \pm 1.3\ \mathrm{km\,s^{-1}\,Mpc^{-1}}$
Dimensionless Hubble parameter[a]	h	0.701 ± 0.013
Dark energy density	Ω_Λ	0.721 ± 0.015
Dark matter density	Ω_c	0.233 ± 0.013
Baryon density	Ω_b	0.0462 ± 0.0015
Physical baryon density	$\Omega_b h^2$	0.02265 ± 0.00059
Scalar spectral index of initial density fluctuations	n_s	$0.960^{+0.014}_{-0.013}$
Reionization optical depth	τ_{reion}	0.084 ± 0.016
Redshift of matter-radiation equality	z_{eq}	3280^{+88}_{-89}
Redshift of decoupling[b]	z_*	$1091.00^{+0.72}_{-0.73}$
Redshift of reionization[c]	z_{reion}	10.8 ± 1.4

[a] $H_0 = 100h\ \mathrm{km\,s^{-1}\,Mpc^{-1}}$.
[b] $\tau(z_*) = 1$.
[c] Assumes instantaneous reionization.

luminosity/distance relationship (Perlmutter et al., 1999; Riess et al., 2004) and a number of other cosmological observations summarised by Spergel et al. (2003, 2007) and Dunkley et al. (2008). Unless stated otherwise, this thesis uses the joint likelihood cosmological parameters for the five year Wilkinson Microwave Anisotropy Probe (WMAP) data combined with distance measurements from Type Ia supernovae (SN) and baryon acoustic oscillations (BAO) in the distribution of galaxies (Komatsu et al., 2009). These parameters are listed in table 2.1.

Although ΛCDM is consistent with many astronomical observations, it has a number of shortcomings (Sellwood and Kosowsky, 2001). Significant is the failure to detect predicted centrally cusped density profiles in dwarf galaxies via their rotation curves (McGaugh and de Blok, 1998). In addition, ΛCDM predicts the formation of many more dwarf galaxies than are observed (Klypin et al., 1999; Moore et al., 1999). It has also been shown that the stellar content of galaxy groups and clusters might disfavour the hierarchical structure formation implied by CDM (Balogh et al., 2008).

Some of these problems can be resolved by altering the properties of dark matter. Variations include warm dark matter and self-interacting dark matter. Warm dark matter (Colombi et al., 1996; Bode et al., 2001) streams freely in the early Universe suppressing small scale density fluctuations. This reduces the number of collapsed objects at high redshifts and so solves the missing dwarf problem. However, it also favours reionization at lower redshifts. WMAP's indication that reionization took place at $z_{reion} \approx 11$ therefore disfavours warm dark matter models (Barkana et al., 2001). Self-interacting dark matter (Spergel and Steinhardt, 2000) scatters strongly with itself causing the density profile of galaxies to spread out and better match observations.

Two solutions to the missing dwarfs problem within the ΛCDM paradigm have been put forward. First, if the IGM is significantly reheated at early times then small dark matter haloes cannot cool, accrete baryons, and form stars (Bullock et al., 2001; Macciò et al., 2006). The dwarfs are thus not observed as they remain dark. Second, it has been proposed that high-velocity clouds of H I observed in the local group may constitute the missing dwarfs (Blitz et al., 1999; Westmeier et al., 2007).

Sellwood and Kosowsky (2001) point out that no single dark matter theory solves all the shortcomings of ΛCDM and suggest investigating modified theories of gravity that do not require dark matter. However, Clowe et al. (2006) found empirical evidence for the existence of dark matter that is independent of any law of gravity. Hence dark matter may still play a role, though possibly less significant, under a modified theory of gravity.

An alternative magnetohydrodynamic theory of structure formation has been proposed in which disordered primordial magnetic fields give rise to Lorentz forces that grow perturbations into protogalaxies (Wasserman, 1978; Kim et al., 1996). This can cause collapse at higher redshifts and can thus accelerate reionization (Sethi and Subramanian, 2005; Tashiro and Sugiyama, 2006).

Proponents of the ΛCDM model, however, do not expect it to perform well on small scales and in regions where baryons dominate, such as the centres of galaxies. ΛCDM provides a model for the collapse of dark matter haloes but does not include the many feedback processes involved in the collapse of baryons and the formation of galaxies. The failure of ΛCDM-based structure formation simulations at small scales may not imply that ΛCDM is wrong but that the correct physics of baryon collapse and feedback has not been included. Much work is now being done on high resolution simulations that include hydrodynamics and feedback. Observations of the redshifted 21 cm line of H I may play a significant role in validating these simulations.

2.2.2 Gravitational Instability

The first stage of large-scale structure formation can be understood as the growth of initial density fluctuations due to gravitational instability. Cosmic expansion is slower in relatively dense regions and faster in relatively sparse regions. This causes the density contrast to increase with time.

The theory of structure growth through gravitational instability was confirmed by the two-degree field (2dF) galaxy redshift survey (Peacock et al., 2001). The hypothesis of growth through gravitational instability predicts systematic infall of galaxies onto forming superclusters of galaxies. The distance to galaxies computed from the measured redshift, using the Hubble law, should be erroneous due to the peculiar velocities associated with the infall of galaxies. The 2dF galaxy red shift survey detected these predicted redshift distance errors in a sample of more than 141,000 galaxy redshifts up to a maximum of $z = 0.25$.

Models of gravitational instability are distinguished by the range of fractional density perturbation they apply to. The fractional density perturbation is defined

by

$$\delta \equiv \frac{\rho - \bar{\rho}}{\bar{\rho}} \tag{2.1}$$

where ρ is the density at a given point in space and $\bar{\rho}$ is the mean density. Linear growth theory applies for $\delta \ll 1$ and nonlinear growth theory applies otherwise. In addition to analytic models of linear and nonlinear growth, many researchers approach gravitational instability numerically through N-body simulations.

Linear Growth

The initial growth of perturbations can be represented by the linearised equations of fluid motion under Newtonian gravity. This method gives a closed form solution for the linear growth of the fractional density perturbation

$$\delta \propto t^{2/3} \propto a \tag{2.2}$$

where $a = (1+z)^{-1}$ is the scale factor. This result is only valid for a matter dominated ($\Omega_m = 1$) universe with a single non-fluid matter density component.

Our Universe has four density components: vacuum energy, dark matter, baryonic matter, and relativistic particles (photons and neutrinos). However, Eq. (2.2) is still approximately valid for an extended period when the matter density dominated the dynamics of the Universe's expansion.

Matter domination commenced at the epoch of matter and relativistic particle equality defined by

$$1 + z_{eq} = \frac{\Omega_m}{\Omega_r} \tag{2.3}$$

where $\Omega_r = 4.15 \times 10^{-5} h^{-2}$ is the relativistic particle density parameter assuming $N_\nu = 3$ species of relativistic neutrinos survive from high redshifts. Substituting WMAP5+BAO+SN cosmological parameters gives a numeric value of $z_{eq} \approx 3{,}300$. Matter domination continues until the epoch of matter and dark energy equality when

$$(1 + z_{\Lambda eq})^{-3} = \frac{\Omega_m}{\Omega_\Lambda} \tag{2.4}$$

which gives $z_{\Lambda eq} \approx 0.4$ for the adopted parameters.

Outside the matter domination redshift range $3{,}300 \gg z \gg 0.4$, and for better accuracy within, the solution for linear growth requires numerical integration. However, Carroll et al. (1992) give a useful approximation in the form of the linear growth factor

$$\begin{aligned} D(z) =& \frac{\delta(z=0)}{\delta(z)} \\ =& \frac{5}{2} \frac{\Omega_m(z)}{1+z} \left[\Omega_m(z)^{4/7} - \Omega_\Lambda(z) + \left(1 + \tfrac{1}{2}\Omega_m(z)\right)\left(1 + \tfrac{1}{70}\Omega_\Lambda(z)\right) \right]^{-1}. \end{aligned} \tag{2.5}$$

This factor is only valid if matter behaves as a single non-fluid component.

Over the redshift range $3{,}300 \gg z \gg 0.4$ the Universe is dominated by baryonic matter which behaves like a fluid and by dark matter which does not. Evolution of

the phase space distribution of fluid and non-fluid components is governed by the Boltzmann equation which is usually solved numerically (Seljak and Zaldarriaga, 1996) and summarised in the form of a matter transfer function

$$T(k) = \frac{\delta(k, z = 0)}{\delta(k, z)D(z)}. \tag{2.6}$$

This is the ratio of the growing mode for a given wave-number $k = 2\pi/\lambda$ at the present day to its value at normalisation redshift z projected to the present day by the linear growth factor. The normalisation redshift chosen is irrelevant so long as structures at scales of interest have not entered the horizon by this time. Useful analytic fitting functions to numerical evaluations of $T(k)$ for the ΛCDM cosmology, amongst others, are given by Eisenstein and Hu (1998).

The matter transfer function $T(k)$ describes the wavelength dependent component of linear growth and the linear growth factor $D(z)$ describes the time dependent component of linear growth. Putting both components back together allows the assumed original power law spectrum

$$\left\langle |\delta_k|^2 \right\rangle \propto k^{n_s} \tag{2.7}$$

to be transformed by linear growth to an arbitrary redshift

$$\frac{k^3 P(k, z)}{2\pi^2} = \left\langle |\delta_k(z)|^2 \right\rangle = \delta_H^2 \left(\frac{ck}{H_0}\right)^{3+n_s} T^2(k) D^2(z). \tag{2.8}$$

Here δ_H is the amplitude normalisation of perturbations on the horizon scale today. For a flat universe with $\Omega_\Lambda + \Omega_m = 1$ this may be obtained by a fit to four year Cosmic Background Explorer (COBE) data (Bunn and White, 1997)

$$\delta_H = 1.94 \times 10^{-5} \Omega_m^{-0.785 - 0.05 \ln \Omega_m} e^{-0.95\tilde{n}_s - 0.169\tilde{n}_s^2} \tag{2.9}$$

where $\tilde{n}_s = 1 - n_s$. For WMAP5+BAO+SN parameters this gives $\delta_H = 1.96 \times 10^{-5}$. Alternatively, the amplitude normalisation can be made in terms of σ_8 which is the standard deviation of fractional density perturbations filtered by a spherical top hat of radius $8h^{-1}$ Mpc. Figure 2.1 shows the resulting linear matter power spectrum, normalised to four year COBE data, for WMAP5+BAO+SN cosmological parameters.

The linear matter power spectrum is often expressed in dimensionless form and projected to the present day

$$\Delta^2(k)|_{z=0} = \frac{k^3}{2\pi^2} P(k) = \delta_H^2 \left(\frac{ck}{H_0}\right)^{3+n_s} T^2(k). \tag{2.10}$$

It is pure notational convenience to project the linear matter power spectrum to the present. Linear growth is of course only valid for redshifts when $\delta \ll 1$.

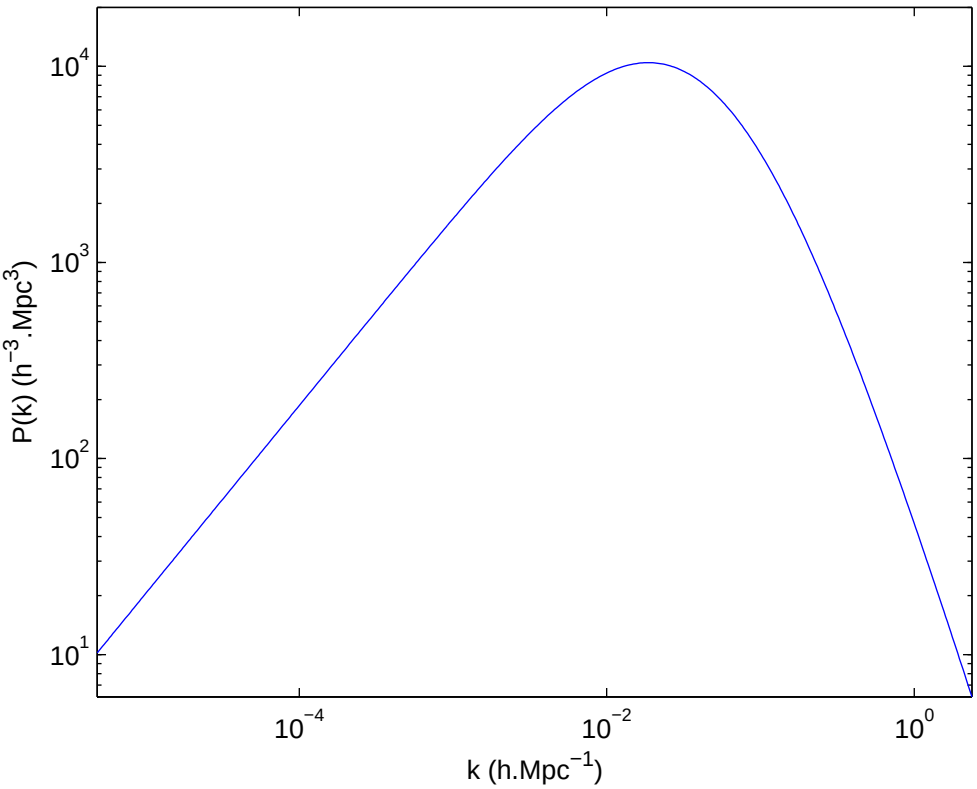

Fig. 2.1: Linear matter power spectrum calculated using a fitting function for the matter transfer function (Eisenstein and Hu, 1998), four year COBE amplitude normalisation (Bunn and White, 1997), and WMAP5+BAO+SN cosmological parameters.

Nonlinear Growth

Linear theory still plays a useful role in approximating nonlinear growth if further assumptions are made. The Press-Schechter (1974) model of hierarchical dark halo formation assumes that the linear spectrum of density fluctuations can be used to predict the nonlinear spectrum of density fluctuations at long wavelengths. Particles at locations more dense than some critical value $\delta > \delta_c$ are considered to have collapsed and formed an object with $\delta = \delta_c$ at a larger scale when the perturbation field is filtered on that scale.

This only accounts for half the mass as the model uses a Gaussian initial perturbation field where half the mass is initially below the mean density and is thus never available for thresholded collapse. Despite this deficiency, when pragmatically corrected by a factor of two, the Press-Schechter model agrees well with detailed simulation (Efstathiou et al., 1988). Bond et al. (1991) give a more rigorous derivation for this factor of two by considering the cloud in cloud problem. Extensions of the model have been made to agree better with simulation (Sheth and Tormen, 1999). A contemporary alternative to the Press-Schechter model is the excursion set model (Sheth and Tormen, 2002).

The Press-Schechter model gives the number density of dark matter haloes with mass in the range $(m, m + dm)$ as

$$n(m)dm = \sqrt{\frac{2}{\pi}} \frac{\bar{\rho}}{m} \left| \frac{d \ln \sigma_R}{d \ln m} \right| \frac{\delta_c(z)}{\sigma_R(m)} exp \left[-\frac{\delta_c^2(z)}{2\sigma_R^2(m)} \right] \frac{dm}{m}. \tag{2.11}$$

Here $\sigma_R(m)$ is the standard deviation of density fluctuations filtered with a spherical top hat filter of radius R corresponding to a volume of universe with mass $m = 4\pi\bar{\rho}R^3/3$ and $\bar{\rho}$ is the mean comoving mass density. The critical density for collapse varies with redshift according to $\delta_c(z) = \delta_c D(0)/D(z)$ where $\delta_c = 1.675$ is the linearised density threshold for collapse in the spherical top hat model for a flat universe with $\Omega_m = 0.28$ (Eke et al., 1996)[3].

The spherical top hat filter of radius R is defined by

$$W_R(r) = \begin{cases} 1 & \text{if } r < R, \text{ and} \\ 0 & \text{otherwise} \end{cases} \tag{2.12}$$

with k-space representation given by the Fourier transform

$$\tilde{W}_R(k) = \frac{3}{(kR)^3} \left[\sin(kR) - kR \cos(kR) \right]. \tag{2.13}$$

The linear matter power spectrum filtered on the scale of R is then $P(k)|\tilde{W}_R(k)|^2$ and the standard deviation of linear density fluctuations on this scale is given by

$$\sigma_R^2(m) = \int_0^\infty \frac{dk}{k} \frac{k^3}{2\pi^2} P(k) \left| \tilde{W}_R(k) \right|^2. \tag{2.14}$$

An advantage of the Press-Schechter model is that it yields a closed form solution for the fraction of mass collapsed into haloes more massive than m_{min}

$$f_{coll}(m_{min}, z) = \int_{m_{min}}^\infty mn(m)dm = \text{erfc} \left[\frac{\delta_c(z)}{\sqrt{2}\sigma(m_{min})} \right]. \tag{2.15}$$

This makes it useful for parameterising structure formation in reionization models.

N-body Simulations

Another line of progress is brute force calculation of the nonlinear N-body problem in an expanding universe. This active field is reviewed by Bagla (2005) and Bertschinger (1998). The first truly cosmological N-body simulations were presented by Press and Schechter (1974) in the same paper as their semi-analytical model discussed above. Current work focuses on including physics other than gravity such as hydrodynamics, chemical reactions, cooling and heating, and radiative transport. There are good prospects for better treatments of feedback and galaxy formation as techniques and hardware advance.

[3] The conventional choice is $\delta_c = 1.686$ for $\Omega_m = 1$.

Tab. 2.2: Working classification of feedback mechanisms in structure formation based on Ciardi and Ferrara (2005).

Negative	Positive
Radiative	
Photoionization	H_2 formation in front of H II regions
Photoevaporation	H_2 formation inside relic H II regions
H_2 photodissociation	H_2 formation by X-ray background
Photoheating filtering	Photoheating smoothing
Mechanical	
Blowout	H_2 formation behind shocks
Blowaway	Shell fragmentation
Impinging shocks	
Convective heating filtering	
Chemical	
Pop III quenching	
Magnetic	
Cloud support	

2.2.3 Feedback

Gravitational instability alone may explain the collapse of dark matter that is weakly coupled, possibly by gravity alone, to baryonic matter. However, the first radiating sources introduce numerous feedback mechanisms that complicate the collapse of baryons and the formation of galaxies.

Effects of the first sources on structure formation were reviewed by Ciardi and Ferrara (2005). Table 2.2 presents a modified version of their working classification of feedback mechanisms. Each mechanism is classified in terms of the polarity of its feedback and the type of physical process involved: radiative, mechanical or chemical. Much effort is being made to include these feedback mechanisms into realistic models and simulations of structure formation.

Radiative

Negative radiative feedback can occur due to photoionization of H I and photodissociation of molecular hydrogen (H_2) by ultraviolet radiation. This suppresses cooling and thus the ability of the baryons to collapse and form further sources. H I can also be photoevaporated out of the host halo if it is heated above the virial temperature of the halo. Further, photoheating of the IGM can raise the Jeans mass at which pressure balances gravity. This suppresses the collapse of baryons into lower mass haloes in the first place and acts as a high-pass filter on the mass distribution of collapsed baryonic objects.

Positive radiative feedback can occur when H_2 reforms in front of ionized hydrogen (H II) regions. It can also occur when H_2 reforms in relic H II regions where

star formation is already suppressed and the gas cools behind shocks produced by gas ejection. An X-ray background can also promote H_2 production by ionizing H I. This produces more free electrons which catalyse the production of H_2 via the creation of negative hydrogen ions (H^-). Another source of positive radiative feedback is photoheating smoothing (Pawlik et al., 2009). Photoionization heating of the IGM by a uniform ultraviolet background smooths out small-scale density fluctuations and therefore reduces the IGM clumping factor defined in § 3.3. This reduces the recombination rate of ionized hydrogen and makes the IGM easier to ionize.

Mechanical

Negative mechanical feedback includes partial *blowout* or complete *blowaway* of gas from galaxies by supernovae. This quenches star formation by removing the material source. Impinging shocks from neighbouring objects can evaporate and/or strip baryonic material. Further, outflows from protogalaxies can heat the IGM by convection. This raises the Jeans mass and prevents baryons from collapsing into lower mass dark matter haloes.

Positive mechanical feedback arises due to the formation of H_2 in cooling gas behind shocks and by the fragmentation of shells. Under some conditions, the expanding shell of gas swept up by the shock of a supernova blast can become unstable and fragment, leading to more star formation.

Chemical

Negative chemical feedback is expected due to the quenching of high-mass population III star formation by the introduction of metals to the IGM from the very same stars. Once metals are present, star formation is biased towards the production of low-mass population II and I stars.

Magnetic

Cosmic magnetic fields may operate as a feedback mechanism. They can be generated by the first generation of supernovae (Miranda et al., 1998) or by the expansion of ionized fronts (Gnedin et al., 2000). Alternatively, primordial fields that exist at recombination may be be amplified by galaxy formation.

Magnetic fields can affect the star formation rate and the stellar mass distribution by raising the magnetic Jeans mass (Rees and Reinhardt, 1972) and by altering the loss of momentum in protostellar collapse to favour flattening along field lines. Frozen-in field lines support clouds across field lines and retard further collapse, fragmentation and thus star formation (Strittmatter, 1966; Kudoh et al., 2007).

2.3 21 cm Cosmology

Observing the redshifted 21 cm line of H I throughout cosmological reionization can constrain the state of baryons throughout structure formation. After recombination

at $z_{rec} \approx 1{,}100$, baryonic matter exists predominantly as H I. The redshifted 21 cm line therefore traces how the baryons cooled from $T_K \approx 3{,}000$ K at recombination, collapsed into the potential wells of dark matter haloes, and were ionized by the first sources of radiation.

Studying the evolution of the 21 cm line with redshift could test hierarchical structure formation theory and identify the significance of the the above feedback mechanisms. Useful determinations might include the time evolution of the temperature, ionization state, density field, velocity field, and chemical make-up of the baryons throughout baryonic collapse; the spectrum of the sources that both heat and ionize the IGM; and the rate and nature of supernovae and mass ejection events in protogalaxies.

Many attempts have been made to detect individual high redshift protoclusters by the 21 cm line with no success. Most current efforts focus on detecting spatial and spectral statistics of 21 cm fluctuations. Fewer efforts are being made to detect the large-scale average (21 cm monopole) that is the focus of this thesis. At least one effort is being made to detect H II bubbles about individual quasars.

2.3.1 21 cm Protocluster Searches

The suggestion that protoclusters might be detectable in redshifted 21 cm emission (Sunyaev and Zeldovich, 1972) prompted a number of searches for discrete sources at high redshifts. The then favoured pancake scenario of structure formation predicted that protoclusters or protosuperclusters would be the first bound objects. Protoclusters were expected to be pancake shaped due to run-away gravitational collapse in one dimension (Zel'Dovich, 1970). Searches for protoclusters were limited by the necessity to search large areas of sky for what were expected to be rare objects.

The first serious search for the redshifted 21 cm line from H I in protoclusters was made at $z = 3.28$ and $z = 4.92$ with the Mk IA telescope at Jodrell Bank (Davies et al., 1978). This search limited the mass of protoclusters to less than $3 \times 10^{15} M_{\odot}$ or the number of protoclusters in the Universe to be less than one million. Further searches were made at $z = 3.3$ using the VLA at Socorro (Hardy and Noreau, 1987; Noreau and Hardy, 1988; Subrahmanyan and Anantharamaiah, 1990; Uson et al., 1991), the Westerbork Synthesis Radio Telescope (de Bruyn et al., 1988; Wieringa et al., 1992), and the Ooty Radio Telescope (Subrahmanyan and Anantharamaiah, 1990). Bebbington (1986) searched at the more interesting redshift of $z = 8.4$ with the Cambridge 6C telescope and placed an upper limit on the number of protoclusters with H I mass greater than $10^{15} M_{\odot}$. An extended list of searches is given by Furlanetto et al. (2006). Despite significant effort, no protoclusters were detected.

The absence of protocluster detections, together with the unimpeded observation of high redshift quasars in Ly-α are consistent with the conclusion that the bulk of structure forming material had been ionized by $z \approx 3.3$ at which most searches were made. It is now appreciated that the Universe is almost completely ionized by $z \approx 6$ due to the incomplete absorption of Ly-α in quasar spectra below this redshift (Becker et al., 2001).

In a modern light, non-detection of the 21 cm line from H I in protoclusters may not come as a surprise. The pancake (top down) theory of structure formation was shown to be incompatible with the normalisation of the linear matter power spectrum by COBE observations of CMBR anisotropy and the observation that galaxies exist at $z \geq 5$. The currently favoured ΛCDM model predicts hierarchical (bottom up) structure formation in which galaxies form first and coalesce into clusters later. Reionization is therefore likely to have completed before clusters and superclusters formed.

2.3.2 21 cm Fluctuation Statistics

Failure to detect isolated protoclusters focused efforts on detecting the smaller, more common, density fluctuations that CDM models predict should form first. Hogan and Rees (1979) suggested a statistical comparison of observed spatial and spectral fluctuations in the 21 cm line to density fluctuations in N-body simulations. Swarup and Subrahmanyan (1987) developed semi-empirical parameters for protocluster searches but also pointed out that sensitivity to density fluctuations in hierarchical CDM models could be enhanced by distinction of 21 cm fluctuations in frequency space or by power spectrum analysis of 21 cm fluctuations.

It was soon realised that measurements of 21 cm fluctuations in hierarchical structure formation scenarios would be limited by sensitivity. The construction of the Giant Metre-wave Radio Telescope (GMRT) in India was largely motivated by the desire to search for both large areas of sky for protoclusters and small areas for faint fluctuations, hoping to distinguish between pancake and CDM scenarios (Swarup, 1984; Swarup and Subrahmanyan, 1987). Scott and Rees (1990) calculated observational parameters for 21 cm line fluctuations under different hierarchical structure formation scenarios. This study showed that a telescope larger than the GMRT might be required to detect 21 cm line fluctuations due to density fluctuations in CDM scenarios.

A number of sensitive, low frequency radio telescope arrays have been proposed to measure the spectrum of 21 cm fluctuations throughout reionization. These include the Low Frequency Array[4] (LOFAR), the 21 Centimetre Array[5] (21CMA), the Murchison Wide-field Array[6] (MWA), the Long Wavelength Array[7] (LWA) and the Square Kilometre Array[8] (SKA).

It is widely perceived that spatial and spectral statistical analysis of data from the above arrays holds the best prospect for detecting and studying the evolution of H I during structure formation. Much work has been put into developing statistical techniques for detection of 21 cm fluctuations with these instruments in the presence of foregrounds (Bharadwaj et al., 2001; Bharadwaj and Srikant, 2004; Bharadwaj and Ali, 2004; Morales and Hewitt, 2004; Furlanetto et al., 2004; Zaldarriaga et al.,

[4] `http://www.lofar.org`
[5] `http://21cma.bao.ac.cn`
[6] `http://www.haystack.mit.edu/ast/arrays/mwa`
[7] `http://lwa.unm.edu`
[8] `http://www.skatelescope.org`

2004; Bharadwaj and Pandey, 2005; Saiyad Ali et al., 2006; Wang et al., 2006; Morales et al., 2006; Datta et al., 2007b).

Understanding of expected 21 cm fluctuations has also progressed significantly. In addition to H I density fluctuations we expect fluctuations due to varying 21 cm spin temperature (Madau et al., 1997) and the peculiar velocity field of H I (Bharadwaj and Ali, 2004; Bharadwaj and Ali, 2005). The assumed set of cosmological parameters can also distort perceived fluctuations along the line of sight (Barkana, 2006). Studying these effects can trace evolution of the large-scale distribution of matter, identify how and when primordial gas was reheated and reionized, identify the sources of radiation and heat, and also constrain cosmological parameters.

Hopes for detecting 21 cm fluctuations at high redshift were recently boosted by the first statistical detection of 21 cm large-scale structure at low redshifts (Pen et al., 2008). This was achieved by correlating the HIPASS 21 cm survey (Barnes et al., 2001) with the six degree field (6dF) galaxy redshift survey (Jones et al., 2004).

2.3.3 21 cm Monopole

Measuring the redshifted 21 cm monopole was suggested by Shaver et al. (1999). The 21 cm monopole is the mean contribution of the redshifted 21 cm H I line on the largest spatial scales. It will be measurable so long as reionization was sufficiently synchronised across different lines of sight and so long as the 21 cm spin temperature decoupled from the radiation temperature of the CBR. Foreground radiation is expected to be sufficiently smooth with frequency to not impede measurements (Shaver et al., 1999).

Measuring the 21 cm monopole would constrain the large-scale average thermal and ionization histories of the IGM, the nature of the first radiating sources, and the cosmological parameters. Much less work has been done on the 21 cm monopole than on 21 cm fluctuation statistics. This is peculiar considering that it may be measured with a single, low cost antenna.

Existing semi-analytic models (Sethi, 2005; Furlanetto, 2006) based on reionization by the overlap of ionized bubbles created by discrete sources show that the information contained in the 21 cm monopole varies through three regimes:

1. absorption (pre-reionization),

2. onset of emission, and

3. emission.

Absorption arises when the spin temperature of H I drops below the radiation temperature of the redshifted CBR. The dense state of the early Universe allows collisions to couple the spin temperature to the matter temperature which falls adiabatically with expansion. Absorption can thus precede the bulk of star and galaxy formation. The onset of emission coincides with the activation of the first significant population of discrete radiation sources. Ly-α radiation from the sources couples the spin temperature to the matter temperature which is concurrently heated above

the CBR temperature by ultraviolet and X-ray radiation from the sources. Emission occurs when the spin temperature of H I is maintained significantly higher than the CBR temperature by an established population of radiation sources.

During absorption, the 21 cm monopole depends only on cosmological parameters, namely $\Omega_m h^2$ and $\Omega_b h^2$, as a significant population of radiation sources has not yet been established. There is significant degeneracy in the determination of these two parameters, but placing a prior on one can allow the determination of the other with comparable precision to WMAP (Sethi, 2005). Determination of $\Omega_m h^2$ through H I absorption is interesting as it is independent of the geometry or the dark energy content of the Universe, unlike CMBR anisotropies and galaxy surveys.

During the onset of emission, the 21 cm monopole depends on the spectrum of the first significant sources of ionizing and heating radiation. The spin temperature is rapidly coupled to the kinetic temperature by Ly-α radiation from the sources. Measurement of the 21 cm monopole at this epoch can determine the ratio of Ly-α to ionizing flux and the volume fraction of the Universe heated by X-rays (Sethi, 2005). The swing from absorption to emission offers the most optimistic monopole amplitudes of order 200 mK. However, this amplitude is much reduced if the IGM is reheated before the spin temperature is coupled to the kinetic temperature (Furlanetto, 2006).

During emission, the 21 cm monopole depends on both cosmological parameters and ionizing sources. The emission traces the ionized fraction which in turn traces the ionizing photon luminosity $\dot{N}_\gamma(0)$, the IGM clumping factor C, and the cosmological parameters $\Omega_m h^2$ and $\Omega_b h^2$. These four parameters can be extracted directly from the signal, albeit with significant degeneracy (Sethi, 2005). In the event that transition from absorption to emission in the monopole is truncated by early heating of the IGM (Furlanetto, 2006), emission alone will still result in a monopole amplitude of order 20 mK. The emission signal is inevitable so long as it is not washed out by variations in reionization history along different lines of sight.

Using WMAP or PLANCK priors on the cosmological parameters allows determination of $\dot{N}_\gamma(0)$ to 50% or 20% respectively (Sethi, 2005). Alternatively, one may extract the ionized fraction in conjunction with $\Omega_m h^2$ and $\Omega_b h^2$. This allows a determination of the ionized fraction that is independent of the underlying source model.

A first effort to detect the 21 cm monopole was made by the Experiment to Detect the Global EOR Signature (Bowman et al., 2007). Early results from this experiment placed an upper limit of 450 mK on the 21 cm monopole assuming a rapid transition to a fully ionized IGM at a redshift of 8. This technique relies on subtracting a polynomial from the system response and detecting the 21 cm monopole in the residual.

This thesis aims for a direct measurement of the monopole rather than a filtered detection. This more general approach requires no assumptions about the expected signal. It however generates stricter requirements for performance and calibration of the measurement system.

2.3.4 H II Bubble Searches

An alternative technique focuses on detecting individual H II bubbles (Wyithe et al., 2005; Datta et al., 2007a). This technique would be particularly relevant in the event that the Universe was reionized by sparsely distributed sources such as the first quasars. In this case fluctuations in 21 cm spin temperature should exist on scales significantly larger than gravitationally induced density fluctuations. First attempts to detect individual H II bubbles are currently being made by GMRT observations targeted on known quasars with Gunn Peterson troughs (Roshi et al., 2006).

Chapter 3

21 CM MONOPOLE PREDICTION

This chapter predicts the 21 cm reionization monopole spectrum using a model that is consistent with contemporary observations. First, the observational constraints on cosmological reionization are reviewed. Second, the state of the intergalactic medium (IGM) prior to cosmological reionization is summarised. Third, general approaches to modelling cosmological reionization are presented. Finally, a specific model for the 21 cm cosmic reionization monopole is presented.

For the power law ΛCDM cosmology described in the previous chapter, the model predicts a reionization monopole with a 282 mK swing from absorption at 101 MHz to emission at 131 MHz. This is followed immediately by 28 mK emission which decays gradually to zero at 193 MHz. This model predicts such a large swing from absorption to emission because it assumes Ly-α coupling of the neutral hydrogen spin temperature to the matter temperature prior to rapid reionization and reheating. The purpose of this assumption is to highlight that models exist that may be usefully constrained by measuring the 21 cm monopole with just 0.1 K sensitivity. However, the swing from absorption to emission may be completely wiped out by pre-heating and so it is conservative to design for 1 mK sensitivity which would resolve the inevitable emission of approximately 28 mK with at least 10% accuracy.

Original contributions in this chapter include:

1. deriving an analytic approximation for the theoretical limit on peak absorption for the 21 cm reionization monopole; and

2. modelling the spectrum of the 21 cm cosmic reionization monopole for power law ΛCDM with WMAP5+BAO+SN cosmological parameters.

3.1 Observational Constraints on Reionization

Observational constraints on cosmological reionization are reviewed by Fan et al. (2006a). Figure 3.1 plots key constraints on the neutral fraction of the intergalactic medium (IGM) and curves for three reionization models: *late*, *early*, and *double*.

The observations do not support rapid and monotonic reionization models such as the *late* and *early* models. *Late* reionization at z = 6-7 (Gnedin, 2004; Gnedin and Fan, 2006) is consistent with measurements of the most distant quasars, particularly observations of Gunn-Peterson troughs in their spectra. However, *late* reionization is inconsistent with the reionization optical depth measured by the Wilkinson Microwave Anisotropy Probe (WMAP). Conversely, *early* reionization at $z \approx 14$ is consistent with WMAP but not the quasar observations. Reionization is therefore likely to be more gradual and/or more complicated than these rapid monotonic models.

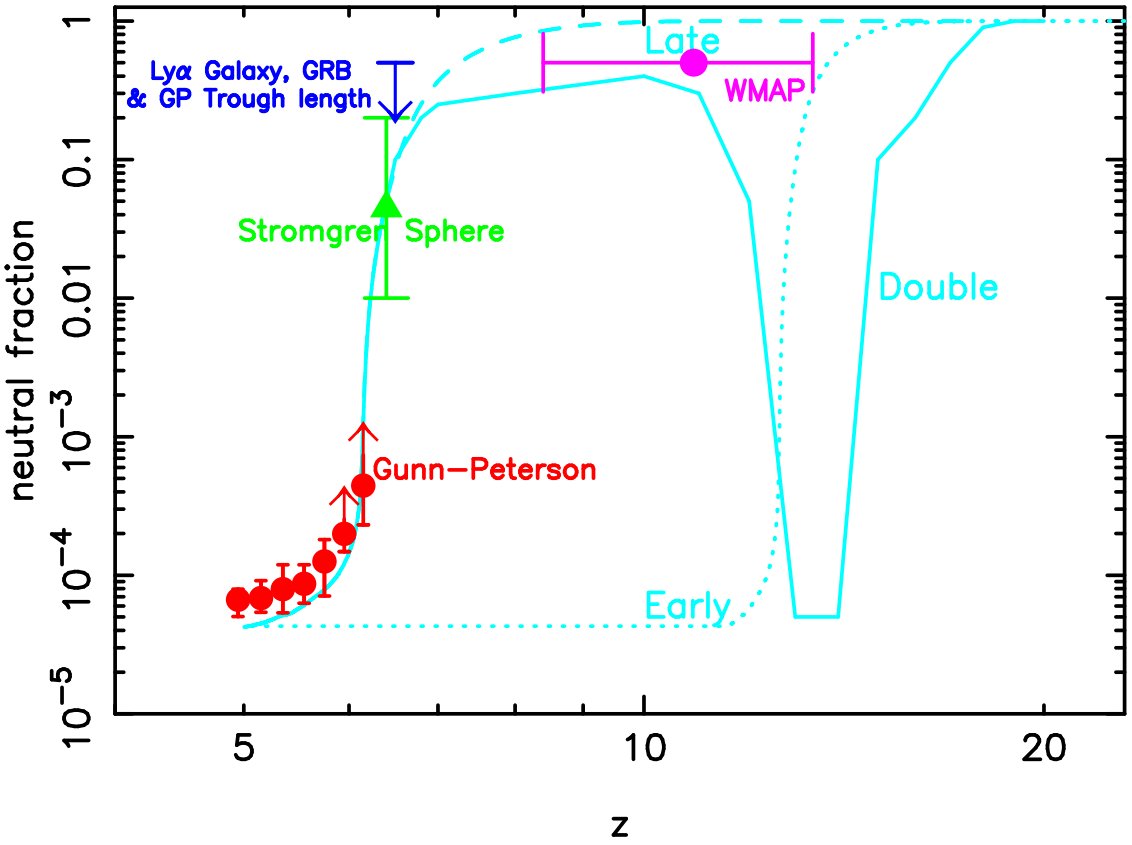

Fig. 3.1: Observational constraints on the volume-averaged neutral fraction of the IGM versus redshift using various techniques (Fan et al., 2006a). The dashed line shows the fiducial model of Gnedin (2004) with late reionization at z = 6-7; see also Gnedin and Fan (2006). The solid line shows an idealised model with double reionization as described in Cen (2003), and the dotted line illustrates the model with early reionization at $z \approx 14$. Reprinted, with permission, from the Annual Review of Astronomy and Astrophysics, Volume 44 © 2006 by Annual Reviews `www.annualreview.org`.

Complex models, including *double* reionization (Cen, 2003), are consistent with the observations but are not strongly constrained by them. More observations are required to test models more complex than the early and late models. This is where observations of the 21 cm reionization monopole could help.

Before turning attention to modelling the 21 cm reionization monopole, this section summarises key observational constraints on the neutral fraction that the 21 cm monopole should be consistent with. The key observations are:

1. temperature and polarization anisotropy of the CMBR;
2. Ly-α line absorption in the spectra of quasars;
3. Strömgren sphere sizes about the most distant quasars; and
4. the luminosity function of Ly-α emitting galaxies.

3.1.1 Cosmic Microwave Background Radiation

Fitting a six parameter ΛCDM model to five year WMAP+BAO+SN data gives a reionization optical depth of $\tau_{reion} = 0.084 \pm 0.016$[1] (Komatsu et al., 2009). This implies a reionization redshift of $z_{reion} = 10.8 \pm 1.4$[1] if reionization was instantaneous (Komatsu et al., 2009).

The WMAP constraint on the reionization optical depth τ_{reion} arises from a joint fit of an instantaneous reionization model to polarisation and total intensity power spectra of CMBR anisotropy. Reionization generates free electrons which can Thomson scatter cosmic background radiation (CBR) photons and therefore generate features in the polarisation spectrum (Page et al., 2007). Reionization also causes a tilt of the total intensity power spectrum.

The reionization optical depth is calculated by integrating the differential optical depth to Thomson scattering

$$d\tau = \sigma_t \bar{n}_e \frac{d\ell}{dz} dz \tag{3.1}$$

from the present ($z = 0$) to the redshift of reionization z_{reion}. In this equation $\sigma_t = 6.65 \times 10^{-29}$ m^2 is the cross section for Thomson scattering of photons by free electrons and $\bar{n}_e$ is the mean number density of free electrons. Integrating this function using the differential metric $d\ell$ for a flat universe with a cosmological constant gives the optical depth τ_{reion} to the redshift of reionization z_{reion}

$$\tau_{reion} = \frac{75\sigma_t(1 - Y_p)\Omega_b hc}{2\pi G m_p} \int_0^{z_{reion}} \frac{x(z')(1 + z')^2 dz'}{\left[\Omega_m(1 + z')^3 + \Omega_\Lambda\right]^{1/2}} \tag{3.2}$$

where $x = \bar{n}_e/\bar{n}_H$ is the ionization fraction, and Y_p is the helium-4 abundance by mass. Here z_{reion} is the redshift of reionization assuming instantaneous reionization.

This calculation neglects the contribution of the ionization of helium to the optical depth. If the reionization of helium is simultaneous with that of hydrogen, it may be included by removing the factor of $(1 - Y_p)$ from the above equation. In

[1] The confidence that the measured value lies in this interval is 68%.

general, a second integral is required for the possibly independent ionization history of helium.

If reionization had not occurred, the optical depth due to Thomson scattering at redshift 10.8 would be approximately 2×10^{-5} which is three orders of magnitude lower than the WMAP measurement of $\tau_{reion} = 0.084 \pm 0.016$. The calculation for the optical depth without reionization assumes that the ionization fraction remains at the residual level expected after recombination. This is approximated by Eq. (3.12) in § 3.2.2.

Reionization models should be made consistent with the WMAP measurement. This can be checked by using Eq. (3.2) to calculate the model optical depth of reionization which should agree with the WMAP measurement. It should be noted that Eq. (3.2) will not be valid for general reionization models (non instantaneous) unless the limit of the integral is made very large. A sensible convention of the upper limit of this integral might be the thermalisation redshift $z_{th} \approx 144$ at which baryons decouple from the thermal background radiation and structure formation can begin. Reionization cannot occur before this time so it makes a useful reference epoch for calculating the reionization optical depth.

3.1.2 Lyman-Alpha Line Absorption

Observations of Ly-α absorption towards high redshift quasars imply a mass averaged neutral fraction in the range $3 \times 10^{-4} < x_{HI} < 0.5$ at $z \approx 6$ (Fan et al., 2006b). The Gunn-Peterson (1965) optical depth due to Ly-α absorption is

$$\tau_{GP} = \frac{\pi e^2}{m_e c} f_\alpha \lambda_\alpha H^{-1}(z) n_{HI} \tag{3.3}$$

where $f_\alpha = 0.4162$ is the upward oscillator strength for the transition and λ_α is the wavelength of the Ly-α transition ($hc/\lambda_\alpha = 10.2$ eV) of atomic hydrogen. At high redshifts, this becomes (Fan et al., 2006a)

$$\tau_{GP}(z) = 4.9 \times 10^5 \left(\frac{\Omega_m h^2}{0.13}\right)^{-1/2} \left(\frac{\Omega_b h^2}{0.02}\right) \left(\frac{1+z}{7}\right)^{3/2} \left(\frac{n_{HI}}{n_H}\right). \tag{3.4}$$

This equation implies that 99.6% of radiation at the Ly-α wavelength is absorbed when the neutral fraction $x_{HI} \equiv n_{HI}/n_H$ is just 10^{-5}. Neutral fractions greater than $x_{HI} \approx 10^{-4}$ are sufficient to cause complete absorption.

As a quasar spectrum redshifts on its journey to the observer, neutral hydrogen along the line of sight causes Ly-α absorption at frequencies progressively more blueward of the quasar's Ly-α emission line. Spectra of quasars at redshifts less than five display a forest of individual absorption lines. These are believed to be caused by velocity and density perturbations in the IGM gas as it falls onto dark matter haloes. Spectra of quasars beyond redshift six are almost completely absorbed blueward of Ly-α. This complete absorption is referred to as the Gunn-Peterson trough and is caused by the fairly uniform neutral gas component of the IGM.

3.1.3 Strömgren Spheres

The size of the ionized region, or Strömgren sphere, around a quasar is a function of the ultraviolet luminosity of the quasar, the quasar's age, and the H I density of the surrounding IGM. The size of a Strömgren sphere is indicated by the difference in the redshift of the onset of Gunn-Peterson absorption and the redshift of the host galaxy. Strömgren sphere sizes about the highest redshift quasars together with quasar population demographics imply that the volume averaged neutral hydrogen fraction was greater than 0.1 at $z \approx 6$ (Wyithe and Loeb, 2004a; Wyithe et al., 2005).

It has since been argued that the systematics of the Strömgren sphere method can lead to order of magnitude uncertainties in the neutral hydrogen fraction (Yu and Lu, 2005). This aside, conservatively assuming that the Strömgren sphere measurement implies $x_{HI} > 1 \times 10^{-2}$ at $z > 6$ yields a lower limit two orders of magnitude above that given by Gunn-Peterson methods.

3.1.4 Luminosity Function of Lyman-alpha Galaxies

The evolution of the luminosity function of Ly-α emitting galaxies constrains the neutral fraction to $x_{HI} \leq 0.25$ at $z = 6.5$ (Haiman and Cen, 2005). As discussed earlier, Ly-α absorption increases strongly with the neutral fraction x_{HI}. At higher neutral fractions this causes significant attenuation and/or distortion of the Ly-α emission line. These effects leave their mark on the luminosity function of Ly-α emitters. A strong drop in their abundance is expected beyond the reionization redshift where the IGM is mostly neutral.

3.2 Initial Conditions of the Baryons

Models of reionization must be consistent with the initial conditions of the baryonic gas prior to reionization. This section summarises the early history of the baryons and highlights important initial conditions for reionization models.

The baryons were generated by big bang nucleosynthesis and were initially hot and ionized. The abundance of free electrons in the early Universe allowed scattering between photons and electrons to keep the baryons in thermodynamic equilibrium with the thermal background radiation.

Following recombination at $z_{rec} \approx$ 1,100, the baryon gas decoupled from the thermal background radiation and was free to cool and fall into the potentials of the large scale dark matter distribution. Important initial conditions of the baryons prior to reionization include their composition, density, temperature, ionization, spatial distribution, and composition. These conditions are well predicted by the cosmological parameters in the ΛCDM model.

3.2.1 Big Bang Nucleosynthesis

Important parameters for the observation of reionization through the 21 cm line of H I include the abundance, density, and temperature of the baryons; and the

H I spin temperature. Prior to recombination, these are determined by big bang nucleosynthesis, cosmic expansion, and the thermal background radiation. The initial conditions of these parameters are summarised here with the exception of the spin temperature which is discussed in detail in § 3.4.

Hydrogen Abundance

The abundances of the elements in the IGM were determined by big bang nucleosynthesis before the commencement of nucleosynthesis in the first stars. This lead to primordial abundances of approximately 75% hydrogen, 25% helium-4, and 0.01% deuterium by mass with smaller amounts of helium-3, lithium and beryllium. Kneller and Steigman (2004) provide a review of big bang nucleosynthesis and Steigman (2006) provides a verification of the theory against observed element abundances.

For the standard models of particle physics and cosmology, the helium-4 abundance by mass is accurately fitted by (Steigman, 2006)

$$Y_p^{FIT} = 0.2384 + \frac{274}{625}\Omega_b h^2, \quad 0.01460 < \Omega_b h^2 < 0.02920. \tag{3.5}$$

This gives $Y_p^{FIT} = 0.248$ for the WMAP5+BAO+SN determination of $\Omega_b h^2 = 0.02265$. Spectroscopy of H II regions yields a primordial helium-4 abundance by mass ranging from $Y_p = 0.223 \pm 0.005$ (Pagel et al., 1992) to Y_p=0.250 ± 0.004 (Fukigita and Kawasaki, 2006). Ignoring isotopes heavier than helium-4, the abundance of hydrogen by mass is approximated by $1 - Y_p$.

Hydrogen Number Density

The proper mean number density of hydrogen nuclei at redshift z in the expanding Universe is

$$\bar{n}_H = (\rho_{crit}/m_H)(1 - Y_p)\Omega_b(1 + z)^3. \tag{3.6}$$

Substituting Y_p^{FIT}, the WMAP5+BAO+SN determination of $\Omega_b h^2$, and the approximation $m_H \approx m_p$ yields the numeric value

$$\bar{n}_H = \left(1.91 \times 10^{-7}\ \mathrm{cm}^{-3}\right)(1 + z)^3. \tag{3.7}$$

Hydrogen Temperature

Before recombination, scattering of photons and electrons keeps the baryonic plasma in thermal equilibrium with the thermal background radiation. The matter temperature T_K therefore follows the same cooling law as the radiation temperature T_γ. This gives

$$T_K = T_\gamma = T_{\gamma 0}(1 + z), \quad z > z_{rec} \tag{3.8}$$

where $T_{\gamma 0} = 2.725 \pm 0.002$ K is the present observed black body temperature of the Cosmic Microwave Background Radiation (CMBR) (Mather et al., 1999).

3.2.2 Cosmological Recombination

Models of cosmological recombination determine the temperature and ionization state of the baryons prior to reionization. As the Universe expanded, it cooled and at some point the thermal background radiation was insufficient to keep the baryons ionized (Peebles, 1968). At this time ($z_{rec} \approx 1{,}100$) the baryonic plasma recombined to form a mostly neutral gas. Later ($z_{th} \approx 144$), scattering due to residual free electrons became ineffective and the baryons decoupled from the thermal background radiation. Baryons, no longer scattered by photons, became free to cool faster and collapse into dark matter haloes allowing galaxy formation. This is known both as the epoch of recombination and the epoch of decoupling.

Ionization Fraction

During the early stages of recombination, the ionization fraction $x = \bar{n}_e/\bar{n}_H$ can be approximated by ignoring everything but hydrogen in the IGM and assuming that thermal equilibrium between electrons, protons, photons, and H I is maintained by the photoionization reaction

$$e + p \leftrightarrow H + \gamma. \tag{3.9}$$

This leads to the Saha (1920) thermal ionization equilibrium equation

$$\frac{x^2}{1-x} = \frac{(2\pi m_e kT)^{3/2}}{n(2\pi\hbar)^3} e^{-B/kT} \tag{3.10}$$

which is accurate for low ionization fractions. After Peebles (1993), substituting the binding energy of hydrogen $B = 13.60$ eV, $n = \bar{n}_H$ from Eq. (3.6), $T = T_\gamma$ from Eq. (3.8), and taking the natural log of both sides gives

$$\ln\left[\frac{x^2}{1-x}\right] = 48.321 - \ln\left[(1-Y_p)\Omega_b h^2 (1+z)^{3/2}\right] - 57916/(1+z). \tag{3.11}$$

Pushing this relationship beyond the appropriate weak ionization fraction domain and solving for $x = 0.5$ gives $z_{rec} \approx 1{,}370$ and $T_{rec} \approx T_{\gamma 0}(1+z_{rec}) \approx 3{,}740$ K. This thermal equilibrium approximation suggests that the primeval plasma is free to combine to atomic hydrogen at this point.

The Saha equation neglects the effect of recombination on the radiation. It assumes that the radiation continues to be a black-body form. However, the temperature of the radiation in the Ly-α line is significantly raised by recombination. This stalls recombination until the excess temperature in the Ly-α line is removed by:

1. two photon decay; or
2. redshifting out of the Ly-α line.

The Saha equation only distinguishes free electrons and those bound in hydrogen atoms, ignoring excitation states and the effects of Lyman series photons generated by electrons relaxing from these states. Hydrogen atoms formed by capturing an

electron to an excited state emit a Lyman series photon when the electron relaxes to the ground state. These photons excite other hydrogen atoms, making them easier to ionize. Further, hydrogen atoms formed by capturing an electron directly to the ground state emit a photon that will very likely ionize other hydrogen atoms.

These considerations imply that two recombination paths will dominate. The first is two-photon decay from the metastable 2s state. The second is the loss of Ly-α photons through the cosmological redshift. This suggests using a three level model (ground/2s/ionized) of the hydrogen atom to calculate the recombination rate and results in a differential equation for the ionized fraction (Peebles, 1968; Zeldovich et al., 1969). Solving this differential equation shows that recombination never completes and that there is a residual ionization fraction at low redshifts. A fit to a numerical solution at $z = 100$ is given by (Peebles, 1993)

$$x_{resid} = 1.2 \times 10^{-5} \frac{\Omega_m^{1/2}}{(1 - Y_p) h \Omega_b} \tag{3.12}$$

which yields $x_{resid} = 2.6 \times 10^{-4}$ for WMAP5+BAO+SN cosmological parameters.

A more detailed treatment of recombination, using a 300-level hydrogen atom model, is given by Seager et al. (1999) and Wong et al. (2007). This model includes the single and double ionization of helium. The code for this model has been made available as RECFAST (Scott, 2008). Figure 3.2 plots the ionization fraction calculated by RECFAST versus redshift with parameters $(\Omega_b, \Omega_c, \Omega_\Lambda, H_0, T_0, Y_p) = (0.0462, 0.233, 0.721, 70.1, 2.725, 0.248)$. Simpler estimates of the ionization fraction from equations (3.11) and (3.12) are plotted on the same axis for comparison.

RECFAST assumes statistical equilibrium for electron shells of principal quantum number $n > 2$. More recently, recombination calculations have been performed for 100-level models but without the assumption of statistical equilibrium (Chluba et al., 2007). The increased accuracy is required for accurate interpretation of CMBR anisotropy measurements. However, the RECFAST calculation is adequate for modelling the 21 cm reionization monopole at this stage where the aim is detection and not yet precision measurement.

Matter Temperature

RECFAST also calculates the drop in the matter temperature below the radiation temperature due to Compton and adiabatic cooling. Figure 3.3 compares the resulting matter temperature to the radiation temperature. The matter temperature does not immediately depart from the radiation temperature upon recombination due to the residual ionization (Peebles, 1968). The matter temperature eventually decouples from the radiation temperature at the thermalisation redshift z_{th}.

The behaviour of the matter temperature may be approximated by

$$T_K \approx \begin{cases} T_{\gamma 0}(1+z) & \text{if } z \geq z_{th} \\ T_{\gamma 0} \frac{(1+z)^2}{1+z_{th}} & \text{if } z < z_{th}. \end{cases} \tag{3.13}$$

The matter temperature is approximated by the radiation temperature for redshifts greater than the thermalisation redshift. Below the thermalisation redshift,

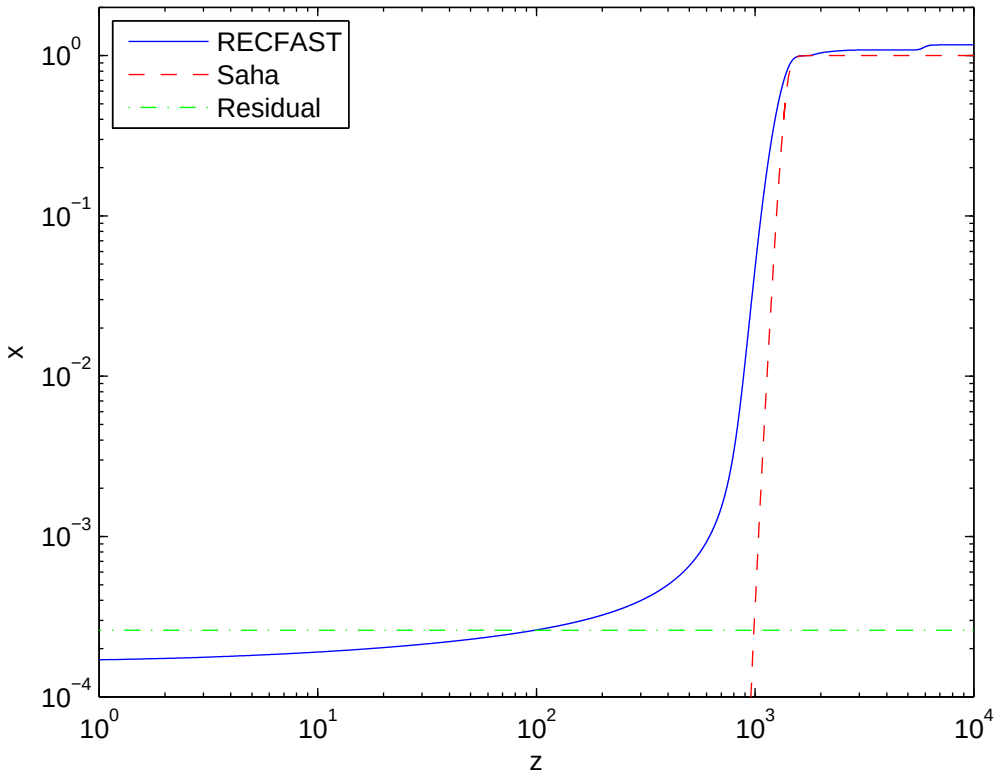

Fig. 3.2: Ionization fraction $x = \bar{n}_e/\bar{n}_H$ during recombination. The solid curve is the RECFAST calculation, including helium, for WMAP3+ALL cosmological parameters and a 300-level hydrogen atom model; the dashed line is the solution of the Saha equation for hydrogen only; and the dash-dot line is the residual ionization at $z = 100$ for a 3-level hydrogen atom model. The ionization fraction calculated by RECFAST exceeds unity at high redshift as it includes the single and double ionization of helium.

the matter temperature is approximated by a pure adiabatic cooling law. Figure 3.3 shows that this approximation agrees reasonably with the detailed RECFAST calculation.

The thermalisation redshift is defined as the redshift at which the characteristic number for the approach to equilibrium between matter and radiation temperature is unity (Peebles, 1993)

$$\frac{t}{T_K}\frac{dT_K}{dt} = \frac{0.0028}{\Omega_m^{1/2} h}\left(\frac{T_\gamma}{T_K} - 1\right)\frac{2x}{1+x}(1+z_{th})^{5/2} = 1. \tag{3.14}$$

Substituting $x = x_{resid}$ from Eq. (3.12) and using $x/(1+x) \approx x$ for $x \ll 1$ gives

$$1 + z_{th} = 740\left[\Omega_b h^2 (1 - Y_p)\right]^{2/5}. \tag{3.15}$$

For WMAP5+BAO+SN cosmological parameters and $Y_p = Y_p^{FIT}$ this gives a numeric value of $z_{th} = 144$. At higher redshifts, the characteristic number is greater

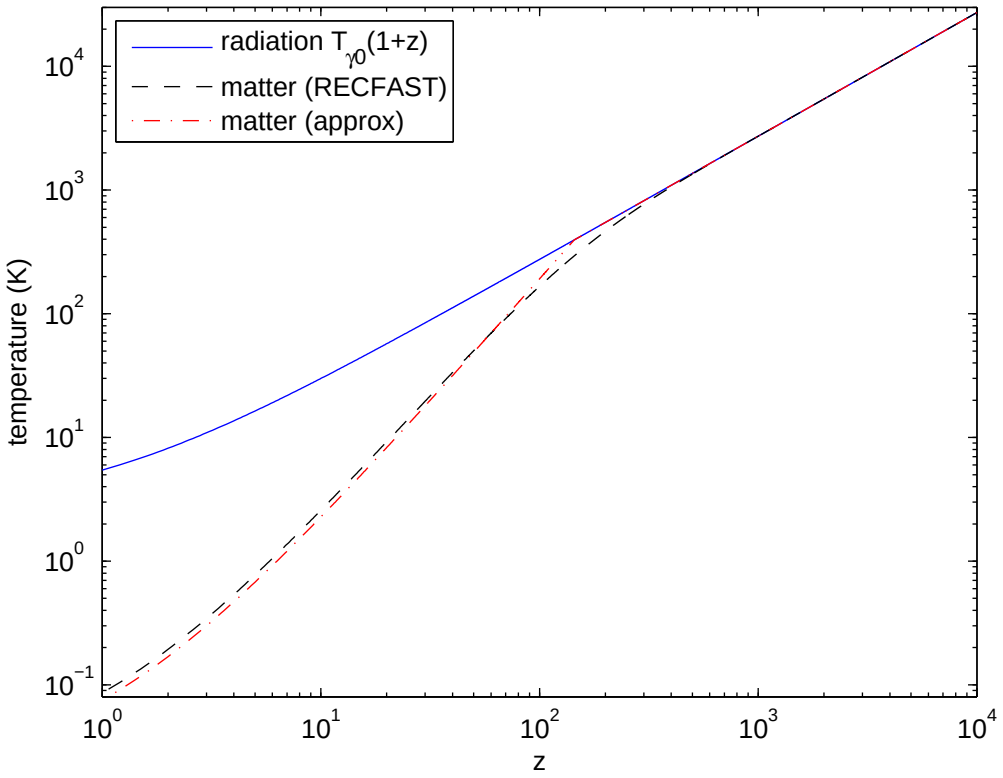

Fig. 3.3: Matter temperature during recombination. The dashed line shows the RECFAST calculation for WMAP3 cosmological parameters; the dash-dot line shows the approximation with pure adiabatic cooling for redshifts lower than the thermalisation redshift z_{th}; and the solid line shows the CBR temperature.

than unity, and the matter temperature is quickly (faster than the expansion time scale) driven to the radiation temperature and is therefore proportional to $1 + z$. At lower redshifts, the universe expands faster than an equilibrium between matter and radiation temperature can be achieved. In this case, the matter temperature cools adiabatically and is proportional to $(1 + z)^2$.

3.3 Modelling Reionization

Physical models of cosmological reionization are reviewed by (Choudhury and Ferrara, 2006). In the the standard model, ionized bubbles grow about discrete ultraviolet sources. Uniform reionization due to distributed sources such as decaying dark matter particles has been suggested (Mapelli et al., 2006) but this is outside the scope of the current work. These models tend to smoothly raise the ionized fraction making it harder to measure than the rapid increase in ionized fraction caused by the overlap of bubbles in the standard model.

The differential change of an ionized volume V_I is the sum of an expansion due to atoms ionized by radiation from the central source and a contract ion due to

recombination (Shapiro and Giroux, 1987). This is represented by the differential equation

$$\frac{dV_I}{dt} = \frac{\dot{N}_\gamma}{\bar{n}_H} - \frac{V_I}{t_{rec}} \tag{3.16}$$

where $\dot{N}_\gamma$ is the rate of ionizing photon emission from the central source, $\bar{n}_H$ is the mean comoving hydrogen density, and t_{rec} is the recombination timescale

$$t_{rec} = \frac{1}{C\alpha_2 \bar{n}_H (1+z)^3}. \tag{3.17}$$

Here $\alpha_2 = 2.6 \times 10^{-13}$ cm^3 s^{-1} is the recombination rate of ionized hydrogen with free electrons to levels $n \geq 2$ and C is the clumping factor which describes the clumpiness of the neutral IGM.

The modelling approach taken in this thesis is to integrate Eq. (3.16) over both time and the mass distribution of collapsed objects given by the Press-Schechter model in Eq. (2.11) to give the ionized fraction $f_{ion}(z)$. The ionized fraction measures the volume fraction of the universe filled by ionized bubbles when $f_{ion} \ll 1$. Simulations show that bubbles begin to overlap at $f_{ion} \approx 0.16$ (ref). Reionization is mostly complete when $f_{ion} = 1$ with only small residual pockets of H I in dense regions.

The clumping factor is defined by (Shapiro and Giroux, 1987)

$$C \equiv \frac{\langle n_H^2 \rangle}{\bar{n}_H^2} \tag{3.18}$$

where the brackets $\langle\rangle$ denote spatial average. It depends on the probability distribution of IGM density fluctuations. This probability distribution cannot be derived analytically due to the many complex hydrodynamic processes involved. However, an empiric probability distribution inspired by hydrodynamic simulations can be chosen (Miralda-Escudé et al., 2000) and its free parameters can be selected so that it is consistent with the distribution of Ly-α absorbers observed in quasar spectra at lower redshifts (Choudhury and Ferrara, 2005).

Alternatively, for a fixed cosmology, a fitting function may be given for the results of numerical hydrodynamic simulations. Pawlik et al. (2009) give the fitting function

$$C_{100}(z) = e^{-0.28z+3.59} + 1.00 \tag{3.19}$$

for the clumping factor in a hydrodynamic simulation using WMAP5 cosmological parameters and no photoheating feedback. C_{100} is specifically the clumping factor for gas with overdensities below a threshold of $\Delta = 100$. This is consistent with threshold densities commonly employed in the literature to calculate the clumping factor. This fitting function is accurate only over $6 \leq z \leq 20$, however it is forced to approach the correct high redshift limit of $C(\infty) = 1$.

3.4 Modelling the 21 cm Line of Neutral Hydrogen

This section summarises basic 21 cm H I line theory that is necessary for developing the 21 cm reionization monopole model in the next section. It shows how 21 cm

emission and absorption can be calculated and presents theoretical limits on peak emission and peak absorption.

A hydrogen atom with parallel electron and proton spins has slightly more energy than a hydrogen atom with antiparallel electron and proton spins. The ground state supports a hyperfine transition where the spin alignment between electron and proton changes from parallel to antiparallel and a photon of frequency $\nu_{21} = 1420.40575$ MHz is emitted in the rest frame. The reverse transition results in absorption of a photon at the same frequency. This phenomenon is known as the 21 cm line of H I.

3.4.1 Spin Temperature

The H I spin temperature is a shorthand means for recording the hyperfine level population distribution of a body of H I. It is the equivalent temperature at which H I in thermal equilibrium would have the same level distribution as the observed gas. Hence the spin temperature is dependent on physical mechanisms that can mix the hyperfine level populations. Such mechanisms include:

1. collisions between H I atoms;

2. collisions between H I atoms and free electrons; and

3. pumping of the levels by Ly-α photons.

The spin temperature can be calculated by (Field, 1958)

$$T_s = \frac{T_\gamma + y_c T_K + y_\alpha T_\alpha}{1 + y_c + y_\alpha} \tag{3.20}$$

where y_c is the collisional de-excitation rate and y_α is the de-excitation rate due to Ly-α pumping. Collisions and Ly-α pumping respectively drive the spin temperature towards the matter temperature T_K and the Ly-α photon "temperature" T_α. In the absence of these mechanisms, the spin temperature relaxes to the background radiation temperature T_γ.

This chapter culminates in a model of the 21 cm monopole for the redshift range $5 < z < 20$. Collisional de-excitation is ignored as the probability of collisions and therefore y_c is small for $z < 20$ due to cosmic expansion. Attention is further limited to models where the Ly-α flux is large enough to give $y_\alpha > T_\gamma/T_\alpha$ and therefore couple the spin temperature to T_α. In regions where Ly-α coupling is effective, T_α quickly relaxes to the matter temperature T_K (Rybicki and dell'Antonio, 1994). The current work therefore uses $T_s = T_K$.

This leads to a larger 21 cm monopole amplitude than would arise from the full treatment of Eq. (3.20). However, $T_s = T_K$ is physically reasonable for the redshift range considered and so it is reasonable to start by trying to constrain this simple optimistic model by observation.

3.4.2 Optical Depth

The optical depth of the 21 cm H I line in the Stefan-Boltzmann limit is given by (Field, 1959)

$$\tau(z) = \frac{3c^3\hbar A_{10}\bar{n}_{HI}}{16k_b\nu_{21}^2 T_s H(z)} \tag{3.21}$$

where $\nu_{21} = 1420.40575$ MHz is the rest-frame frequency of the transition, $A_{10} = 2.85 \times 10^{-15}$ s^{-1} is the Einstein coefficient for spontaneous emission, T_S is the spin temperature and $\bar{n}_{HI}$ is the mean number density of neutral hydrogen atoms. For WMAP5+BAO+SN cosmological parameters, and $Y_p = Y_p^{FIT} = 0.248$ from Big Bang Nucleosynthesis, this becomes

$$\begin{aligned}\tau(z) \approx 1.11 \times 10^{-2}\bar{x}_{HI}&\left(\frac{T_{\gamma 0}(1+z)}{T_S}\right) \\ &\times \left(\frac{1-Y_p}{0.752}\right)\left(\frac{\Omega_b h^2}{0.0227}\right)\left[\left(\frac{0.137}{\Omega_m h^2}\right)\left(\frac{1+z}{12}\right)\right]^{1/2}.\end{aligned} \tag{3.22}$$

where the mean neutral hydrogen fraction $\bar{x}_{HI}$ was introduced by making the substitution $\bar{n}_{HI}{=}\bar{x}_{HI}\bar{n}_H$ in Eq. (3.6). The approximation $H(z) \approx H_0\Omega_m^{1/2}(1+z)^{3/2}$ was also used which is reasonable for redshifts relevant to reionization ($z > 6$).

Eq. (3.22) shows that the 21 cm line is optically thin unless the spin temperature falls more than a factor of 100 below the CBR temperature. In the absence of heating sources independent of the CBR, the spin temperature may drop below the CBR temperature by coupling to the matter temperature. This unlikely scenario results in a minimum spin temperature no more than a factor of 20 below the CBR temperature for $z \geq 6$ (see figure 3.3). The 21 cm line is therefore optically thin.

3.4.3 Excess Brightness Temperature

Absorption or emission due to the 21cm H I line changes the observed brightness temperature of the CBR according to the radiative transfer equation. In the Rayleigh-Jeans limit

$$T(\tau) = T_{CBR}e^{-\tau} + T_s(1 - e^{-\tau}) \tag{3.23}$$

where $T_{CBR} \equiv T_{\gamma 0}(1+z)$. The quantity of interest to the observer is the excess brightness temperature, over the CBR, redshifted to the local rest frame

$$\delta T_b = \frac{T(\tau) - T_{CBR}}{1+z}. \tag{3.24}$$

The fact that the line is optically thin ($\tau << 1$) allows the approximation

$$\delta T_b \approx \frac{(T_s - T_{CBR})\tau}{1+z}. \tag{3.25}$$

Substituting τ from Equation (3.6) then gives

$$\begin{aligned}\delta T_b \approx (30\text{ mK})\, x_{HI}&\left(\frac{T_s - T_{CBR}}{T_s}\right) \\ &\times \left(\frac{1-Y_p}{0.752}\right)\left(\frac{\Omega_b h^2}{0.0227}\right)\left[\left(\frac{0.137}{\Omega_m h^2}\right)\left(\frac{1+z}{12}\right)\right]^{1/2}.\end{aligned} \tag{3.26}$$

Following (Bharadwaj and Ali, 2005), it is useful to separate this into two factors by writing $\delta T_b \approx \eta_{HI} \bar{T}$. The first factor is the "21 cm radiation efficiency" defined by (Madau et al., 1997)

$$\eta_{HI} \equiv x_{HI} \left(\frac{T_s - T_{CBR}}{T_s} \right) \tag{3.27}$$

and the second factor depends only on cosmological parameters and basic constants as follows

$$\bar{T} \equiv (30 \text{ mK}) \left(\frac{1 - Y_p}{0.752} \right) \left(\frac{\Omega_b h^2}{0.0227} \right) \left[\left(\frac{0.137}{\Omega_m h^2} \right) \left(\frac{1+z}{12} \right) \right]^{1/2} . \tag{3.28}$$

3.4.4 Peak Emission and Absorption

Theoretical upper and lower limits can be placed on the mean differential brightness temperature of the 21 cm line during reionization. This defines the maximum possible amplitude of the 21 cm monopole and is therefore provides a useful check of the detailed 21 cm monopole model developed in the next chapter.

Peak possible 21 cm monopole emission of $\max(\delta T_b) = \bar{T}$ occurs when the the 21 cm radiation efficiency η_{HI} defined in Eq. (3.27) saturates at unity. This corresponds to a completely neutral IGM and a spin temperature much higher than the CBR temperature.

Peak possible 21 cm monopole absorption occurs when the IGM is completely neutral and the spin temperature is coupled by Ly-α radiation to the matter temperature predicted in the absence of radiation sources independent from the CBR. Substituting $T_S = T_K$ into Eq. (3.26) and using the approximate matter temperature model of Eq. (3.13) for T_K gives the peak possible 21 cm monopole emission

$$\begin{aligned} \min(\delta T_b) \approx (-333 \text{ mK}) & \left(\frac{z_{th} - z}{z_{th} - 11} \right) \\ & \times \left(\frac{1 - Y_p}{0.752} \right) \left(\frac{\Omega_b h^2}{0.0227} \right) \left[\left(\frac{0.137}{\Omega_m h^2} \right) \left(\frac{12}{1+z} \right) \right]^{1/2} \end{aligned} \tag{3.29}$$

where z_{th} is the thermalisation redshift defined by Eq. (3.15).

These limits are plotted versus redshift in figure 3.4 and versus frequency in figure 3.5. The 114 MHz to 228 MHz ($11.5 > z > 5.2$) range of the second plot corresponds to the operating band of the telescope built for this thesis. A more accurate limit on peak absorption is also calculated using RECFAST to calculate the matter temperature instead of Eq. (3.13).

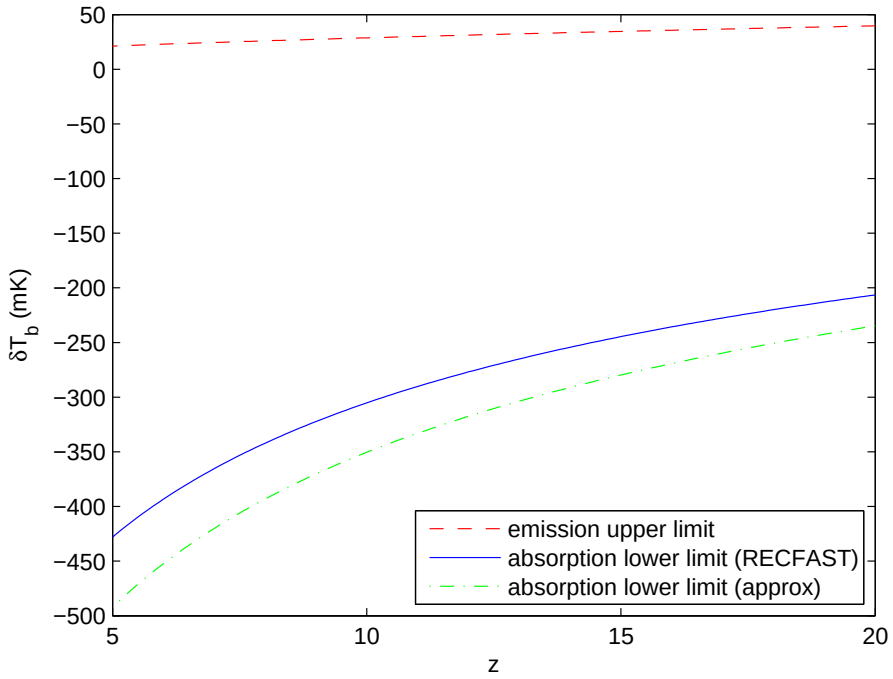

Fig. 3.4: Theoretical limits on 21 cm monopole absorption and emission in standard power law ΛCDM with WMAP5+BAO+SN parameters.

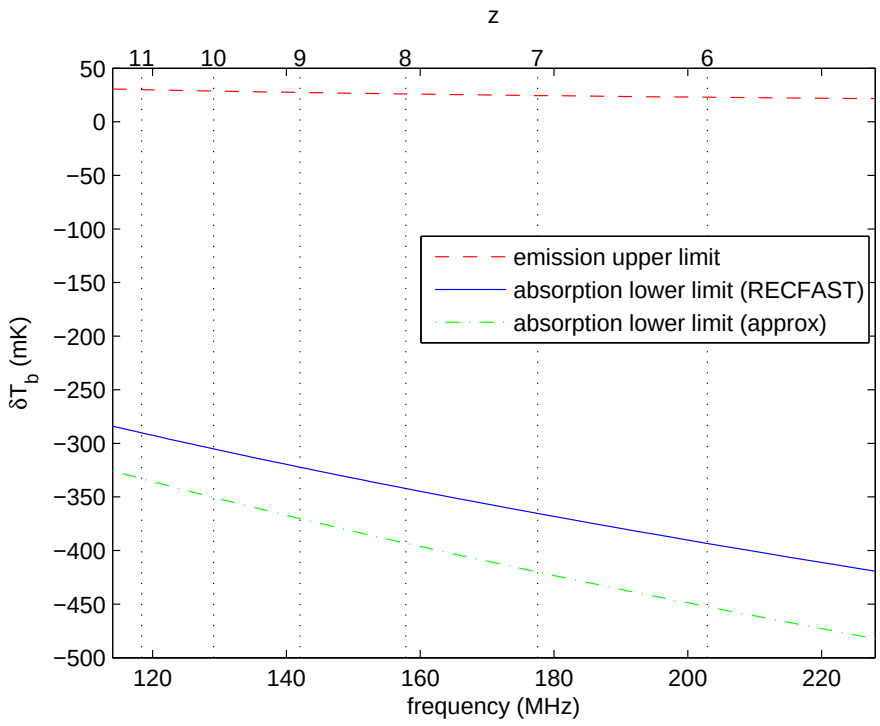

Fig. 3.5: Theoretical limits on 21 cm monopole absorption and emission in standard power law ΛCDM with WMAP5+BAO+SN parameters.

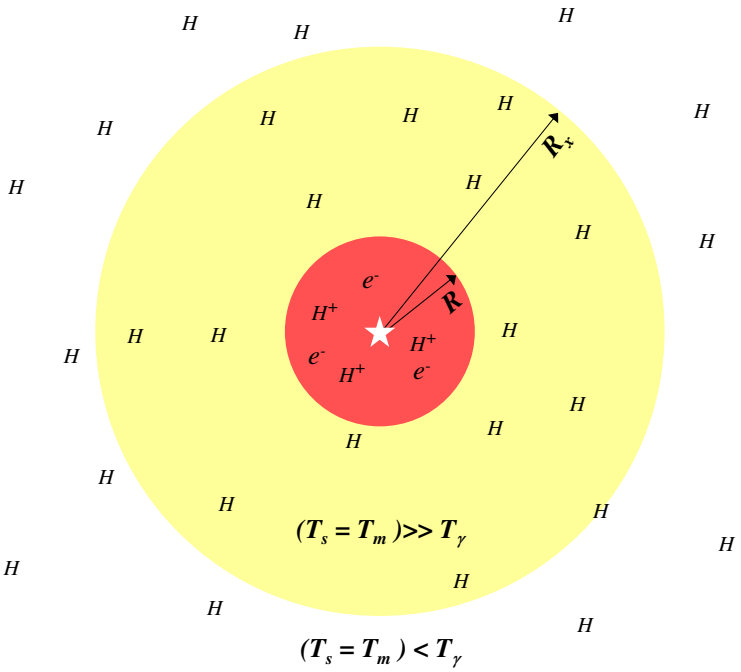

Fig. 3.6: Spherical bubble model for a single source that ionizes a sphere of radius R and X-ray heats a sphere of radius R_x. The spin temperature equals the matter temperature throughout (due to Ly-α coupling) and the matter temperature is heated above the CBR temperature T_γ within the X-ray heated sphere.

3.5 21 cm Monopole Model

This section develops a semi-analytic model for the 21 cm reionization monopole following (Sethi, 2005). The model commences by using the Press-Schechter (1974) method to generate the number density of dark haloes per unit mass. Each halo is assumed to be an ionizing source with luminosity proportional to its mass. Figure 3.6 illustrates the ionized region of radius R and the X-ray heated region of radius R_x that grow about each source. A differential equation that defines the growth of each region is integrated over both time and the mass distribution of collapsed objects given by the Press-Schechter model in Eq. (2.11) to give the ionized fraction $f_{ion}(z)$ and the X-ray heated fraction $f_x(z)$.

An assumption of the model described above is that reionization occurred synchronously over all lines of sight. A full treatment requires consideration of the statistical distribution of the monopole owing to statistical variations between different lines of sight. A weighted average should be formed over different lines of sight to predict the true smoothed (all-sky average) monopole. This averaging would smooth out the sharper features predicted in figures 3.9 and 3.10.

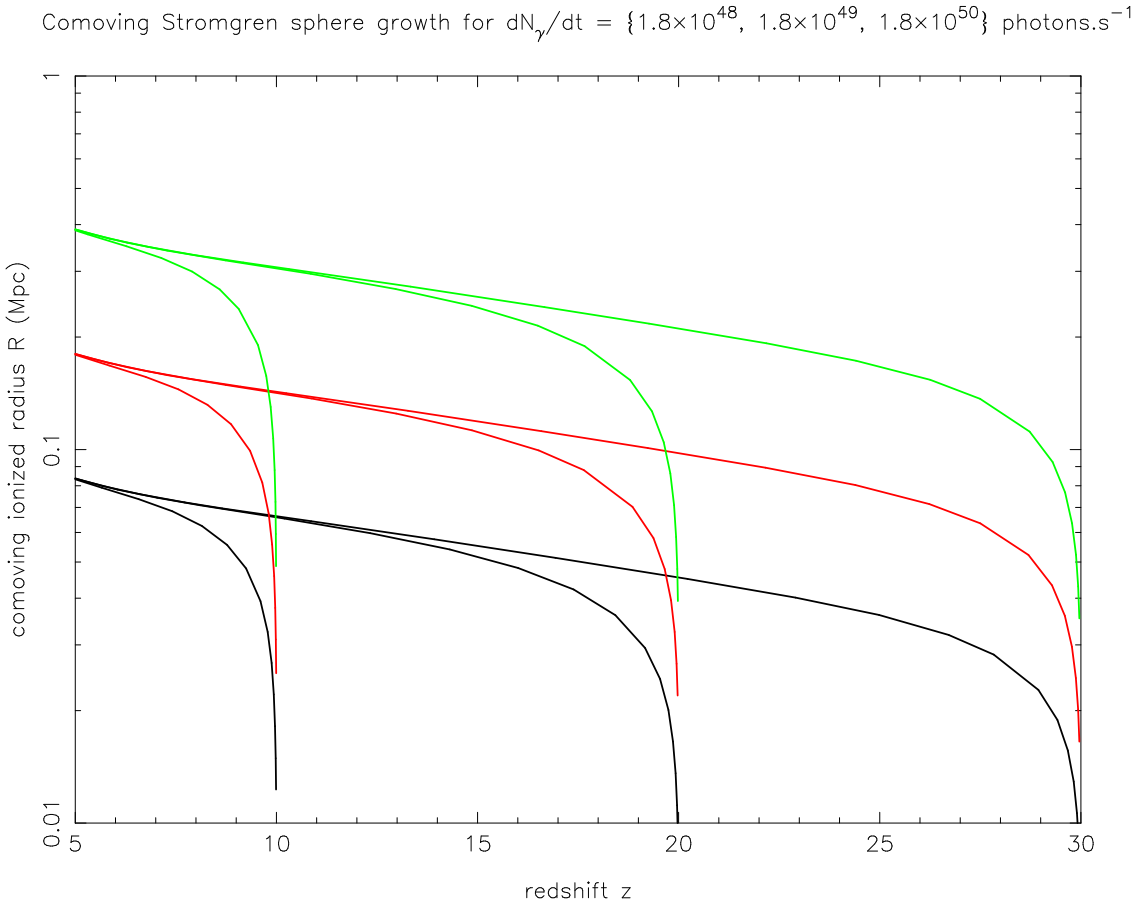

Fig. 3.7: Growth of comoving Strömgren sphere radius according to solution of Eq. (3.30) for different ignition redshifts and central source ionizing luminosities $\dot{N}_\gamma$.

3.5.1 Ionized Fraction

The next step is to determine the volume ionized fraction. The growth of a cosmological Strömgren sphere of comoving radius R about a source of ionizing luminosity $\dot{N}_\gamma$ is described by the differential equation (Shapiro and Giroux, 1987; Wyithe and Loeb, 2004b)

$$\frac{dR}{dt} = c(1+z)\frac{\dot{N}_\gamma - \frac{4}{3}\pi R^3 (1+z)^3 \bar{n}_{H_0}^2 x_{eff} x C \alpha_2}{\dot{N}_\gamma + 4\pi R^2 (1+z) c \bar{n}_{H_0} x_{eff}} \tag{3.30}$$

The ionization of helium is approximately accounted for by $x_{eff} = 1 + pA(\mathrm{He})$ where $p = 0$, 1, or 2 depending on whether helium is mostly neutral, singly ionized or doubly ionized and $A(\mathrm{He}) \approx 0.1$ is the helium abundance by weight relative to hydrogen (Shapiro and Giroux, 1987).

Figure 3.7 shows the evolution of Strömgren sphere radii for a variety of central source luminosities. For this plot and the following work I have adopted the fiducial values $C = C_{100}$ from Eq. (3.18), and $x = x_{eff} = 1$. This ignores helium and assumes that all hydrogen within the bubble is ionized.

It is now possible to combine expressions for the collapsed fraction and the cos-

mological Strömgren sphere radius to yield f_{ion} the volume fraction of the universe that is ionized. The full expression is given by (Sethi, 2005)

$$f_{ion}(z) = \frac{4\pi}{3} \int_{\infty}^{z} \int_{M_{min}}^{\infty} dM \frac{dn}{dM}(M, z') R^3(M, z', z) dz' \tag{3.31}$$

where $R(M, z', z)$ is the radius of the ionized region at redshift z surrounding a halo of mass M that collapsed and ignited at redshift z'. This double integral may be separated if the observation is made that the radius of the ionized region scales approximately linearly with the halo mass: $R^3(M, z'z) \approx M\tilde{R}^3(z', z)$ where $\tilde{R}(z', z) = R(M, z'z)/\sqrt{M}$ (Haiman and Holder, 2003). Substituting this and simplifying gives

$$f_{ion}(z) = \frac{4\pi\rho_{m,0}}{3} \int_{\infty}^{z} \tilde{R}^3(z', z) \int_{M_{min}}^{\infty} dM \frac{dn}{dM}(M, z') M dz' \tag{3.32}$$

Finally, substituting the definition of the collapsed fraction from Eq. (2.15)

$$f_{ion}(z) = \frac{4\pi\rho_{m,0}}{3} \int_{\infty}^{z} \tilde{R}^3(z', z) f_{coll}(m_{min}, z') dz' \tag{3.33}$$

It is now appropriate to recall that the universe is not completely neutral outside the H II bubbles. The actual ionized fraction F_{ion} is a weighted sum of two phases, one completely ionized within the bubbles and one at the primordial residual ionization given by Eq. (3.12) outside of the bubbles. Further, the ionized fraction x has a maximum value of unity whereas f_{ion} exceeds unity once the bubbles overlap. Simulations show that bubbles begin to overlap at $f_{ion} \approx 0.16$. At this point, the above method of calculating the ionized fraction might be abandoned and the equation for the growth of a single ionized volume Eq. (3.16) could be used with an equivalent rate of ionizing photon emission $\sum \dot{N}_\gamma$ representing the combined ionizing background of all ionizing sources within the horizon. For now the following approximation is made

$$F_{ion} = \max[f_{ion} + (1 - f_{ion})x_{resid}, 1] \tag{3.34}$$

This leads to an unphysically sharp completion of reionization rather than a more natural asymptotic reionization as the residual H I is etched away.

The reference ionizing luminosity $\dot{N}_\gamma(0) = 1.8 \times 10^{49}$ photons.s^{-1} was selected to give an optical depth to reionization of $\tau_{reion} = 0.085$, calculated by Eq. (3.2), that agrees well with the WMAP5+BAO+SN measurement of $\tau_{reion} = 0.084 \pm 0.016$. The instantaneous ionizing luminosity is assumed to be proportional to the mass of the ionizing source according to Sethi (2005)

$$\dot{N}_\gamma = \left(\frac{M}{5 \times 10^7 M_\odot} \right) \dot{N}_\gamma(0). \tag{3.35}$$

The minimum star-forming mass $M_{min} = 10^7 M_\odot$ was used as this is found to be the minimum dark matter halo size in which baryons can cool sufficiently quickly to form stars. Sethi (2005) also shows that the ionized fraction predicted by Eq. (3.31) presented in this section is insensitive to the particular value of M_{min}.

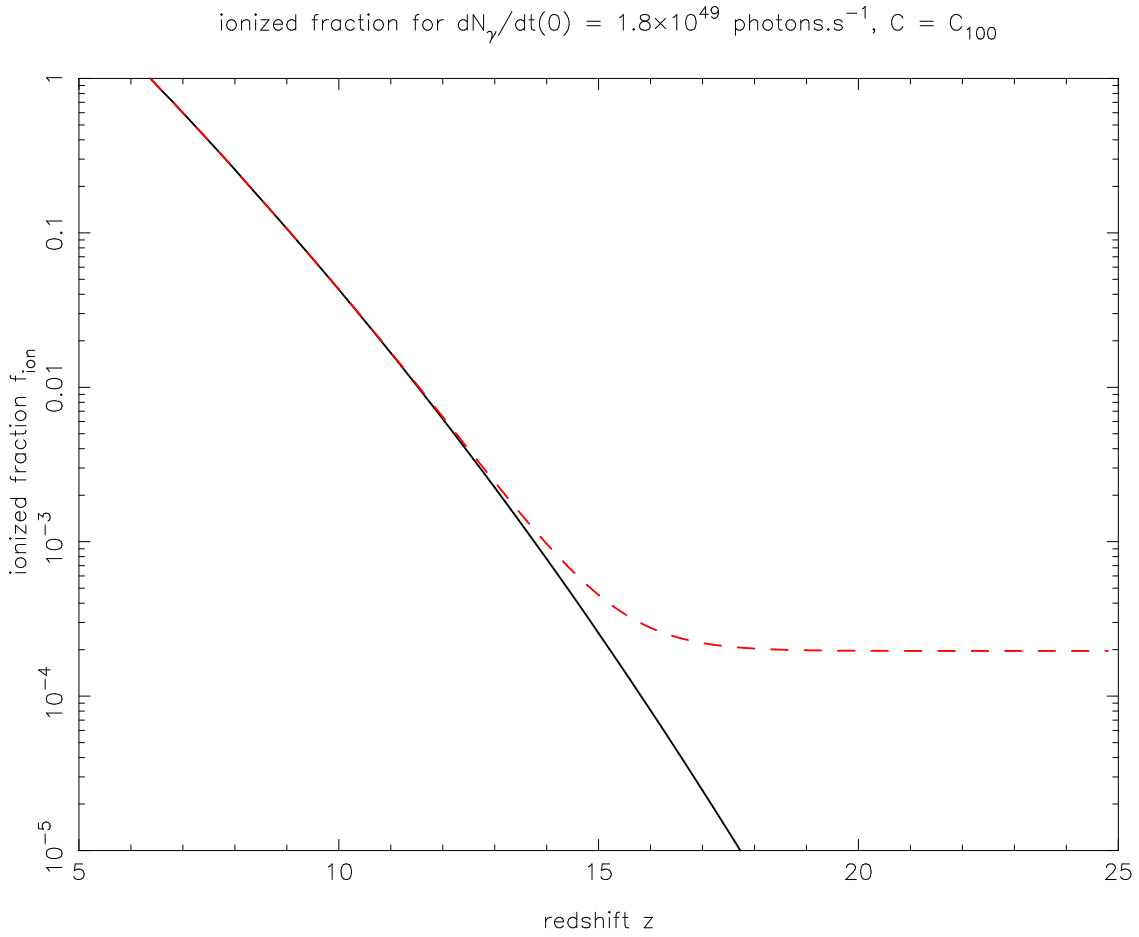

Fig. 3.8: Ionized fraction due to expanding cosmological Strömgren spheres calculated by Eq. (3.33) with fiducial values. Dashed line shows total weighted ionized fraction taking into account residual ionization following recombination (Eq. (3.12)).

3.5.2 X-ray Heated Fraction

Now we turn to the fraction of the universe $f_x(z)$ that is heated significantly above the thermal temperature of CMBR photons at a given redshift. This can be attained by determining the radius R_x about a primordial source where energy injection from X-rays can raise the matter temperature $T_K = qT_{CMBR}$ in the local time. This is done by solving (Sethi, 2005)

$$\frac{\Delta \dot{E}_x(R_x, z)}{H(z)} = k_B q T_{CMBR} \tag{3.36}$$

where the X-ray heating rate at radius R_x is given by

$$\begin{aligned} \Delta \dot{E}_x = \frac{f \dot{N}_\gamma h}{r \pi R^2} \int_{\nu_0}^{\infty} & d\nu \nu^{-1-\alpha} \nu_0^\alpha \\ & \times \left[(\nu - \nu_0) \sigma_{nu}^{HI} + \chi (\nu - \nu_1) \sigma_\nu^{HII} \right] \\ & \times \exp \left[-(n_{HI} \sigma_\nu^{HI} + n_{HII} \sigma_\nu^{HII})(R - r_s) \right] \end{aligned} \tag{3.37}$$

As before, it is assumed that the radius R_x is linearly proportional to collapsed halo mass such that

$$R_x(q, z', z, M) = M\tilde{R}_x(q, z', z) \tag{3.38}$$

and it follows that

$$f_x(z) = \frac{4\pi\rho_{m,0}}{3}\int_{\infty}^{z}\tilde{R}_x^3(q, z', z)f_{coll}(z')dz'. \tag{3.39}$$

The X-ray heated fraction discounting overlapped regions is approximated by

$$F_x = \max[f_x, 1] \tag{3.40}$$

3.6 Monopole Excess Brightness Temperature

The excess brightness temperature of the CBR due to the 21 cm reionization monopole is given by extending Eq. (3.25) to take into account the two phases in the current reionization model:

1. X-ray heated neutral hydrogen of volume fraction $f_x - f_{ion}$ which is seen in emission; and

2. unheated neutral hydrogen of volume fraction $1 - f_x$ which is seen in absorption.

This gives

$$\delta T_b \approx \frac{(T_s - T_{CBR})\tau_{em}}{1+z} + \frac{(T_s - T_{CBR})\tau_{ab}}{1+z} \tag{3.41}$$

where τ_{em} is the H I optical depth of the phase in emission and τ_{ab} is the H I optical depth of the phase in absorption. Substituting Eq. (3.22) for τ and assuming that $T_s >> T_{CBR}$ in the emission phase and $T_s = T_K$ due to Ly-α coupling in the absorption phase leads to

$$\begin{aligned}\delta T_b \approx (30\text{ mK})&\left[(F_x - F_{ion}) + (1 - F_x)\left(1 - \frac{T_{CBR}}{T_K}\right)\right] \\ &\times \left(\frac{1 - Y_p}{0.752}\right)\left(\frac{\Omega_b h^2}{0.0227}\right)\left[\left(\frac{0.137}{\Omega_m h^2}\right)\left(\frac{1+z}{12}\right)\right]^{1/2}\end{aligned} \tag{3.42}$$

Figures 3.9 and 3.10 show an evaluation of the above model for parameters $\dot{N}_\gamma(0) = 1.8 \times 10^{49}$, $C = C_{100}$, $q = 1$, $\alpha = 1.5$. the model predicts a reionization monopole with a 282 mK swing from absorption at 101 MHz to emission at 131 MHz. This is followed by immediately by 28 mK emission which decays gradually to zero at 193 MHz.

The location and steepness of the swing from absorption to emission depends on model parameters. It's location depends upon cosmological parameters, the clumping factor of the IGM, the specific intensity of the ionizing sources, and the X-ray spectral index. It's steepness and overall amplitude are affected by all of the model parameters but are particularly sensitive to the X-ray spectral index and the

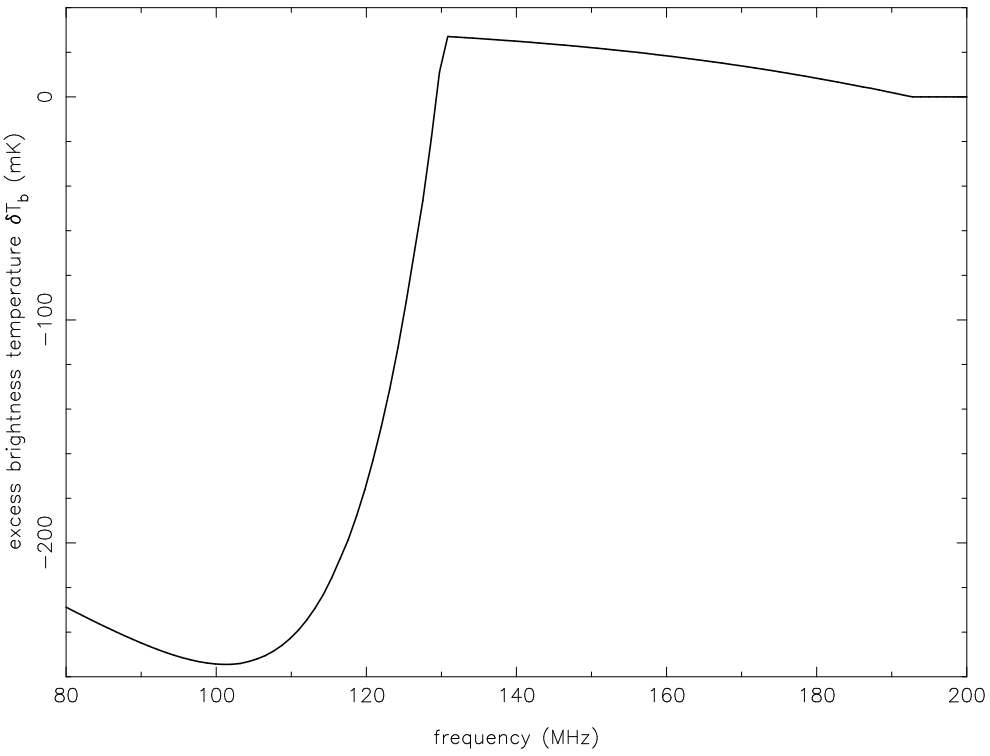

Fig. 3.9: Predicted differential brightness temperature of 21 cm reionization monopole.

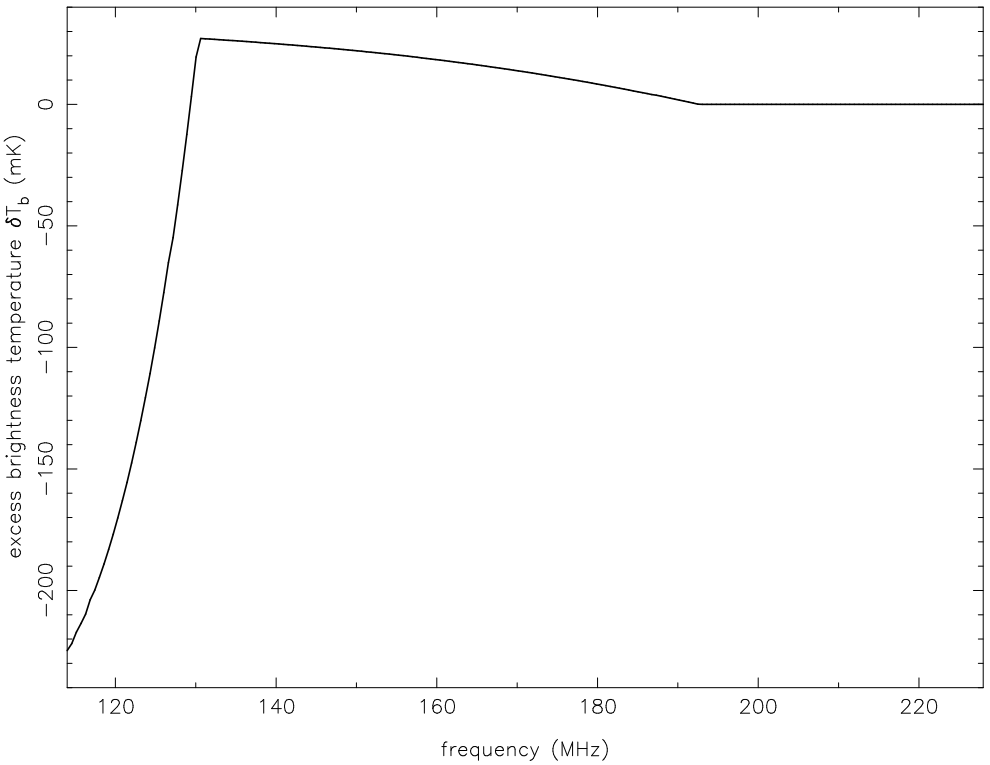

Fig. 3.10: Predicted differential brightness temperature of 21 cm reionization monopole over observation band of this thesis.

ratio of Ly-α to ionizing flux. The current model assumes an arbitrarily high ratio of Ly-α to ionizing flux which promotes a steeper and larger amplitude swing from absorption to emission. The purpose of this bias is to show that there are physically sensible models that can be ruled out by the experiment presented in this thesis even with order 0.1 K sensitivity.

The swing from absorption to emission therefore contains rich information about the spectrum of the ionizing sources. The emission stage depends more on cosmological parameters and the ionized fraction.

3.7 Foreground Emission

A sky brightness model that scales with frequency is necessary to make the calculation of T_A. A simple model consists of a position dependent component $T_g(l, b)$ due to Galactic synchrotron emission, and an isotropic component T_x due to the integrated emission from extragalactic sources.

$$\begin{aligned} T_{sky}(l, b, f) =& T_{g,408}(l, b) \left(\frac{f_c}{408}\right)^{-\beta_1} \left(\frac{f}{f_c}\right)^{-\beta_0} \\ &+ T_{x,178} \left(\frac{f}{178}\right)^{-\alpha} + T_{CMB} \end{aligned} \tag{3.43}$$

The isotropic, extragalactic emission at 178 MHz is $T_{x,178} = 30 \pm 7$ K with an associated temperature spectral index of $\alpha = 2.75 \pm 0.2$K (Bridle, 1967). This spectral index should be flat over the frequency range of interest as there is good evidence that about 80% of extragalactic sources have straight spectra from 26.3 MHz to 1500 Mhz (Bridle, 1967).

The position dependent component also follows a power law, but has a gradual bend in the vicinity of 200 MHz. From 0.5 MHz to 100 MHz, it has a spectral index of $\beta_0 = \beta(0.5, 100) = 2.4 \pm 0.05$ (Clark et al., 1970). From 100 MHz upwards the spectral index gradually increases, approaching 2.9 above 1 GHz. From the 408 MHz, the frequency of the Haslam et al. (1995) map, to $f_c = 151.5$ MHz near our band centre, the mean spectral index is $\beta_1 = \beta(151.5, 408) \approx 2.6$ (Sironi, 1974). There is a position dependent variation of about ± 0.3 about this mean value with lower values towards the local spiral arm and higher values towards regions of minimum sky brightness. This is ignored in the present sky brightness model but could be dealt with by comparing the 408 MHz map with a lower frequency map as done by the LFmap code (Polisensky, 2007).

Part II

SYSTEM DESIGN

Chapter 4

ANTENNA

A single antenna with modest collecting area but good frequency behaviour may be used to detect the 21 cm cosmological reionization monopole. This antenna must facilitate accurate bandpass calibration in the presence of strong foregrounds that are smooth with frequency but spatially complex.

This chapter finds that the antenna's power pattern must vary by less than 4% peak-to-peak at its half-power points to detect 1 mK spectral features in in the presence of a foreground that is 10^5 to 10^6 times stronger. This requirement lead to an investigation of the class of frequency independent antennas.

Two arm, conical log-spiral antennas were explored by method of moments simulation. Log-spirals wound on pyramids rather than cones were also explored as they are easier to construct. Pyramidal log-spiral antennas are log-periodic rather than frequency independent, but still perform well if they have a high aspect ratio and tightly wrapped spirals. It was found that a square based, pyramidal log-spiral antenna can achieve a power pattern with 4% peak-to-peak variation at its half-power points and thus be calibrated to 1 mK accuracy at 1 MHz resolution.

A two arm, square based, pyramidal log-spiral antenna was constructed by winding copper wire on a styrofoam pyramid. This antenna should achieve:

- a full width half maximum (FWHM) beamwidth of 63.8°;
- gain of 9.5 dB over isotropic;
- input return loss higher than 16 dB from 100 MHz to 250 MHz when fed by a 300 Ω impedance;
- a peak side lobe more than 25 dB below the peak response;
- more than 25 dB attenuation towards the horizon when the peak response is directed at the zenith;
- front-to-back ratio exceeding 30 dB;
- ohmic emission ranging from 54 K to 77 K over 114 MHz to 228 MHz at 300 K ambient temperature; and
- left-hand circular polarisation with an axial ratio better than 1.6 for directions with gain within 10 dB of peak.

Original contributions in this chapter include:

1. determining the antenna pattern requirement for measuring the metre-wave sky spectrum with 1 mK accuracy;
2. simulating, constructing, and evaluating a two arm, square based pyramidal log-spiral antenna; and
3. deriving a design equation for the conduction loss of conical log-spiral antennas.

Fig. 4.1: The two arm, pyramidal, log-spiral antenna built for this work.

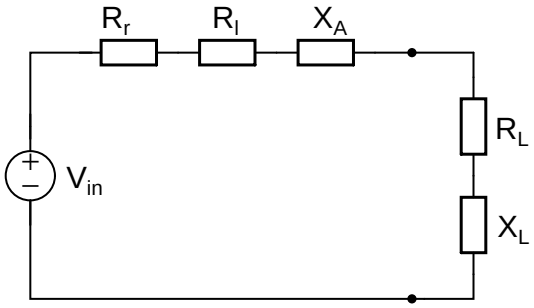

Fig. 4.2: Thévenin equivalent circuit of an antenna in receive mode.

4.1 Antenna Theory

Antenna theory is reviewed in detail by Balanis (2004). The general model of an antenna in receive mode is summarised here for convenience and applied throughout this chapter. This model is distilled into Eq. (4.14), the fiducial antenna measurement equation. Chapter 7 uses this equation to calibrate measurements made with the pyramidal log-spiral antenna introduced in this chapter.

4.1.1 Thévenin Equivalent Circuit

The Thévenin equivalent circuit in figure 4.2 models an antenna in receive mode. This circuit has a voltage source V_{in} that is induced by incident electromagnetic radiation. In series with this source is the antenna input impedance

$$Z_A = R_r + R_l + jX_A. \tag{4.1}$$

This consists of the antenna radiation resistance R_r, the antenna loss resistance R_l, and the antenna reactance X_A. The antenna is connected to a receiver which is modelled as a series load impedance

$$Z_L = R_L + jX_L. \tag{4.2}$$

Power dissipated in the load resistance is delivered to the receiver, power dissipated in the loss resistance heats the antenna, and power dissipated in the radiation resistance is scattered. Modelling the loss as a series resistance is not valid if there is significant dielectric loss or the antenna is situated over a lossy ground.

4.1.2 Antenna Efficiency

Antenna efficiency is the ratio of the power delivered to the receiver to the power captured from free space that is not scattered. It can be broken into two parts: the conduction-dielectric efficiency e_{cd} and the reflection efficiency e_r.

Conduction-dielectric efficiency is the ratio of the captured power that is not dissipated in losses to the total captured power. Network analysis of the equivalent circuit in figure 4.2 shows that the conduction-dielectric efficiency can be expressed as

$$e_{cd} = \frac{R_r}{R_r + R_l}. \tag{4.3}$$

Reflection efficiency is the ratio of the power delivered to a load of arbitrary impedance to the power delivered to a matched load. It arises due to mismatch of the antenna impedance Z_A and the load impedance Z_L and is calculated by

$$e_r = 1 - |\Gamma|^2 \tag{4.4}$$

where Γ is the voltage reflection coefficient

$$\Gamma = \frac{Z_A - Z_L}{Z_A + Z_L}. \tag{4.5}$$

4.1.3 Power at the Receiver Terminals

The power delivered to the receiver P_a can be modelled as the noise power of a resistor, with equivalent noise temperature T_a, that replaces the antenna and is matched to the receiver. The power transferred to the receiver in bandwidth Δf is

$$P_a = kT_a\Delta f \tag{4.6}$$

where k is Boltzmann's constant. When the antenna is matched to the receiver, the equivalent noise temperature T_a at the receiver terminals is the weighted sum of the antenna temperature T_A and the equivalent noise temperature of the antenna losses T_{cd}

$$T_a = e_{cd}T_A + (1 - e_{cd})T_{cd}. \tag{4.7}$$

For a mismatched receiver this becomes

$$T_a = e_r \left[e_{cd}T_A + (1 - e_{cd})T_{cd}\right]. \tag{4.8}$$

The antenna temperature T_A represents the power that the antenna captures from free space that is not scattered. It is a function of the antenna's power pattern and the brightness temperature of the surrounding environment. For conduction losses, the equivalent noise temperature of the antenna losses T_{cd} is the physical temperature of the antenna conductors.

4.1.4 Power Pattern

The directivity pattern $D(\theta, \phi)$, commonly called the power pattern, determines how an antenna couples to electromagnetic radiation as a function of direction. The power pattern and the brightness temperature of the surrounding environment T_B determine the antenna temperature through

$$T_A = \frac{\int_\Omega T_B(\theta, \phi)D(\theta, \phi)d\Omega}{\int_\Omega D(\theta, \phi)d\Omega}. \tag{4.9}$$

Here θ is the zenith angle, ϕ is the azimuth angle, and the integral is made over the solid angle Ω for which the power pattern and brightness temperature are non-negligible. Both the power pattern and the brightness temperature may be functions of frequency.

In a transit observation, the brightness of the surrounding environment is equal to the sky brightness T_s in the forward hemisphere and the ground brightness T_g in the backward hemisphere of the integral. This leads to

$$T_A = \frac{\int_{\Omega_f} T_s(\theta,\phi)D(\theta,\phi)d\Omega}{\int_\Omega D(\theta,\phi)d\Omega} + \frac{\int_{\Omega_b} T_g(\theta,\phi)D(\theta,\phi)d\Omega}{\int_\Omega D(\theta,\phi)d\Omega}. \tag{4.10}$$

For a first approximation, the ground temperature may be assumed to be constant which simplifies the above equation to

$$T_A = \frac{\int_{\Omega_f} T_s(\theta,\phi)D(\theta,\phi)d\Omega}{\int_\Omega D(\theta,\phi)d\Omega} + (1-e_f)T_g \tag{4.11}$$

where e_f is the forward efficiency of the antenna defined by

$$e_f = \frac{\int_{\Omega_f} D(\theta,\phi)d\Omega}{\int_\Omega D(\theta,\phi)d\Omega}. \tag{4.12}$$

For greater accuracy, the ground brightness should be represented by

$$T_g(\theta,\phi) = \left[1 - |\Gamma|^2(\theta,\phi)\right] T_g + |\Gamma|^2(\theta,\phi)T_s \tag{4.13}$$

where Γ is the reflection coefficient of the surface for the polarisation of the wave and T_g is the physical temperature of the ground. This assumes that the ground is in the far field and requires the full evaluation of Eq. (4.10). The final term represents a reflection of the sky brightness in the ground which is seen if the ground reflectivity is high.

4.1.5 Antenna Measurement Equation

The above theory can be distilled into a measurement equation that relates measured and desired quantities. In the present case it relates the measured noise temperature at the receiver terminals T_a to the actual sky brightness T_S. This equation is

$$T_a = e_r \left[e_{cd} \frac{\int_{\Omega_f} T_s(\theta,\phi)D(\theta,\phi)d\Omega}{\int_\Omega D(\theta,\phi)d\Omega} + e_{cd}(1-e_f)T_g + (1-e_{cd})T_{cd} \right] \tag{4.14}$$

All variables in this equation, with the exception of T_{cd} and possibly T_g, may be functions of frequency and thus mask the reionization signal if not accurately calibrated. The goal of this chapter is to find an antenna for which this equation may be successfully inverted by practical calibration methods.

4.2 Requirements for Calibration

The antenna measurement equation identifies five errors that must be calibrated in transit measurements of the radio sky:

1. multiplicative error due to impedance mismatch;
2. multiplicative error due to conduction and dielectric losses;
3. additive error due to conduction and dielectric losses;
4. additive error due to ground emission; and
5. confusion of spatial and spectral features through frequency dependence of the power pattern.

This section determines limits on allowable frequency variation of the antenna pattern for calibration of error (5) with millikelvin accuracy. The initial calibration plan is to model and subtract additive errors (3) and (4) and then use the position dependent component of the galactic foreground as a bandpass calibrator to remove multiplicative errors (1) and (2).

It is assumed that additive errors (3) and (4) can be modelled and subtracted. If this proves insufficient, the conduction loss error could be calibrated by observing the same sky with the same antenna at different physical temperatures. The ground loss error could be identified by inserting absorber, a ground screen, or a transmitter beneath the antenna. Alternatively, a transit observation may be made with the antenna tilted off the horizontal.

Different methods of calibrating the additive contributions have their inherent limitations. The bandpass calibration for the multiplicative terms is done using the galaxy transit. The additive terms due to ground pick-up and conductive losses are expected to be smooth; however antenna mismatch would introduce a frequency dependence. This chapter presents a design for a frequency independent antenna so that error (5) is avoided.

4.2.1 Error Due to a Frequency Dependent Power Pattern

Frequency dependence of the power pattern introduces an additive error. The convolution of Eq. (4.9) can be partitioned into the sum of one convolution with the mean power pattern $\bar{D}(\theta,\phi)$ and one convolution with a delta pattern $\Delta D(\theta,\phi,f)$ describing frequency dependent fluctuations about the mean

$$\begin{aligned} T_A &= \frac{\int_\Omega T_B(\theta,\phi,f)\bar{D}(\theta,\phi)d\Omega}{\int_\Omega D(\theta,\phi)d\Omega} + \frac{\int_\Omega T_B(\theta,\phi,f)\Delta D(\theta,\phi,f)d\Omega}{\int_\Omega D(\theta,\phi)d\Omega} \\ &= \frac{T'_B(f)\int_\Omega \bar{T}_B(\theta,\phi)\bar{D}(\theta,\phi)d\Omega}{\int_\Omega D(\theta,\phi)d\Omega} + \Delta(f). \end{aligned} \tag{4.15}$$

Here the frequency and position dependent sky brightness $T_B(\theta,\phi,f) = T'_B(f)\bar{T}_B(\theta,\phi)$ has been factored into a bandshape $T'_B(f)$ and frequency average position dependent amplitude $\bar{T}_B(\theta,\phi)$. The frequency dependent error $\Delta(f)$ should vary smoothly through a transit observation provided the antenna pattern has no significant side lobes. This variation might be detected and used to form a template for $\Delta(f)$ that can be subtracted. The following section proposes an algorithm that calculates the

error $\Delta(f)$ for a given sky brightness distribution and antenna pattern distribution. This algorithm is used to define the degree of frequency independence required of the antenna pattern for subtraction of $\Delta(f)$ with millikelvin accuracy.

An alternative method of calibrating the additive error due to power pattern frequency dependence $\Delta(f)$ might be to build up a delta pattern model $\Delta D(\theta, \phi, f)$, convolve it with the model sky, and subtract the result from measured spectra. A simulated power pattern could be used to form an initial estimate of the delta pattern. An iterative algorithm could be applied that makes small changes to the delta pattern at each step, convolves it with the model sky, subtracts the result from the measured spectra, and then maximises the smoothness of the corrected spectrum over many such iterations. The correction could be masked at frequencies where features due to reionization are expected and later interpolated to avoid accidental removal of the reionization spectrum.

4.2.2 Error Calculation for a Model Power Pattern

Frequency variation in the power pattern confuses spatial and frequency variations in the brightness temperature. The error $\Delta(f)$ due to this confusion was calculated by numerically evaluating Eq. (4.9) for models of sky brightness and power pattern. Sky brightness temperature was modelled by scaling a 408 MHz all-sky map (Haslam et al., 1981, 1995) to observation frequencies according to the model of Eq. (3.43). It was assumed that the spectral index was -2.4 over the 114 MHz to 228 MHz band. In reality, it varies by ± 0.3 with lower values towards the local spiral arm and higher values towards regions of minimum sky brightness (Sironi, 1974).

The antenna power pattern was modelled as a Gaussian beam

$$G_A(\theta, f) = e^{-(\theta/\gamma)^2} \tag{4.16}$$

perturbed by edge errors

$$\gamma_{edge} = \alpha - \frac{\alpha}{\beta}\frac{|f - 171|}{57}, \quad 114 \ \leq f \leq 228 \tag{4.17}$$

or periodic errors

$$\gamma_{periodic} = \alpha - \frac{\alpha}{2\beta}\left(\cos(f/6) + 1\right). \tag{4.18}$$

Here f is the frequency in megahertz, β determines the magnitude of the frequency dependent perturbations, and α defines the unperturbed beamwidth according to

$$\alpha = \frac{\theta_{FWHM}}{2\sqrt{\ln 2}}. \tag{4.19}$$

The value of α was fixed at 0.67083 corresponding to a FWHM beamwidth of 64°. The edge model is representative of edge effects as it is ideal at the centre of the band and worse towards the edges. Edge effects are expected as a truly frequency independent antenna must be infinite in extent (Mayes, 1992). The periodic model is motivated by the fact that pyramidal approximations of frequency independent antennas are periodic structures.

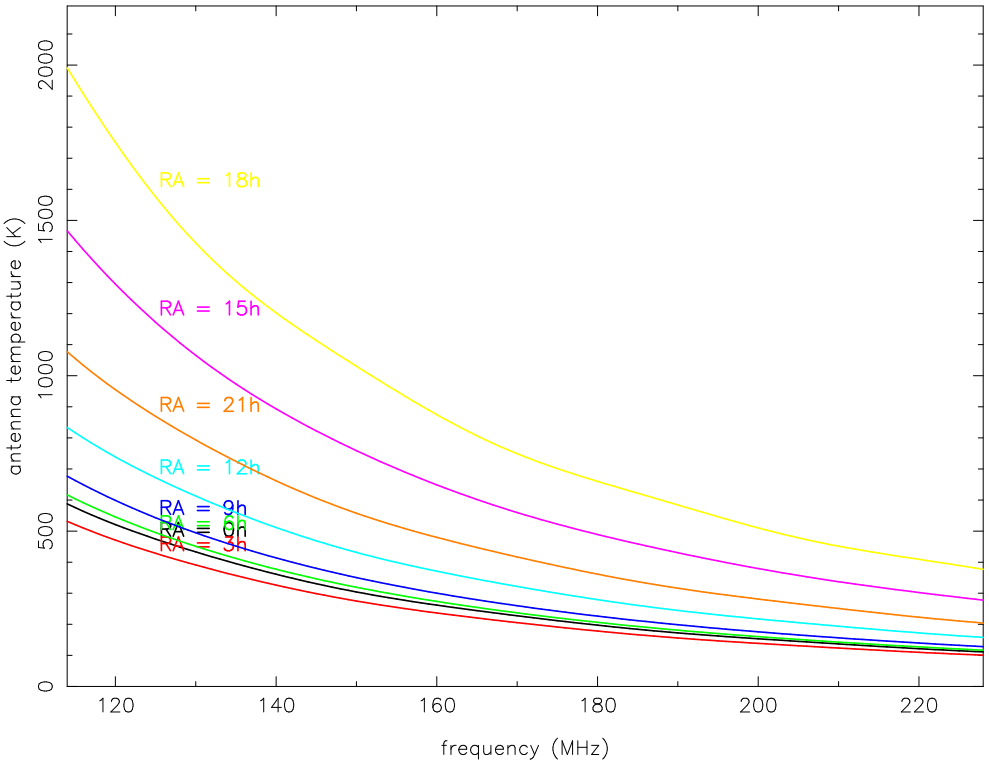

Fig. 4.3: Raw spectrum at antenna terminals for Gaussian power pattern with 64° FWHM and 4% peak-to-peak error at the half-power points caused by periodic perturbations ($\alpha = 0.67083$, $\beta = 37$).

The antenna temperature spectrum was calculated numerically by Eq. (4.9) for eight local sidereal times, 0 hr to 21 hr in 3 hr steps. Figure 4.3 shows simulated spectra for the periodically perturbed Gaussian beam model with $\alpha = 0.67083$ and $\beta = 37$ which generates 4% peak-to-peak error at the half-power points. The power pattern was pointed at the zenith from a latitude of 26° 44.2′ S corresponding to the location at the Murchison Radioastronomy Observatory (MRO) where later measurements were made.

The following algorithm was applied to the simulated spectra in order to determine the error due to frequency dependence of the power pattern:

1. Estimate the antenna bandpass by subtracting the 3 h spectrum from each of the other spectra. These spectra correspond to the differential component of the sky brightness, dominated by local galactic emission, times any bandpass the antenna may have.

2. Normalise the bandpass estimates by their band averages. This stops the total power level from being lost when a given raw spectrum is divided by the bandpass estimate.

3. Calibrate the raw 3 h spectrum by dividing it by each of the normalised bandpass estimates. This flattens the galactic contribution making it easy to separate from the antenna frequency dependence residual in the next step.

4. Subtract the mean from each of the calibrated 3 h spectra to remove the galactic contribution. This leaves the antenna frequency dependence residual divided by the normalised differential galactic contribution with its mean subtracted. Subtracting the mean from the residual is okay as its fluctuation with frequency limits the reionization experiment whereas its absolute level does not.

5. Multiply each of the residuals from the calibrated 3 h spectra generated in the previous step by a normalised template of the galactic contribution given by

$$\frac{T_g}{\langle T_g \rangle} = \frac{f^{-n}}{\frac{1}{f_2 - f_1}\int_{f_1}^{f_2} f^{-n} df}. \tag{4.20}$$

   This is required to correct the residual for having been divided by the normalised differential galactic contribution in the previous step.

6. Subtract the residual spectrum that was bandpass calibrated by the 18 h spectrum from the spectrum calibrated by the 0 h spectrum. This is a template for errors due to frequency dependence of the antenna gain. It would be zero for a frequency independent antenna.

7. Subtract a best fit scaled version of this template from all the other residual spectra generated in step (5).

8. Create a second template by subtracting the residuals of step (7) for 12 h from that for 6 h.

9. Subtract a best fit scaled version of the second template (8) from the residuals of step (7).

The residual spectrum, after the subtraction of two templates, represents the expected bandpass calibration error due to frequency dependence of the antenna's power pattern. Figure 4.4 shows the residuals for a Gaussian power pattern with $\alpha = 0.67083$ and periodic error perturbation with $\beta = 37$ that correspond to the raw spectra in figure 4.3. Table 4.1 gives the residuals for both edge and periodic perturbation models for a 64° FWHM Gaussian power pattern. The phase variation of the periodic residuals in Figure 4.4 suggests that the worst case may be improved upon by averaging calibrated measurements at many hour angles.

4.2.3 Power Pattern Requirement

The above simulations show that the variation of the power pattern with frequency must be limited to 4% peak-to-peak at the half-power points to keep residuals below 1 mK. Both edge and periodic power pattern perturbations gave similar residuals. The amplitude of residuals varies for spectra measured at different hour angles but only the minimum residuals are reported in table 4.1. The worst case residuals are typicaly four times larger, except for the $\beta = 148$ case where they are 7 and 11 times larger for periodic and edge perturbations respectively.

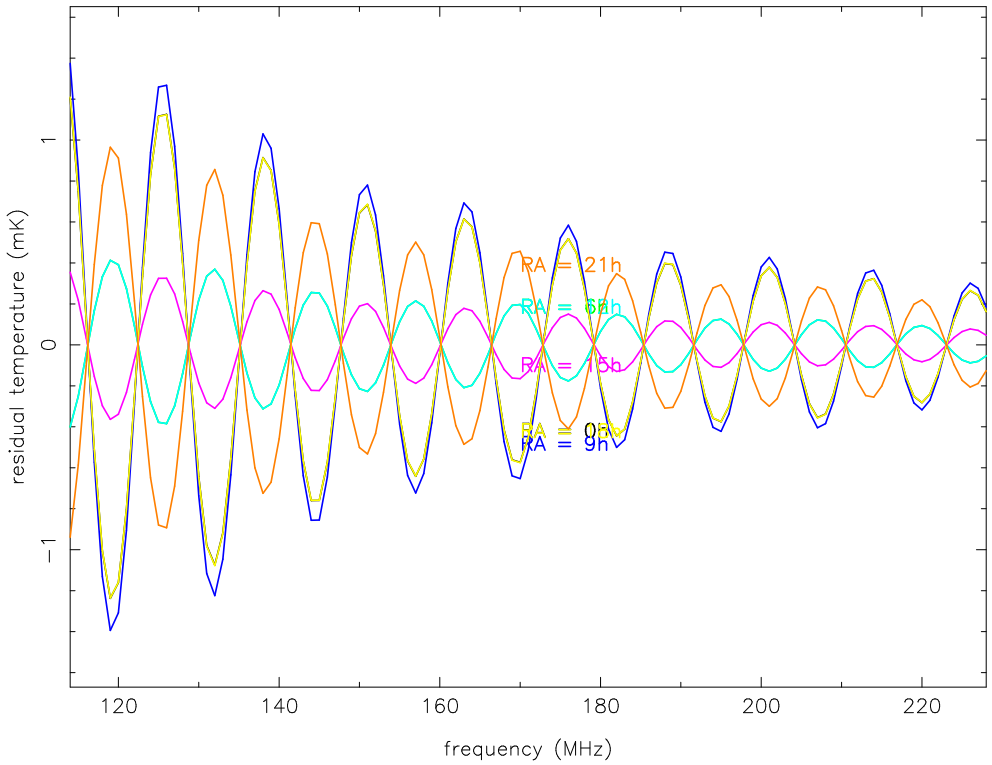

Fig. 4.4: Residual spectra after subtraction of two templates for Gaussian power pattern with 64° FWHM and 4% peak-to-peak error at the half-power points caused by periodic perturbations ($\alpha = 0.67083$, $\beta = 37$).

Tab. 4.1: Additive error $\Delta(f)$ due to frequency dependent power pattern after removal of two templates. Power pattern was modelled by 64° FWHM Gaussian with edge and periodic perturbations.

β	Power pattern error at half-power (pk-pk)	Error in spectrum $\Delta(f)$ (pk-pk)	
		edge	periodic
148	1.0%	0.013 mK	0.012 mK
74	2.0%	0.10 mK	0.096 mK
37	4.1%	0.74 mK	0.72 mK
19	8.1%	4.4 mK	4.2 mK
10	16%	8.9 mK	12 mK

Numerical error was investigated by applying the above algorithm to a 64° FWHM Gaussian power pattern with no frequency dependence. The residuals should have been zero for ideal arithmetic. Double precision floating point arithmetic achieved residuals due to numerical error of 1×10^{-12} K.

4.3 Candidate Antenna Families

The requirement for a near frequency independent power pattern derived in the previous section led to the investigation of two broadband antenna families:

1. frequency independent antennas (Rumsey, 1957, 1966); and

2. log-periodic antennas (DuHamel and Isbell, 1957).

4.3.1 Frequency Independent Antennas

Frequency independent antennas (Rumsey, 1957, 1966) have geometry that is defined only by angles. This leads to frequency independent performance, including impedance and power pattern, so long as low loss conductors are used. Frequency independent antennas have been reviewed by Rumsey (1966), Mayes (1992), Kraus and Marhefka (2002), and Balanis (2004).

The emergence of frequency independent performance from geometry defined completely by angles is backed by two observations:

1. that a low loss antenna maintains the same pattern and impedance when all of its physical dimensions, and the operating wavelength, are scaled by a common arbitrary factor; and

2. that geometry defined completely by angles is congruent with itself when all of its dimensions are scaled by a common arbitrary factor.

Frequency independent performance is more rigorously predicted by showing that, under certain conditions, solutions of Maxwell's equations applied to an antenna geometry that is invariant under scaling are themselves invariant under scaling. This was demonstrated by Rumsey (1966) for lossless materials and is repeated here for the more general case of lossy materials.

Take Maxwell's equations in time harmonic form

$$\nabla \wedge \mathbf{E} = -j\omega\mu\mathbf{H} \tag{4.21}$$

$$\nabla \wedge \mathbf{H} = -(\sigma + j\omega\epsilon)\mathbf{E} \tag{4.22}$$

and make the substitutions

$$\omega\sqrt{\epsilon\mu} = 2\pi/\lambda \tag{4.23}$$

$$Z_0 = \sqrt{\epsilon\mu}. \tag{4.24}$$

Scaling the spatial dimensions with wavelength such that $x = \lambda x'$, $y = \lambda y'$, and $z = \lambda z'$ gives the result

$$\nabla' \wedge \mathbf{E} = -j2\pi Z_0 \mu \mathbf{H} \tag{4.25}$$

$$\nabla' \wedge \mathbf{H} = -(\sigma\lambda + j2\pi Z_0^{-1})\mathbf{E}. \tag{4.26}$$

This shows that the electric field will be independent of frequency under the condition that μ and ϵ are independent of frequency and that the antenna and surrounding media are lossless ($\sigma = 0$). This implies that an antenna's electromagnetic performance will be independent of frequency so long as its geometry is invariant under scaling where angles are preserved. This argument also applies to antennas that include dielectric and/or magnetic material(s). However, as for conductors, the geometry of any such material must be defined completely by angles.

For the case of lossy materials, Eq. (4.26) shows that solutions to Maxwell's equations are independent of frequency only if the conductivity is inversely proportional to wavelength. Therefore, the conductivity of a frequency independent antenna's conductors must vary inversely with the width of the conductors.

Geometry defined only by angles is infinite in extent but a practical antenna must be finite. This places a further requirement on a practical frequency independent antenna: that it must attenuate (radiate) continuously along its length. This allows the antenna to be truncated at its larger end, at a point where the majority of power has been radiated, without causing large reflections that destroy frequency independent performance. A practical frequency independent antenna must also be truncated at its smaller end where it is fed. The points of truncation are additionally limited at the small end by manufacturing accuracy and at the large end by the requirement for a manageable antenna size.

Examples of frequency independent antennas include the planar log-spiral and the conical log-spiral which is illustrated in figure 4.5. These spiral antennas require only a rotation to be congruent with themselves after scaling. Their electromagnetic properties are therefore independent of frequency to within pattern rotation. They are good candidate antennas for the reionization experiment if their patterns can be made rotationally symmetric, or if errors due to pattern rotation can be calibrated.

4.3.2 Log-Periodic Antennas

Log-periodic antennas (DuHamel and Isbell, 1957) are another family of broadband antennas that may satisfy the near frequency independent power pattern requirement of the reionization experiment. These antennas have impedance and pattern properties that vary periodically with the logarithm of frequency. Their geometry is only self congruent after scaling by integer powers of the geometric ratio τ

$$\tau = \frac{R_n}{R_{n+1}},\ 0 < \tau \leq 1. \tag{4.27}$$

In this relationship R may chosen as any convenient physical dimension of the antenna. These antennas have performance that repeats at wavelengths satisfying

$$\tau = \frac{\lambda_n}{\lambda_{n+1}}. \tag{4.28}$$

These wavelengths are evenly spaced in log space

$$\log \lambda_{n+1} - \log \lambda_n = \log \left(\frac{1}{\tau} \right) \tag{4.29}$$

therefore antenna performance is periodic with the logarithm of frequency. As for frequency independent antennas, conductors should be practically lossless. If not, their conductivity should scale in inverse proportion to physical dimensions according to

$$\tau = \frac{\sigma_{n+1}}{\sigma_n}. \tag{4.30}$$

This is usually ignored for small antennas made from good conductors.

Log-periodic antennas can approach frequency independence if the variation in performance over one period is made small. Alternatively, the value of τ can be increased which shortens the period of performance repetition. Some log-periodic antennas approach frequency independence in the limit as τ tends to unity. These antennas may be useful for the reionization experiment if power pattern variation over the period is small, or if the period is shorter than the required spectral resolution and can therefore be averaged over. Systematic errors due to antenna performance may be reduced by averaging spectra over integer log-periods. This implies an averaging bin bandwidth that scales with the logarithm of frequency. If performance variation is exactly log-periodic, it might be detected and removed by Fourier analysis in log-frequency space.

4.4 Conical Log-Spiral Antenna

The balanced, two arm conical log-spiral antenna (Dyson, 1959) was investigated for this experiment as its unidirectional antenna pattern, circular polarisation, and matchable input impedance are all stable over 12:1 and possibly 30:1 bandwidths. The unidirectional pattern reduces additive contributions due to ground emission. Circular polarisation is an advantage as polarisation of the galaxy dominated sky-brightness tends to be linear. Using a circularly polarised antenna reduces fluctuations in the measured spectrum due to variations in orientation of the antenna with respect to the polarisation angle of the sky-brightness.

4.4.1 Geometry

The geometry of the conical log-spiral antenna is illustrated in figure 4.5. It is defined by the half-cone angle θ_0, the wrap rate angle of the spiral arms α, and the angular width of the conductors δ. The otherwise infinite spiral is truncated at the small end where the cone has diameter d and at the large end where the cone has diameter D.

For a constant thickness ($\delta = 0°$) spiral, the radius ρ in the plane of the cone from the virtual apex to a point on the first spiral arm can be parameterised in terms of angle the angle ϕ. The parametric equation for the first spiral arm is

$$\rho = \rho_0 e^{b\phi} \tag{4.31}$$

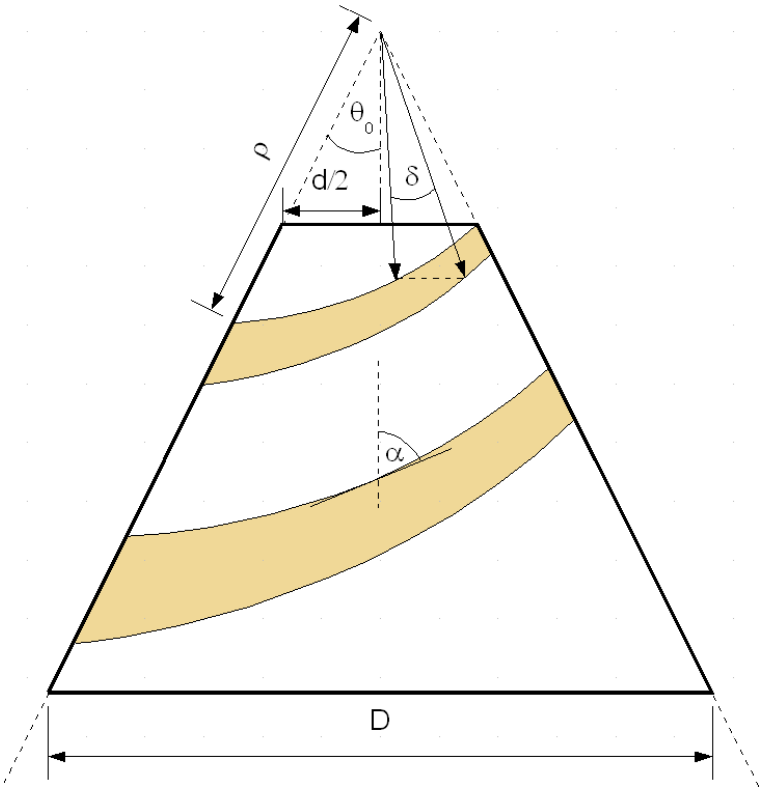

Fig. 4.5: Conical log-spiral antenna geometry.

where

$$b = \frac{\sin\theta_0}{\tan\alpha}. \tag{4.32}$$

and ρ_0 is the radius to the start of the first spiral arm. The radius to the second arm of a two-arm spiral is obtained by multiplying Eq. (4.31) by $e^{-b\pi}$. Distance along the conductor from its imagined beginning at the virtual apex is given by

$$l = \rho \sec\alpha. \tag{4.33}$$

4.4.2 Principle of Operation

Partitioning the antenna into a transmission line region and an active region facilitates understanding of its operation. In the first section of the spiral, the spiral arms have diameters small compared to a wavelength. When the two arms are fed out of phase they are sufficiently coupled to act as a transmission line. Little power is radiated in the transmission line region and it therefore has little affect on the antenna's pattern properties.

The active region occurs further along where the spiral arms have diameters close to one wavelength. Here the relative phasing of the two arms changes significantly over each turn of the spiral. The resultant current distribution causes the active region to behave as an end-fire array that radiates towards the apex of the cone. The amplitude weighting of the effective array elements is to first order governed by the match between wavelength and loop circumference. This makes

the amplitude weighting qualitatively comparable to that of a binomial array in that it is symmetric and has a peak in the centre. The active region determines the antenna's pattern properties as it is where the majority of power is radiated. Frequency independence is achieved when the current distribution in the active region is not significantly altered by the truncation necessary to make a practical antenna.

4.4.3 Design and Performance

The guide for designing conical log-spiral antennas given by Dyson (1965) was used to design an antenna that is practically frequency independent over a large bandwidth. The design space was limited to the more manufacturable subset of antennas made from constant width conductors ($\delta = 0°$) of constant conductivity. Using constant width conductors increases the antenna impedance but has little effect on the pattern so long as $\theta_0 \leq 10°$ and $\alpha \geq 75°$ (Dyson, 1965). It also reduces the front-to-back ratio which is maximised for a self complementary antenna with $\delta = 90°$. This can be compensated for by using a smaller half-cone angle θ_0 and/or a higher wrap-rate angle α, both of which increase the front-to-back ratio.

Dyson (1965) measured the size of the active region by changing the frequency of measurement to move the active region of an antenna relative to its truncation points. He found that the far field pattern was insignificantly altered so long as the near field was at least 15 dB down from its maximum at the large end of the antenna and at least 3 dB down from its maximum at the small end. The operating bandwidth of the active region can be defined empirically as

$$B_{ar} = \frac{a_{15^+}}{a_{3^-}} \tag{4.34}$$

where a_{3^-} is the radius of the cone at the point on the feed side of the active region where the near field is 3 dB below its peak. Similarly, a_{15^+} is the radius of the cone on the far side of the active region at the point where the near field is 15 dB below its peak.

The structural bandwidth of the antenna structure is defined by

$$B_s = \frac{D}{d} \tag{4.35}$$

where D is the diameter of the cone at the base and d is the diameter of the cone at the point where it is truncated near the apex. The active region must fit within the antenna structure for acceptable performance. This requirement defines the operating bandwidth

$$B = \frac{B_s}{B_{ar}}. \tag{4.36}$$

The active region bandwidth is reduced, and hence the operating bandwidth is increased, for smaller half-cone angles θ_0 and higher wrap-rate angles α.

The geometry of the closest conical spiral antenna to the pyramidal spiral built for this experiment is summarised in table 4.2. It adopts $\theta_0 = 10°$ and $\alpha = 87.5°$ corresponding to the higher active region bandwidth end of the parameter space explored by Dyson (1965). Dyson explored up to $\theta_0 = 2°$ and $\alpha = 85°$. The built

Tab. 4.2: Antenna geometry for this work.

Symbol	Value	Description
θ_0	10°	cone half-angle
α	87.5°	rate of wrap of spiral arms
δ	0°	angular width of spiral arms
D	1,163.4 mm	diameter of cone at base
d	56.6 mm	diameter of cone at apex
a_w	0.28 mm	conductor radius

Tab. 4.3: Antenna performance predicted according to (Dyson, 1965).

Symbol	Value	Description
B_{ar}	1.5	bandwidth of the active region
B_s	21:1	structural bandwidth
B	14:1	antenna operating bandwidth
$\overline{\text{HPBW}}$	$56° + 8°$	average half-power beamwidth
ΔHPBW	5°	approximate variation in half-power bandwidth over wide bandwidths
D_0	10 dB	approximate maximum directivity
FBR	$\geq$ 15 dB	minimum front to back ratio
Z_A	300 Ω	approximate characteristic impedance

antenna has a larger θ_0 which makes it a more stable and manageable structure. The resulting reduction in active region bandwidth is compensated by the built antenna's higher value of α.

Performance of the conical log-spiral antenna defined in table 4.2 was predicted according to Dyson (1965) and is summarised in table 4.3. The expected active region bandwidth is 1.7:1 and the expected operation bandwidth is 12:1. Extrapolating the empirical a_{3^-}/λ versus a_{15^+}/λ chart made by Dyson (1965) suggested an active region bandwidth of 1.5:1 for a self-complementary ($\delta = 90°$) antenna. This was increased by a factor of 1.1 to account for constant conductor width ($\delta = 0°$).

Front to back ratio and directivity also increase with reducing cone angle and increasing wrap rate. This leads to a higher number of turns in the active region. The directivity increase can be understood in terms of an equivalent array with more elements and hence a higher array factor. A first order estimate of the antenna's beam pattern can be obtained by considering the active region as an array of isotropic radiators phased for end-fire.

4.4.4 Conduction Loss

Higher wrap-rate spirals have higher bandwidths, but also higher conduction losses. Electromagnetic waves travel through more lossy conductor in a higher wrap-rate spiral before being radiated in the active region. The bandwidth versus conduction loss trade-off was not explored for the antenna designed in this chapter. No simple design formula for estimating the losses of these antennas was found in the literature. Such a design formula can be derived by approximating the antenna loss resistance as

$$R_l \approx r_{ac} l_{ar} \tag{4.37}$$

where r_{ac} is the AC resistance of the conductor per unit length and l_{ar} is the distance along the conductor to the active region.

The AC resistance per unit length can be estimated by assuming a uniform current distribution in an annulus of unit skin depth on the outside of an isolated cylindrical conductor. This leads to

$$r_{ac} \approx \frac{1}{2a_w}\sqrt{\frac{\mu_0 c}{\pi\sigma\lambda}} \tag{4.38}$$

which is valid for good conductors with radius a_w much greater than the skin depth. In the current design, the wire radius is 46 times greater than the skin depth at the lower operating frequency of 114 MHz.

Distance along the conductor to the active region can be estimated if the active region is assumed to be at the point where the circumference of the cone is equal to one wavelength. This gives

$$l_{ar} \approx \frac{\sec\alpha}{2\sin\theta_0}\left(\frac{\lambda}{\pi} - d\right), \text{ and} \tag{4.39}$$

$$R_l \approx \frac{\sec\alpha}{4a_w\sin\theta_0}\sqrt{\frac{\mu_0 c}{\pi\sigma\lambda}}\left(\frac{\lambda}{\pi} - d\right). \tag{4.40}$$

As expected, this approximation of the loss resistance is independent of frequency if the conductivity σ scales inversely with wavelength and the wire radius a_w scales directly with wavelength.

The loss resistance increases with increasing α and decreasing θ_0. This conflicts directly with maximizing the operating bandwidth with frequency independent performance. The loss resistance is frequency dependent for the practical case of constant wire radius and conductivity. However, the frequency dependence is smooth for this first approximation and may not impede detection of spectral features due to cosmological reionization.

Figure 4.6 compares the loss resistance approximated by Eq. (4.40) to that simulated by the method of moments for the conical log-spiral antenna defined in table 4.2. The approximation is accurate to within 16% in this case with larger error at lower frequencies where the wave traverses more conductor. The method of moments as implemented by the NEC2 code (Burke and Poggio, 1981) was used for simulation.

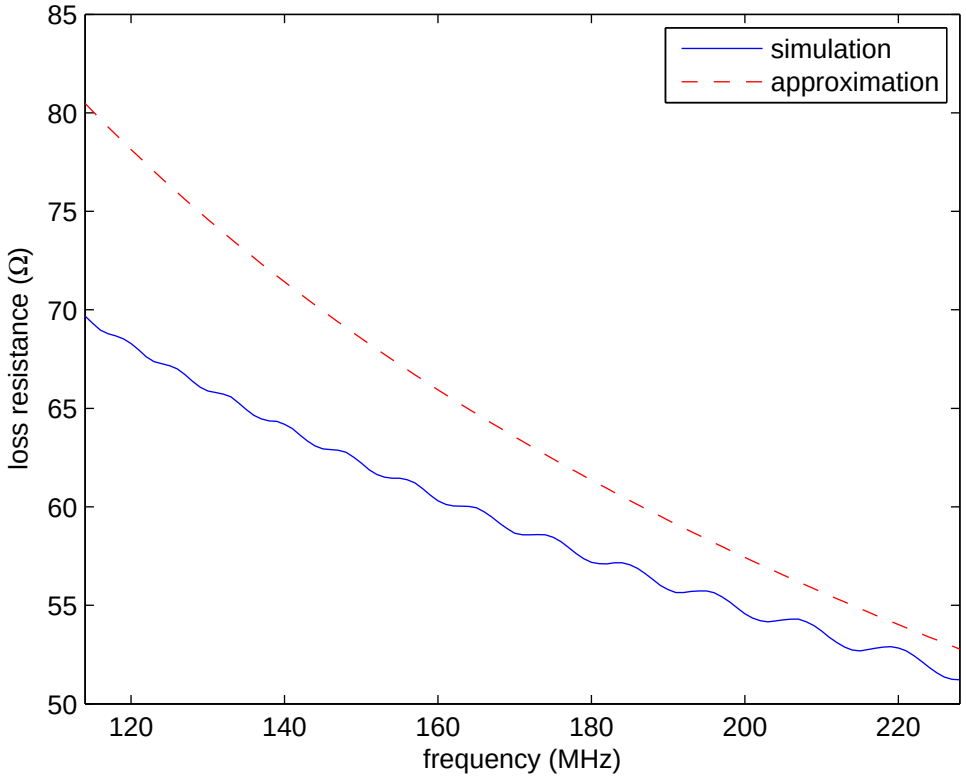

Fig. 4.6: Loss resistance of the conical spiral antenna with geometry defined in table 4.2. The approximation of Eq. (4.37) is compared to method of moments simulation results using the NEC2 code.

4.5 Pyramidal Log-Spiral Antenna

Pyramidal log-spiral antennas were explored as they can be easier to construct than conical spirals. A pyramidal spiral is formed by sampling a conical spiral at angles of $2\pi/N$ and joining these points with straight wires. This creates a log-periodic antenna that asymptotically approaches the frequency independent conical spiral antenna as N tends to infinity. Interestingly, $N = 2$ results in the log-periodic zigzag antenna.

Method of moments simulations showed that the square based pyramidal spiral ($N = 4$) derived from the conical spiral of table 4.2 maintains significant frequency independence. The small cone angle and the large wrap-rate angle mean that the active region has more spiral loops in it. This makes the antenna pattern less dependent on the shape of the individual loops. Thinking of the antenna as an array makes the reason for this clear. More loops in the active region mean that the power pattern is dominated by the array pattern and not the element (loop) pattern.

The geometric ratio τ of the pyramidal spiral is not the ratio between the lengths of wire segments above each other, but that between adjacent wire segments whose

beginnings are separated by $2\pi/N$. This gives

$$\tau = e^{-b2\pi/N}. \tag{4.41}$$

The antenna is self congruent when scaled by τ and then rotated by $2\pi/N$. The chosen geometry of table 4.2 with $N = 4$ gives $\tau = 0.988$ meaning that performance will repeat every 1.4 MHz at 114 MHz and every 2.7 MHz at 228 MHz. The geometric ratio τ increases with decreasing θ_0, increasing α, and increasing N.

4.6 Simulations of a Pyramidal Log-Spiral Antenna

Performance of a two arm pyramidal log-spiral antenna was predicted by the method of moments numerical solution to the electric field integral equation implemented by the NEC2 code (Burke and Poggio, 1981). The square based pyramidal spiral was derived by sampling the conical spiral in table 4.3 at angles of $\pi/2$ and joining those points with straight wires. The simulations were used to explore the power pattern, efficiency, impedance, and polarisation response of this antenna.

4.6.1 Power Pattern

The simulated power pattern is highly symmetric, near frequency independent, and has no significant side lobes. The dominance of the main lobe and its symmetry is illustrated by the three dimensional plot of the power pattern at 171 MHz in figure 4.7. Figure 4.8 shows a constant azimuth $\phi = 0°$ cut of the power pattern on a decibel scale. This identifies a single, frequency dependent side lobe of magnitude -30 dB at $\theta = 86°$. This side lobe is absent at 114 MHz and gradually becomes more defined towards 228 MHz. The best fit Gaussian beam has an average full width half maximum (FWHM) of 63.8° over the band. Deviations from this mean FWHM have a range of 0.9° and a standard deviation of 0.2°. Figure 4.8 also shows a $\cos^4\theta$ beam model is more accurate than a Gaussian model beyond zenith angles of 46°.

Power pattern stability with frequency is shown by figure 4.9 which overlays $\phi = 0°$ pattern cuts at 1 MHz intervals for the 114 MHz to 228 MHz band. Closer inspection of the frequency variation of the power pattern at the half-power point is made in figure 4.10 for various azimuth cuts. This identifies 4% peak-to-peak variation over the band and less than 1% variation with azimuth for the chosen cuts. Figure 4.11 shows the standard deviation of the power pattern over all frequencies for four azimuth cuts. This plot highlights that the largest absolute variations in the power pattern occur near the half-power points. It also shows that the 64° FWHM Gaussian beam model with edge perturbations defined by Eq. (4.17) with $\alpha = 0.66907$ and $\beta = 42$ generates a similar beam variance versus zenith angle.

4.6.2 Conduction Efficiency

Figure 4.12 shows the conduction efficiency of the antenna and the resulting ohmic emission from the antenna at an ambient temperature of 300 K. The antenna's

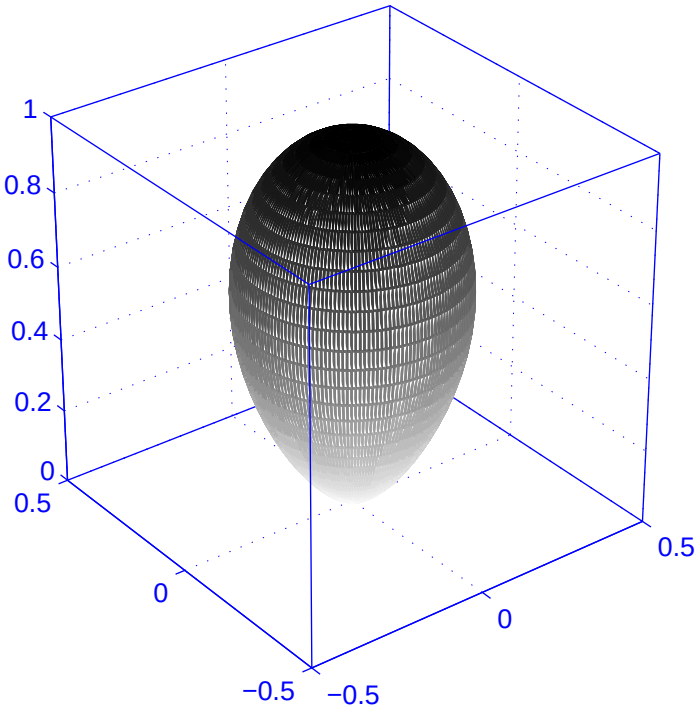

Fig. 4.7: Normalised power pattern of pyramidal spiral antenna on linear scale at 171 MHz.

conduction efficiency ranges from 0.80 at 114 MHz to 0.85 at 228 MHz and the band average efficiency is 0.82. The conduction losses represented by this efficiency generate ohmic emission ranging from 77 K to 54 K with a band average of 64 K. The worst case slope of the additive ohmic emission is -360 mK/MHz at 116 MHz. This is more than three times larger than an optimistic amplitude for the cosmological reionization monopole. Even after fitting and subtracting a third order polynomial, the worst case residual slope due to the ohmic emission is still 120 mK/MHz. This residual is zero-mean and log-periodic. A calibration approach might be to model the ohmic emission with a third order polynomial and then average over integer log-periods of the antenna performance to reduce the log-periodic residuals.

Accurate simulation of the ohmic emission is therefore required to measure the cosmological reionization monopole with this antenna. It might also be possible to calibrate the ohmic emission by making repeating measurements with the antenna at different ambient temperatures. If this fails, an antenna with conductivity that scales inversely with linear dimensions might be investigated. This scaling of conductivity is required of a truly frequency independent antenna as shown in §4.3.1. If conductivity scaling is impractical, thicker conductors with lower loss can be used to reduce ohmic emission. Gold plated conductors of the original diameter could be used if thickening the conductors alters the antenna impedance too much.

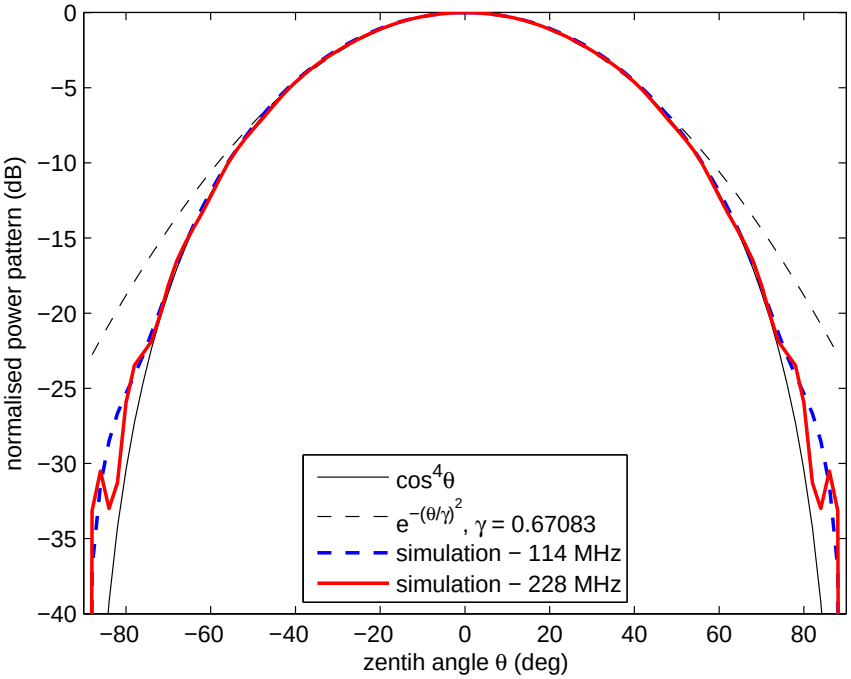

Fig. 4.8: Normalised power pattern cuts at $\phi = 0°$ for MoM simulations of the pyramidal spiral antenna. Gaussian and $\cos^4\theta$ beam models are also shown. The simulated patterns are normalised is to the antenna's forward gain of 9.5 dB over isotropic.

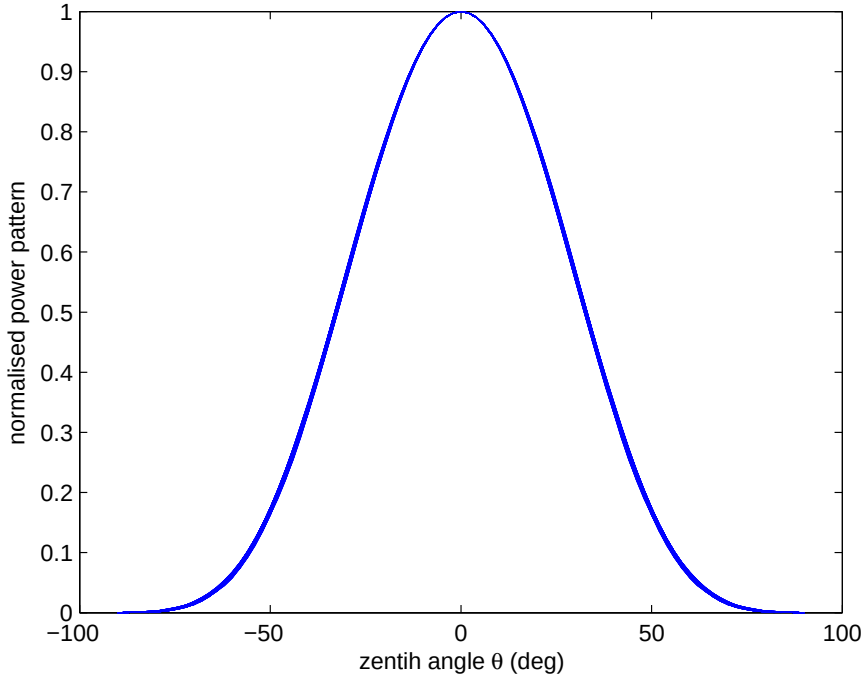

Fig. 4.9: Overlay of normalised power pattern cuts at $\phi = 0°$ for simulations at frequencies from 114 MHz to 228 MHz in 1 MHz steps.

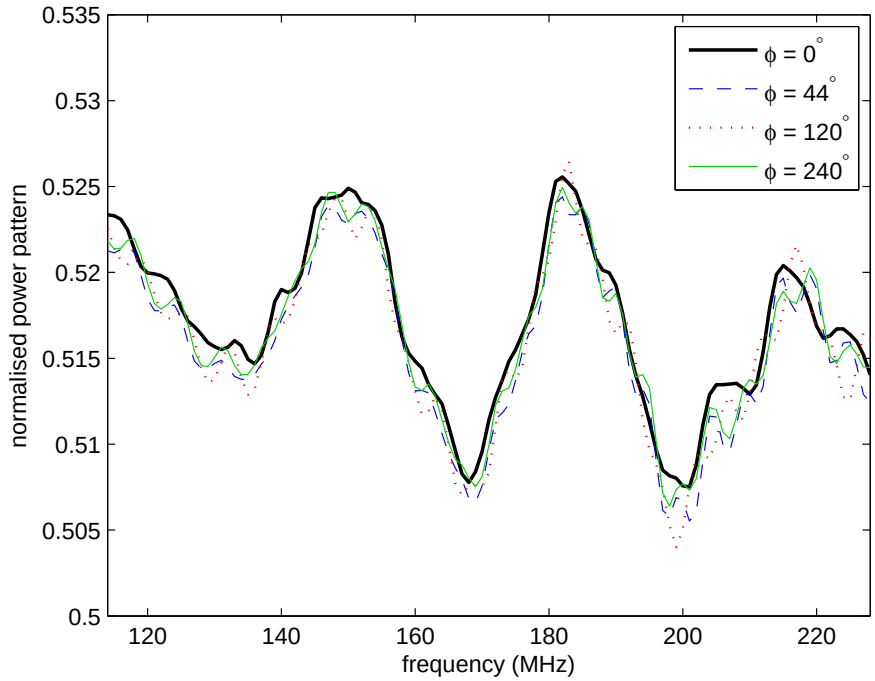

Fig. 4.10: Normalised power pattern at approximate half-power point ($\theta = 32°$) versus frequency for different azimuthal angles.

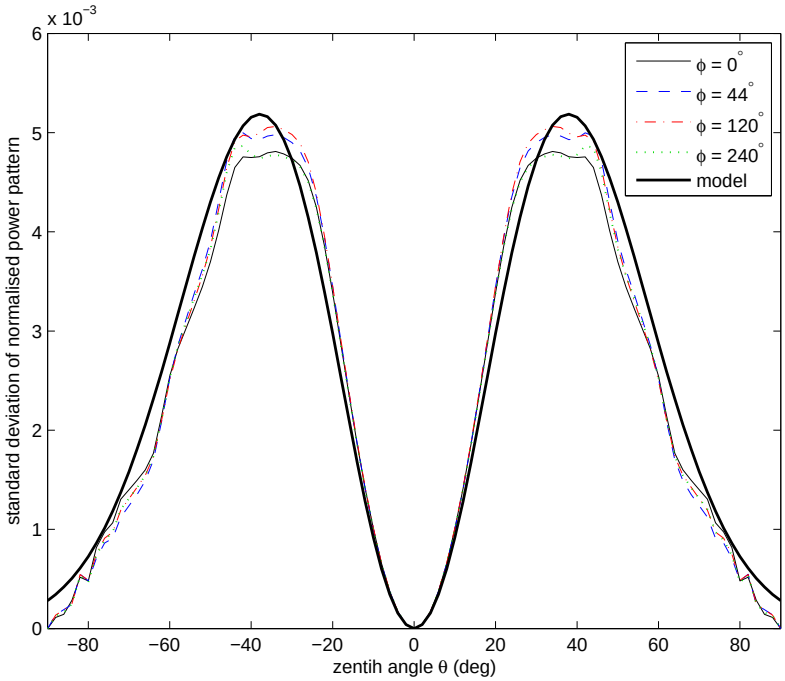

Fig. 4.11: Standard deviation of normalised power pattern over all simulated frequencies (114-228 MHz in 1 MHz steps.) The thin solid line shows the edge perturbed Gaussian beam model of (4.17) with $\alpha = 0.66907$ and $\beta = 42$.

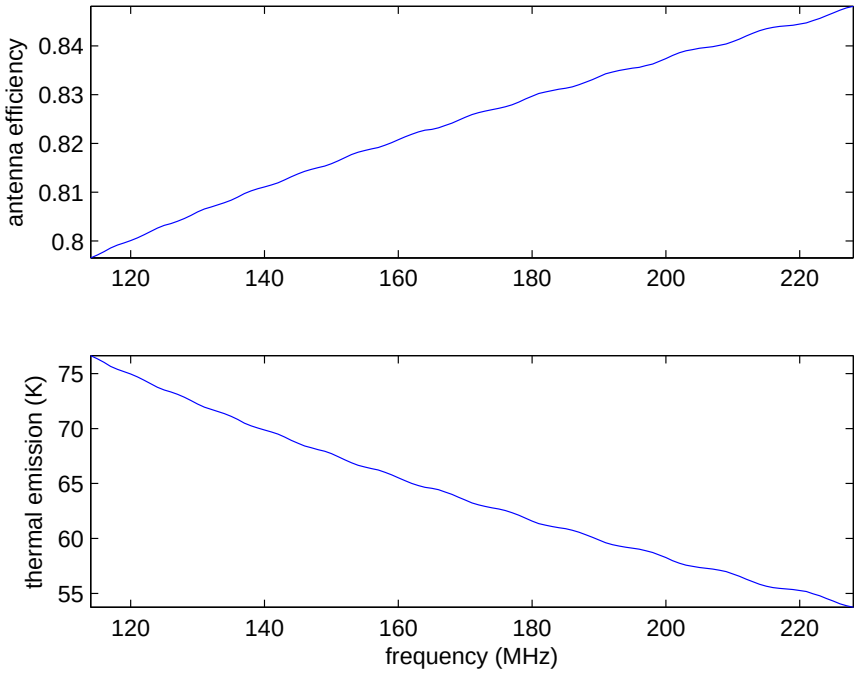

Fig. 4.12: Simulated antenna efficiency and corresponding thermal emission for a nominal physical temperature of 300 K.

4.6.3 Impedance

Figure 4.13 shows the simulated input impedance of the antenna. The simulated band average antenna impedance is $Z_A = 310 + j72.9\ \Omega$. Equation (4.5) predicts a band average voltage reflection coefficient of $|\Gamma| = 0.12$ when the antenna is fed by a 300 Ω impedance. This equates to a return loss of $-20 \log_{10} |\Gamma| = 18$ dB. Figure 4.14 shows the expected and measured reflection coefficient for two 300 Ω feed arrangements. This was measured at the 50 Ω single ended input to the balun using a spectrum analyser with a tracking generator and a bridge. The balun converts the single ended 50 Ω to balanced 100 Ω which is then converted to 300 Ω by a 3:1 impedance transformer. The network between the balun input and the antenna terminals was assumed to be symmetric. The reflection coefficient was estimated by dividing the measured reflection coefficient with the antenna in place by the reflection coefficient measured with the antenna replaced by a short.

The first measurement was made with a long 6.74 m balanced 100 Ω feed cable up the centre of the antenna joining the balun at the base of the antenna and the impedance transformer at the apex which was connected directly to the antenna terminals. This measurement agreed well in magnitude with the calculated reflection coefficient for the simulated antenna impedance terminated by a 300 Ω load. The measurement was made with the antenna on its side. The shielded balanced 100 Ω line was implemented by two pieces of 50 Ω coax with connected shields

The second measurement was made with a short 18 cm 300 Ω ribbon cable joining the antenna terminals and the impedance transformer. The balun was also

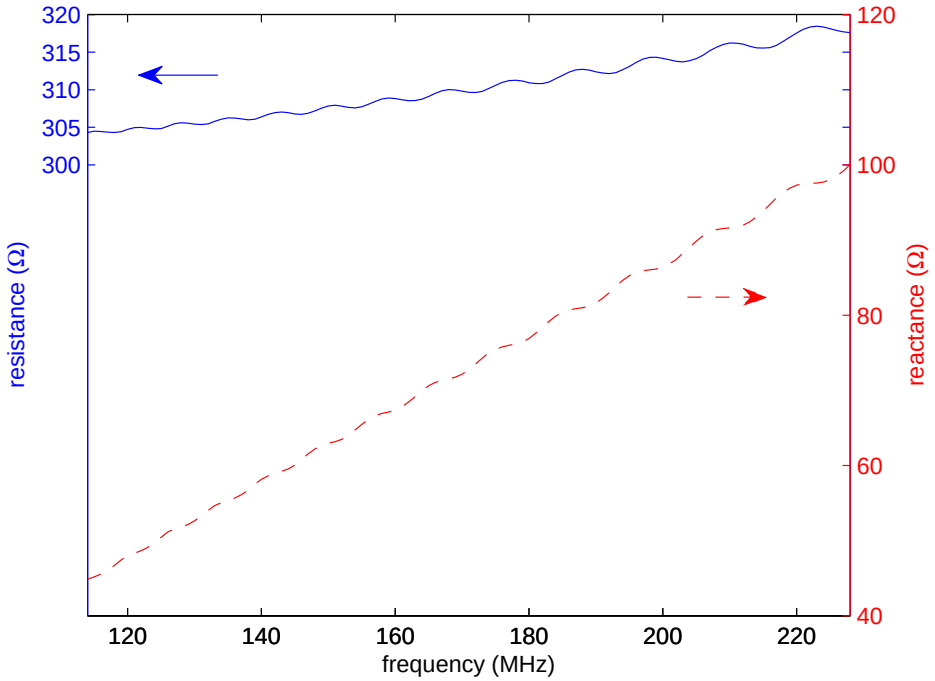

Fig. 4.13: Simulated antenna input impedance.

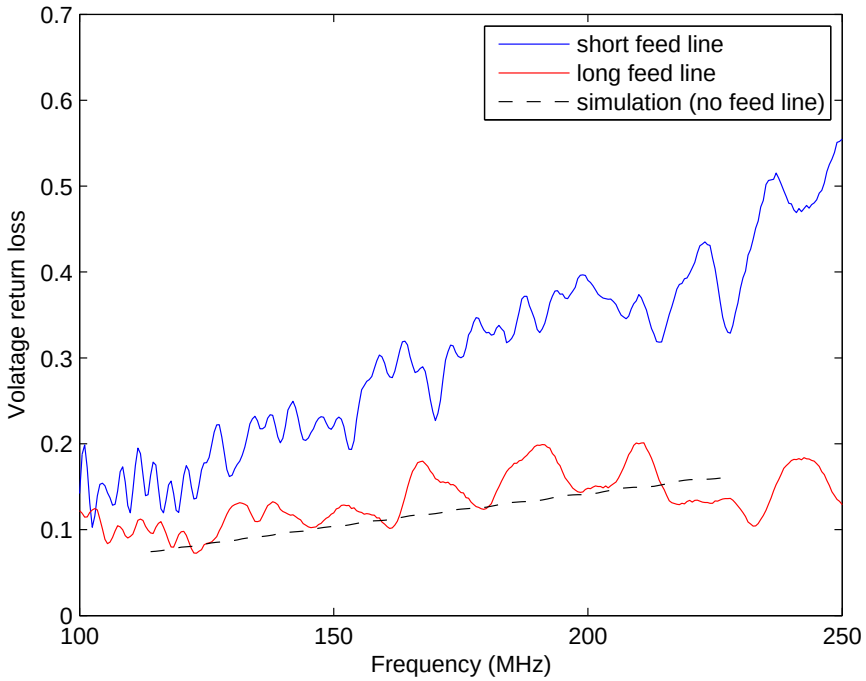

Fig. 4.14: Measured voltage reflection coefficient of antenna. Measured at the MRO with antenna on side and short distance from balun to feed point. Dashed line shows simulated value for simulated antenna impedance with 300 Ω load.

located at the apex and was joined to the impedance transformer by a further 30 cm of shielded balanced 100 Ω line. This arrangement was trialled to reduce the distance from the antenna terminals to the low noise amplifiers (LNAs) and thus reduce the rate of standing waves caused by the antenna reflection. The impedance transformer was also packaged in a brass box to mitigate variability of the reflection coefficient with temperature and humidity observed in the first measurement. Figure 4.14 shows that the reflection coefficient for this short feed line was significantly higher than that measured for the short feed line. The variability of the reflection coefficient and the rate of resulting standing waves were thus reduced at the expense of the magnitude of the reflection coefficient.

The second arrangement with the short feed line was used for measurements at the MRO. The calibration of these measurements in § 7.5.2 suggests that the increased reflection may be due to inductance of the ribbon cable 300 Ω. This should be further investigated by measuring the reflection coefficient of just the impedance transformer and 300 Ω ribbon cable in the lab.

4.6.4 Polarisation

The simulated and built antenna was right-hand wound and therefore transmits and receives a left-hand circularly polarised wave. The purity of the circular polarisation is measured by the axial ratio. This is the ratio of the major axis to the minor axis of the polarisation ellipse. It ranges from one for pure circular polarisation to infinity for linear polarisation. Figure 4.15 shows the median axial ratio versus zenith angle and the range of its fluctuation with frequency. This shows that the axial ratio is less than 1.6 for zenith angles less than 56° where the power pattern is less than 10 dB below its maximum. The antenna is therefore significantly circularly polarised in all directions that it has significant gain.

4.6.5 Simulation Details

The pyramidal log-spiral antenna is a fairly simple wire structure, and when constructed with accuracy may be expected to have a close to ideal performance, excepting for the errors arising from non-ideal balun at the apex and ground reflections. The wire geometry may be simulated with relatively unsophisticated NEC2 models.

The base of the spiral was located 0.5 m above the ground for the simulations, and for the built antenna. Ground conductivity of 1 mS and relative permittivity of 4 were incorporated through the Sommerfeld/Norton method (Lager and Lytle, 1975) implemented in NEC2. These values are consistent with the ranges of 0.1 mS $\leq \sigma \leq$ 10 mS and $4 \leq \epsilon_r \leq 10$ measured for dry sandy soil at 100 MHz (Daniels, 2004). At the MRO the ground is predominantly dry sandy soil with significant amounts of weathered granite often not far below the surface.

The conductivity of copper $\sigma = 5.9595 \times 10^7$ S.m^{-1} was used for all wires. Each straight section of wire that spans a face of the pyramid was broken into 11 segments for simulation. At the base of the active region we expect the cone radius $a_{15^+} \approx 0.165\lambda$ from (Dyson, 1965). When approximated as a pyramid, this yields a $0.164\sqrt{2}\lambda = 0.233\lambda$ distance across the face of the pyramid at the base of the active

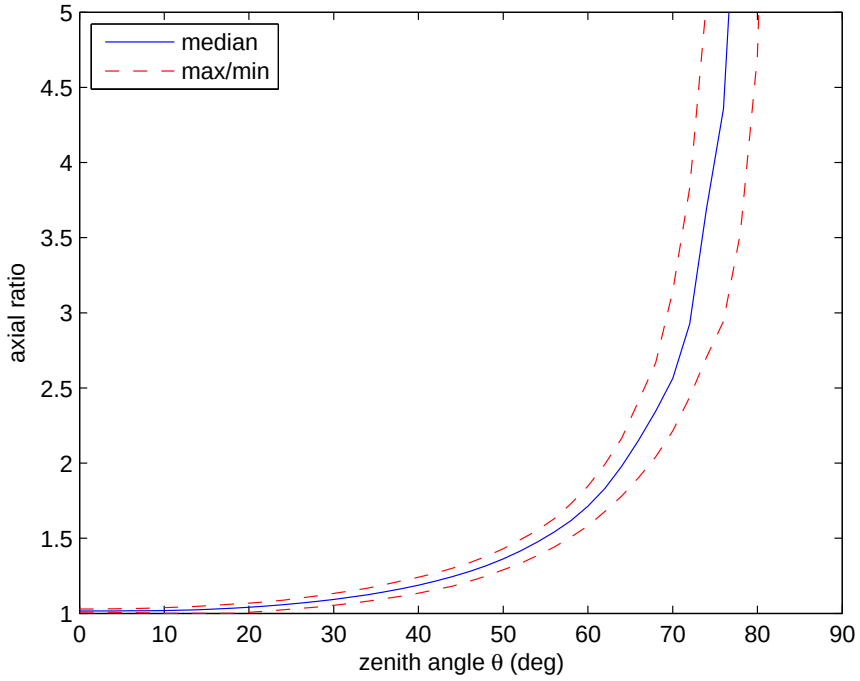

Fig. 4.15: Median, minimum and maximum axial ratio over all azimuth angles and frequencies.

region. Dividing each wire into 11 segments yields a maximum segment length of 0.021λ in the active region. This meets the recommended NEC-2 segment length of 0.1λ at the desired frequency and 0.05λ or less at critical regions of the antenna. Beyond the active region, wires are sampled more coarsely, but the majority of power has been radiated by this point. The transmission line region is segmented more finely than necessary.

The default thin-wire and extended thin-wire kernel used by NEC-2 both require $2\pi a_w \ll \lambda$. This is satisfied at the upper frequency of 228 MHz and wire radius a_w of 0.28 mm. For the default thin-wire kernel, the ratio of segment length to wire radius Δ/a_w must be greater than 8 for errors less than 1%. The smallest segment in the model is about 5 mm giving $\Delta/a_w \approx 18$ therefore the default thin-wire kernel is adequate and was used for all simulations.

The feed was modelled by placing a wire across the diagonal of the narrow end of the truncated Pyramid, directly from the beginning of one spiral arm to the beginning of the other. This wire was divided into 11 segments and a voltage source was defined across the sixth segment. The size of this segment is equal to the 8 mm spacing of the 300 Ω ribbon used to feed the antenna. The simulations yielded power pattern, input impedance, and efficiency in 1 MHz steps over 114 MHz to 228 MHz.

4.7 Construction of a Pyramidal Log-Spiral Antenna

The antenna was constructed by winding copper wires on a square-based pyramid made from styrofoam. The pyramid is supported in an upright position by a wooden base. A dimensioned sketch of the styrofoam pyramid and its wooden base is provided in Appendix A and the completed antenna is shown in figure 4.1. The pyramid was partitioned into three polyhedrons for easy transport and can be assembled by two people in the field. Each polyhedron is hollow and has 75 mm thick walls. The three polyhedrons are assembled into a pyramid lying on its side and a PVC conduit is run from the centre of the pyramid's base to its apex through holes drilled for this purpose. The ends of the conduit are threaded so that nuts can be screwed on at either end to hold the antenna together. Electrical connections are made to the antenna and front-end components located at the antenna's apex by running coaxial cables through the conduit.

The complex dielectric constant of the SMTG styrofoam was measured by placing a sheet of it over the L-band feed horn of one antenna of the Australia Telescope Compact Array (Frater et al., 1992) and phasing up a two antenna interferometer on a point source. Comparing measurements with and without the foam in place yielded a dielectric constant of $\epsilon_r = 1.032$ and loss tangent $\tan\delta = 4.2 \times 10^{-4}$. A one metre thick slab of this material would give approximately 0.2 K emission.

The above measurements were performed at 1,384 MHz, 2,368 MHz, 4,800 MHz, and 8640 MHz. The antenna system temperature increase as well as phase change were measured when a styrofoam slab was placed in front of the feed of one antenna of an interferometer observing an unresolved calibrator source. The slab properties were extrapolated to the operating frequencies of the pyramidal log-spiral antenna.

One component polyurethane adhesive was used to join the foam sheets into polyhedrons. The completed antenna was painted with white, water-based acrylic paint to provide a protective layer. Further interferometer testing showed that the paint and glue increased the loss of a sheet by 100% and 50% respectively.

The spiral arms were wrapped with 0.56 mm diameter (24 SWG) enamelled copper wire. Wires were wrapped independently on the three foam polyhedrons. These were joined by soldering when the antenna was assembled in the field.

The wooden base as well as the rest of the structural elements were constructed without using nails, screws, or any metal fasteners. Plastic L-angles were placed along the edges of the pyramid with grooves cut at the locations where wires were to be positioned. The mating surfaces of the three polyhedrons were shaped to hold these L-angles in place.

Chapter 5

FRONT-END

The front-end includes all analogue components between the antenna output and the sampler inputs. Its role is to to deliver maximum desired signal to the samplers with minimised noise and distortion. This requires sharp bandpass selection, minimal added noise, linear gain, and the correct amount of gain to optimise the performance of the samplers. Further, these characteristics must be stable in time to allow calibration to the desired precision.

The reionization experiment requires sensitivity to 1 mK signals. Both distortion and unwanted additive components that may confuse the reionization monopole must be smaller than 1 mK. This is 60 dB to 65 dB below the total system equivalent noise power. A minimum spectral dynamic range of 60 dB is therefore required of the front-end.

This chapter derives front-end requirements for 1 mK calibration at 1 MHz resolution. First, the correlation radiometer front-end architecture is presented along with a power level analysis. Second, band selection requirements are discussed including out of band rejection and bandpass stability. Finally, linearity requirements for the low noise amplifiers (LNAs) and radio frequency (RF) amplifiers are explored for expected levels of broadband noise and narrowband interference. It is found that the front-end described in this chapter can achieve dynamic range of 60 dB if either:

1. data containing the passband aliases of second order harmonics and second order intermodulation products of narrowband interference stronger than -160 dBW.Hz^{-1} $\times$ 100 kHz at the antenna terminals are rejected (this level of interference is rare at the Murchison Radio Observatory); or

2. sharper bandpass filters are used prior to the final RF amplifier; or

3. the front-end gain is reduced.

The main original contribution in this chapter is:

- a system level method for estimating nonlinear distortion of broadband noise plus narrowband interference using readily available amplifier parameters.

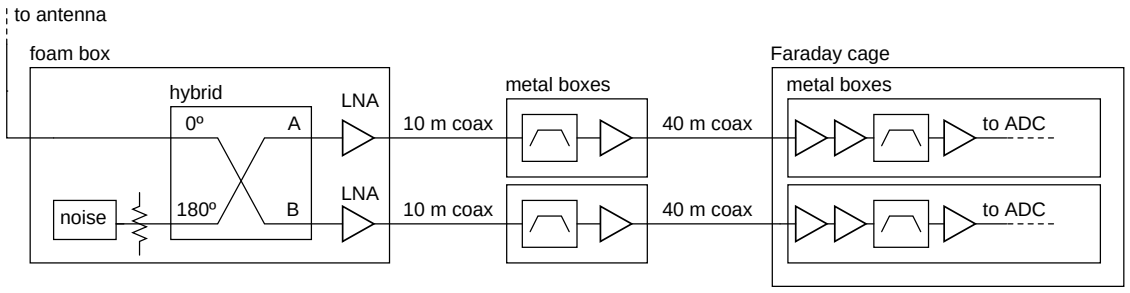

Fig. 5.1: Front-end block diagram.

5.1 Front-end Architecture

The front-end includes all components between the antenna's impedance transformer and the back-end's samplers. The architecture of the correlation radiometer front-end is illustrated by the block diagram of figure 5.1. The signal from the antenna described in the previous chapter is split by a 180° hybrid. The antenna is connected to the in-phase (sum) port of the hybrid and a noise source is connected through a fixed attenuator to the anti-phase (difference) port of the hybrid. The front-end bandpass filters and amplifies both halves of the signal before they are correlated by the back-end described in the next chapter. The completed system forms a correlation radiometer as shown by the system block diagram in figure 1.1. The cross-correlation of the two front end signals is proportional to the difference between the power delivered by the antenna and that delivered by the noise source and attenuator. This reduces errors due to gain fluctuations by allowing them to act only on the difference between the antenna signal and the reference load signal. In the ideal case of a perfectly balanced receiver, the difference is zero and the output is independent of gain fluctuation.

5.2 Implementation

The two front-end chains should be well balanced in gain amplitude and phase to optimise the receiver's insensitivity to gain fluctuations (Harris, 2005). Identical components were used for each receiver chain. Amplitude mismatch was measured by subtracting a noise source off autocorrelation from a noise source on autocorrelation for one chain and comparing it to that measured for the other. The mean amplitude mismatch was 0.3 dB with a standard deviation of 0.2 dB over the passband. Phase mismatch was measured by the phase of the cross-correlation for the difference of noise source on and noise source off measurements. A mean phase mismatch of 13° with an RMS of 1.3° was measured after removing a $-0.4°/\text{MHz}$ phase slope that is probably caused by one chain having a longer path length than the other. This delay mismatch causes an unnecessary 46° variation in the phase across the band. This should be corrected by adding 22 cm of coax with a velocity factor of 66% to one of the chains.

Harris (2005) also recommended using a common power supply for both front-end chains and keeping both chains in good thermal contact. This reduces differ-

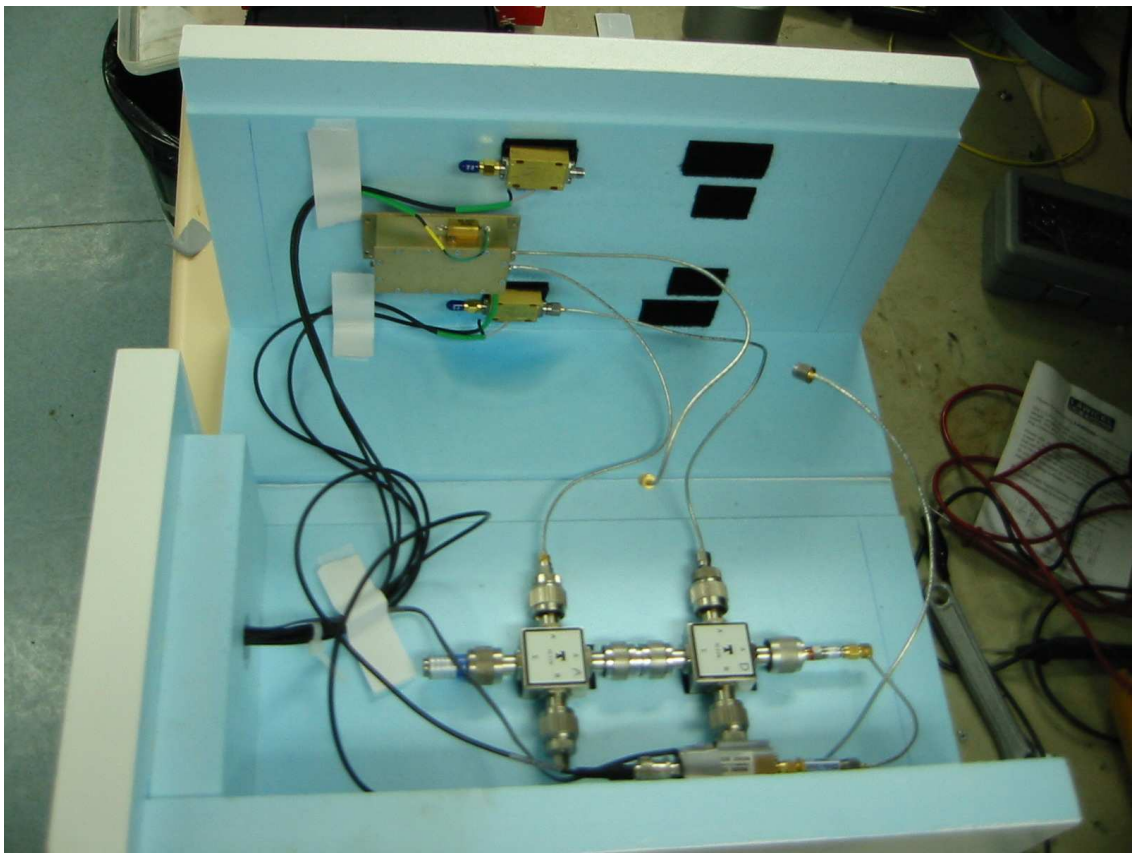

Fig. 5.2: Components from the splitter through LNA velcro-mounted in styrofoam box.

ential gain and phase fluctuations due to differential power and temperature fluctuations. However, this conflicts with the desire to minimise RF coupling between the two chains.

Coupling via the ground and via power supplies may be highly frequency dependent and result in additive components with substantial frequency structure. This is highly undesirable for the current experiment. Gain instability may be calibrated using the noise source whereas additive components arising from frequency dependent coupling may be show-stoppers, particularly if they are time varying.

For this reason, the components for each chain were packaged in independent enclosures with independent power supplies. Coupling was measured at -33 dB with respect to input power by calculating the normalised correlation coefficient for an integration with independent 50 Ω loads on the LNA inputs. The enclosures for each section of one receiver chain were placed in thermal contact with those of the other receiver chain except for the LNAs. In the future, both LNAs might be screwed onto a common brass plate.

Components from the splitter through to the LNAs were velcro-mounted in a styrofoam box at the apex of the antenna as shown in figure 5.2 and 5.3. This keeps the distance from the antenna to the LNAs small so that any ripples due to impedance mismatch have longer periods and so are smoother with frequency.

Ripples due to later components were damped by attenuators. This approach can be taken after sufficient gain has been applied at low noise. Isolators are prefer-

Fig. 5.3: LNA box fitted at antenna apex.

able to attenuators but none could be obtained that cover the 114 MHz to 228 MHz band. The foam box was chosen over a metal one because it might yield a smaller scattering cross-section for components placed in front of the antenna. The styrofoam used for the box is the same as that used for the antenna.

The first RF amplifiers and the first bandpass filters were bolted onto brass plates housed in waterproof metal boxes at the base of the antenna. RF connections to the antenna apex were made by 10 m of RG174 coaxial cable and DC connections to the apex were made by 10 m of RG223 coaxial cable. Each RF box contains a bias tee at the output allowing combined RF and DC connection to the remainder of the front-end by two 40 m FSJ1 (Heliax equivalent) coaxial cables. The remainder of the front-end was collocated with the back-end and power supplies in a Faraday cage.

5.3 Noise Power Level Analysis

Table 5.1 summarises expected total power levels at the input of each component in the front-end. These were calculated for the maximum band average antenna temperature of 951 K expected for the pyramidal spiral antenna operating in transit mode at the Murchison Radio Observatory (MRO). The critical point for system linearity is the final RF amplifier. Its worst case operating point is 28 dB below its one decibel compression point. This occurs at maximum antenna temperature when the noise source injects an additional 983 K into the difference port of the hybrid.

Tab. 5.1: Noise power level analysis for maximum predicted band average antenna temperature of 951 K.

	Component	Gain (dB)	OP_{tot}[a] noise off (dBm)	OP_{tot}[b] noise on (dBm)	ΔT_{sys}[c] Auto (K)	ΔT_{sys}[c] Cross (K)
Sky			-83.4	-83.4	951	951
Antenna	Antenna wires	-0.8	-83.9	-83.9	60.7	60.7
	Impedance transformer	-0.5	-84.2	-84.2	44.0	44.0
	180° hybrid (balun)	-0.5	-84.5	-84.5	49.4	49.4
Front-end	180° hybrid (splitter)	-3.5	-86.2	-83.5	562.5	55.4
	LNA	18.5	-67.3	-64.8	159.3	79.8
	Coaxial cable (10 m)	-3.6	-70.9	-68.3	18.5	9.3
	Attenuator	-3.0	-73.8	-71.3	32.7	16.4
	Bandpass filter 1	-0.5	-78.6	-76.1	8.7	4.4
	Attenuator	-3.0	-81.4	-79.0	74	37.1
	RF amplifier 1	24.2	-56.8	-54.5	200.7	100.6
	Bias tee	-0.3	-57.1	-54.8	< 0.1	< 0.1
	Coaxial cable (40 m)	-3.1	-60.2	-57.9	0.6	0.3
	Bias tee	-0.3	-60.5	-58.2	0.1	< 0.1
	Attenuator	-3.0	-63.5	-61.2	1.3	0.7
	RF amplifier 2	24.2	-39.3	-37.0	3.6	1.8
	Attenuator	-6.0	-45.3	-43.0	< 0.1	< 0.1
	RF amplifier 3	24.2	-21.1	-18.8	< 0.1	< 0.1
	Attenuator	-7.0	-28.1	-25.8	< 0.1	< 0.1
	Bandpass filter 2	-0.7	-29.6	-27.4	< 0.1	< 0.1
	Attenuator	-3.0	-32.6	-30.4	< 0.1	< 0.1
	RF amplifier 4	24.2	-8.4	-6.2	< 0.1	< 0.1

[a] Total power in band at output of given component in dB relative to 1 mW.

[b] Additional 983 K injected from noise source into the hybrid's difference port.

[c] Change in system temperature due to component at ambient temperature of 300 K.

The noise power level analysis of table 5.1 predicts front-end contributions of 306 K to cross-correlation system temperature and 1,062 K to autocorrelation system temperature. The equivalent noise temperatures of the LNAs and RF amplifiers are 47 K and 406 K respectively.

The auto and cross-correlation system temperatures are defined so that they may be used to calculate the limiting sensitivity according to (Rohlfs and Wilson, 2006)

$$\Delta T = \frac{K T_{sys}}{\sqrt{\delta \nu \tau}} \tag{5.1}$$

where

$$K = \begin{cases} 1 & \text{for the autocorrelations (total power receiver); and} \\ \sqrt{2} & \text{for the cross-correlation (correlation receiver).} \end{cases} \tag{5.2}$$

Both autocorrelation and cross-correlation system temperature were calculated using Friis' formula for noise temperature. They differ in that the autocorrelation system temperature includes both the 3 dB splitting loss and the 0.5 dB insertion loss of the 180° hybrid, whereas the cross-correlation system temperature only

Tab. 5.2: Headroom to one decibel compression point for maximum expected input noise power.

Component	$OP_{1\text{dB}}$[a] (dB)	OP_{tot}^{b} (dBm[c])	Headroom (dB)
LNA	13.6	-64.8	78.4
RF Amplifier 1	22.0	-54.5	76.5
RF Amplifier 2	22.0	-37.0	59.0
RF Amplifier 3	22.0	-18.8	40.8
RF Amplifier 4	22.0	-6.2	28.2

[a] Output power at one decibel compression point.

[b] Total power at output of given component for maximum expected antenna temperature and additional 983 K injected from noise source into the hybrid's difference port.

includes the insertion loss. For the cross-correlations, the 3 dB splitting loss is absorbed by the factor of $K = \sqrt{2}$ in Eq. (5.1).

The cross-correlation receiver temperature is dominated by noise from the first RF amplifier. This is due to a 3 dB attenuator erroneously left at its input. This attenuator was introduced to damp reflections in an earlier set-up when the LNA and first RF amplifier were collocated in the RF box at the base of the antenna. In the current set-up, the LNA is located at the antenna's apex and is connected to the first RF amplifier by a 10 m coaxial cable. This cable has sufficient loss to perform the reflection damping function and so the 3 dB attenuator should have been removed.

Removing the attenuator would lead to a front-end noise contribution to the cross-correlation of 217 K with the largest contribution of 80 K from the LNA. There would still be a significant contribution of 50 K from the first RF amplifier. Moving the first bandpass filter after the first RF amplifier would improve things further. This would allow unnecessary noise and interference power into the first RF amplifier. However, the first RF amplifier would operate with comparable headroom to the LNA and should not degrade performance any more than the LNA. Making this change would reduce the front-end noise contribution to the cross-correlation to 168 K with a 22 K contribution from the first RF amplifier. A further 13 K reduction could be made by moving the first RF amplifier to the antenna apex with no attenuator between it and the LNA.

The front-end contributes 0.32 to 1.1 times as much noise as the radio sky to cross-correlations depending on which part of the sky is passing through the antenna pattern. The band average antenna temperature is expected to vary from 289 K to 951 K for transit observations of the radio sky dominated by galactic emission. This was calculated for sky brightness scaled from the Haslam et al. (1995) map, the sky brightness model of Eq. (3.43), and the antenna pattern simulated by the method of moments in §4.2.2.

5.4 Band Selection Requirements

Band selection is important to reject out-of-band signals that are aliased into the passband by analogue to digital conversion. Band selection also limits the noise bandwidth and rejects out-of-band interference that can drive the amplifiers non-linear. This prevents out-of-band noise and interference from generating significant bandpass distortions and in-band intermodulation products. Further, the bandpass must be stable with time to allow calibration to the desired accuracy.

5.4.1 Out-of-Band Rejection

Two lumped component filters define the system bandpass. The first has a broader passband with shallow roll-off but higher overall rejection. It is placed early in the system, after the LNA, to limit the response to broadband noise and out-of-band interference. This is important as the frequency independent antenna has a 14:1 operational bandwidth. The second filter is narrower with a steeper roll-off but lower overall rejection. It is placed immediately prior to the final RF amplifier to reduce distortion due its nonlinear response to out-of-band interference and noise. It also reduces the response to out-of-band signals and noise that are aliased into the passband by the ADCs that follow the final amplifier. Figure 5.4 shows the power transfer functions of both filters.

The two filters are applied in series to limit the RF signal to an octave spanning 114 MHz to 228 MHz. The bandlimited signal is then sampled at 228 MHz. This captures all the information in the passband, but also folds information below 114 MHz and above 228 MHz back into the passband.

The frequency response of the concatenated filters, including the aliased response, is illustrated in figure 5.5. The aliased response is low, but not sufficiently low to be ignored when a dynamic range of greater than 15 dB is desired. The aliased response is 15 dB down at the band edges and at least 40 dB down over 125 MHz to 206 MHz. Spectral features more than 15 dB down may be confused by aliases of stronger, out-of-band features. Signals from adjacent alias bands can be isolated by switching the clock frequency. This moves passband signals in one direction and aliased signals in the other.

The limitation of the passband to one octave is important for rejecting second order harmonics and intermodulation products. The band-edge attenuation of 15 dB for a signal at 114 MHz ensures that the second harmonic at 228 MHz is reduced by a further 24 dB than if the band-edge attenuation were only 3 dB. This is because the the second harmonic is reduced by 2 dB for every 1 dB reduction of the fundamental.

5.4.2 Front-end Bandpass Stability

The front-end bandpass may fluctuate due to temperature and supply voltage variations. The measured spectrum may also wander due to clock drift. Broadband noise is periodically injected into the difference port of the hybrid to calibrate the

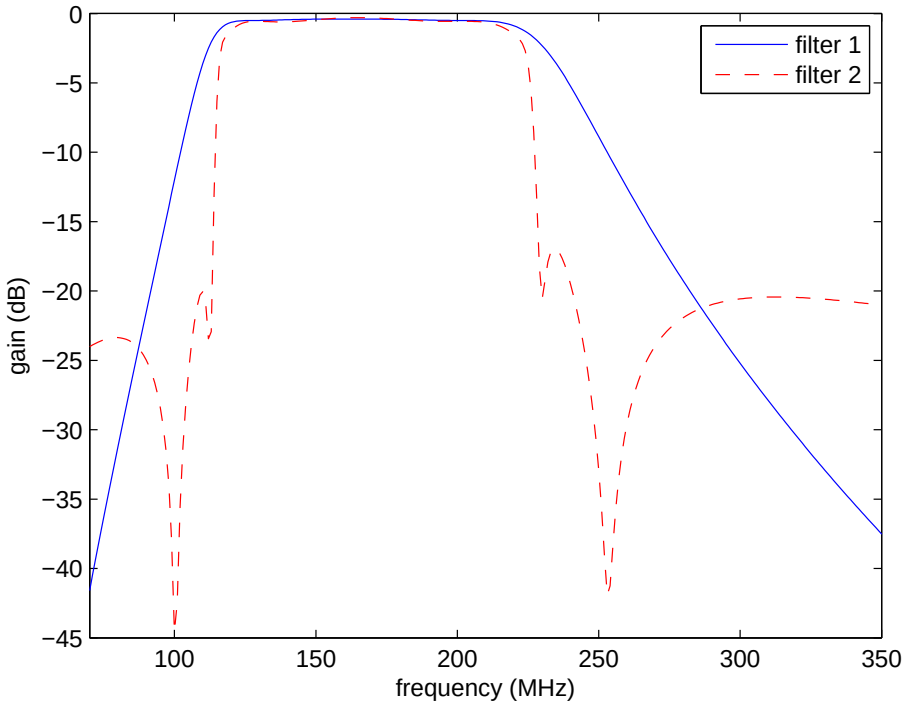

Fig. 5.4: Front-end filter frequency responses.

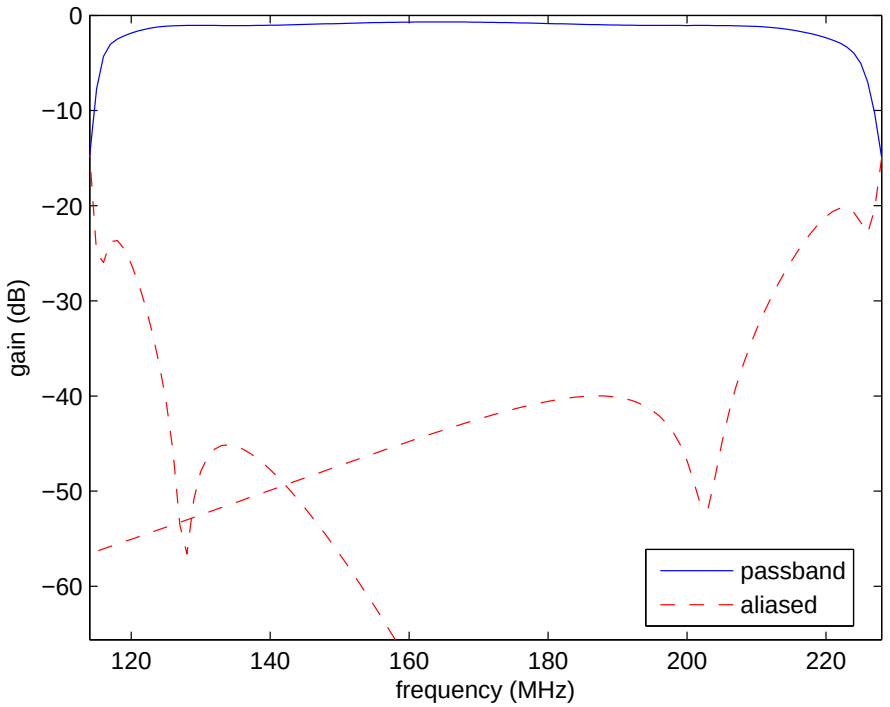

Fig. 5.5: Combined filter frequency response with aliased response shown as a broken line for sampling at 228 Msps.

front-end bandpass. This works so long as the noise spectrum is stable and so long as the noise switching timescale is faster than the bandpass fluctuation timescale.

Clock drift causes the measured spectrum to drift across the spectrometer channels as the sampling rate changes. It is caused by temperature fluctuations or ageing of the oscillator crystal. The maximum allowable sampling clock drift was determined by calculating the fractional change in sampling frequency that causes 10^{-6} fractional change in gain given the maximum slope of the system's passband. This provides a limit for allowable clock drift on the timescale of the bandpass calibration.

The maximum passband slope for the concatenated filters is 2×10^{-7} Hz^{-1} at 1 MHz resolution. The maximum allowable clock frequency drift is 5 Hz to limit the fractional change in gain to 10^{-6}. For a 228 MHz clock this requires fractional stability of 2×10^{-8}. The frequency drift of the synthesiser used is less than 2×10^{-8} over 0 °C to 55 °C. Frequency drift of the synthesiser due to aging is less than 5×10^{-10} day^{-1}. This is just sufficient to maintain the required 60 dB spectral dynamic range.

5.5 Amplifier Distortion

Distortion due to amplifier nonlinearity can limit the spectral dynamic range of the front-end. The reionization experiment requires sensitivity to 1 mK signals. Distortion may confuse the spectrum of the reionization monopole and so must be less than 1 mK which is 60 dB to 65 dB below the system temperature equivalent noise power. This section shows that the amplifiers in the front-end meet this requirement.

At the outset of this project the aim was to assess the impact of amplifier nonlinearity before purchasing amplifiers. This required making decisions based on readily available amplifier parameters. These are often limited to the power gain, the one decibel compression point, and the second and third order intercepts. These parameters support a simplified distortion analysis when the input power spectrum is dominated by narrowband interference. Harmonics and intermodulation products of the interference can be estimated but broadband noise is not considered.

A more general analysis is required for the current experiment where the input spectrum has significant contributions from both broadband noise and narrowband interference. In this scenario, amplifier nonlinearities cause distortions characterised by:

1. narrowband interference mixing with narrowband interference;
2. narrowband interference mixing with broadband noise; and
3. broadband noise mixing with broadband noise.

The following analysis uses readily available amplifier parameters to derive a third order polynomial appropriate for modelling a weakly nonlinear, broadband amplifier. The relationship between input and output power spectral densities is determined by Volterra series analysis. Finally, a linear bandpass filter is placed in front of the nonlinear model to create a bandlimited Wiener model that is more realistic.

This model is used to calculate the level of distortion due to nonlinearity in the front-end of the current experiment. Table 5.2 shows that the critical point for this analysis is the fourth and final RF amplifier, which is operated 28 dB below its one decibel compression point. When limited by this amplifier, the front-end can achieve a dynamic range of 60 dB if data containing passband aliases of second order harmonics and intermodulation products of narrowband interference stronger than -160 dBW.Hz^{-1} $\times$ 100 kHz at the antenna terminals are rejected.

5.5.1 Volterra Series Analysis

Several of models have been proposed for nonlinear amplifiers. This work uses the Volterra series because there are well developed methods for calculating its output spectrum for practical inputs including the combination of Gaussian noise and sinusoids. A comprehensive review of the Volterra series and its application to nonlinear systems is given by Schetzen (1989) and a useful tutorial is given by Cherry (1994). Bedrosian and Rice (1971) present a number of useful results including the output spectral density of a nonlinear system with Gaussian noise plus sinusoid input.

The Volterra series is useful for modelling weakly nonlinear systems for which high order terms may be truncated. It is similar to the Taylor series, but more general as it applies to systems with memory. Terms of the Volterra series are multidimensional convolutions of the system input with multidimensional impulse responses called Volterra kernels. The Volterra kernels can be extracted from multidimensional correlations of system output with input for a Gaussian input. These are involved measurements and their results are not generally reported for off the shelf components.

Simpler models have been proposed for power amplifiers that are based on complex gain measurements for single tones (Saleh, 1981). Amplitude compression (AM/AM conversion[1]) and phase deviation (AM/PM conversion[2]) are measured for a single input tone of varying power. These measurements are simpler and are reported on some RF and power amplifier data sheets. It has also been shown that a fifth order Taylor series expansion of the measured complex gain function can accurately predict the response of a nonlinear power amplifier to bandlimited Gaussian noise (Ermolova, 2001).

This work uses a memoryless third order polynomial preceded by a linear filter to calculate the response of a weakly nonlinear amplifier to Gaussian noise and sinusoidal interference. The polynomial coefficients are derived from commonly available AM/AM measurements: the power gain, the one decibel compression point, and the second and third order intercept points. The combined bandpasses of the two front-end filters shown in figure 5.5 were used for the linear filter component of the model.

The model described above consists of a linear block with memory followed by a nonlinear block without memory. This is known as a Wiener model. The coeffi-

[1] Amplitude modulation to amplitude modulation conversion.
[2] Amplitude modulation to phase modulation conversion.

cients of the memoryless polynomial correspond to Volterra kernels of a degenerate, memoryless Volterra series. Volterra series analysis can therefore be used to calculate the output spectrum of the Wiener model for inputs including Gaussian noise and sinusoids.

5.5.2 Third Order Memoryless Model

A system is memoryless if its output depends only on the current input and not on past inputs. For a linear system, this implies a delta function impulse response and therefore a frequency independent bandpass. For a nonlinear system, it implies multidimensional delta function Volterra kernels and therefore frequency independent system behaviour. The gain, one decibel compression point, and second and third order intercept points should be frequency independent for a memoryless system.

The output $y(t)$ of a memoryless system depends only on the instantaneous input $x(t)$ and can thus be represented by a power series

$$y(t) = \sum_{i=0}^{\infty} \alpha_i x^i(t). \tag{5.3}$$

For an amplifier, $x(t)$ and $y(t)$ are the input and output voltages as functions of time. This equation may model both AM/AM and AM/PM effects if the coefficients α_i are allowed to be complex. The current work only considers AM/AM effects and so requires the coefficients to be real.

Power series for weakly nonlinear amplifiers may be truncated to fifth (Ermolova, 2001) and even third order (Wambacq et al., 2000; Li et al., 2003) depending on how close they are driven to compression. The critical component in this work is the final RF amplifier which was operated 28 dB lower than its one decibel compression point and 42 dB below its third order intercept point. This amount of headroom should make truncation to third order reasonable. Truncation to third order is also pragmatic as third order effects are the highest that are commonly reported on data sheets. The result of the truncation is an approximate third order polynomial relationship between the amplifier's input and output voltages

$$\tilde{y}_3(t) = \alpha_0 + \alpha_1 x(t) + \alpha_2 x^2(t) + \alpha_3 x^3(t). \tag{5.4}$$

The zeroth order coefficient α_0 is ignored when convenient as it represents a DC offset that is blocked by AC coupled amplifiers. First through third order coefficients may be estimated from readily available amplifier performance parameters by considering the response of Eq. (5.4) to single and dual tone inputs.

Response to a Single Sinusoid

The response of Eq. (5.4) to a single sinusoid $x(t) = A\cos\omega t$ is

$$\begin{aligned}\tilde{y}_3(t) &= \alpha_0 + \frac{\alpha_2 A^2}{2} && \text{(DC offset)}\\ &+ \left(\alpha_1 + \frac{3\alpha_3 A^2}{4}\right) A\cos\omega t && \text{(gain compression)}\\ &+ \frac{\alpha_2 A^2}{2}\cos 2\omega t && \text{(second harmonic)}\\ &+ \frac{\alpha_3 A^3}{4}\cos 3\omega t && \text{(third harmonic).}\end{aligned} \tag{5.5}$$

This equation, together with those that follow, is written in terms of peak voltage A. Most amplifier measurements are reported as mean power P in dBm (decibels referred to 1 mW). The two are related by

$$P = 10\log_{10}\frac{A^2}{2R} + 30 \text{ dBm} \tag{5.6}$$

where R is the system impedance, which is usually 50 Ω. Distortions imparted by the second and third order terms include:

1. a DC offset;
2. gain compression; and
3. harmonic responses at multiples of the input frequency.

The output frequency range is not limited to the input frequency range.

Response to Two Sinusoids

A common test for second and third order effects is to inject two closely spaced sinusoids of the same amplitude: $x(t) = A\cos\omega_1 t + A\cos\omega_2 t$. The response of Eq. (5.4) to two sinusoids is

$$\begin{aligned}\tilde{y}_3(t) &= \alpha_0 + \alpha_2 A^2 && \text{(DC offset)}\\ &+ \left(\alpha_1 + \frac{9}{4}\alpha_3 A^2\right) A(\cos\omega_1 t + \cos\omega_2 t) && \text{(gain compression)}\\ &+ \frac{\alpha_2 A^2}{2}(\cos 2\omega_1 t + \cos 2\omega_2 t) && \text{(second harmonic)}\\ &+ \frac{\alpha_3 A^3}{4}(\cos 3\omega_1 t + \cos 3\omega_2 t) && \text{(third harmonic)}\\ &+ \frac{\alpha_2 A^2}{2}(\cos(\omega_1+\omega_2)t + \cos(\omega_1-\omega_2)t) && (2^{\text{nd}} \text{ order intermods})\\ &+ \frac{3\alpha_3 A^3}{4}(\cos(\omega_1 \pm 2\omega_2)t + \cos(2\omega_1 \pm \omega_2)t) && (3^{\text{rd}} \text{ order intermods}).\end{aligned} \tag{5.7}$$

This response includes distortions similar to the single tone case of Eq. (5.5) with the addition of intermodulation products at the sum and difference frequencies of the input tones and their harmonics.

First Order Coefficient from Linear Gain

An amplifier's linear response is characterised by its small signal voltage gain

$$\alpha_1 = \lim_{x(t)\to 0} \frac{y(t)}{x(t)}. \tag{5.8}$$

This is often reported as a power gain in decibels

$$G = 10\log_{10}\left(\alpha_1^2 \frac{R_i}{R_L}\right) \text{ dB} \tag{5.9}$$

where R_i and R_L are the input and load impedances of the amplifier. For the usual case of equal input and output impedance, the first order coefficient is

$$\alpha_1 = 10^{G/20}. \tag{5.10}$$

Second Order Coefficient from Second Order Intercept

Second order intermodulation is the name given to the effect seen in the fifth term of Eq. (5.7). It appears at the sum and difference of the input sinusoid frequencies $(\omega_1 \pm \omega_2)$. This behaviour is characterised by the input second order intercept point (IIP_2). It measures the input power at which second order intermodulation products $\frac{\alpha_2 A^2}{2}(\cos(\omega_1+\omega_2)t + \cos(\omega_1-\omega_2)t)$ are equal in magnitude to the extrapolated linear response $\alpha_1 A(\cos\omega_1 t + \cos\omega_2 t)$. This gives

$$\frac{\alpha_2}{\alpha_1} = \frac{2}{A_{IIP_2}}. \tag{5.11}$$

Third Order Coefficient from Gain Compression

The gain compression of an amplifier is usually quantified by the input one decibel compression point $P_{1\text{dB}}$ for a single tone input. This is the input power for which the output power is one decibel less than predicted by the small signal gain. Comparing this definition to the third term of Eq. (5.5) gives

$$20\log_{10}(\alpha_1) - 20\log_{10}\left(\alpha_1 + \frac{3\alpha_3 A_{1dB}^2}{4}\right) = 1. \tag{5.12}$$

This can be rearranged to give the ratio of the third order coefficient to the linear coefficient in terms of the input one decibel compression point

$$\begin{aligned}\frac{\alpha_3}{\alpha_1} &= \frac{4}{3A_{1\text{dB}}^2}\left(\frac{1-10^{\frac{1}{20}}}{10^{\frac{1}{20}}}\right) \\ &\approx \frac{-0.145}{A_{1\text{dB}}^2}.\end{aligned} \tag{5.13}$$

Third Order Coefficient from Third Order Intermodulation Point

Third order intermodulation appears as responses at $\omega_1 \pm 2\omega_2$ and $2\omega_1 \pm \omega_2$, and is demonstrated by the sixth term of Eq. (5.7). This effect is measured by the input third order intermodulation product (IIP_3). Analogous to IIP_2, IIP_3 is defined as the input power level at which the magnitudes third order intermodulation products $\frac{3\alpha_3 A^3}{4}(\cos(\omega_1 \pm 2\omega_2)t + \cos(2\omega_1 \pm \omega_2)t)$ are equal to the extrapolated linear response $\alpha_1 A(\cos\omega_1 t + \cos\omega_2 t)$. This gives

$$\frac{\alpha_3}{\alpha_1} = \frac{4}{3A^2_{IIP_3}}. \tag{5.14}$$

This is redundant as the ratio α_3/α_1 was already determined in Eq. (5.13). The three parameter model of Eq. (5.4) is overdetermined by the four available measurements. This redundancy can be used to check the validity of the model for a given amplifier. Equating the two determinations shows that the model requires

$$\frac{A^2_{IIP_3}}{A^2_{1dB}} \approx 9.20. \tag{5.15}$$

If the third order model of Eq. (5.4) is valid the input third order intercept point should be approximately 9.6 dB higher than the input one decibel compression point. This criterion helps identify amplifiers for which the current model is adequate for describing operation at the compression point.

Coefficients for Selected Amplifier

It has been shown that third order polynomial coefficients $(\alpha_1, \alpha_2, \alpha_3)$ may be calculated from measured amplifier parameters $(G, P_{1\text{dB}}, IIP_2, IIP_3)$. Table 5.3 presents the measured parameters and calculated coefficients of the memoryless, polynomial model for the RF amplifier used in the front-end. The fourth and final RF amplifier limits the linearity of the front-end as it operates closer to compression than the other amplifiers.

Frequency independent performance is an indicator of a memoryless system. The RF amplifier's gain varies by 0.2 dB, its one decibel compression point varies by 0.2 dB, and its third order intercept point varies by 1 dB over the 114 MHz to 228 MHz band. However, the second order intercept point varies by 9 dB over the band. In the following work the worst case second order intercept is used. The resulting memoryless model should only be used to determine the worst case level of second order distortion. However, it should give reasonable spectra of first and third order distortions for which the memoryless assumption is more reasonable. This is adequate for the current goal of determining the worst case level of nonlinear distortion at a given operating point.

Another indicator that a third order polynomial does not fully capture the amplifier's behaviour is that its third order intercept exceeds its one decibel compression point by 14 dB instead of by 9.6 dB as predicted by Eq. (5.15). This suggests that terms higher than third order are required to model the amplifier when it is operated at or beyond its one decibel compression point. In the current work, the

Tab. 5.3: Parameters for QB300 1 MHz to 300 MHz RF amplifier.

Measured Parameter	Value	Calculated Coefficient	Value
G	24.2 dB	α_1	16.2
IIP_2	27.8 dBm	α_2	4.18 v^{-1}
IIP_3	12.8 dBm	α_3	-11.3 v^{-2}
P_{1dB}	-1.2 dBm	α_3	-31.0 v^{-2}

amplifier is operated at least 28 dB below its one decibel compression point and the third order model may be reasonable. The third order coefficient α_3 derived from the third order intercept point is used in preference to α_3 derived from the one decibel compression point. This is because the third order intercept point is measured with lower input power and that, by definition, it traces third order rather than a possible combination of higher order effects.

Frequency Response of a Volterra Model

To calculate the frequency response of the memoryless, power series of Eq. (5.3) it is convenient to express it as a Volterra series

$$y(t) = \sum_{n=0}^{\infty} \mathbf{H}_n[x(t)] \tag{5.16}$$

where

$$\mathbf{H}_n[x(t)] = \int_{-\infty}^{\infty} \cdots \int_{-\infty}^{\infty} h_n(\tau_1, \ldots, \tau_n) x(t-\tau_1) \cdots x(t-\tau_n) d\tau_1 \cdots d\tau_n \tag{5.17}$$

and h_n are the n^{th} order Volterra kernels. For a linear system ($n = 1$) the Volterra series reduces to the usual convolution relationship between input, output, and the impulse response $h_1(\tau_1)$

$$\mathbf{H}_1[x(t)] = \mathbf{L}_1[x(t)] = \int_{-\infty}^{\infty} h_1(\tau_1) x(t-\tau_1) d\tau_1. \tag{5.18}$$

The n^{th} order Volterra kernel can be interpreted as a multidimensional impulse response. It can be calculated from correlations of system output with n delayed copies of a Gaussian input. Varying the n delays independently allows measurement of the kernel in n dimensions. The n^{th} order kernel may also be measured through the impulse response to n impulses at different delays, or by differentiating the response to n step functions at different delays. These three methods are discussed by Schetzen (1989).

The kernels of the third order, memoryless model degenerate to a constant and three delta functions:

$$\begin{aligned} h_0 &= \alpha_0, \\ h_1 &= \alpha_1 \delta(\tau_1), \\ h_2 &= \alpha_2 \delta(\tau_1, \tau_2), \text{and} \\ h_3 &= \alpha_3 \delta(\tau_1, \tau_2, \tau_3). \end{aligned} \tag{5.19}$$

The Fourier transforms of these kernels are

$$\begin{aligned} H_0 &= 2\pi\alpha_0 \delta(j\omega), \\ H_1(j\omega_1) &= \alpha_1, \\ H_2(j\omega_1, j\omega_2) &= \alpha_2, \text{and} \\ H_3(j\omega_1, j\omega_2, j\omega_3) &= \alpha_3. \end{aligned} \tag{5.20}$$

Following Schetzen (1989), the frequency response of the third order system $\tilde{Y}_3(j\omega)$ for harmonic input $X(j\omega)$ is written in terms of the kernel Fourier transforms

$$\begin{aligned} \tilde{Y}_3(j\omega) =& H_0 \\ &+ H_1(j\omega)X(j\omega) \\ &+ \frac{1}{2\pi}\int_{-\infty}^{\infty} H_1(j\omega - j\omega_1, j\omega_1)X(j\omega - j\omega_1)X(j\omega_1)d\omega_1 \\ &+ \frac{1}{4\pi^2}\int_{-\infty}^{\infty}\int_{-\infty}^{\infty} H_2(j\omega - j\omega_1, j\omega_1 - j\omega_2, j\omega_2) \\ &\quad \times X(j\omega - j\omega_1)X(j\omega_1 - j\omega_2)X(j\omega_2)d\omega_1 d\omega_2. \end{aligned} \tag{5.21}$$

Substituting Eq. (5.20) into Eq. (5.21) yields

$$\begin{aligned} \tilde{Y}_3(j\omega) =& 2\pi\alpha_0\delta(j\omega) \\ &+ \alpha_1 X(j\omega) \\ &+ \frac{\alpha_2}{2\pi}\int_{-\infty}^{\infty} X(j\omega - j\omega_1)X(j\omega_1)d\omega_1 \\ &+ \frac{\alpha_3}{4\pi^2}\int_{-\infty}^{\infty}\int_{-\infty}^{\infty} X(j\omega - j\omega_1)X(j\omega_1 - j\omega_2)X(j\omega_2)d\omega_1 d\omega_2. \end{aligned} \tag{5.22}$$

This is more compactly expressed as

$$\begin{aligned} \tilde{Y}_3(j\omega) =& 2\pi\alpha_0\delta(j\omega) + \alpha_1 X(j\omega) \\ &+ \frac{\alpha_2}{2\pi}X(j\omega) * X(j\omega) + \frac{\alpha_3}{4\pi^2}X(j\omega) * X(j\omega) * X(j\omega) \end{aligned} \tag{5.23}$$

where $*$ denotes convolution. This result is useful for calculating the output spectrum when the input power is dominated by deterministic signals such as sinusoids. Calculating the response to a noise-like signal requires the use of random processes and is simplified by the use of Wiener functionals.

Frequency Response for Random Processes

The frequency response of a p^{th} order system to a random process is defined by the output power spectral density

$$\Phi_{yy}(j\omega) = \int_{-\infty}^{\infty} \phi_{yy}(\tau) e^{-j\omega\tau} d\tau \tag{5.24}$$

where

$$\begin{aligned} \phi_{yy}(\tau) &= \overline{y(t)y(t+\tau)} \\ &= \sum_{m=0}^{p} \sum_{n=0}^{p} \overline{\mathbf{H}_m[x(t)]\mathbf{H}_n[x(t+\tau)]}. \end{aligned} \tag{5.25}$$

This leads to an expansion with $(p+1)^2$ terms. Calculation is simplified if Wiener G-functional representation is used in place of the Volterra series expansion (Schetzen, 1989). Each Wiener G-functional is orthogonal to all lower order G-functionals if the input is white Gaussian noise. Thus only $p+1$ terms need to be evaluated in the autocorrelation of the system output. Hence Eq. (5.25) becomes

$$\phi_{yy}(\tau) = \sum_{m=0}^{p} \sum_{n=0}^{p} \overline{\mathbf{G}_m[k_m; x(t)]\mathbf{G}_n[k_n; x(t+\tau)]} \tag{5.26}$$

which simplifies to

$$\phi_{yy}(\tau) = \sum_{n=0}^{p} \overline{\mathbf{G}_n[k_n; x(t)]\mathbf{G}_n[g_n; x(t)]}. \tag{5.27}$$

Here g_n is the Wiener kernel k_n shifted along each of its coordinates by τ

$$g_n(\tau_1, \ldots, \tau_n) = k_n(\tau_1 + \tau, \ldots, \tau_n + \tau). \tag{5.28}$$

The autocorrelation of the output for white Gaussian input $\phi_{xx}(\tau) = \psi\delta(\tau)$ is given by (Schetzen, 1989)

$$\phi_{yy}(\tau) = \sum_{n=0}^{p} n!\psi^n \int_{-\infty}^{\infty} \cdots \int_{-\infty}^{\infty} k_n(\tau_1, \ldots, \tau_n) g_n(\tau_1, \ldots, \tau_n) d\tau_1 \ldots d\tau_n. \tag{5.29}$$

The necessary Wiener kernels for a third order system may be written in terms of the Volterra kernels of Eq. (5.19) as follows:

$$\begin{aligned} k_3(\tau_1, \tau_2, \tau_3) &= h_3(\tau_1, \tau_2, \tau_3), \\ k_2(\tau_1, \tau_2) &= h_2(\tau_1, \tau_2), \\ k_1(\tau_1) &= h_1(\tau_1) + 3\psi \int_{-\infty}^{\infty} h_3(\tau_1, \tau_2, \tau_2) d\tau_2, \text{ and} \\ k_0 &= h_0 + \psi \int_{-\infty}^{\infty} h_2(\tau_1, \tau_1) d\tau_1. \end{aligned} \tag{5.30}$$

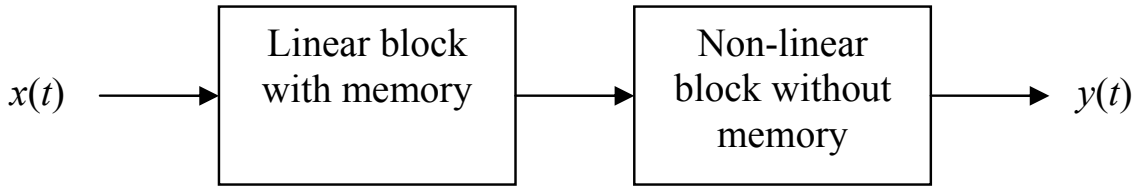

Fig. 5.6: The Wiener model.

Substituting in the Volterra kernels of the memoryless model in Eq. (5.19) yields

$$\begin{aligned} k_3(\tau_1,\tau_2,\tau_3) &= \alpha_3\delta(\tau_1,\tau_2,\tau_3), \\ k_2(\tau_1,\tau_2) &= \alpha_2\delta(\tau_1,\tau_2), \\ k_1(\tau_1) &= (\alpha_1+3\psi\alpha_3)\delta(\tau_1), \text{ and} \\ k_0 &= \alpha_0+\psi\alpha_2. \end{aligned} \tag{5.31}$$

Eq. (5.29) is then applied to give the autocorrelation of the output of a memoryless, third order system with white Gaussian input $\phi_{xx}(\tau) = \psi\delta(\tau)$

$$\begin{aligned} \phi_{yy}(\tau) =& (\alpha_0+\psi\alpha_2)^2 && \text{(DC offset)} \\ &+ \psi(\alpha_1+3\psi\alpha_3)^2\delta(\tau) && \text{(gain compression)} \\ &+ 2\psi^2\alpha_2^2\delta(\tau) && (2^{\text{nd}} \text{ order distortion)} \\ &+ 6\psi^3\alpha_3^2\delta(\tau) && (3^{\text{rd}} \text{ order distortion}). \end{aligned} \tag{5.32}$$

The corresponding output PSD is

$$\begin{aligned} \Phi_{yy}(j\omega) =& 2\pi(\alpha_0+\psi\alpha_2)^2\delta(j\omega) && \text{DC offset} \\ &+ \psi(\alpha_1+3\psi\alpha_3)^2 && \text{(gain compression)} \\ &+ 2\psi^2\alpha_2^2 && (2^{\text{nd}} \text{ order distortion)} \\ &+ 6\psi^3\alpha_3^2 && (3^{\text{rd}} \text{ order distortion}). \end{aligned} \tag{5.33}$$

5.5.3 Wiener Model

Analysis has been limited to a memoryless model with frequency independent parameters. Real amplifiers must at least have frequency dependent gain. Otherwise their bandwidth would be infinite. The frequency dependence of the front-end gain is largely determined by filters prior to the final RF amplifier. A simple way forward is the Wiener model shown in figure 5.6. It consists of a linear block with memory, followed by a memoryless nonlinear block. In this case the linear block corresponds to the bandpass filters and the nonlinear block corresponds to the RF amplifier. This model is appropriate when the amplifier is memoryless over the band defined by the preceding filter, and so has frequency independent parameters over that band.

A more detailed diagram for the model with linear block $\mathbf{L}_1[x(t)]$ and third order Volterra model $\sum_{n=0}^{3}\mathbf{H}_n[x(t)]$ for the nonlinear block is shown in figure 5.7. The Wiener functional representation $\sum_{n=0}^{3}\mathbf{G}_n[k_n;x(t)]$ of the model in figure 5.7

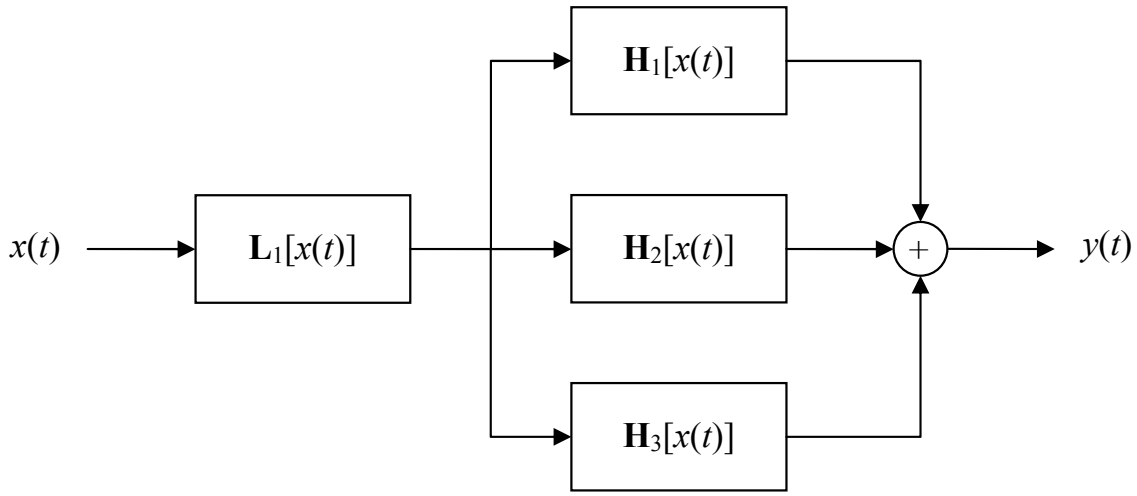

Fig. 5.7: Wiener model with third order nonlinear block.

is now derived for the case that the memoryless nonlinear block is the third order polynomial of Eq. (5.4). The Volterra kernels of the resulting Wiener model are (Schetzen, 1989; Zhang et al., 1998)

$$\begin{aligned} h_0 &= 0 \\ h_1(\tau_1) &= \alpha_1 l_1(\tau_1), \\ h_2(\tau_1,\tau_2) &= \alpha_2 l_1(\tau_1) l_1(\tau_2), \text{and} \\ h_3(\tau_1,\tau_2,\tau_3) &= \alpha_3 l_1(\tau_1) l_1(\tau_2) l_1(\tau_3) \end{aligned} \tag{5.34}$$

where $l_1(\tau)$ is the impulse response of the linear block in the Wiener model. The DC kernel h_0 was zeroed as the front-end output was AC coupled to the back-end input. Applying Eq. (5.30) to the above Volterra kernels gives the Wiener kernels

$$\begin{aligned} k_3(\tau_1,\tau_2,\tau_3) &= \alpha_3 l_1(\tau_1) l_1(\tau_2) l_1(\tau_3), \\ k_2(\tau_1,\tau_2) &= \alpha_2 l_1(\tau_1) l_1(\tau_2), \\ k_1(\tau_1) &= (\alpha_1 + 3\psi C \alpha_3) l_1(\tau_1), \text{and} \\ k_0 &= \psi C \alpha_2 \end{aligned} \tag{5.35}$$

where

$$C = \int_{-\infty}^{\infty} l_1^2(\tau_1) d\tau_1. \tag{5.36}$$

The output autocorrelation for Gaussian input is calculated by Eq. (5.29)

$$\begin{aligned} \Phi_{yy}(f) = {} & \psi^2 C^2 \alpha_2^2 \delta(f) \\ & + \psi(\alpha_1 + 3\psi C \alpha_3)^2 L_1(f) L_1(-f) \\ & + 2\psi^2 \alpha_2^2 \{L_1(f) L_1(-f)\} * \{L_1(f) L_1(-f)\} \\ & + 6\psi^3 \alpha_3^2 \{L_1(f) L_1(-f)\} * \{L_1(f) L_1(-f)\} * \{L_1(f) L_1(-f)\}. \end{aligned} \tag{5.37}$$

The substitution $\omega = 2\pi f$ was made to move from the algebraic convenience of angular frequency back to temporal frequency which is more common for measurements. For a linear block with an even frequency response, that is $L_1(f) = L_1(-f)$,

the output autocorrelation becomes

$$\begin{aligned}\Phi_{yy}(f) &= \psi^2 C^2 \alpha_2^2 \delta(f) && \text{(DC offset)} \\ &+ \psi(\alpha_1 + 3\psi C \alpha_3)^2 L_1^2(f) && \text{(gain compression)} \\ &+ 2\psi^2 \alpha_2^2 L_1^2(f) * L_1^2(f) && (2^{\text{nd}} \text{ order distortion}) \\ &+ 6\psi^3 \alpha_3^2 L_1^2(f) * L_1^2(f) * L_1^2(f) && (3^{\text{rd}} \text{ order distortion}). \end{aligned} \tag{5.38}$$

The convolutions required by the above equation can be efficiently calculated by circular convolution implemented with an FFT and sufficient zero padding for equivalence with standard convolution.

Output spectra are now calculated for the final RF amplifier in the front-end. The model input to this amplifier includes noise and interference levels predicted for the reionization experiment. The input consists of the sky noise, the receiver noise, and radio interference. Two closely spaced interferers were included at power levels typically observed at the MRO where the system was deployed. A calculation was also made for stronger interference levels typical of Narrabri where the system was integrated and tested. Output spectra were calculated with 100 kHz resolution so that they are comparable with spectra from the actual back-end which has 111 kHz resolution.

For the reionization experiment, the input noise is not white. It has a spectrum determined by the power law of the galactic radio emission, the bandpass of the front-end, and the receiver noise. These spectral shapes can be rolled into the frequency response of the linear block

$$L_1^2(f) = L_{gxy}^2(f) G_{rx} L_{rx}^2(f) \left(1 + \frac{2T_{rx}}{T_{150} L_{gxy}^2(f)}\right) \tag{5.39}$$

if the variance of the Gaussian input to $\psi = \frac{1}{2} k T_{150}$. Here $L_{gxy}(f)$ is the spectral shape of the galactic emission; G_{rx} is the band average linear power gain of the front-end up to the input of the final RF amplifier; and $L_{rx}^2(f)$ is the frequency response of the front-end which is estimated as the product of the two filter frequency responses plotted in figure 5.4. The last factor in Eq. 5.39 adds the receiver noise.

The spectral shape of the galactic emission $L_{gxy}(f)$ is defined by the power law

$$L_{gxy}^2 = \left(\frac{f}{150 \text{ MHz}}\right)^{-2.4}. \tag{5.40}$$

Setting $T_{150} = 1106$ K simulates an antenna temperature of 1106 K at 150 MHz. This is the maximum antenna temperature expected for transit observations with the pyramidal spiral antenna. A pre-final amplifier gain of 52.3 dB was used along with the worst case autocorrelation receiver temperature with the noise source on $T_{rx} = 1{,}216$ K determined by the power level analysis of figure 5.1. This consists of a front-end contribution of 1,062 K and an antenna contribution of 154 K.

Narrowband interferers of equal power were added at 119 MHz and 122 MHz. Narrowband interference was approximated by adding delta functions to the linear filter response of Eq. (5.39) at the 100 kHz resolution of calculation. This is

representative of a sinusoid that is amplitude modulated by noise. The output spectrum for true Gaussian noise plus sinusoid input could be calculated from the results of Bedrosian and Rice (1971).

Figures 5.8, 5.9, and 5.10 show evaluations of Eq. (5.38) for the sky and system noise model of Eq. (5.39) plus interference with power densities of -190 dBW.Hz^{-1}, -160 dBW.Hz^{-1}, and -140 dBW.Hz^{-1} over 100 kHz at the antenna terminals. These levels correspond approximately to the 90^{th} percentile interference observed at the MRO, the strongest interference observed at the MRO, and typical interference levels observed at Narrabri with the completed system. Actual interference spectra for Narrabri and the MRO are presented in figures 7.1 and 7.2.

Dynamic range of 60 dB is comfortably achieved at the MRO for typical interference levels as shown by Figure 5.8. However, Figure 5.9 shows that second order harmonics and intermodulation products of the strongest interference may alias into the measured spectrum at levels less than 60 dB below the linear passband response. Data containing aliases of harmonics and intermodulation products must be rejected to maintain 60 dB dynamic range.

Narrabri provided a more challenging interference environment. Figure 5.10 shows that typical interference at Narrabri gives rise to in-band third order intermodulation products that are just over 10 dB below the linear passband response. Aliased second order harmonics and intermodulation products are stronger than the linear passband response. The system gain must be reduced for linear operation.

The next chapter shows that the system gain reduction at Narrabri is also required to maintain 60 dB dynamic range to clipping distortion caused by the samplers. Gain was reduced by removing the final RF amplifier from each receiver chain for initial testing at Narrabri.

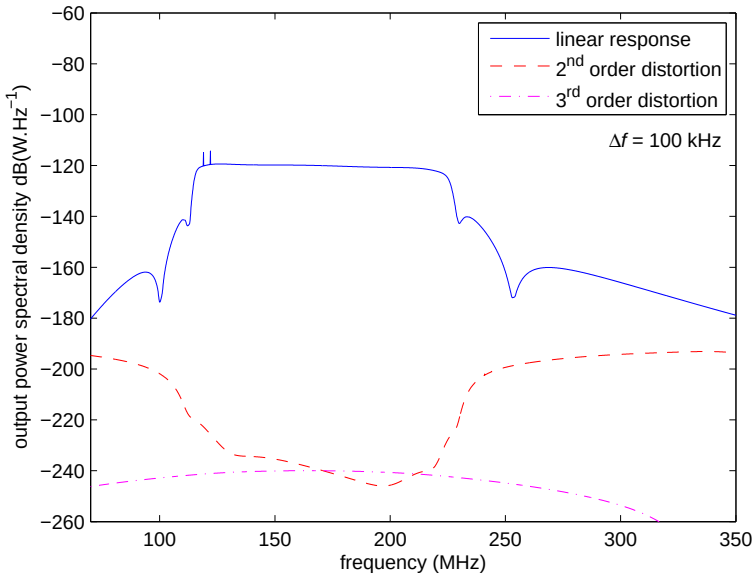

Fig. 5.8: Wiener model response for QB300 amplifier for two -190 dBW.Hz$^{-1} \times 100$ kHz interferers and peak galactic noise expected at galactic transit. This interference level corresponds to the 90^{th} percentile at the MRO.

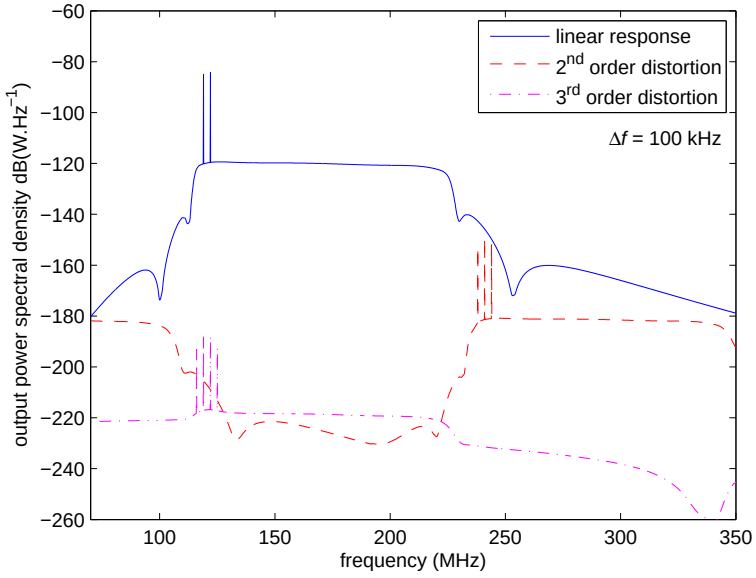

Fig. 5.9: Wiener model response for QB300 amplifier for two -160 dBW.Hz$^{-1} \times 100$ kHz interferers and peak galactic noise expected at galactic transit. This interference level corresponds to the strongest interference at the MRO.

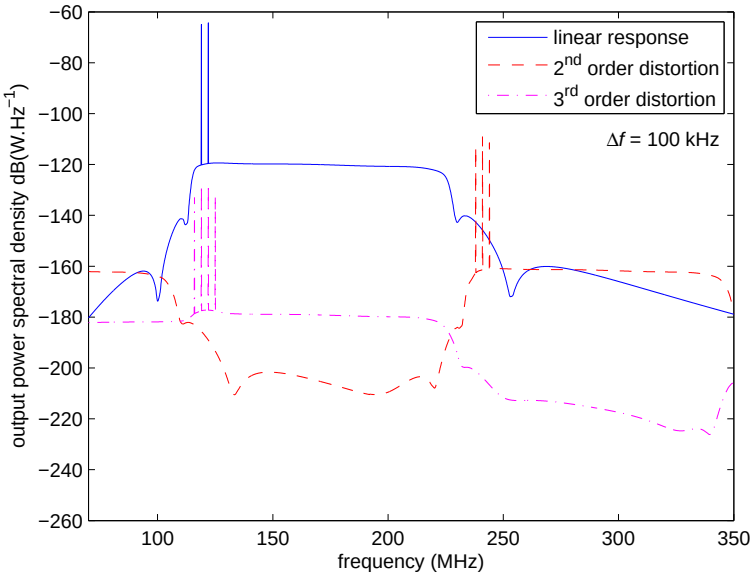

Fig. 5.10: Wiener model response for QB300 amplifier for two -140 dBW.Hz$^{-1} \times 100$ kHz interferers and peak galactic noise expected at galactic transit. This interference level corresponds to typical interference at Narrabri.

Chapter 6

BACK-END

This chapter discusses the specification and implementation of the back-end, which consists of two samplers and a correlation spectrometer. Distortions due to the quantisation of noise and interference are assessed and the correlator implementation is explained. Spectral dynamic range of 60 dB is required to measure the sky spectrum with 1 mK accuracy when the total system equivalent noise power is of order 1,000 K

Simulations show that 1-bit quantisation is sufficient for measuring the cosmological reionization monopole on a radio quiet site such as the Murchison Radioastronomy Observatory (MRO). Bussgang's theorem is extended and applied to show that 6-bit quantisation without correction is sufficient in the absence of interference. The back-end was implemented with 8-bit quantisation. Optimising the input power level makes 60 dB dynamic range to bandpass quantisation distortion possible for spectra with interference to noise ratios below 225.

The correlator was implemented in a field programmable gate array (FPGA) on a SERENDIP V spectrometer board acquired from the the University of California, Berkeley.

Original contributions in this chapter include:

1. showing that 1-bit quantisation with the van Vleck correction is sufficient to measure the 21 cm cosmological reionization monopole at the MRO;

2. showing that 1-bit quantisation distortion can be corrected in the presence of interference by inverting McFadden's approximation of the 1-bit correlation function for Gaussian noise plus sinusoid input;

3. showing that Bussgang's theorem holds in the total power limit for a memoryless, nonlinear system with Gaussian noise plus sinusoid input;

4. calculating the signal to clipping distortion ratio and signal to quantisation noise ratio at the output of a uniform, saturating quantiser with Gaussian noise plus sinusoid input;

5. developing a guide for selecting analogue to digital converter (ADC) resolution and input power level to meet target spectral dynamic range and sensitivity in a given interference environment;

6. modifying the firmware of a SERENDIP V board to act as a correlation spectrometer at twice the clock speed of the original design; and

7. integrating a SERENDIP V board with external ADCs to facilitate data capture twice as fast as the on-board ADCs in the original design.

The work on 1-bit quantisation distortion was published as:

A. P. Chippendale, R. Subrahmanyan, R. D. Ekers, "Effects of Interference on the ATNF Cosmological Reionization Experiment at Mileura", in *Proceedings of the XXIXth General Assembly of the International Union of Radio Science*, Delhi, 23-29 October 2005.

6.1 Introduction

This chapter presents the specification and implementation of the back-end. First, distortion due to 1-bit quantisation of Gaussian noise plus a sinusoid is characterised via numerical simulation. Second, distortion due to multi-bit quantisation of Gaussian noise plus a sinusoid is explored theoretically. Finally, the specific implementation using 8-bit ADCs and an FPGA-based FX correlator is summarised.

The back-end's main functions are analogue to digital conversion, channelisation, correlation detection, averaging and storage. It consists of two 10-bit 250 Msps ADCs of which the eight most significant bits are used at 228 Msps; a dual input FX correlator with 1,024 channels across 114 MHz; a control computer; and a notebook PC for data storage.

The following section calculates the number of bits required to achieve 60 dB spectral dynamic range to quantisation distortion in an ideal sampler. Other practical ADC errors are avoided by using the 8 most significant bits of a 10-bit ADC with 70 dB spurious free dynamic range and 65 dBc dynamic range to two-tone intermodulation products for inputs at -7 dBFS (referenced to full scale). The dynamic range to spurious responses therefore meets the 60 dB requirement for near full-scale inputs and full-scale inputs will be rare on a radio quiet site like the MRO.

6.2 Quantisation Distortion

It is important to prevent quantisation distortion from confusing the weak spectrum of the cosmological reionization monopole. Quantisation causes nonlinear distortions that are exacerbated by fewer quantisation levels and stronger interference. The distortions include harmonics of the interference, intermodulation products between multiple interferers, and bandpass distortions arising from mixing of interference and broadband system noise. Bandpass distortion due to 1-bit and multi-bit quantisation was assessed for interference levels characteristic of the MRO.

6.2.1 1-bit Quantisation

An early task of this project was to determine how many bits are necessary to measure the sky spectrum with millikelvin accuracy in a given interference environment. This question was first posed as: is it possible to measure the sky spectrum with millikelvin accuracy on a radio quiet site? A 1-bit back-end is simpler to build, but 1-bit data requires amplitude information for absolute calibration. This could be measured by adding a coupler and a total power detector to the system.

Simulations were made to determine the distortion induced by 1-bit quantisation on the autocorrelation of Gaussian noise plus a sinusoid. The effectiveness of correcting the autocorrelation function for the distortion was also tested. Results show that 1-bit quantisation with the van Vleck (1943) correction is sufficient for measuring the cosmological reionization monopole at the radio quiet MRO. Further, a correction based on the work of McFadden (1956) could make the experiment possible with 1-bit quantisation on less radio quiet sites.

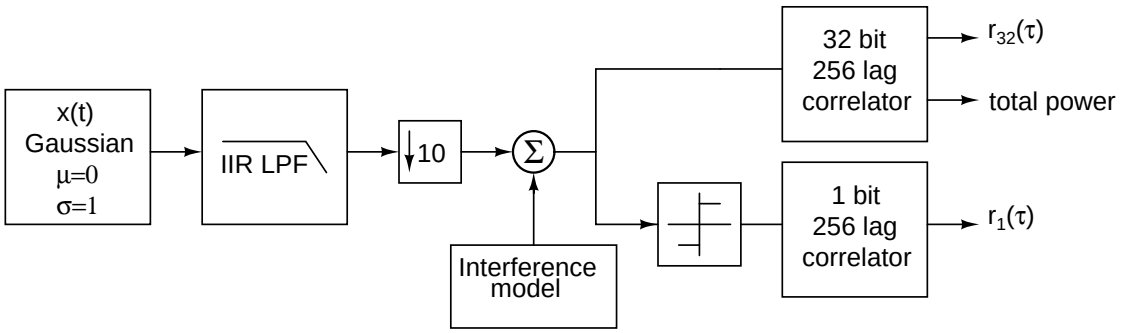

Fig. 6.1: 1-bit quantisation simulation architecture.

Simulation Architecture

Correlation with both 32-bit floating point and 1-bit quantisation was simulated according to figure 6.1. Gaussian pseudorandom numbers were generated by the method of Matsumoto and Nishimura (1998) implemented by Galassi et al. (2009). These numbers were low-pass filtered by a fourth order Chebyshev filter and down-sampled by a factor of 10. The filter had 1 dB passband ripple and 20 dB attenuation at the Nyquist frequency. A sinusoid was added to the band limited noise before correlation and accumulation by 32-bit and 1-bit correlator algorithms with 256 lags. The correlation functions were Fourier transformed and the 32-bit spectrum was subtracted from the 1-bit spectrum to determine the distortion caused by 1-bit quantisation with respect to the 32-bit "ideal". Corrections to the 1-bit correlation function were then assessed for their ability to suppress quantisation distortion in the presence of sinusoidal interference.

The van Vleck Correction

The van Vleck correction (van Vleck, 1943; van Vleck and Middleton, 1966) exactly transforms the distorted 1-bit correlation function $r_1(\tau)$ of a Gaussian input into the true correlation function

$$\rho(\tau) = \sin\left(\frac{\pi}{2} r_1(\tau)\right). \tag{6.1}$$

McFadden (1956) renormalised the van Vleck correction to make it work for Gaussian noise with the addition of a weak sinusoid. For a sinusoid at frequency f the correction becomes

$$\tilde{\rho}_{\mathrm{v}}(\tau) = (1+a)\sin\left(\frac{\pi}{2} r_1(\tau)\right) - a\cos 2\pi f\tau + O(a^2) \tag{6.2}$$

where a is the interference to noise power ratio defined in terms of the amplitude A of the sinusoid and the variance σ_n^2 of the Gaussian noise

$$a = \frac{A^2}{2\sigma_n^2}. \tag{6.3}$$

The renormalised correction is accurate to first order in a and therefore appropriate for scenarios where $a \ll 1$.

The McFadden Correction

McFadden (1956) also derived a more accurate relationship between the 1-bit correlation function and the true correlation function of Gaussian noise plus a sinusoid. This relationship is a Maclaurin series evaluated to terms of second order in a

$$\begin{aligned} r_1(\tau) =& \frac{2}{\pi}\left[\sin^{-1}\rho(\tau) + a\frac{\cos 2\pi f\tau - \rho(\tau)}{(1-\rho^2(\tau))^{\frac{1}{2}}}\right. \\ & \left. - \frac{a^2}{4}\frac{(\cos 2\pi f\tau - \rho(\tau))\,(2-\rho(\tau)\cos 2\pi f\tau - \rho^2(\tau))}{(1-\rho^2(\tau))^{\frac{3}{2}}} + O(a^3)\right] \\ =& g(\rho(\tau), \tau, f, a). \end{aligned} \tag{6.4}$$

Inverting this expression numerically gives what might be called the McFadden correction

$$\tilde{\rho}_{\mathrm{m}}(\tau) = g^{-1}(r_1(\tau), \tau, \tilde{f}, \tilde{a}). \tag{6.5}$$

This estimates the true normalised correlation function $\rho(\tau)$ from the 1-bit correlation function $r_1(\tau)$ given estimates of the interference to noise total power ratio $\tilde{a}$ and frequency $\tilde{f}$ of the interferer.

Interference Model

During early design, the reference site for the reionization experiment was Mileura Station in the shire of Murchison, Western Australia and the planned operating band was 100 MHz to 200 MHz. Interference levels at Mileura were surveyed for the SKA and LOFAR site selection processes (Chippendale et al., 2003). Data in the 100 MHz to 200 MHz band were used to predict interference levels for an experiment to detect the cosmological reionization monopole.

The analysis predicted total interference power significantly less than total system noise power for the reionization experiment. Total noise power referenced to the reionization antenna terminals of -85 dBm is expected based on the peak system temperature of 2,167 K expected over the 114 MHz to 228 MHz band when the antenna temperature is maximum and the noise diode is turned on. The strongest interferer in the radio frequency interference (RFI) survey would appear 33 dB below the expected total noise power of the reionization receiver. This assumes a reionization antenna pointed at the zenith with 20 dB less response towards the horizon than the RFI survey antenna. The next strongest signal was a further 6 dB down and the median level would appear 59 dB below the expected total noise power. Hence, the interference to noise total power ratio was expected to rarely exceed $a \approx 1 \times 10^{-3}$.

The experiment was deployed to the MRO, approximately 80 km from Mileura. The interference environment was comparable to that expected from measurements at Mileura. At the MRO it was found that $a < 2 \times 10^{-3}$ for 90% of the time and $a < 3$ for 99.98% of the time in the 114 MHz to 228 MHz band. This is based on 24 hours of data collected with the experimental system on universal time (UT) date 4 December 2007 and assumes there is no extensive population of interferers just below the noise floor.

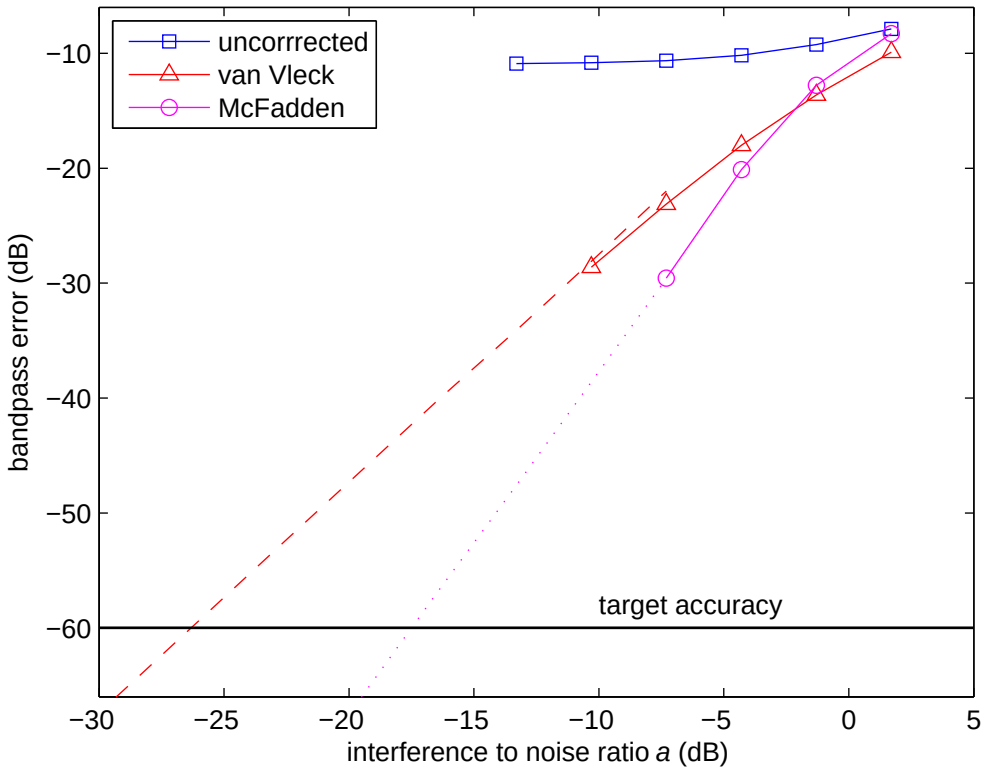

Fig. 6.2: Simulated bandpass error for 1-bit quantisation of Gaussian noise plus interference. Decibels are referenced to total input noise power. The solid lines show the simulation results. The dashed line is an analytic prediction for the van Vleck correction and the dotted line is an extrapolation for the McFadden correction with slope fixed by theory. A single sinusoid was injected in channel 8 of 256 to simulate interference.

Results

Bandpass distortion due to quantisation is of primary concern as it can mask the spectrum of the cosmological reionization monopole. Harmonics and intermodulation products occur in distinct and predictable channels and so that data affected by them can be rejected.

Bandpass error was quantified by measuring the standard deviation of the error spectrum generated by subtracting the 32-bit spectrum from the 1-bit spectrum. Frequencies containing harmonics of the interfering sinusoid were excluded from this calculation. Defined in this way, the bandpass error measures shape variation of the measured spectra due to quantisation distortion. It discounts total power offset which is unimportant for measuring the shape of the spectrum and therefore the cosmological reionization monopole. Figure 6.2 plots simulated bandpass error due to 1-bit quantisation against the input interference to noise power ratio. It also shows how the van Vleck and McFadden corrections reduce quantisation error and highlights the 60 dB dynamic range desired for the reionization experiment.

An analytical calculation was made for the expected bandpass error after application of the renormalised van Vleck correction of Eq. (6.2). This was achieved by substituting the van Vleck correction of Eq. (6.2) into Eq. (6.4) which is McFaddens expression for the 1-bit correlation function. The resulting error estimate is consistent with extrapolation of the simulated results as shown by the dashed line in figure 6.2. Theory and simulation agree that bandpass distortion due to 1-bit quantisation should not impede measurement of the cosmological reionization monopole at the MRO where the interference to noise ratio is expected to be less than -27 dB ($a = 2 \times 10^{-3}$) most of the time.

The McFadden correction reduces the bandpass error two orders of magnitude further than the van Vleck correction for a -27 dB interference to noise ratio. This was determined by extrapolating the simulated bandpass error, after applying the McFadden correction of Eq. (6.5), to lower interference levels as shown by the dotted line in figure 6.2. The level of this extrapolation was calibrated by the simulated results but the slope with respect to $\log a$ was fixed to three as predicted by theory. McFadden's expression for the 1-bit correlation function in Eq. (6.4) is a Maclaurin series expanded to terms of second order in a. The residual error after correction should thus be proportional to a^3. The simulation results at low interference levels match this theoretical slope.

The McFadden correction could be used in cases where there is stronger interference dominated by a single interferer. The series expansion leading to the McFadden correction can be evaluated to higher orders for better correction. The series could also be evaluated for scenarios with multiple sinusoids. However, these techniques do not appear necessary at the radio quiet MRO where the renormalised van Vleck correction is sufficient.

6.2.2 Multi-bit Quantisation Distortion

Two distortions are imparted by quantisation with a finite number of levels: quantisation distortion and clipping distortion. Quantisation distortion for a Gaussian input is itself white, Gaussian noise and is thus called quantisation noise. Quantisation noise reduces as the probability density of the input function is better sampled by the quantisation function. This can be achieved by increasing the number of quantisation levels or by increasing the input power to better spread its probability density function across quantisation levels. Clipping distortion is minimised by reducing the power level of the input signal and hence reducing the probability of the signal being clipped at the peak quantisation level. This leads to a trade-off between quantisation noise and clipping distortion when setting the input power level.

Gray and Zeoli (1971) separately calculated the total power in quantisation noise and the total power in clipping distortion at the output of a multi-bit quantiser with evenly spaced steps and white Gaussian input. Dardari (2006) introduced a combined signal to distortion and quantisation noise ratio (SDQNR) that is rigorously derived from Bussgang's theorem (Bussgang, 1975).

Hereafter, the SDQNR is separated into a signal to quantisation noise ratio (SQNR) and a signal to clipping distortion ratio (SCDR) that are both based on

Bussgang's theorem. It is then shown that Bussgang's theorem holds in the total power limit for a memoryless, nonlinear system with Gaussian noise plus sinusoid input. This allows the SDQNR, SQNR and SCDR to be defined for a quantiser with Gaussian noise plus sinusoid input. Finally, these three ratios are calculated for expected interference levels at the MRO and used to select an appropriate quantiser bit-resolution and input power level for the reionization experiment.

Bussgang's Theorem

Bussgang's theorem (Bussgang, 1975; Bendat, 1990) relates the input/output cross-correlation $R_{xy}(\tau)$ of a memoryless nonlinear system $y = g(x)$ to its input autocorrelation $R_{xx}(\tau)$ for Gaussian input $x(t)$ of variance σ_x^2

$$R_{xy}(\tau) = \left(\frac{E[xg(x)]}{\sigma_x^2} \right) R_{xx}(\tau). \tag{6.6}$$

It follows that a memoryless, nonlinear transformation of a Gaussian input produces an output power spectral density $s_{yy}(f)$ that is a scaled version of the input power spectral density $s_{xx}(f)$ plus distortion $d(f)$ (Bendat, 1990)

$$s_{yy}(f) = \alpha^2 s_{xx}(f) + d(f). \tag{6.7}$$

The distortion $d(f)$ is not correlated with the input and is not necessarily Gaussian. The scaling factor α is given by Bussgang's theorem

$$\begin{aligned} \alpha &= \frac{R_{xy}(\tau)}{R_{xx}(\tau)} = \left(\frac{E[xg(x)]}{\sigma_x^2} \right) \\ &= \frac{1}{\sigma_x^2} \int_{-\infty}^{\infty} xg(x)P(x)dx \end{aligned} \tag{6.8}$$

where $P(x)$ is the Gaussian probability density function (PDF) of the input

$$P(x) = \frac{1}{\sigma_n \sqrt{2\pi}} e^{-x^2/2\sigma_n^2} \tag{6.9}$$

and σ_n is the standard deviation of the Gaussian noise component of the input signal. When there is no interference, the standard deviation of the input signal σ_x is equal to σ_n.

Signal to Distortion and Quantisation Noise Ratio

Bussgang's theorem can be used to to calculate the SDQNR for a memoryless nonlinear system with Gaussian input (Dardari, 2006)

$$SDQNR = \frac{\alpha^2 \sigma_n^2}{\sigma_y^2 - \alpha^2 \sigma_n^2}. \tag{6.10}$$

The output variance σ_y^2 contains both scaled input power and distortion power as indicated by the total power form of Eq. (6.7)

$$\sigma_y^2 = \alpha^2 \sigma_x^2 + \delta^2 \tag{6.11}$$

where δ^2 is the variance of the distortion. Subtracting the scaled input variance from the output variance therefore yields the distortion variance required in the denominator of the SDQNR. The output variance is calculated by

$$\sigma_y^2 = \int_{-\infty}^{\infty} g^2(x)P(x)dx - \left[\int_{-\infty}^{\infty} g(x)P(x)dx\right]^2. \tag{6.12}$$

For odd $g(x)$ and even $P(x)$ this simplifies to

$$\sigma_y^2 = \int_{-\infty}^{\infty} g^2(x)P(x)dx. \tag{6.13}$$

Dardari (2006) calculated the SDQNR for a Gaussian input quantised by an L level uniform mid-raiser staircase function and clipped to the range $[-M, M]$. This nonlinear operation is defined by the quantisation function

$$y = Q(x) = \sum_{-L/2+1}^{L/2} q_i r(x, \hat{x}_{i-1}, \hat{x}_i) \tag{6.14}$$

where $\hat{x}_i$ are the quantisation thresholds, q_i are the quantisation levels and $r(x, a, b)$ is a rectangular function defined by

$$r(x, a, b) = \begin{cases} 1 & \text{if } a \leq x < b, \text{ or} \\ 0 & \text{otherwise.} \end{cases} \tag{6.15}$$

The quantisation levels for uniform step size $\Delta = 2M/(L-1)$ are given by

$$q_i = i\Delta - \Delta/2 \tag{6.16}$$

and the quantisation thresholds are given by

$$\hat{x}_i = \begin{cases} i\Delta & \text{if } |i| < L/2, \\ -\infty & \text{if } i = -L/2, \text{ or} \\ \infty & \text{if } i = L/2. \end{cases} \tag{6.17}$$

Substituting the Gaussian PDF and the quantisation function of Eq. (6.14) into Eq. (6.8) gives the scaling factor α for the L level uniform quantiser (Dardari, 2006)

$$\alpha = \frac{k}{\sqrt{2\pi}} \sum_{i=-L/2+1}^{L/2} q_i \left[e^{-k^2\hat{x}_{i-1}^2/2} - e^{-k^2\hat{x}_i^2/2}\right]. \tag{6.18}$$

The saturation level M was arbitrarily set to unity and clipping factor $k = M/\sigma = 1/\sigma$ was introduced to define the truncation point in terms of standard deviations of the input noise distribution. Making the same substitutions into Eq. (6.13) gives the output variance of the L level uniform midraiser quantiser with Gaussian input (Dardari, 2006)

$$\sigma_y^2 = \frac{1}{2} \sum_{i=-L/2+1}^{L/2} q_i^2 \left[\operatorname{erfc}\left(\frac{k\hat{x}_{i-1}}{\sqrt{2}}\right) - \operatorname{erfc}\left(\frac{k\hat{x}_i}{\sqrt{2}}\right)\right]. \tag{6.19}$$

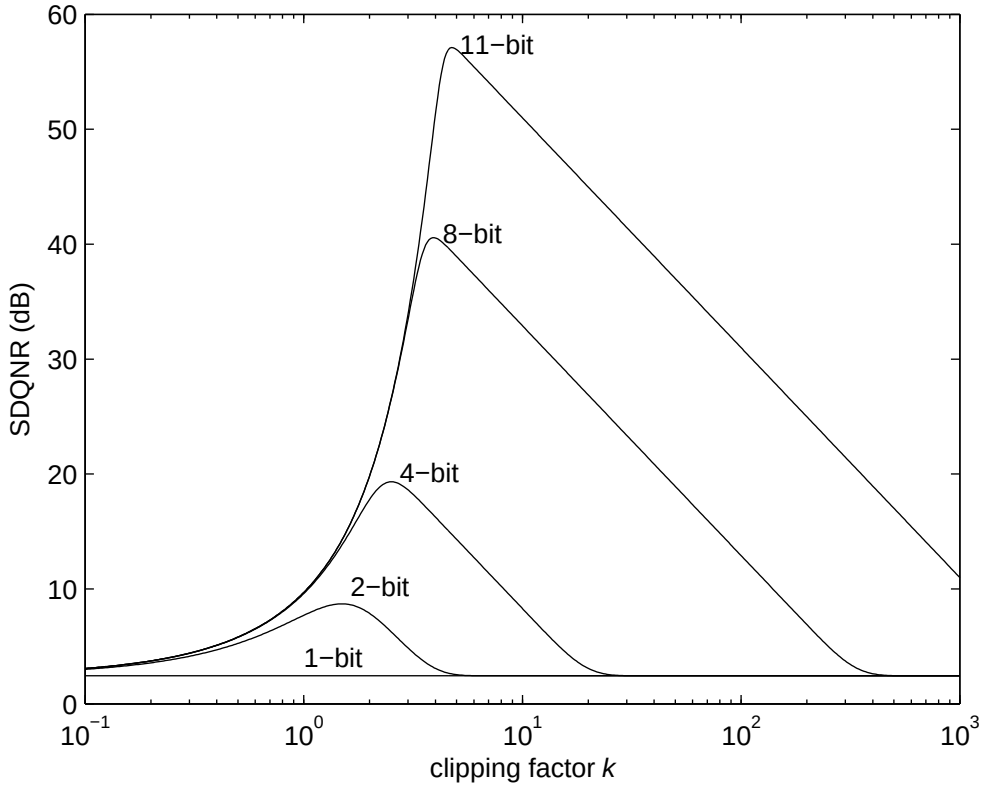

Fig. 6.3: Signal to distortion and quantisation noise ratio (SDQNR) for quantisers with different bit resolutions.

These results were substituted into Eq. (6.14) to calculate the SDQNR. Figure 6.3 plots the SDQNR versus clipping factor for b-bit quantisers with $L = 2^b$ levels. Except for the degenerate 1-bit case, each quantiser has an optimum saturation factor k_0 that maximises its SDQNR and defines an optimum input power level. The plot suggests that an 11-bit ADC is needed to measure the cosmological reionization monopole 55 dB below the system noise.

This is not the case, however, as a significant component of the distortion spectrum $d(f)$ is quantisation noise that decreases sensitivity but will not confuse the reionization spectrum. Quantisation noise is the distortion $d_q(f)$ due to uniform quantisation of bandlimited Gaussian noise without saturation. It is white Gaussian noise with variance $\delta_q^2 = \Delta^2/12$ (Widrow, 1956; Widrow et al., 1996) that depends only on the quantisation step size. Although its spectrum is flat and featureless, it is an unwanted additive contribution that must be estimated and subtracted prior to the calibration of spectra.

Maximising the SDQNR, and therefore the signal to noise ratio, is appropriate for communications. This is because channel capacity monotonically increases with the signal to noise ratio for a channel subject to additive white Gaussian noise (Shannon, 1948). Maximising the SDQNR is also appropriate for radio transient detection with negligible integration time. However, it is not appropriate for the current experiment that attempts to measure the spectrum of quasi-stationary noise

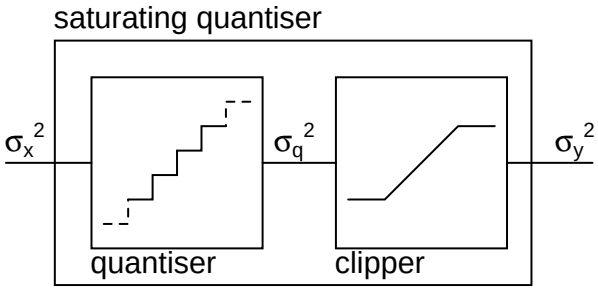

Fig. 6.4: The saturating quantiser as the concatenation of an infinite quantiser and a clipper.

very accurately with an integrating radiometer. It is useful to partition the SDQNR into a signal to quantisation noise ratio (SQNR) that is benign for the current experiment and a signal to clipping distortion ratio (SCDR) that is performance limiting.

Separating Quantisation Noise and Clipping Distortion

The saturating uniform quantiser is equivalent to the concatenation of an infinite, uniform quantiser and a clipper as shown by figure 6.4. Applying Eq. (6.7) to the concatenated system, the clipper alone, and the quantiser alone gives

$$\sigma_y^2 = \alpha^2\sigma_x^2 + \delta^2, \tag{6.20}$$

$$\sigma_y^2 = \alpha_c^2\sigma_q^2 + \delta_c^2, \quad \text{and} \tag{6.21}$$

$$\sigma_q^2 = \alpha_q^2\sigma_x^2 + \delta_q^2. \tag{6.22}$$

Here δ_c^2 is the variance of the clipping distortion. The above equations identify that the overall scaling factor is $\alpha^2 = \alpha_c^2\alpha_q^2$ and yield a representation of the output power from which the distortion due to quantising and clipping may be separated

$$\sigma_y^2 = \alpha^2\sigma_x^2 + \alpha_c^2\delta_q^2 + \delta_c^2. \tag{6.23}$$

Together with the approximation $\delta_q^2 = \Delta^2/12$ this leads to the definition of the output signal to quantisation noise ratio

$$SQNR = \frac{\alpha^2\sigma_n^2}{\alpha_c^2\Delta^2/12} \tag{6.24}$$

and the output signal to clipping distortion ratio

$$SCDR = \frac{\alpha^2\sigma_n^2}{\sigma_y^2 - \alpha^2\sigma_n^2 - \alpha_c^2\Delta^2/12}. \tag{6.25}$$

Calculating the SQNR and the SCDR requires the scaling factor α_c of the clipper. This is derived by applying Eq. (6.8) to the clipping function

$$c(x) = \begin{cases} x & \text{if } |x| \le M \\ M\text{sgn}(x) & \text{otherwise.} \end{cases} \tag{6.26}$$

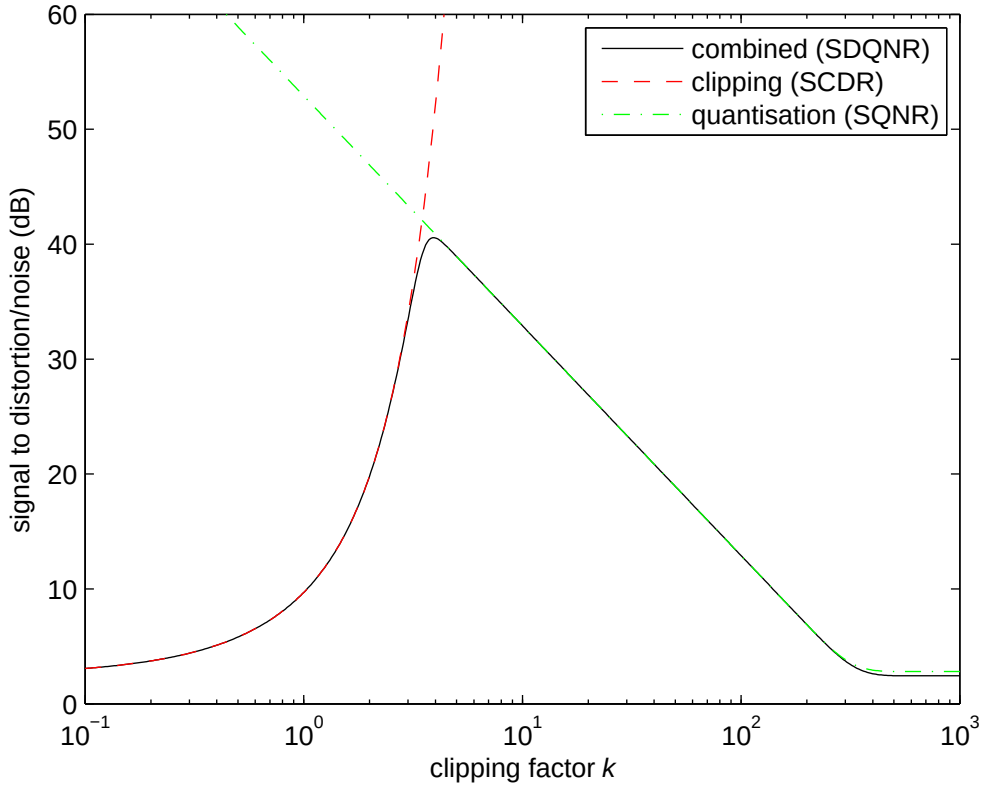

Fig. 6.5: Separation of output signal to distortion and quantisation noise ratio (SDQNR) for 8-bit quantiser into signal to clipping distortion ratio (SCDR) and signal to quantisation noise (SQNR). The input is Gaussian and the peak quantiser level is $k\sigma$.

For the current case of $M = 1$ and $k = 1/\sigma$ this gives

$$\alpha_c = \operatorname{erf}\left(\frac{k}{\sqrt{2}}\right). \tag{6.27}$$

Figure 6.5 shows the resulting partitioning of the SDQNRR into the SQNR and the SCDR for an 8-bit quantiser. The SQNR shows a small error for $k > 300$. Here the input power is so low that the Gaussian PDF changes rapidly over a single quantisation step and invalidates the $\delta_q^2 \approx \Delta^2/12$ approximation. The system would not be operated with such low input power as quantisation distortion would increase the system temperature by 57% as in the case of a 1-bit quantisation.

Effects of Sinusoidal Interference

The current analysis can be extended to determine the effects of sinusoidal interference on the quantisation of Gaussian noise. Bussgang's theorem does not hold in general for input distributions that are not Gaussian. However, it does hold in the total power limit for Gaussian noise plus a sinusoid. The PDF for a Gaussian

noise plus a sinusoid is given by (Bennett, 1944)

$$P(x) = \frac{1}{\pi\sigma_n\sqrt{2\pi}} \int_0^{\pi} e^{-(x-A\cos\theta)^2/2\sigma_n^2} d\theta. \tag{6.28}$$

Substituting this into the proof of Bussgang's theorem offered by Bendat (1990) leads to the relationship

$$R_{xy}(\tau) = \frac{1}{\pi\sigma_n\sqrt{2\pi}} \int_{-\infty}^{\infty} g(x) \int_0^{\pi} e^{\frac{-(x-Acos(\theta+\omega\tau))^2}{2\sigma_n^2}} \times \{\rho_{xx}(\tau)x + A\cos\theta - \rho_{xx}(\tau)A\cos(\theta+\omega\tau)\}\, d\theta dx. \tag{6.29}$$

This is equivalent to Bussgang's theorem for the total power case of $\tau = 0$

$$R_{xy}(0) = \left(\frac{E[xg(x)]}{\sigma_x^2}\right) R_{xx}(0). \tag{6.30}$$

The definition of the scaling factor α in Eq. (6.8) therefore holds for an input consisting of Gaussian noise plus a sinusoid. Note that the input variance becomes $\sigma_x^2 = (1+a)\sigma_n^2$ where a is the interference to noise power ratio. Eq. (6.18) may now be evaluated for the Gaussian noise plus sinusoid PDF and the quantisation equation of Eq. (6.14). This gives α for an L level, midraiser, uniform quantiser with Gaussian noise plus sinusoid input

$$\alpha = \frac{k}{\pi(1+a)\sqrt{2\pi}} \int_0^{\pi} \sum_{i=-L/2+1}^{L/2} q_i \Bigg\{ \left[e^{-\left(\frac{k\hat{x}_{i-1}}{\sqrt{2}} - \sqrt{a}\cos\theta\right)^2} - e^{-\left(\frac{k\hat{x}_i}{\sqrt{2}} - \sqrt{a}\cos\theta\right)^2} \right] + \sqrt{\pi a}\cos\theta \left[\operatorname{erfc}\left(\frac{k\hat{x}_{i-1}}{\sqrt{2}} - \sqrt{a}\cos\theta\right) - \operatorname{erfc}\left(\frac{k\hat{x}_i}{\sqrt{2}} - \sqrt{a}\cos\theta\right) \right] \Bigg\} d\theta. \tag{6.31}$$

Making the same substitutions into Eq. (6.19) gives the output variance

$$\sigma_y^2 = \frac{1}{2\pi} \int_0^{\pi} \sum_{i=-L/2+1}^{L/2} q_i^2 \left[\operatorname{erfc}\left(\frac{k\hat{x}_{i-1}}{\sqrt{2}} - \sqrt{a}\cos\theta\right) - \operatorname{erfc}\left(\frac{k\hat{x}_i}{\sqrt{2}} - \sqrt{a}\cos\theta\right) \right] d\theta. \tag{6.32}$$

The SDQNR must be updated to subtract the power of the input sinusoid from the output variance

$$\text{SDQNR} = \frac{\alpha^2\sigma_n^2}{\sigma_y^2 - (1+a)\alpha^2\sigma_n^2}. \tag{6.33}$$

The SQNR does not change form, but the SCDR must be updated, in the same fashion as the SDQNR, to account for the sinusoid's contribution to the output variance

$$\text{SCDR} = \frac{\alpha^2\sigma_n^2}{\sigma_y^2 - (1+a)\alpha^2\sigma_n^2 - \alpha_c^2\Delta^2/12}. \tag{6.34}$$

Evaluation of the SQNR and the SCDR requires the scaling factor for a clipper with Gaussian noise plus a sinusoid at its input

$$\alpha_c = \frac{1}{\pi(} \int_{-\infty}^{\infty} \left\{ (2a\cos^2\theta + 1) \left[\operatorname{erf}\left(\frac{k}{\sqrt{2}} - \sqrt{a_c}\cos\theta \right) + \operatorname{erf}\left(\sqrt{a_c}\cos\theta\right) \right] \right.$$
$$+ k\sqrt{2a}\cos\theta \operatorname{erfc}\left(\frac{k}{\sqrt{2}} - \sqrt{a_c}\cos\theta \right) + \frac{2\sqrt{a_c}\cos\theta}{\sqrt{\pi}} e^{-a_c\cos^2\theta}$$
$$\left. - \frac{2\sqrt{a_c}\cos\theta}{\sqrt{\pi}} e^{-\left(\frac{k}{\sqrt{2}} - \sqrt{a_c}\cos\theta\right)^2} \right\} d\theta. \tag{6.35}$$

Here $a_c = a/(1 + k^2\delta_q^2)$ is the slightly lower interference to noise ratio seen at the input of the clipper due to quantisation noise. Figure 6.6 plots the SDQNR of an 8-bit quantiser versus clipping factor for various interference to noise power ratios a. Figure 6.7 shows the separation of the SCDR from the SDQNR of an 8-bit quantiser for various interference to noise power ratios.

Selecting Bit Resolution and Input Power

Three important clipping factors guide the selection of bit resolution and input power level for the quantisation of noise in the presence of interference:

1. k_0 that maximises the SDQNR;

2. k_1 that gives the lowest acceptable SCDR
   (60 dB for measuring 1 mK on an order 1,000 K foreground); and

3. k_2 that gives the lowest acceptable SQNR
   (20 dB to limit quantisation noise T_{sys} increase to 1%).

The optimum clipping factor for communications and transient detection is k_0 that maximises the SDQNR. It is referred to as k_{opt} in the literature (Gray and Zeoli, 1971) but it is not optimum for measuring the power spectral density of quasi-stationary noise.

Spectral analysis of quasi-stationary noise requires a trade-off between sensitivity and dynamic range to bandpass distortion. The clipping factor must be set above k_1 to achieve an acceptable SCDR but below k_2 to stop quantisation noise degrading system temperature. In this work k_1 was set for a minimum SCDR of 60 dB and k_2 was set for an SQNR of 20 dB. Clipping factors between k_1 and k_2 maintain a 60 dB dynamic range to bandpass distortion and stops quantisation noise from increasing the system temperature by more than 1%. Table 6.1 provides k_0, k_1, and k_2 for 4-bit to 12-bit quantisers and interference to noise power ratios a ranging from 0 to 1,000.

Spectral dynamic range and sensitivity requirements for spectral analysis of quasi-stationary noise may be jointly met if $k_2 > k_1$. Most headroom is allowed for interference and fluctuations in noise power level if the clipping factor is set to k_2 at the minimum expected noise power level. For the current experiment, the

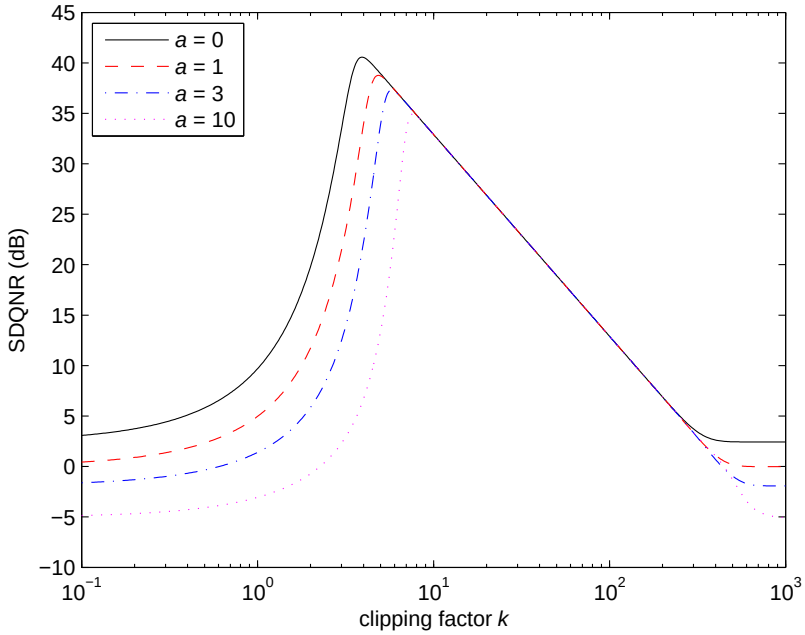

Fig. 6.6: Signal to distortion and quantisation noise ratio (SDQNR) versus clipping factor for 8-bit quantisation of Gaussian noise plus a sinusoid. Repeated for various interference to noise power ratios a.

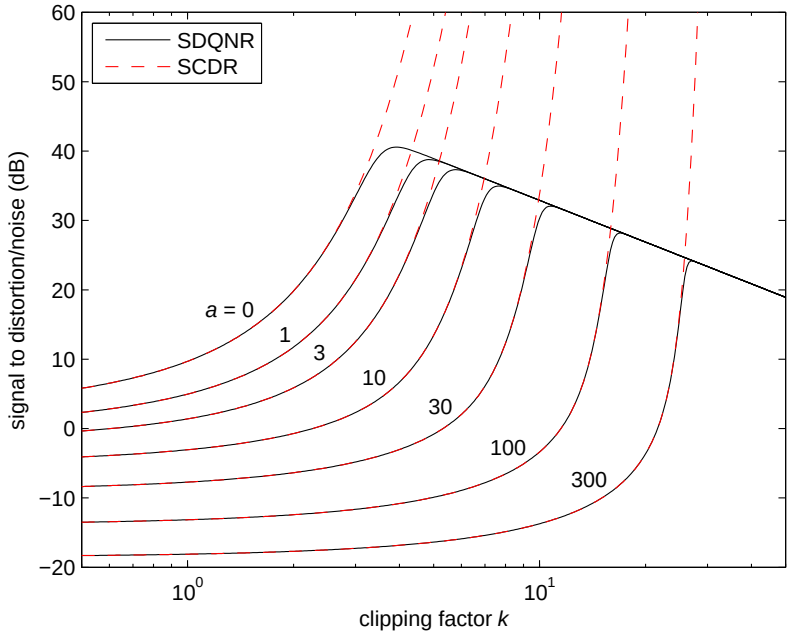

Fig. 6.7: Signal to distortion and quantisation noise ratio (SDQNR) and signal to clipping distortion ratio (SCDR) versus clipping factor for 8-bit quantisation of Gaussian noise plus a sinusoid. Repeated for various interference to noise power ratios a.

requirement becomes $k_2 > 2.5k_1$ assuming a receiver temperature of $T_{rx} = 1{,}216$ K that is increased by $\Delta T = 1{,}669$ K when the noise source is turned on, a maximum band average antenna temperature $T_a = 951$ K, and a minimum band average antenna temperature of $T_a = 290$ K. The clipping factor at minimum antenna temperature may be set by replacing the antenna with a matched load of physical temperature T_p and varying the receiver gain to give a clipping factor of $k = k_2(\min(T_a) + T_{rx})/(T_p + T_{rx})$.

An 8-bit ADC was used for measurements at the MRO with $k = 7.8$ at minimum antenna temperature with the noise source off rather than $k = k_2 = 44.2$ as prescribed by the current analysis. This requires rejecting any spectra with $a > 7.7$ to maintain an SCDR above 60 dB at minimum antenna temperature. At maximum antenna temperature, when the noise source is off, the clipping factor will be $k = 5.6$. In this case spectra with $a > 1.3$ must be rejected to maintain an SCDR above 60 dB. When the noise source is turned on at maximum antenna temperature, the clipping factor will be $k = 3.1$ and the SCDR will be 36 dB even in the absence of RFI. Hence, the noise source on spectra may contain quantisation distortion residuals of order 1 K at peak antenna temperature when the noise source is on[1].

Future experiments with the 8-bit system should set $k = k_2 = 44.2$ at minimum antenna temperature. This will fall to $k = 17.7$ at galactic transit and necessitate the rejection of spectra with $a > 97$ to maintain 60 dB SCDR at all times. For this correct setting of input power level, no spectra would need to be rejected to maintain a 60 dB SCDR at the radio quiet MRO. It is clear that ADCs with more than 8-bits are required for further work at Narrabri where the typical interference to noise power ratio is $a \approx 300$.

6.3 Implementation

6.3.1 Analogue to Digital Converters

Although the spectrometer board used for the correlator was designed for 100 Msps sampling, it included four ADCs that can operate up to 200 Msps. However, the single-ended digital outputs of the ADCs are not powerful enough to drive the capacitive load of the microstrip lines to the correlator FPGA fast enough for 200 Msps operation. This arose as the board was designed for another purpose and for which for another purpose with was not an issue for the the spectrometer board was designed for a 100 Msps sample rate.

10-bit 250 Msps ADCs with low voltage differential signalling (LVDS) outputs were selected to replace the on-board ADCs. Their outputs were routed to the spectrometer board via a compact peripheral component interconnect (cPCI) bus backplane and a purpose designed auxiliary interface board. All ten ADC outputs were routed to the FPGA, but only the eight least significant bits are used by the correlator firmware. The ADCs have 70 dB spurious free dynamic range and

[1] This may introduce a 0.1% error in the bandpass estimate formed by subtracting noise on spectra from noise off spectra considering that the noise source calibration step is 983 K.

Tab. 6.1: Important clipping factors for different interference to noise power ratios a: k_0 maximises the SDQNR, k_1 gives an SCDR of 60 dB, and k_2 gives an SQNR of 20 dB.

M	a	k_0	k_1	k_2	$SDQNR(k_0)$ dB	$SCDR(k_0)$ dB
4 bits	0	2.5	4.5	2.6	19.3	26.3
5 bits	0	2.9	4.4	5.4	24.6	32.5
	1	3.7	5.4	5.4	22.5	31.0
	10	6.4	8.3	5.4	18.0	28.3
6 bits	0	3.3	4.4	10.9	29.8	38.6
	1	4.2	5.4	10.9	27.9	37.2
	10	6.9	8.3	10.9	23.7	34.7
7 bits	0	3.6	4.4	22.0	35.2	44.6
	1	4.5	5.4	22.0	33.3	43.3
	10	7.3	8.3	22.0	29.3	40.9
	100	16.5	17.9	22.0	22.3	36.9
8 bits	0	3.9	4.4	44.2	40.6	50.5
	1	4.9	5.4	44.2	38.8	49.3
	10	7.6	8.3	44.2	35.0	47.1
	100	16.9	17.9	44.2	28.2	43.3
	1,000	47.0	48.3	44.2	19.4	38.4
9 bits	0	4.2	4.4	88.5	46.0	56.5
	1	5.2	5.4	88.5	44.3	55.3
	10	8.0	8.3	88.5	40.6	53.2
	100	17.3	17.9	88.5	34.0	49.6
	1,000	47.5	48.3	88.5	25.4	44.8
10 bits	0	4.5	4.4	177.2	51.6	62.5
	1	5.5	5.4	177.2	49.9	61.4
	10	8.3	8.3	177.2	46.4	59.4
	100	17.7	17.9	177.2	39.9	55.8
	1,000	47.8	48.3	177.2	31.3	49.8
11 bits	0	4.8	4.4	354.6	57.1	68.5
	1	5.8	5.4	354.6	55.5	67.4
	10	8.6	8.3	354.6	52.1	65.5
	100	17.9	17.9	354.6	45.8	62.0
	1,000	48.2	48.3	354.6	37.3	57.5
12 bits	0	5.0	4.4	709.3	62.7	74.4
	1	6.0	5.4	709.3	61.1	73.4
	10	8.9	8.3	709.3	57.9	71.6
	100	18.3	17.9	709.3	51.7	68.2
	1,000	48.6	48.3	709.3	43.3	69.6

65 dBc dynamic range to two-tone intermodulation products for inputs at -7 dBFS (referenced to full scale). The dynamic range to spurious responses is therefore greater than 60 dB for near full-scale inputs and full-scale inputs will be rare on a radio quiet site like the MRO.

One ADC was mounted in each of the two receiver boxes and their LVDS outputs were connected to the auxiliary interface board by twisted pair ribbon cables. This solution worked but, despite the use of differential signals, radiation from the ribbon cables dominated self-generated interference.

Future solutions might involve mounting the ADCs on the auxiliary cPCI board and running coax directly from the receiver boxes to the correlator chassis. This approach would likely trade isolation between the inputs for reduced leakage from the existing ribbon cables into the antenna. This could be pursued later if self generated interference was found to be significant. Presently the correlator and receiver boxes are mounted in a Faraday cage. With this arrangement system operation does not appear to be limited by self interference.

6.3.2 Correlator

The correlator was implemented on a SERENDIP V[2] spectrometer board provided by the University of California at Berkeley (Parsons et al., 2004). At the time of acquisition, the board was being used as a polyphase filter bank spectrometer with 100 MHz bandwidth for each of two complex sampled inputs. The current experiment required addition of a cross multiply function and an increase of the bandwidth to accommodate two 114 MHz bandwidth real inputs. This involved clocking the FPGA at 228 MHz, more than twice as fast as the original firmware. Adding the cross-multiply was straight forward, but increasing the bandwidth required significant changes.

The JFFT signal processing library (Mock, 2004) used for the original spectrometer firmware was adopted for the correlator design. This library generates synthesisable Verilog for streaming Fast Fourier Transforms (FFTs) and polyphase filter-banks (PFBs). The library was used to synthesise a 2,048 point PFB consisting of a 2,048×4 tap decimated FIR filter and a 2,048 point, radix-2, biplex, pipelined FFT. Pipelining the FFT reuses multipliers to calculate multiple butterflies (Crochiere and Rabiner, 1983). This allows FFTs to be performed on streaming data with a near minimum number of multipliers operating at the same rate as the input stream. Although this is an efficient implementation, the multipliers only operate on meaningful data 50% of the time.

The biplex pipelined FFT (Emerson, 1976) shuffles and buffers both input data and interim butterfly results such that the multipliers operate on meaningful data 100% of the time . This allows two streaming FFTs to be calculated simultaneously with no extra multipliers. Figure 6.8 gives the schematic of an 8 point biplex pipelined FFT.

[2] SERENDIP is the Search for Extraterrestrial Radio Emissions from Nearby Developed Intelligent Populations. It is an ongoing project that "piggybacks" on radio telescopes simultaneously with conventional radio astronomy observations. See `http://seti.ssl.berkeley.edu/serendip/`.

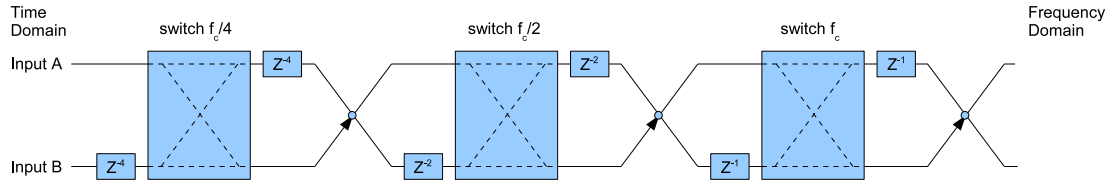

Fig. 6.8: 8 point biplex pipelined FFT.

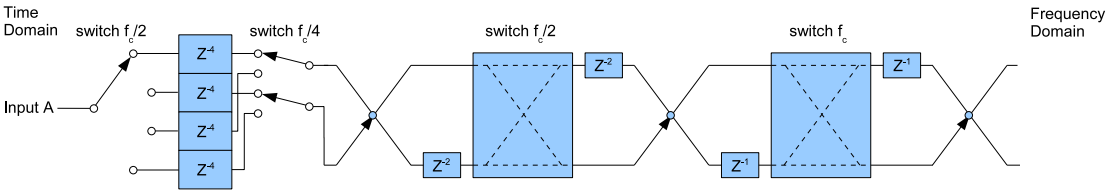

Fig. 6.9: 8 point half-rate pipelined FFT.

A further variation in input buffering yields the half-rate butterfly pipelined FFT (Emerson, 1976). This allows a single streaming FFT to be calculated using multipliers clocked at half the sample rate. Figure 6.9 gives the schematic of an 8 point half-rate pipelined FFT. Once again, multipliers are 100% usefully employed.

The biplex, pipelined FFT in the 2,048 point × 4 tap PFB generated by JFFT was modified to operate as a half-rate pipelined FFT. This enabled the resulting FFT to operate on a single input at twice the bandwidth. The resulting PFB achieves a 228 MHz real sample rate with multipliers clocked at 114 MHz. Only the ADCs and input buffers operate at the full 228 MHz.

The original plan was to use the Hermitian symmetry of the DFT of real data to perform two real DFTs with the half-rate complex FFT. This would allow two real data streams at 228 MHz sample rate to be processed simultaneously. However, the required buffering and shuffling exceeded available FPGA resources. As a stop gap, the complex transform was time multiplexed between the two inputs leading to an integration duty cycle of 50% and sensitivity reduction of $\sqrt{2}$. This is acceptable as the experiment is not yet sensitivity limited. The original real valued transform design might be achieved by halving the length of the FFT. This would not alter the resolution as the current complex FFT only uses half of its channels as the spectrum of the real input is reflected about the origin.

Data Format

Each correlator file contains multiple spectra of 0.439 s integration time. Each spectrum takes 0.877 s to generate as the FFT is time multiplexed between the two real inputs, switching every FFT frame (8.98 μs for a 2,048 point FFT frame and 228 MHz clock). There are 1,023 useful 111 kHz frequency channels from 114 MHz to 227.96 MHz. There is a system generated spike at 228 MHz (DC) and the upper 1,023 channels are a mirror of the lower 1,023 as a complex FFT is applied to real data.

Each spectrum is time stamped with the UT at which integration commenced with μs resolution, a sequence number, an error vector identifying accumulator overflows, the air temperature inside the correlator chassis, and the temperatures of the two FPGAs on the spectrometer board. The format of the binary correlator files is given in Appendix B.

6.4 Performance

The stability of the back-end, and implicitly that of the front-end connected to it, was tested by an eight hour integration with the system set-up as per figure 1.1, but with 50 Ω loads on both sum and difference ports of the 180° hybrid. The first hour of data was discarded while the system came to thermal equilibrium.

The sample standard deviation of the measured power was calculated according to

$$s_\tau(y) = \sqrt{\frac{1}{N-1}\sum_{n=1}^{N}(y_{\tau n} - \bar{y}_\tau)^2} \tag{6.36}$$

where $y_{\tau n}$ is the n^{th} sample of the measured power $y(t) = v^2(t)/R$ averaged over the period τ

$$y_{\tau n} = \frac{1}{\tau}\int_{n\tau}^{(n+1)\tau} y(t)dt. \tag{6.37}$$

Figure 6.10 plots the sample standard deviation of the measured power $s_\tau(y)$ versus integration time τ for the long integration on 50 Ω loads. Integration times between the fixed correlator accumulation time of 0.4 s and one hour were achieved by averaging appropriate numbers of correlator spectra in software.

As the overall measurement was of finite duration, the number of integrated samples N reduces in proportion to integration time τ. As N reduces, the statistical error in the sample standard deviation $s_\tau(y)$ increases. If $y(t)$ is taken from a population with a Gaussian distribution the standard deviation of the sample standard deviation is given by (Weisstein, 2009)

$$\sigma_s = s\sqrt{\frac{1}{N}\left(N - 1 - \frac{2\Gamma^2\left(\frac{N}{2}\right)}{\Gamma^2\left(\frac{N-1}{2}\right)}\right)}. \tag{6.38}$$

For large values of N this asymptotically approaches

$$\sigma_s \approx \frac{0.71s}{\sqrt{N}}. \tag{6.39}$$

Eq. (6.38) was used to generate the 1σ error bars plotted in figure 6.10 for $N \leq 198$. The approximation of Eq. (6.39) was used for $N > 198$ to avoid overflow of the numeric Gamma function. This approximation results in less than 0.5% error in σ_s. A more accurate treatment of error in the sample standard deviation is given by Ossenkopf (2008) along with elegant methods for its calculation.

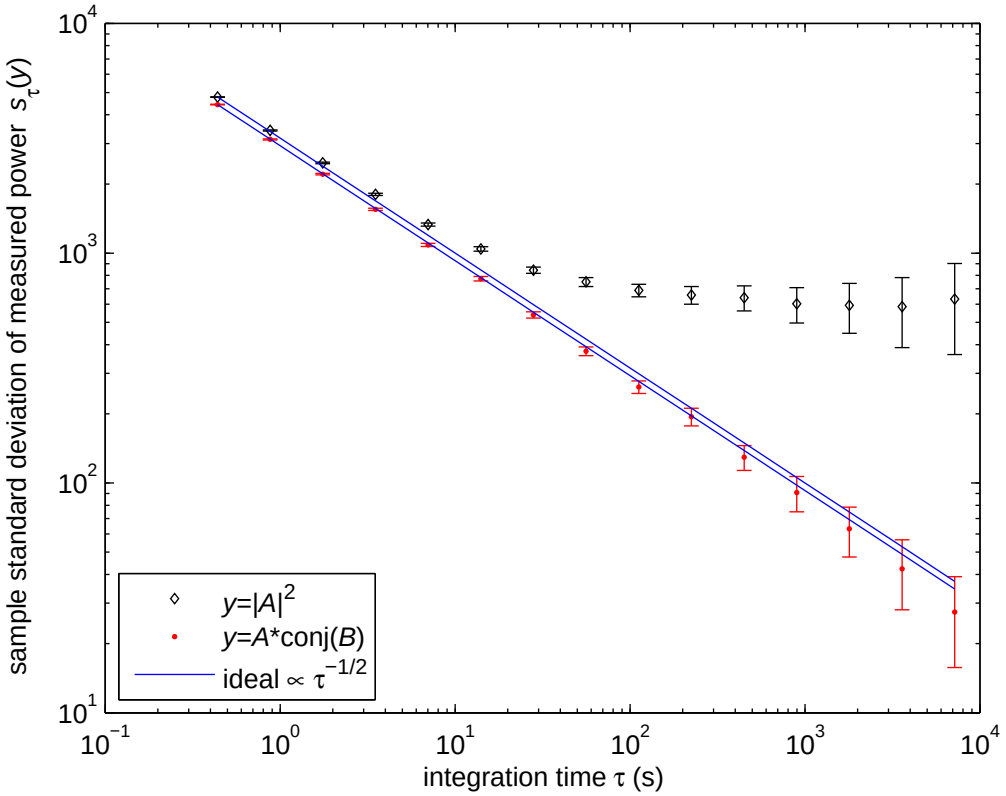

Fig. 6.10: Sample standard deviation $s_\tau(y)$ of measured power versus integration time τ for single channel at 181.35 MHz. Both ports of splitter hybrid terminated in 50 Ω loads at room temperature. Open markers show autocorrelation and filled markers show the cross-correlation. Solid line shows ideal reduction of standard deviation in proportion to $\tau^{-1/2}$

The standard deviation of the cross-correlation σ_{ab} is less sensitive to gain fluctuations than that of the autocorrelations. This is expected from theory and demonstrated by figure 6.10. The standard deviation is given by

$$\sigma_{prac} = KT_{sys}\sqrt{\frac{1}{\Delta\nu\tau} + \left(\frac{\Delta g}{g}\right)^2} \tag{6.40}$$

where $K = 1$ for the autocorrelations, $K = \sqrt{2}$ for the cross-correlations and $\Delta\nu$ is the bandwidth of the measurement. In the ideal case with no gain fluctuations this is equivalent to Eq. (5.1). It should be noted that T_{sys} is calculated differently for the auto and cross-correlations as outlined in § 5.3. The autocorrelation system temperature includes both the 3 dB splitting loss whereas the cross-correlation system temperature does not. For the cross-correlations, the 3 dB splitting loss is absorbed by the factor of $K = \sqrt{2}$.

The variance of both auto and cross-correlations reduces as $1/\sqrt{\tau}$ until a hard limit of $T_{sys}\Delta g/g$ is reached due to gain fluctuations. The standard deviation of the autocorrelation for channel A in figure 6.10 deviates from the ideal $1/\sqrt{\tau}$ reduction

by a factor of 2 at 80 s. Channel B is not shown in the figure, but it deviates from the ideal by a factor of 2 at 25 s. The magnitude of the gain fluctuations responsible for this may be determined by dividing Eq. (6.40) by the ideal $\Delta g/g = 0$ case and rearranging

$$\frac{\Delta g}{g} = \sqrt{\frac{\left(\frac{\sigma_{prac}}{\sigma_{ideal}}\right)^2 - 1}{\Delta\nu\tau}}. \tag{6.41}$$

Relative gain errors of approximately 6×10^{-4} are found for channel A and 1×10^{-3} for channel B. Inspection of the measured power time series for channel B shows impulsive gain dropouts where the gain drops by up to 3.6% and fluctuates for a minute before returing to its normal level. This only happened once during the eight hour measurement, but should be fixed.

The standard deviation of the cross-correlation reduces proportional to $\tau^{-1/2}$ for much longer than the auto-correlation. This is because the cross-correlation measures the difference in noise power generated by the two 50 Ω loads at a common ambient temperature. Mistaking a gain fluctuation Δg for an input noise power fluctuation ΔT leads to the following error in measured noise temperature

$$\Delta T = (T_2 - T_1)\frac{\Delta g}{g} \tag{6.42}$$

where T_1 and T_2 are the equivalent noise temperatures of the two 50 Ω loads. When the difference in temperature between the loads is small compared to the system temperature, the error in measured noise temperature is much smaller than the auto-correlation case which is given by

$$\Delta T = T_{sys}\frac{\Delta g}{g}. \tag{6.43}$$

During the measurement, the two loads were in close thermal contact. It is thus reasonable to believe that their physical temperatures were within 1 K of each other. The effect of the gain fluctuations on the cross-correlation should therefore be reduced by a factor of order $T_{sys}/(T_2 - T_1) \approx 1{,}000$. The 10^{-3} gain fluctuations measured from the autocorrelations can then be used to predict the integration time τ_c at which the reduction in variance of the cross-correlations will cease to follow $\tau^{-1/2}$

$$\tau_c = \frac{1}{\Delta\nu\left(\frac{\Delta g}{g}\right)^2}. \tag{6.44}$$

This gives $\tau_c = 100$ days. During the reionization experiment, the temperature will not be so well controlled. The difference will be between the sky spectrum and the reference load. At the peak expected band average antenna temperature of 951 K, the difference will be 651 K for a load temperature of 300 K. The effect of gain fluctuations will only be reduced by $T_{sys}/(T_2 - T_1) \approx 3$ for a system temperature of 2,167 K. This would allow useful integration of the cross-correlations for 80 seconds. At the minimum expected band average antenna temperature of 290 K, the difference will be 10 K for a load temperature of 300 K. The effect of gain

fluctuations will be reduced by $T_{sys}/(T_2 - T_1) \approx 150$ for a system temperature of 1,505 K. This would allow useful integration of the cross-correlations for 56 days.

In the worst case scenario of maximum antenna temperature, it is not useful to integrate for longer than 80 seconds without gain calibration. For field measurements at the MRO, the noise source was switched on and off every 88 s to calibrate the gain.

The above calculations were made only for the band average antenna temperature. The galactic emission has a significant spectral slope so that the difference between the sky brightness and the thermal noise from the load will also have a slope. Therefore, the effect of gain fluctuations will also vary across the band. In the future, this could be improved by using a filter to equalise the sloping spectrum of the sky brightness to the flat spectrum of the load. If the noise power level of the noise injected into the reference port were set appropriately, it could be used to reduce the difference between the sky and reference signals at maximum antenna temperature. The added noise would cancel the increased antenna temperature at maximum antenna temperature. Noise source off measurements would be used when the antenna temperature is low and noise source on measurements would be used when antenna temperature is high.

With a cross-correlation system temperature (defined in § 5.3) of 805 K corresponding to the expected median antenna temperature of 345 K and a cross-correlation receiver temperature of 460 K, 1 mK sensitivity would be reached in 1 MHz channels after 15 days integration if the correlator duty cycle was increased to 100%. Sensitivity of 10 mK can be achieved in 1 MHz channels after 7 hours integration without increasing the correlator duty cycle from 50%.

Part III

EXPERIMENT

Chapter 7

MEASUREMENTS AND CALIBRATION

This chapter presents the calibration of drift-scan measurements made at the Murchison Radioastronomy Observatory. Antenna bandpass calibration left 11 K peak-to-peak residuals with a peak spectral slope of 5 K/MHz on 1 MHz scales. The antenna's half-power beamwidth and pointing both varied with frequency by one degree. Antenna pattern frequency dependence was evaluated using difference spectra where additive contributions cancel along with the reionization spectrum. Overall calibration was limited to 60 K when a model for the additive contributions was subtracted before bandpass calibration. Peak-to-peak calibration residuals were 600 times larger than an optimistic reionization spectrum.

Recommendations to improve calibration include:

- using a 90° hybrid instead of a 180° hybrid to reduce LNA noise coupling between receiver chains;
- improving the phase balance of the balun to reduce frequency dependent antenna pattern squint; and
- rotating the antenna during or between observations to synthesise a symmetric time average antenna pattern.

Original contributions in this chapter include:

1. testing the frequency independence of an antenna's power pattern through drift-scan measurements;
2. deriving the measurement equation for a correlation radiometer and extending it to include lossy components and reflections;
3. measuring the receiver feed point impedance of a correlation radiometer by replacing the antenna with resistors of different values; and
4. showing that using a 90° hybrid in place of a 180° hybrid in a correlation radiometer reduces the correlation of:
    - noise from the LNA inputs that travels via the antenna mismatch reflection; with
    - noise from the LNA outputs that travels directly through the receiver.

7.1 Introduction

This chapter presents the calibration of drift-scan measurements made at the Murchison Radioastronomy Observatory (MRO). First, the data are rejected for interference and instrumental effects. Second, the data are calibrated according to a simplified measurement equation that neglects reflections. This is then extended to include reverse travelling LNA noise coupling across an impedance mismatch at the antenna terminals. Third, limiting factors in the calibration are summarised and suggestions are made to improve the system and its calibration.

7.2 Measurements

System verification measurements were made in a screened room laboratory and in the field at the Australia Telescope Compact Array site at Narrabri. Screened room tests of the receiver and back-end identified self interference. This was fixed by placing a low pass filter on the DC power line to the noise source. The Narrabri tests identified variation of the antenna impedance match with temperature and/or humidity. This was improved by packaging the surface mount impedance transformer, and its PCB, in a sealed and connectorised metal box. Narrabri measurements were not used beyond system integration and verification due to strong and continuous radio interference from TV transmitters on a direct line of sight.

Drift-scan measurements were made at the radio quiet MRO. The peak power pattern response was directed at the zenith so that a null was directed towards the horizon where there is radio interference. The receiver was configured as a correlation radiometer as per Figures 1.1 and 5.1. Table 7.1 summarises useful data collected with the antenna located at 26° 44.201′ S 116° 39.971′ E and 375 m above mean sea level[1].

Collection of data with the antenna in different azimuthal orientations was scheduled to explore possible asymmetries in the antenna power pattern. Strong winds and correlator crashes interrupted the schedule from which two drift-scans of reasonably complete local sidereal time (LST) coverage and almost common azimuthal orientation were salvaged[2].

The correlator dumped spectra of 0.44 s integration time every 0.88 s. The correlator control computer toggled a broadband noise source on the hybrid difference port and opened a new correlator file every 100 spectra (88 s). This noise was injected to calibrate the bandpass of the system referred to the hybrid difference port. Files were labelled CAL when the noise source was on and OBS when the

[1] About half way along the runway near Top Shed at the MRO.

[2] The azimuthal orientation of the antenna fluctuated during 4/12/2007 due to strong winds that commenced near sunset (2:28 UTC) and continued through the evening. The antenna weather-vaned, presenting one of its corners to the wind. At 13:42 UTC, the antenna had rotated clockwise by 45°, translated by a metre, and was rocking. This occurred because guy ropes were fixed to the antenna's apex but the centres of pressure and gravity of the pyramidal antenna are low. Thus the base of the antenna was blown out from under the apex causing a tipping risk. Both rocking and weather-vaning were brought under control at 14:19 UTC by attaching guy ropes to the antenna base.

Tab. 7.1: Summary of observations made at the Murchison Radioastronomy Observatory.

Date	Usable Data[a]	LST Range	Solar RA[b]	Antenna Orientation	Comments
1/4/2007	17 h 21 m	complete	0:39:41	N	system very stable
3/12/2007	4 h 44 m	20:55 to 12:22	16:34:48	N	
4/12/2007	13 h 55 m	complete	16:39:08	N to NE	strong winds
5/12/2007	8 h 39 m	12:43 to 11:27	16:43:28	NE	

[a]Including data with noise source on data but excluding data affected by interference or correlator drop-outs.
[b]At 00:00 UTC.

noise source was off. System stability was tracked by monitoring CAL-OBS spectra versus time and the bandpass was calibrated by calculating OBS/(CAL-OBS). The temperature of the reference load on the hybrid was measured by a thermistor connected to a data logger. The clocks of the data logger, the correlator control computer, and the data storage computer were synchronised at the beginning and compared at the end of each field trip.

7.3 Radio Frequency Interference

Figures 7.1 and 7.2 compare radio interference levels at Narrabri and at the MRO. These show equivalent noise temperature at the antenna terminals measured in 111 kHz channels. Equivalent noise temperature was estimated by scaling the median noise power to the median system temperature of 1,000 K.

At Narrabri, received total power was dominated by interference with a typical interference to noise total power ratio of 300:1. The system did not have sufficient dynamic range to measure thermal noise from a 50 Ω load at ambient temperature without being overdriven by interference when the load was replaced by the antenna. Therefore, the stability of the system could not be tested in the field by a long integration on a load. Further, the impedance match of the antenna could not be measured by replacing the antenna with loads of known impedance.

At the MRO, galaxy and receiver noise dominated received total power. The interference to noise total power ratio was less than 2×10^{-3} for 90% of the time and less than 3 for 99.98% of the time[3]. A tone had to be radiated into the antenna to determine if it was connected.

[3] This assumes there is not an extensive population of interferers just below the noise floor.

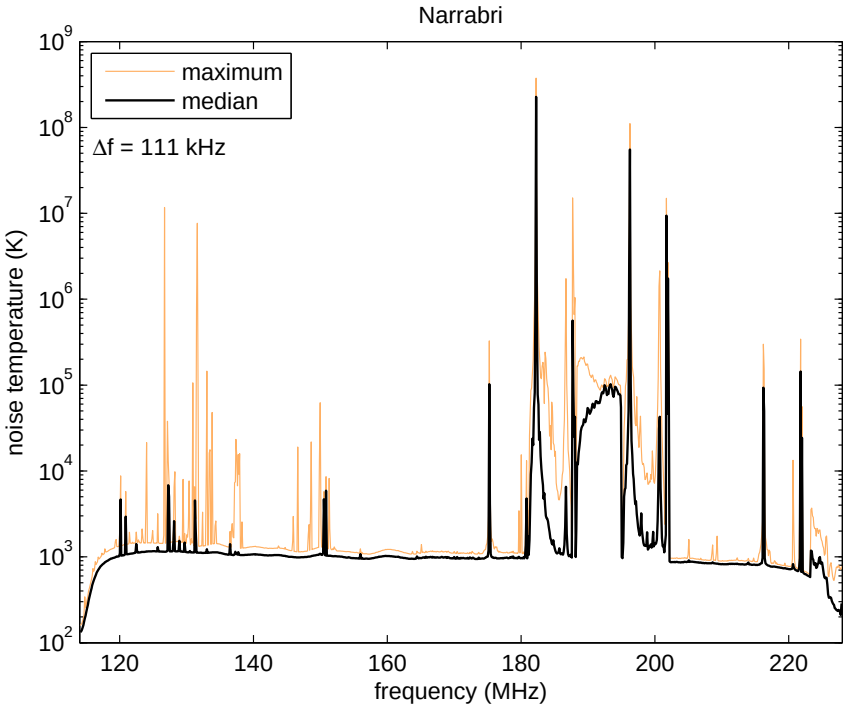

Fig. 7.1: RFI spectrum for 12 hr 44 min overnight observation at Narrabri on 29/7/2006. Typical interference to noise total power ratio $a \approx 300$.

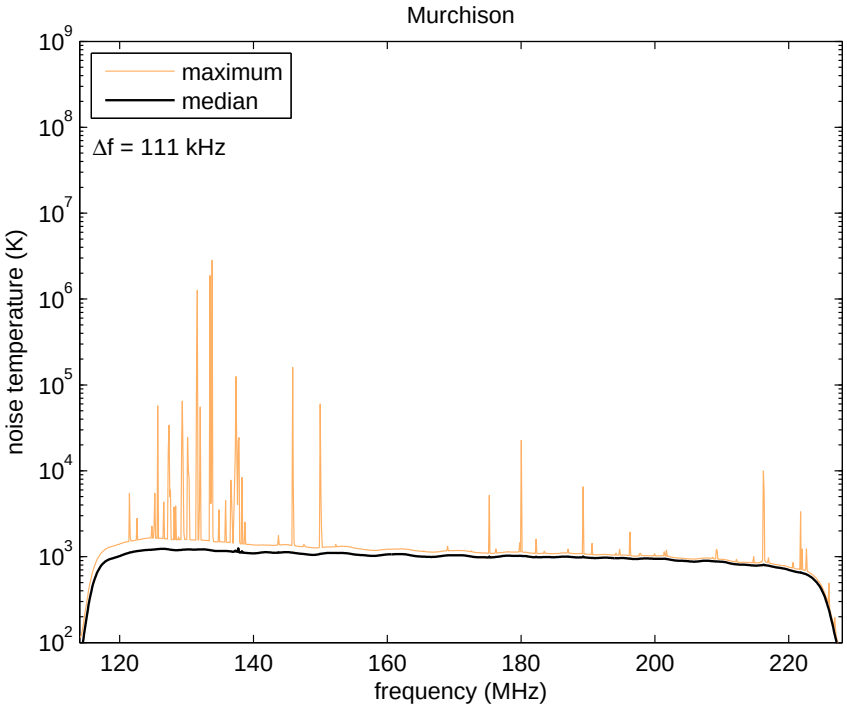

Fig. 7.2: RFI spectrum for 24 hr observation at the MRO on 4/12/2007. Interference to noise total power ratio $a < 2 \times 10^{-3}$ for 90% of the time and $a < 3$ for 99.98% of the time.

7.4 Data Rejection

Data were rejected for interference and instrumental effects. Rejection was predominantly automatic and conservative in that it removed channels containing interference at any time from further analysis. The rejection algorithm is explained in Appendix C.

To summarise briefly, complete spectra were rejected for receiver drop-outs, interference strong enough to generate clipping distortion above the target spectral accuracy, and epochs of broadband interference sufficient to make the total power time series depart from a smooth curve.

Narrowband interference was identified by a number of methods in both the frequency and time domains. Results were summarised by the mask $W(k)$ where k is the discretised frequency index. It was set to zero for channels in which interference was detected at any time in a 24 hr period, and was set to unity for the remaining channels.

This conservative approach was sufficient for the ensuing study of systematic errors in calibration. However, it reduced sensitivity by 17% due to the rejection of 27% of data for interference and poor system behaviour as summarised by table 7.2. It also removed 17% of frequency channels from analysis as summarised by table 7.3. Future experiments might include more sensitive and less biased interference rejection algorithims based on the real time calculation of Kurtosis. This is discussed in Appendix C.

Tab. 7.2: Observing time reduction factor due to interference and poor system behaviour.

Effect	Multiplier
Peak interference rejection	1.00
Drop-out rejection	0.74
Band average time domain interference rejection	0.99
Total	0.73

Tab. 7.3: Bandwidth reduction factor due to interference and poor system behaviour.

Effect	Multiplier
Instrumental artefacts	0.999
Frequency domain interference rejection	0.95
Time domain interference rejection	0.91
Manual interference rejection	0.96
Total	0.83

Tab. 7.4: Observing time reduction factor due to system design.

Effect	Multiplier
Correlator duty cycle	0.5
Noise source calibration	0.5
Noise source time constant	0.91
Total	0.23

Table 7.4 shows that the system as designed only collects observation data 23% of the time due to a 50% correlator duty cycle, rejection of 8% of data due to the noise source's switching time constant, and due to the fact that calibration mesurements are made 50% of the time.

7.5 Calibration

This section builds up a measurement equation and applies it to calibrating the system. First, the system is analysed in terms of a reflectionless model that assumes all components are perfectly impedance matched. The following systematic contributions are investigated within this context:

1. antenna bandpass and power pattern;
2. ohmic emission from the antenna;
3. ohmic emission from the load on the difference port of the hybrid; and
4. front-end bandpass.

Second, a single reflection due to a mismatched antenna impedance is considered. This couples reverse travelling LNA noise from each receiver chain into the other and creates a standing wave. The standing wave accounts for the shape of calibration residuals from the reflectionless measurement equation. Finally, observed systematic contributions are summarised and methods for reducing them are discussed.

7.5.1 Reflectionless Model

Calibrating the sky signal may only require a basic bandpass calibration, which includes effects arising from mismatches and reflections. However, this is complicated by additive contributions that have differing signal paths and hence frequency responses that differ from the response to the sky signal. Reflections can cause differing frequency response between additive contributions and the sky signal. When reflections are present, additive contributions must be carefully isolated and the bandpass of their path through the system must be determined accurately.

First, the basic bandpass calibration is explored in isolation by assuming a perfect impedance match between all components. This provides a simplified measurement equation for exploring major elements of the bandpass calibration. In

the absence of additive contributions, the effects of reflections can be absorbed by and calibrated away with the system bandpass. It is found that a straight forward bandpass calibration fails due to additive LNA noise coupling via reflection off the antenna mismatch.

The correlator output is proportional to the difference between the antenna temperature and the equivalent noise temperature presented to the difference port of the hybrid. A noise source was connected via an attenuator to the difference port of the hybrid and was toggled every 100 correlator cycles. The correlation radiometer set-up, in which the sky signal is split by a 180° hybrid, is illustrated by figure 5.1.

The correlator output satisfies

$$r_{off} \propto g_A^* g_B \left(|g_a|^2 T_a S_{A\Sigma}^* S_{B\Sigma} + T_{pad} S_{A\Delta}^* S_{B\Delta} \right) \tag{7.1}$$

when the noise source is off and

$$r_{on} \propto g_A^* g_B \left(|g_a|^2 T_a S_{A\Sigma}^* S_{B\Sigma} + (T_{pad} + T_{cal}) S_{A\Delta}^* S_{B\Delta} \right) \tag{7.2}$$

when the noise source is on. The symbols used have the following definitions:

r_{on} is the integrated correlator output $\langle v_A^* v_B \rangle$ when the noise source is on;

v_A is the complex voltage sampled by receiver chain A;

x^* denotes the complex conjugate of x;

g_A is the complex voltage gain of receiver chain A;

g_a is the complex RF voltage gain between the antenna terminals and the splitter hybrid[4];

T_a is the total antenna temperature (including ohmic emission) referred to the antenna terminals as defined by Eq. (4.7);

T_{pad} is the physical temperature of the attenuator between the noise source and the difference port of the hybrid;

T_{cal} is the step in the noise source's equivalent temperature when turned on; and

$S_{A\Sigma}$ is the scattering parameter of the hybrid corresponding to the complex voltage ratio of the response at port A to a stimulus at the sum port.

The manufacturers of the noise source measured its excess noise ratio (ENR) which was 32.3 dB at 100 MHz. Connecting the noise source to the difference port of the 180° hybrid through a 27 dB attenuator resulted in a calibration step of $T_{cal} \approx 983\ K$.

[4] $|g_A|^2$ is replaced by the multiplicative term e_l and the additive term $(1 - e_l)T_l$ in the later section on additive contributions

Front-end Bandpass Calibration

The front-end bandpass is proportional to the difference of noise source *on* and noise source *off* measurements

$$\begin{aligned} G &\equiv \left(r_{on-pre} + r_{on-post}\right)/2 - r_{off} \\ &\propto g_A^* g_B T_{cal} S_{A\Delta}^* S_{B\Delta}. \end{aligned} \tag{7.3}$$

Each *off* measurement is subtracted from the average of the preceding and following *on* measurements. This handles fluctuations in T_{pad} and T_a to first order on the switching time-scale by linearly interpolating them to their expected levels during the *off* measurements.

The bandpass can be separated into a time dependent DC gain $G_0(i)$, a normalised and time averaged bandpass $\bar{G}(k)$, and residual fluctuations $G_r(i,k)$

$$G(i,k) = G_0(i)\bar{G}(k)G_r(i,k)T_{cal}. \tag{7.4}$$

Indices i and k represent discretised time and frequency respectively. The calibration step T_{cal} is assumed to be independent of time and frequency.

The DC gain is calculated by averaging the instantaneous bandpass at each epoch ignoring interference affected channels according to the data rejection mask W(k)

$$G_0(i)T_{cal} = \frac{1}{\sum_{k=1}^{N} W(k)} \sum_{k=1}^{N} G(i,k)W(k). \tag{7.5}$$

The DC gain is a near linear function of the temperature of the attenuator between the hybrid and the noise source. The DC gain fluctuated by 4.7% to 9.5% for temperature fluctuations of 2.9% to 8.4% with lower gain for higher temperature. However, the absolute level of the spectrum is not as important as the bandpass shape and its temporal fluctuations.

The normalised and time averaged bandpass is given by

$$\bar{G}(k) = \sum_{i=1}^{M} \frac{G(i,k)W(k)}{G_0(i)T_{cal}}. \tag{7.6}$$

Figure 7.3 plots this for the data of 5/12/2007. A 4% amplitude ripple with a 9 MHz period dominates the lower half of the band and a 2% amplitude ripple with a 2.9 MHz period that dominates the upper half of the band[5]. Leaving these uncalibrated would lead to 9 K/MHz errors in the measured spectrum.

[5] If caused by reflections, the 9 MHz ripple corresponds to a 100 ns delay between direct and reflected paths. This is the expected delay for two way propagation between the hybrid at the apex of the antenna and the RF boxes at the base of the antenna. This path is comprised of 16 cm of RG-405 coax with a velocity factor of 0.71 and 10 m of RG-223 coax with a velocity factor of 0.66.

The 2.9 MHz ripple may correspond to a reflected path with 340 ns delay relative to a direct path. This just exceeds the expected delay of 330 ns for two way propagation between the bias Tees in the RF boxes at the base of the antenna and the bias Tees in the sampler boxes in the Faraday cage. This path is comprised of 40 m of FSJ1 coax with a velocity factor of 0.84 m and 1.2 m of LMR-195 coax with a velocity factor of 0.80.

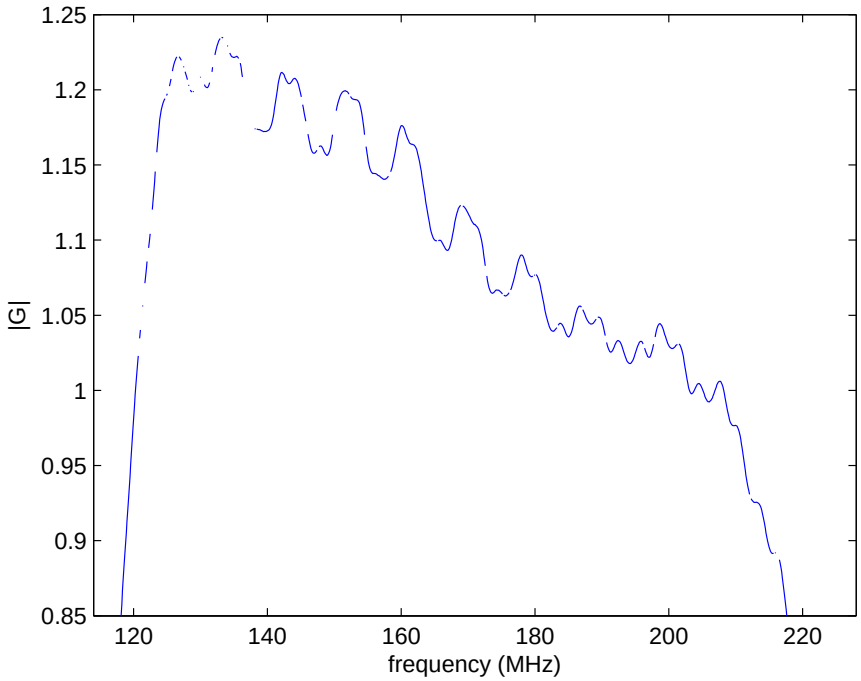

Fig. 7.3: Normalised and time averaged bandpass $\bar{G}(k)$ for 5/12/2007.

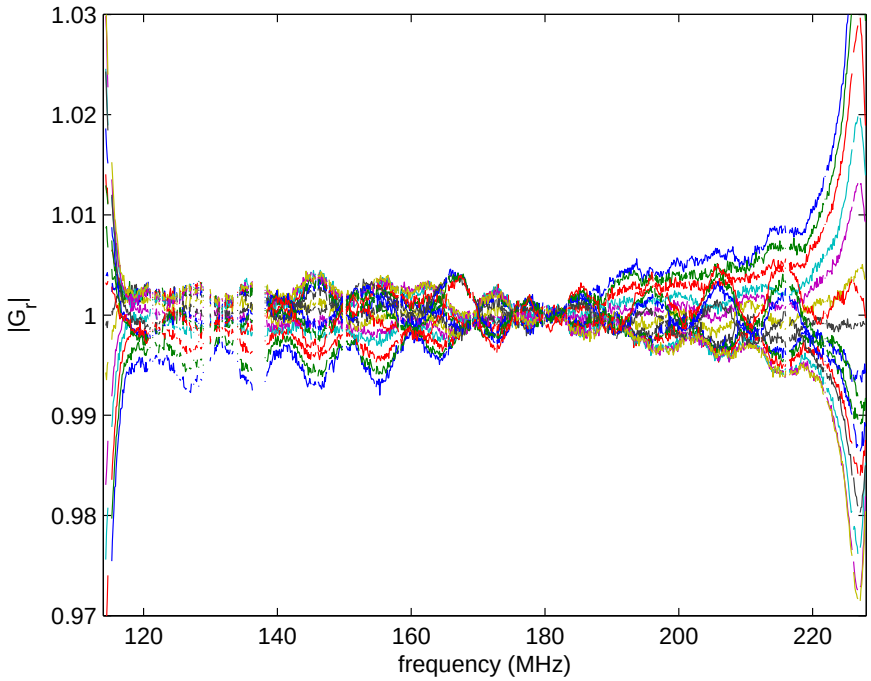

Fig. 7.4: Amplitude of residual bandpass fluctuations $|G_r(i,k)|$ for 5/12/2007. All epochs are overlayed.

Residual bandpass fluctuations are defined by

$$G_r(i,k) = \frac{G(i,k)}{G_0(i)\bar{G}(k)T_{cal}}. \tag{7.7}$$

Figure 7.4 overlays the amplitude of residual bandpass fluctuations for the data of 5/12/2007. The bandpass ripple fluctuates in amplitude at the 0.5% level. There are a handful of epochs when the 9 MHz ripple is enhanced in the upper part of the band. There is also a significant change in gain slope with time leading to a 1% fluctuation across the entire band. If the mean bandpass was calibrated successfully, fluctuation of the 9 MHz ripple causes 1 K/MHz errors, and fluctuation of the slope causes 90 mK/MHz errors. Bandpass calibration of the front-end using the noise source is therefore necessary for achieving the science goals.

The front-end bandpass was calibrated by dividing *off* measurements by the difference of *on* and *off* measurements. In the absence of reflections this gives the quotient

$$q(i,k) \equiv -\frac{r_{off}}{(r_{on-pre} + r_{on-post})/2 - r_{off})} = -\left|g_a\right|^2 \frac{T_a}{T_{cal}} \frac{S^*_{A\Sigma} S_{B\Sigma}}{S^*_{A\Delta} S_{B\Delta}} - \frac{T_{pad}}{T_{cal}}. \tag{7.8}$$

An ideal 180° hybrid has the scattering matrix (Pozar, 1998)

$$\mathbf{S} = \frac{-j}{\sqrt{2}} \begin{bmatrix} 0 & 1 & 1 & 0 \\ 1 & 0 & 0 & -1 \\ 1 & 0 & 0 & 1 \\ 0 & -1 & 1 & 0 \end{bmatrix} \tag{7.9}$$

where ports $(1,2,3,4)$ correspond to ports (Σ, A, B, Δ) referred to so far. An ideal 180° hybrid therefore has the bandpass factor

$$\frac{S^*_{A\Sigma} S_{B\Sigma}}{S^*_{A\Delta} S_{B\Delta}} = -1 \tag{7.10}$$

and reduces Eq. (7.8) to

$$q(i,k) = \left|g_a\right|^2 \frac{T_a}{T_{cal}} - \frac{T_{pad}}{T_{cal}}. \tag{7.11}$$

The bandpass factor of the actual hybrid measured $-1.01\angle -0.33°$ with a standard deviation of 6×10^{-3} on a four port vector network analyser. Assuming an ideal hybrid with a bandpass factor of -1 is therefore reasonable.

The system nominally measures the difference between the antenna temperature T_a and the noise temperature T_{pad} seen at the difference port of the hybrid. Assuming that T_{cal} is well behaved leaves three major components to be calibrated by transit observations of the galactic foreground:

1. the antenna bandpass and power pattern;
2. the noise temperature T_{pad} of the attenuator between the noise source and the difference port of the hybrid; and
3. ohmic emission from the antenna.

Test of Antenna Pattern Frequency Dependence

Additive contributions were approximately removed by subtracting the quotient for the epoch of minimum antenna temperature i_{min} from the quotients for all other epochs

$$q(i,k) - q(i_{min},k) \approx |g_a|^2 \, \frac{T_a(i) - T_a(i_{min})}{T_{cal}} \, \frac{S^*_{A\Sigma} S_{B\Sigma}}{S^*_{A\Delta} S_{B\Delta}}. \tag{7.12}$$

Dividing each difference by the difference at the epoch of maximum antenna temperature i_{max} calibrates the antenna and hybrid bandpasses

$$p(i,k) \equiv \frac{q(i,k) - q(i_{min},k)}{q(i_{max},k) - q(i_{min},k)} \approx \frac{T_a(i,k) - T_a(i_{min},k)}{T_a(i_{max},k) - T_a(i_{min},k)}. \tag{7.13}$$

This yields a metric that would be a smooth function of frequency for an antenna with a frequency independent pattern. The metric may vary slightly in slope due to position dependence of the spectral index of the galactic foreground. Time variations in the system bandpass should not cause the metric to vary so long as bandpass calibration using the noise source is successful. Figure 7.5 shows measured results that have ripples superimposed upon a smooth large scale trend. Multiplying the metric $p(i,k)$ by the predicted antenna temperature difference from models of the antenna pattern and radio sky places them on a Kelvin scale

$$T_a(i,k) - T_a(i_{min},k) \approx p(i,k) \left[T_a(i_{max}) - T_a(i_{min}) \right]_{model}. \tag{7.14}$$

Figure 7.6 applies this simulation based scaling. Subtracting a power law representing the galactic foreground gives the bandpass calibration residuals on a Kelvin scale. The median peak-to-peak residual in a spectrum was 62 K. The power law used for the subtraction was the same power law used for the simulation. The spectra in figure 7.6 therefore represent the power law used for the simulation distorted by the deviation from flatness seen in figure 7.5.

Figure 7.5 shows a stable pseudoperiodic pattern with a 180° phase shift upon galactic transit. Therefore it was decided to adopt the average of two reference measurements spaced symmetrically about galactic transit for $q_{min}(k)$. This gives a symmetrised metric

$$p_{sym}(i,k) \equiv \frac{q(i,k) - \bar{q}_{min}(k)}{q(i_{max},k) - \bar{q}_{min}(k)} \tag{7.15}$$

where

$$\bar{q}_{min}(k) = \frac{q(i_{min,A},k) + q(i_{min,Z},k)}{2}. \tag{7.16}$$

Epochs A and Z are chosen symmetrically in time about maximum antenna temperature. Forming a reference spectrum from the average of the two interpolates fluctuations in additive contributions to the centre of the LST range. Additive contributions thus cancel better at the centre of the LST range when the reference spectrum is subtracted.

A stable pseudoperiodic pattern with a 180° phase shift upon galactic transit emerges when the symmetric calibration is applied to measured data. Figure 7.7 shows the symmetric bandpass calibrated quotients p_{sym} for data taken on

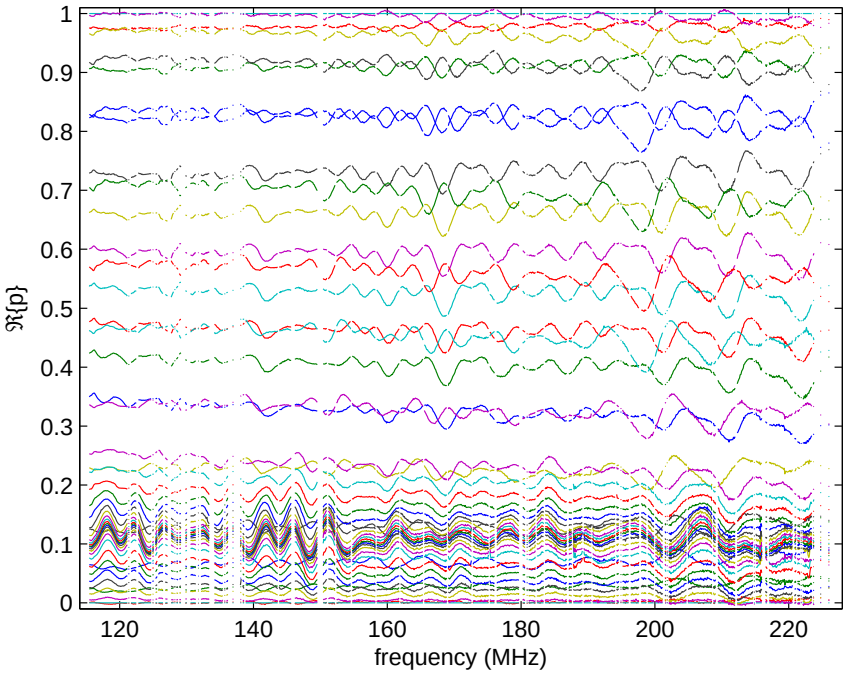

Fig. 7.5: Antenna frequency independence metric p from Eq. (7.13) for data of 4/12/2007. These would be smooth for a frequency independent antenna.

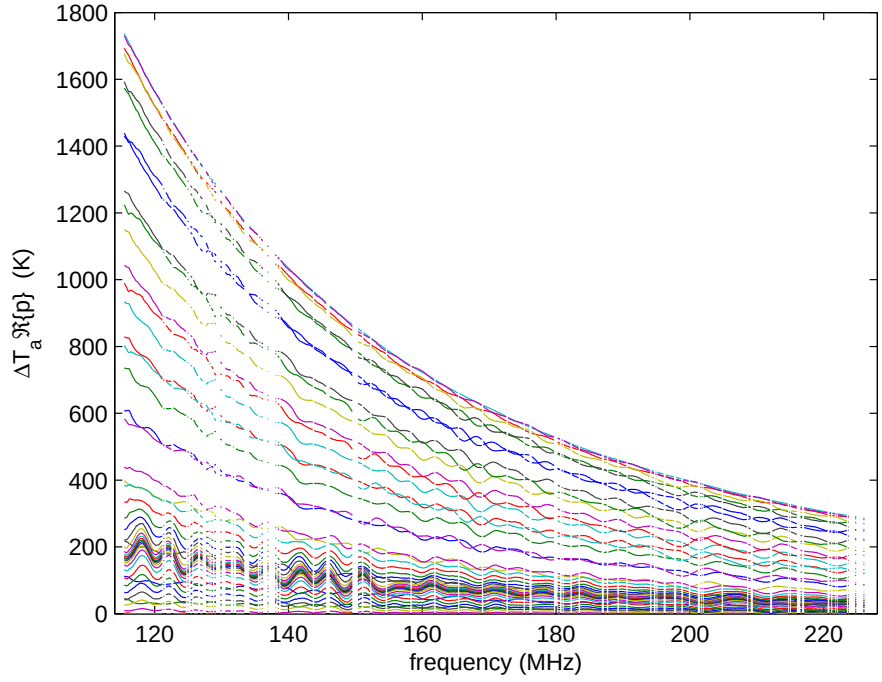

Fig. 7.6: Bandpass calibrated difference spectra from Eq. (7.14) for data of 4/12/2007. The scale is calibrated by simulating the antenna pattern and sky brightness.

4/12/2007. The median peak-to-peak residual amplitude over all epochs was 58 K. The 180° phase shift might be expected for an asymmetric antenna pattern rotating about the boresight if the sky brightness distribution is predominantly symmetric. The sun did not significantly break this symmetry on 4/12/2007 as it was only 15°33′ away from the galactic centre.

Log-periodic antenna theory requires asymmetry in the antenna pattern to rotate periodically about the boresight with the logarithm of frequency. The antenna's geometric ratio τ determines the period through Eq. (4.29). A model sky brightness scaled from the Haslam et al. (1995) map was observed by a model antenna pattern squinted off the zenith by 1° and rotating about the zenith log-periodically with the appropriate frequency for the antenna's geometric ratio of $\tau = 0.9535$.

Comparing the simulated data in figure 7.8 to the measured data in figure 7.7 shows that the amplitude of the ripples in the measured data is consistent with a pattern squinted by less than 1°. However, the measured ripple period is half that predicted by the antenna's geometric ratio. It appears that the antenna pattern varies by more than a pure squint. One possibility is a flattening of what should be a circular beam into an elliptical beam.

Simulations with a rotating, elliptical beam pattern that was not squinted produced a ripple of the correct period for the antenna's geometric ratio but did not reproduce the observed phase reversal about the galactic transit. Simulations with a rotating, elliptical beam that was squinted also failed to reproduce the phase reversal. Repeating simulations with the addition of a top-hat model of the quiet sun ($T_\odot = 10^6$ K, $R_\odot = 0.33°$) ruled out generation of the observed ripple by the sun.

The amplitude of the ripple can be reduced by more than a factor of six by combining bandpass calibrated ratios on either side of the galactic transit. The factor of six reduction indicates that the ripple is dominated by sources near the galactic centre which nearly crosses the zenith at transit. The 180° phase difference of the ripples about the galactic transit causes them to partially cancel. A simplex search method (Lagarias and Wright, 1998)[6] was used to find a weighted combination of p_{sym} that minimised the standard deviation of the residual ripple. The peak-to-peak residual across the band was 11 K. The maximum residual slope was 5 K/MHz when smoothed to 1 MHz resolution.

A Method of Moments simulation of the antenna pattern identified that a path-length mismatch of 7.3 mm in the antenna's balanced feed line can result in a 1.5° beam squint. At 170 MHz this is equivalent to a phase unbalance of 2°. The 180° hybrid used for the balun was balanced within 0.2° from 50 MHz up to 150 MHz after which it linearly degraded to 0.8° at 228 MHz. This was measured on a four port vector network analyser.

Nature of Antenna Pattern Frequency Dependence

The previous section showed that calibration of the antenna bandpass is limited by frequency dependence of the antenna pattern. This section explores the antenna pattern by comparing the shapes of drift-scans across the observing band using

[6] This multidimensional minimisation algorithm is used for all model fitting in this thesis unless stated otherwise.

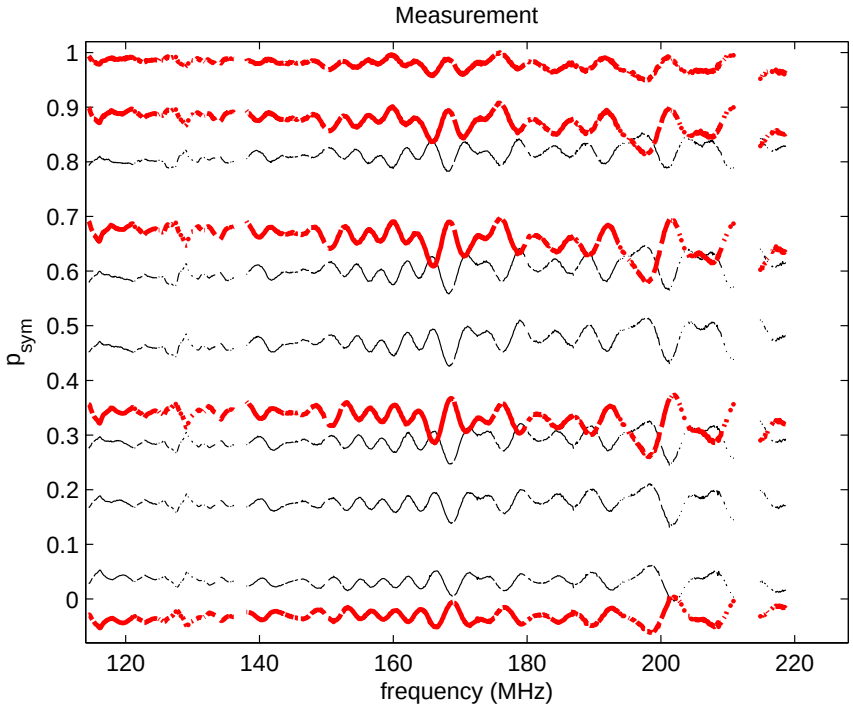

Fig. 7.7: The symmetrised metric p_{sym} of Eq. (7.15) for measured data of 4/12/2007. Thin lines precede and thick lines follow galactic transit.

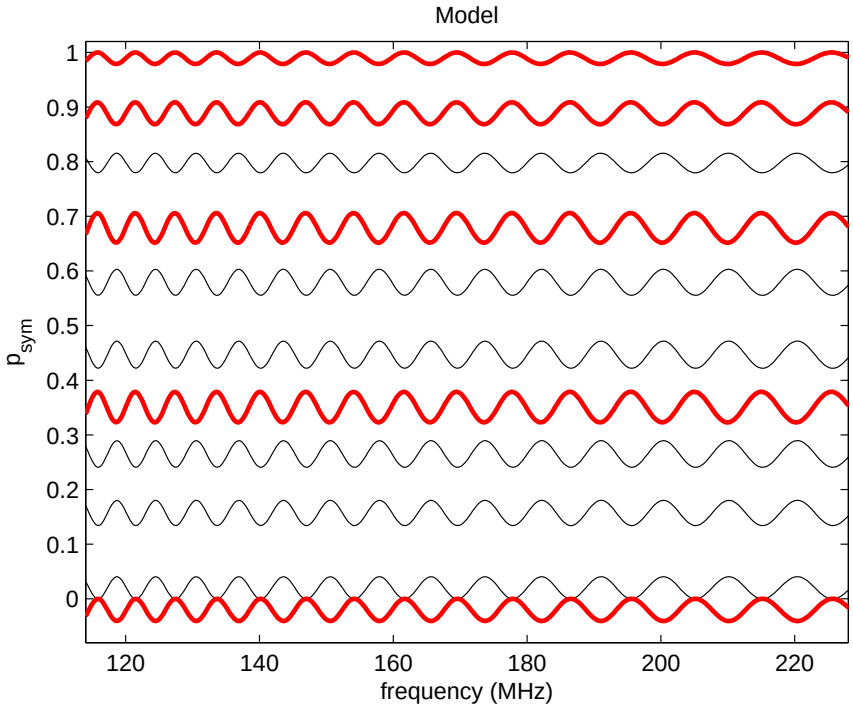

Fig. 7.8: The symmetrised metric p_{sym} of Eq. (7.15) for a simulation with an antenna pattern squinted by 1° and rotating log-periodically according to $\tau = 0.9535$. Thin lines precede and thick lines follow galactic transit.

bandpass calibrated cross-correlation spectra $q(i,k)$. This confirms the hypothesis of a squinted beam pattern but also shows that the antenna pattern agrees with simulation beyond the squint.

The system yields a spread in antenna temperature with frequency 10 times greater than that predicted by modelling. Figures 7.9 and 7.10 show normalised overlays of drift-scans at all frequencies for measured and modelled data respectively. The model antenna pattern was generated by a Method of Moments simulation for a perfectly balanced feed. The model sky brightness was scaled from the Haslam et al. (1995) map and included a top-hat model of the quiet sun ($T_\odot = 10^6$ K, $R_\odot = 0.33°$). Drift-scans were normalised at each frequency by subtracting the minimum antenna temperature at that frequency from all other epochs and then dividing by the peak value. The mean drift-scan across all frequencies is close to that predicted by simulation as shown by Fig 7.11. This suggests that the general shape of the antenna pattern is as predicted leaving the variations about the mean for further investigation.

Finally, it was identified that both the beamwidth and pointing of the antenna varied by order 1° with frequency. A Gaussian of fixed width and variable LST offset (beam squint) was fitted to the drift-scan at each frequency. The mean drift-scan peak was at LST 17:39:16 with a standard deviation of 0:3:31 (53 arc seconds). Next, a Gaussian of variable width and fixed LST offset was fitted. This gave a mean half-power drift-scan width of 45.5° with a standard deviation of 1.2°. The RMS errors for these two fits were within 20% of each other. The RMS error for a third fit, where both the width and offset of the Gaussian are free parameters, was a factor of 3 lower.

Full Calibration Including Additive Contributions

Additive contributions must be subtracted prior to bandpass calibration. The previous sections used difference measurements, which cancels the additive contributions to within their temporal variation, to test the antenna performance. Difference measurements also used to bandpass calibrate standard single dish measurements through the technique of position switching. However, in this experiment difference measurements cancel the expected isotropic reionization spectrum which is present over the whole sky. Therefore, additive contributions including ohmic emission of the antenna, balun, hybrid, and reference load must be minimised and a model must be used to subtract their vestiges from measurements rather than subtracting a spectrum from a different epoch.

Ohmic emission from components between the antenna and the hybrid can be investigated by comparing measurements at the same LST on different days when the temperature has changed. This is possible because ohmic emission is proportional to the physical temperature of the emitting component. Figure 7.12 shows the noise source calibrated quotient q for two epochs separated by 23 hr 56 m corresponding to an LST of 22:52 on 1/4/2007 and 2/4/2007. The temperature of the attenuator on the difference port of the hybrid increased by 1 K (0.3%) between these epochs and the ambient temperature rose by 2 K over the same time. The predicted 64 K ohmic emission from the antenna would be expected to rise by 0.4 K. The quotient

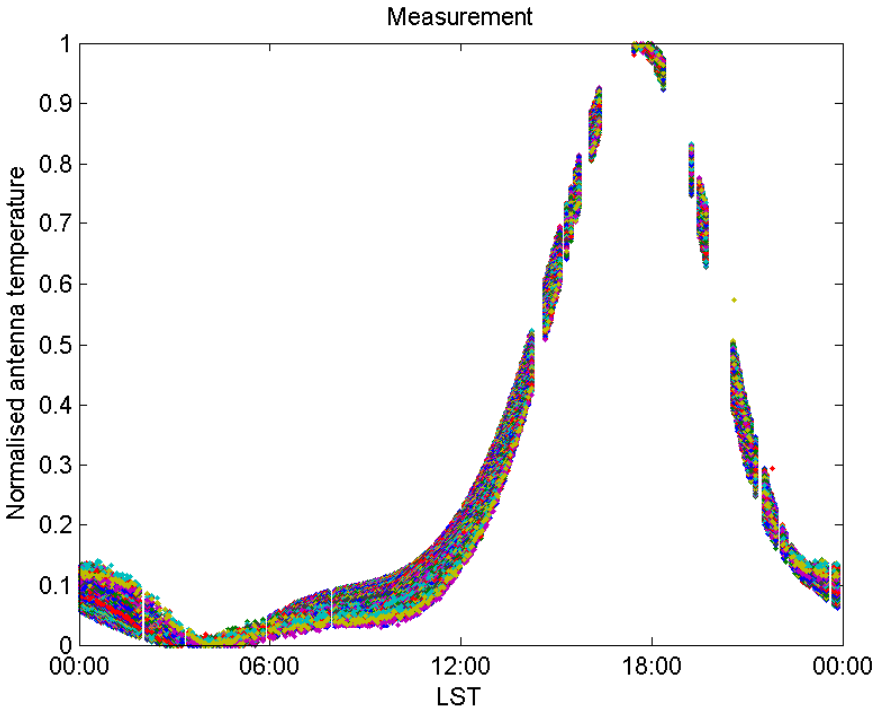

Fig. 7.9: Normalised drift-scans overlayed for all frequencies measured at the MRO on 1/4/2007.

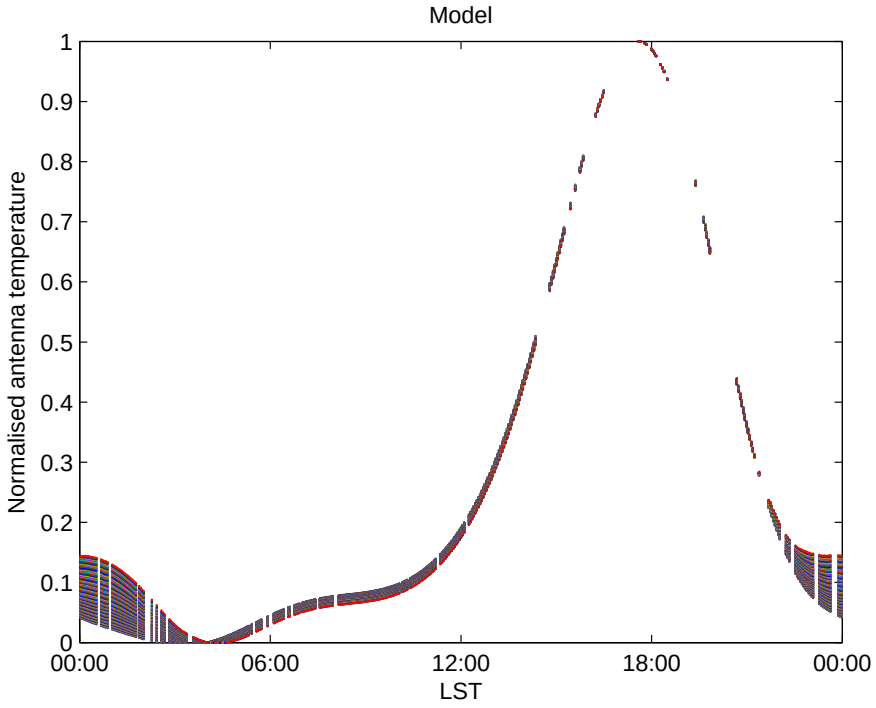

Fig. 7.10: Normalised drift-scans overlayed for all frequencies calculated for MoM antenna model observing sky brightness scaled from 408 MHz Haslam et al. (1995) map with an additional top-hat model of the sun ($T_\odot = 10^6$ K, $R_\odot = 0.33°$).

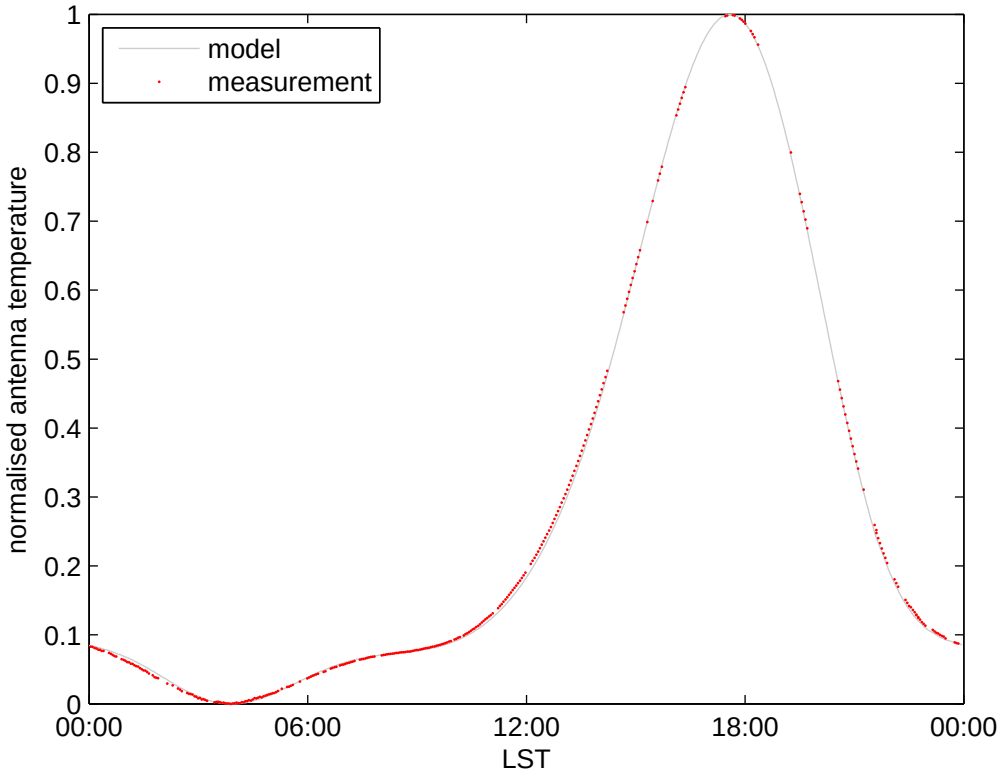

Fig. 7.11: Comparison of measured band average drift-scan of 1/4/2007 to model (MoM) antenna pattern observing sky brightness scaled from 408 MHz Haslam et al. (1995) map with an additional top-hat model of the sun ($T_\odot = 10^6$ K, $R_\odot = 0.33°$).

is proportional to the difference between the antenna and load temperatures and should change by approximately 0.6 K. An increase of 1 K is observed at the bottom of the band. Of the 0.4 K excess, 0.3 K can be explained by losses in the impedance transformer and balun which are expected to be 1 dB and therefore contribute 78 K at 300 K ambient temperature.

Scaling by T_{cal} shows that the noise RMS of the difference of the quotients measured at the two epochs of identical LST is about 0.4 K at 120 MHz and 0.6 K at 220 MHz. The design of the front end and simulation of the model sky and antenna pattern predict an RMS of 1 K at 120 MHz and 0.5 K at 220 MHz for this difference of quotients. The signal to noise ratio (SNR) of the above difference measurement is thus no better than 1.5. The low SNR of this measurement and the potential for a number of other temperature dependencies in the system suggest that comparing data taken 24 hrs apart should only be treated as an order of magnitude check on the antenna's ohmic emission.

Passing DC current through the antenna conductors might provide such a more significant temperature step on demand through resistive heating. Rapidly changing the antenna temperature by 10 K between measurements at the same LST would allow measurement of ohmic emission from the antenna with a more useful

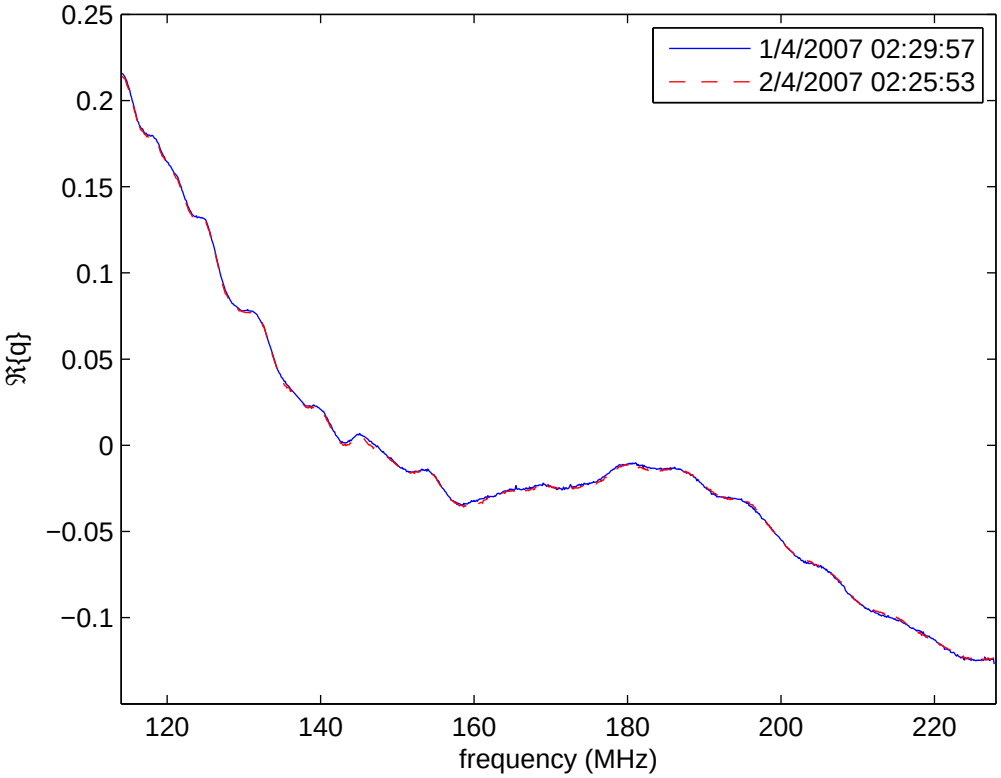

Fig. 7.12: Two noise diode calibrated spectra separated by 23 h 56 m corresponding to an LST of 22:52 showing stability of antenna bandpass and additive contributions.

SNR of 15. An advantage of rapid control of the antenna temperature is that the temperature of the reference load would remain stable through the measurement and thus be isolated. Each additive contribution might be calibrated directly if the equivalent temperature of every noisy component in the system could be stepped.

The additive contributions must be modelled in the absence of active control over the equivalent noise temperature of each component. First, Eq. (4.8) is substituted into Eq. (7.11) for the noise source calibrated cross-correlation in the case of an ideal 180° hybrid. This extends the measurement equation to include conductive and dielectric antenna efficiency e_{cd} and reflection efficiency e_r for a possible antenna and receiver impedance mismatch. A combined efficiency[7] e_l is introduced for the impedance transformer, balun and any other lossy components between the antenna and the hybrid. These components are assumed to be at the common physical temperature T_l. This results in

$$q = e_r e_l \left[\frac{e_{cd} T_A + (1 - e_{cd}) T_{cd}}{T_{cal}} \right] + (1 - e_l) \frac{T_l}{T_{cal}} - \frac{T_{pad}}{T_{cal}}. \tag{7.17}$$

The antenna is bandpass calibrated by dividing through by the same measurement

[7] This replaces $|g_{ant}|^2$, the noiseless RF gain between antenna terminals and hybrid, introduced in §7.5.1.

differenced over a period where the sky brightness has changed significantly but the physical temperatures T_{cd}, T_l, and T_{pad} have changed negligibly

$$\frac{q}{\Delta q} = \frac{T_A}{\Delta T_A} + \frac{1-e_{cd}}{e_{cd}}\frac{T_{cd}}{\Delta T_A} + \frac{1-e_l}{e_r e_l e_{cd}}\frac{T_l}{\Delta T_A} - \frac{T_{pad}}{e_r e_l e_{cd}\Delta T_A}. \tag{7.18}$$

Noting that

$$\Delta q = \frac{e_r e_l e_{cd}\Delta T_A}{T_{cal}} \tag{7.19}$$

the reflection efficiency can be eliminated from Eq. (7.18)

$$\frac{q}{\Delta q} = \frac{T_A}{\Delta T_A} + \frac{1-e_{cd}}{e_{cd}}\frac{T_{cd}}{\Delta T_A} + \frac{(1-e_l)T_l}{\Delta q T_{cal}} - \frac{T_{pad}}{\Delta q T_{cal}}. \tag{7.20}$$

Bandpass calibration is therefore not affected by reflections so long as any additive contributions introduced by them are sufficiently stable to cancel in Δq. Finally, the antenna temperature is expanded into galactic T_g, extragalactic T_x, cosmological microwave background T_{CMB}, and reionization absorption or emission ΔT_{ion}. The expression is then rearranged to solve for ΔT_{ion}

$$\Delta T_{ion} = \Delta T_g \left[\frac{q}{\Delta q} - \frac{(1-e_l)T_l - T_{pad}}{\Delta q T_{cal}}\right] - \frac{1-e_{cd}}{e_{cd}}T_{cd} - T_g - T_x - T_{CMB}. \tag{7.21}$$

Substituting measured and modelled values into the above equation and then fitting it to a single measurement of $q/\Delta q$ with free parameters for T_x and e_l yielded the residuals of figure 7.13. They follow a sinusoidal pattern of almost one period over 114 MHz to 228 MHz that is 125 K peak to trough. There is also structure on higher frequency scales. These large residuals suggest that something is missing from the measurement equation (7.21).

7.5.2 Single Reflection Model

A better measurement equation is developed by introducing a single complex reflection coefficient Γ_A due to the antenna impedance mismatch

$$\Gamma_A = \frac{Z_A - Z_L}{Z_A + Z_L}. \tag{7.22}$$

The antenna impedance is Z_A and the receiver impedance seen at the antenna terminals is Z_L. Extending Eq. (7.8) to include Γ_A, equivalent noise temperatures T_{na} and T_{nb} for the two LNAs, and assuming that forward and reverse travelling LNA noise are equal leads to

$$\begin{aligned} q = &- \frac{e_l T_a + (1-e_l)T_l}{T_{cal}}\frac{S^*_{A\Sigma}S_{B\Sigma}}{S^*_{A\Delta}S_{B\Delta}} - \frac{T_{pad}}{T_{cal}} \\ &- \frac{e_l T_{na}}{T_{cal}}\frac{S_{A\Sigma}S_{B\Sigma}}{S^*_{A\Delta}S_{B\Delta}}\Gamma e^{-2j(\theta_a+\theta_c)} - \frac{e_l T_{nb}}{T_{cal}}\frac{S^*_{A\Sigma}S^*_{B\Sigma}}{S^*_{A\Delta}S_{B\Delta}}\Gamma^* e^{2j(\theta_b+\theta_c)} \\ &- \frac{e_l T_{na}}{T_{cal}}|S_{A\Sigma}|^2\frac{S^*_{A\Sigma}S_{B\Sigma}}{S^*_{A\Delta}S_{B\Delta}}|\Gamma|^2 - \frac{e_l T_{nb}}{T_{cal}}|S_{B\Sigma}|^2\frac{S^*_{A\Sigma}S_{B\Sigma}}{S^*_{A\Delta}S_{B\Delta}}|\Gamma|^2. \end{aligned} \tag{7.23}$$

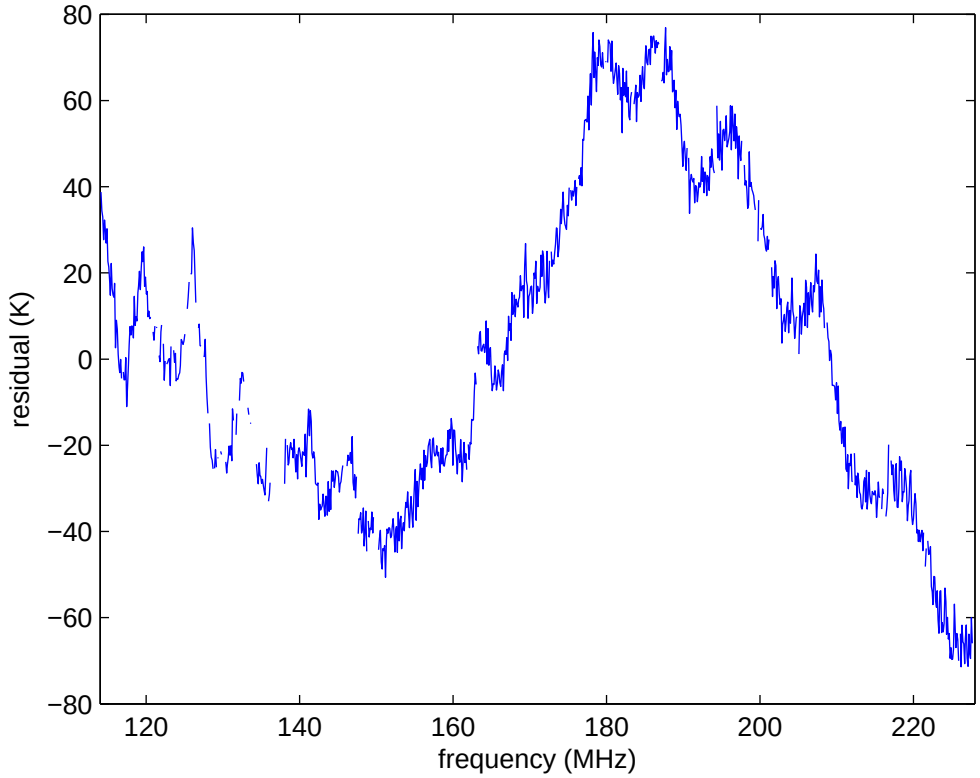

Fig. 7.13: Residuals from fitting Eq. (7.21) to drift-scan measurements.

The terms involving Γ may be rearranged to highlight the effects of LNA noise amplitude and phase balance

$$\begin{aligned} q = &- \frac{e_l T_a + (1-e_l)T_l}{T_{cal}} \frac{S^*_{A\Sigma} S_{B\Sigma}}{S^*_{A\Delta} S_{B\Delta}} - \frac{T_{pad}}{T_{cal}} \\ &- \frac{T_{na}}{T_{cal}} \frac{e^{j(\theta_b - \theta_a)}}{S^*_{A\Delta} S_{B\Delta}} 2\,|S_{A\Sigma} S_{B\Sigma} \Gamma| \cos(\theta_a + \theta_b + 2\theta_c + \angle S_{A\Sigma} + \angle S_{B\Sigma} + \angle \Gamma) \\ &- \frac{T_{nb} - T_{na}}{T_{cal}} \frac{S^*_{A\Sigma} S^*_{B\Sigma}}{S^*_{A\Delta} S_{B\Delta}} \Gamma^* e^{2j(\theta_b + \theta_c)} \\ &- \frac{T_{na}}{T_{cal}} |S_{A\Sigma}|^2 \frac{S^*_{A\Sigma} S_{B\Sigma}}{S^*_{A\Delta} S_{B\Delta}} |\Gamma|^2 - \frac{T_{nb}}{T_{cal}} |S_{B\Sigma}|^2 \frac{S^*_{A\Sigma} S_{B\Sigma}}{S^*_{A\Delta} S_{B\Delta}} |\Gamma|^2. \end{aligned} \tag{7.24}$$

Perfect amplitude balance of the LNA noise $T_{na} = T_{nb} = T_n$ reduces the above to

$$\begin{aligned} q = &- \frac{e_l T_a + (1-e_l)T_l}{T_{cal}} \frac{S^*_{A\Sigma} S_{B\Sigma}}{S^*_{A\Delta} S_{B\Delta}} - \frac{T_{pad}}{T_{cal}} \\ &- \frac{e_l T_n}{T_{cal}} \frac{e^{j(\theta_b - \theta_a)}}{S^*_{A\Delta} S_{B\Delta}} 2\,|S_{A\Sigma} S_{B\Sigma} \Gamma| \cos(\theta_a + \theta_b + 2\theta_c + \angle S_{A\Sigma} + \angle S_{B\Sigma} + \angle \Gamma) \\ &- \frac{e_l T_n}{T_{cal}} \frac{S^*_{A\Sigma} S_{B\Sigma}}{S^*_{A\Delta} S_{B\Delta}} |\Gamma|^2 \left(|S_{A\Sigma}|^2 + |S_{B\Sigma}|^2 \right). \end{aligned} \tag{7.25}$$

An ideal 180° hybrid reduces it further to

$$q = \frac{e_l T_a + (1-e_l)T_l - T_{pad}}{T_{cal}} - \frac{e_l T_n}{T_{cal}} e^{j(\theta_b - \theta_a)} 2\,|\Gamma| \cos(\theta_a + \theta_b + 2\theta_c + \angle\Gamma) + \frac{e_l T_n}{T_{cal}} |\Gamma|^2. \tag{7.26}$$

This suggests that the largest term in T_n can be moved into the imaginary part of q by choosing $\theta_b - \theta_a = 90°$. This can be done at a particular frequency by increasing the path length from the hybrid to one of the LNAs by $\lambda/4$ at that frequency. It can be achieved across the band by inserting a 90° phase shift between the hybrid and one of the LNAs or, more elegantly, by replacing the 180° hybrid with a 90° hybrid.

The scattering matrix for an ideal 90° hybrid is given by (Pozar, 1998)

$$\mathbf{S} = \frac{-1}{\sqrt{2}} \begin{bmatrix} 0 & j & 1 & 0 \\ j & 0 & 0 & 1 \\ 1 & 0 & 0 & j \\ 0 & 1 & j & 0 \end{bmatrix} \tag{7.27}$$

where ports $(1, 2, 3, 4)$ correspond to ports (Σ, A, B, Δ). Substituting this into Eq. (7.25) and making the electrical lengths between each LNA and the hybrid equal $(\theta_b = \theta_a)$ gives

$$q = \frac{e_l T_a + (1-e_l)T_l - T_{pad}}{T_{cal}} - \frac{e_l T_{na}}{T_{cal}} 2j\,|\Gamma| \cos(\theta_a + \theta_b + 2\theta_c + \angle\Gamma) + \frac{e_l T_n}{T_{cal}} |\Gamma|^2. \tag{7.28}$$

Using a 90° hybrid and processing the real part of q would remove the first order term in $|\Gamma|$. This is confirmed by substituting non-zero correlations $\langle x n_b \rangle$ and $\langle y n_a \rangle$ into the correlation radiometer measurement equation derived by Harris (2005). Harris also showed that a 90° hybrid always rejects correlated signals introduced after the hybrid better than a 180° hybrid.

Measuring the Receiver Impedance

The receiver input impedance Z_L can be determined from two measurements of q where the antenna is replaced by two different known impedances. Such measurements were made with the antenna replaced by 300 Ω and 390 Ω resistors with 1 cm leads. Eq. (7.26) shows that $\Re q$ should be a cosine with DC and phase offsets. The cosine amplitude is proportional to $|\Gamma|$ and the phase is offset by $\angle\Gamma$. If the amplitudes A_n and the phases ϕ_n of the cosines are deduced for two q measurements we may recover the ratio of complex voltage reflections for the two terminating impedances

$$Y = \frac{\Gamma_2}{\Gamma_1} = \frac{A_2}{A_1} e^{j(\phi_2 - \phi_1)}. \tag{7.29}$$

Measurements for $Z_1 = 300\,\Omega$ and $Z_2 = 390\,\Omega$ give $Y = 0.998\angle{-41.1}°$. Substitution of the voltage reflection coefficient definition into the above equation leads to a quadratic in the unknown receiver impedance

$$(1 - Y)Z_L^2 + (Z_1 - Z_2)(Y + 1)Z_L + Z_1 Z_2(Y - 1). \tag{7.30}$$

Rejecting the solution with an unphysical negative real impedance yields $Z_L = 321 + j121\ \Omega$. This suggests an inductance at the feed point of 112 nH at 171 MHz. This is equivalent to the inductance of a 14 cm length of 1.5 mm diameter wire that is isolated when calculated according to Grover (1946). The inductance might arise due to the 18 cm length of 300 Ω balanced line between the feed point and the impedance transformer. This balanced line remains at its design spacing of 9 mm for 4 cm of its length but is then spread to a width of 9 cm to attach to the antenna.

Feed inductance is beneficial as the antenna reactance is inductive and of similar magnitude. The model antenna impedance at 171 MHz is $Z_A = 310 + j73\ \Omega$ and so the expected reflection coefficient for the antenna and receiver is $\Gamma_A = 0.07\angle 76°$, slightly better than $\Gamma_A = 0.1\angle -120°$ expected for the design receiver impedance of 300 Ω. Figure 4.14 shows that $0.2 < |\Gamma_A| < 0.3$ is measured at the balun's balanced port by a spectrum analyser with tracking generator and bridge. The higher than expected antenna reflection may be due to the fact that the spectrum analyser measurement was made with the antenna lying on its side whereas the antenna impedance was simulated with the antenna standing vertically. Alternatively, the antenna's impedance may generally deviate from the simulated impedance independent of the antenna's orientation.

Figure 7.14 shows a fitting of Eq. (7.26) to the measurements for resistor values $Z_1 = 300\ \Omega$ and $Z_2 = 390\ \Omega$. The RMS of the fit is 1.6 K for both measurements. The fit was made with free parameters for:

- the reflection path length,
- the constant phase offset in the reflection path,
- the common physical temperatures for the balun and the attenuator pad on the hybrid difference port,
- the mean equivalent noise temperature of the LNAs, and
- the spectral slope of the equivalent noise temperature of the LNAs.

The fit gives a 90 K equivalent noise temperature for the LNAs which is believable considering they were advertised as 51 K amplifiers and were run in a hot environment without proper thermal dissipation. This noise temperature determination gives an order of magnitude consistency check for the model.

More parameters could be fitted if measurements were made for more resistor values. The receiver feed point impedance might be measured more accurately than the two resistor technique where residual amplitude and phase estimates are corrupted by the fact that the residuals are not pure sinusoids.

Figure 7.15 shows that the bandpass of the residuals after the model has been fitted. This reflects something more complex than smooth LNA noise coupling

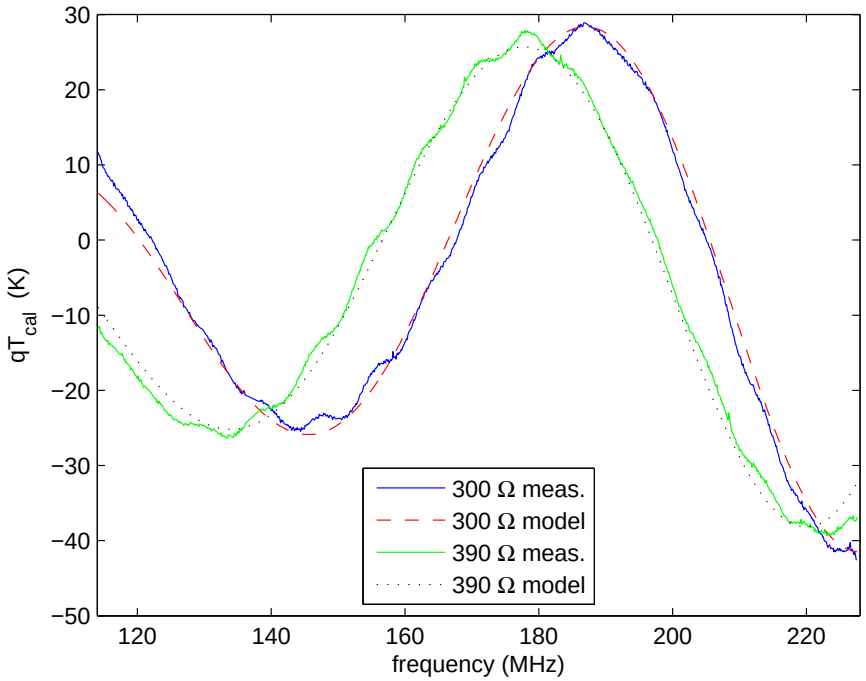

Fig. 7.14: Joint fitting of Eq. (7.26) to measurements where the antenna is replaced by 300 Ω and 390 Ω resistors.

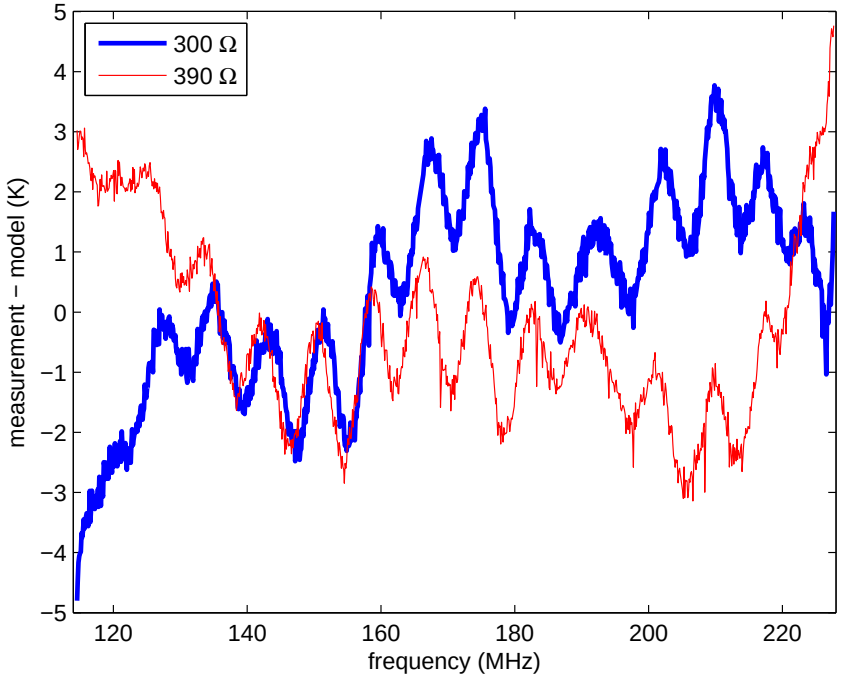

Fig. 7.15: Residuals from joint fitting of Eq. (7.26) to measurements where the antenna is replaced by 300 Ω and 390 Ω resistors.

across a single reflection at the antenna terminals at the 2 K level. It has a period of 8.1 MHz which corresponds to a 123 ns delay. It is possible that this is RF amplifier noise coupling across the antenna reflection from the RF boxes at the base of the antenna. Also, the residuals are largest at the band edges suggesting that mismatch and temperature variability of the RF filters may be contributing.

The residual is not constant in shape for the two measurements so it may be fluctuating with time. It is possible that this would have upset the antenna bandpass calibration in §7.5.1 as it made the assumption that additive contributions were constant with time.

Calibrating Drift-scans with a Mismatched Antenna

Eq. (7.21) may be augmented to include terms due to the antenna mismatch

$$\begin{aligned}\Delta T_{ion} = \Delta T_g \Bigg[& \frac{q}{\Delta q} - \frac{(1-e_l)T_l - T_{pad}}{\Delta q T_{cal}} \\ & - \frac{e_l T_n}{\Delta q T_{cal}} e^{j(\theta_b - \theta_a)} 2\,|\Gamma| \cos(\theta_a + \theta_b + 2\theta_c + \angle\Gamma) \\ & - \frac{e_l T_n}{\Delta q T_{cal}} |\Gamma|^2 \Bigg] - \frac{1-e_{cd}}{e_{cd}} T_{cd} - T_g - T_x - T_{CMB}. \end{aligned} \tag{7.31}$$

Fitting this extended model to the same $q/\Delta q$ data used for figure 7.13 yielded the residuals shown in figure 7.16. In this fit e_l, the feed point inductance, and T_x were made free parameters and measured or simulated values were used for the rest. The period and amplitude of the ripples is considerably different to those shown in figure 7.15. When the free parameters solved for in this fit are applied to data from different epochs the residuals remain of comparable amplitude. This suggests that the model is successfully fitting the reflection induced cosine. Future work must determine the origin of the 55 K peak-to-peak residuals of figure 7.16 that have significant frequency structure.

7.5.3 Multiple Reflection Model

One possible source of the residual ripple is multiple reflections. Including reflections at the LNA inputs leads to an infinite series of reflections between the antenna and the LNAs. Deriving the appropriate measurement equation requires a full S-parameter network analysis.

Such analysis can be achieved by applying the S-parameter network reduction algorithm of Liao et al. (1993) symbolically. S-parameter matrices are taken two by two and merged until a single S-parameter matrix representing the entire network remains. A computer program has been written to do this and will be applied once residuals are better characterised and tested for consistency with multiple reflections.

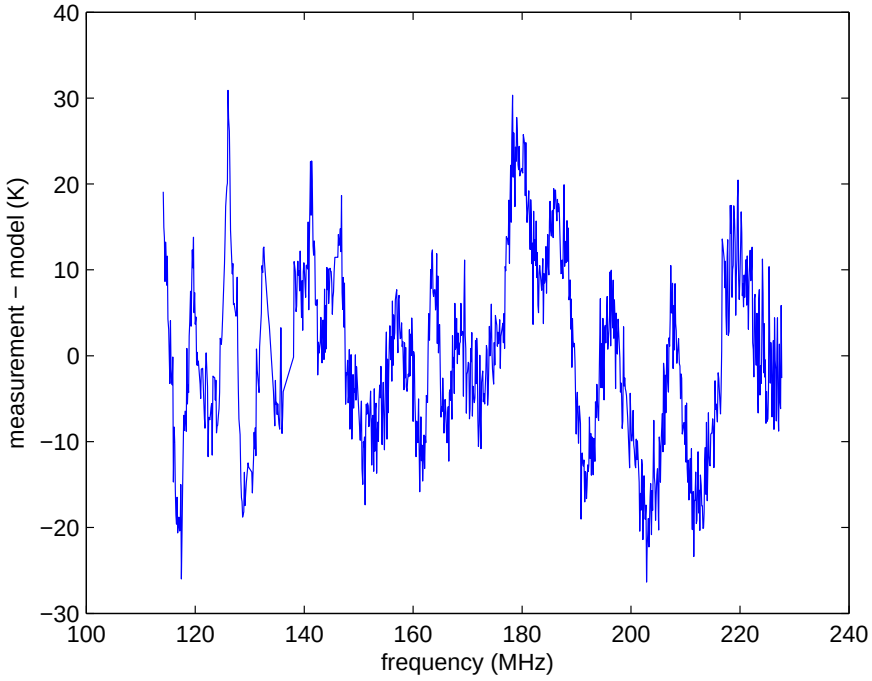

Fig. 7.16: Residuals from fitting Eq. (7.31) to drift-scan measurements.

7.6 Summary

Bandpass calibration was limited to 11 K peak-to-peak and 5 K/MHz by frequency dependence of the antenna pattern. Calibration of additive contributions was limited to 60 K peak-to-peak after a model was fitted for LNA noise coupling across a single reflection due to antenna impedance mismatch. Future work should prioritise the calibration of additive contributions.

The next steps to improve calibration of the additive contributions are:

1. Replace the 180° hybrid with a 90° hybrid of equivalent or better phase and amplitude balance to reduce correlated noise from the LNAs.

2. Make measurements with the antenna replaced by three or more different resistances to better characterise the receiver feed point impedance as a function of frequency.

3. Switch a DC current through the antenna to heat it rapidly and extract the bandshape of the antenna's ohmic emission to compare it to theory.

The next steps to improve bandpass calibration are:

1. Improve the phase balance of the balun to reduce antenna pattern squint.

2. Make measurements with the antenna at multiple azimuthal orientations and combine them to smooth out antenna pattern asymmetry.

3. Rotate the antenna continuously (on a turntable) during observations to smooth out antenna pattern asymmetry.

Chapter 8

CONCLUDING REMARKS

A portable radio telescope was built to measure the 21 cm cosmological reionization monopole. System components were specified for calibration of the sky spectrum to 1 mK/MHz relative accuracy. Simulations showed that the antenna power pattern must vary by less than 4% peak-to-peak at its half-power points to measure the sky spectrum with 1 mK accuracy at 1 MHz resolution. A two-arm pyramidal log-spiral antenna that can meet this requirement was designed and built. Nonlinear modelling of the front-end and back-end showed that unwanted distortion of noise and interference can be kept below 1 mK, given radio interference levels at the Murchison Radioastronomy Observatory where the telescope was deployed.

Comparing simulated and measured spectra showed that the system bandpass calibration is limited to 11 K, that is 1% of the foreground emission, due to larger than expected frequency dependence of the antenna pattern. Overall calibration, including additive contributions from the system and the radio foreground, is limited to 60 K. This is 160 times larger than the maximum possible monopole amplitude at a redshift of eight.

An optimistic 21 cm monopole model with Lyman-alpha line radiation coupling the spin temperature to the matter temperature prior to rapid reionization and reheating was presented. It predicts a 282 mK swing from absorption at 101 MHz to emission at 131 MHz. The emission commences with an amplitude of 28 mK and decays gradually to zero at 193 MHz. This gives a 21 cm monopole amplitude of 282 mK, not far from the maximum possible amplitude of 370 mK for instantaneous reionization and reheating at a redshift of eight.

This experiment may therefore constrain models of reionization if its sensitivity and calibration can be improved to 0.1 K. Future work will refine and extend this experiment known as the Cosmological Reionization Experiment Mark I (CoRE Mk I). New versions are planned that use two antennas and move the split into free space as shown in figure 8.1. This removes the need to calibrate additive emission from the antennas so long as scattered coupling between the antennas is small.

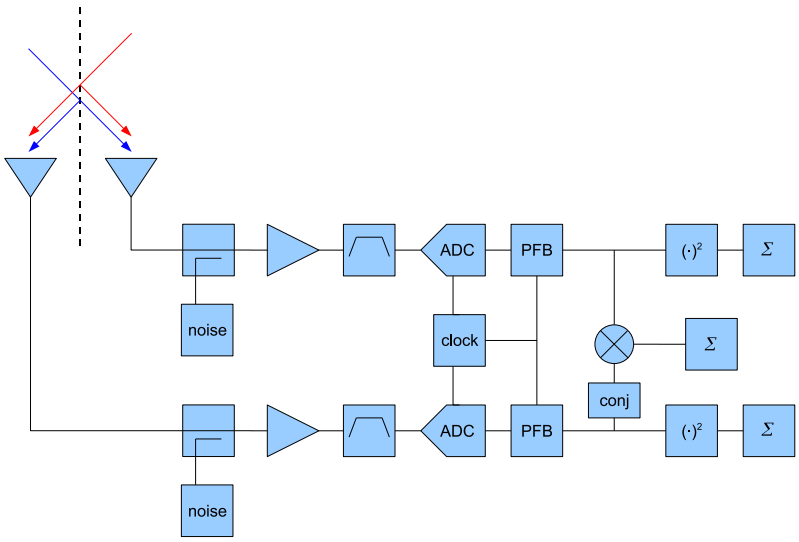

Fig. 8.1: Future plan: correlation radiometer splitting the signal in free space.

8.1 Summary of Contributions

The key contributions of this thesis include:

1. deriving an analytic approximation for the theoretical limit on maximum absorption for the 21 cm monopole;

2. modelling the spectrum of the 21 cm monopole for power law ΛCDM with WMAP5+BAO+SN cosmological parameters;

3. determining the antenna pattern requirement for measuring the metre-wave sky spectrum with 1 mK accuracy;

4. simulating, constructing, and evaluating a two arm, square based pyramidal log-spiral antenna;

5. testing the frequency independence of the antenna's power pattern through drift-scan measurements;

6. deriving a design equation for the conduction loss of conical log-spiral antennas;

7. developing a system level method for estimating nonlinear distortion of broadband noise plus narrowband interference using readily available amplifier parameters;

8. showing that 1-bit quantisation with the van Vleck correction is sufficient to measure the 21 cm monopole at the MRO;

9. showing that 1-bit quantisation distortion can be corrected in the presence of interference by inverting McFadden's approximation of the 1-bit correlation function for Gaussian noise plus sinusoid input;

10. showing that Bussgang's theorem holds in the total power limit for a memoryless, nonlinear system with Gaussian noise plus sinusoid input;

11. calculating the signal to clipping distortion ratio and signal to quantisation noise ratio at the output of a uniform, saturating quantiser with Gaussian noise plus sinusoid input;

12. developing a guide for selecting analogue to digital converter (ADC) resolution and input power level to meet target spectral dynamic range and sensitivity in a given interference environment;

13. modifying the firmware of a SERENDIP V board to act as a correlation spectrometer at twice the clock speed of the original design;

14. integrating a SERENDIP V board with external ADCs to facilitate data capture twice as fast as the on-board ADCs in the original design;

15. deriving the measurement equation for a correlation radiometer and extending it to include lossy components and reflections;

16. measuring the receiver feed point impedance of a correlation radiometer by replacing the antenna with resistors of different values; and

17. showing that using a 90° hybrid in place of a 180° hybrid in a correlation radiometer reduces the correlation of:

    - noise from the LNA inputs that travels via the antenna mismatch reflection; with
    - noise from the LNA outputs that travels directly through the receiver.

Appendix A

ANTENNA SUPPORT STRUCTURE DESIGN SKETCH

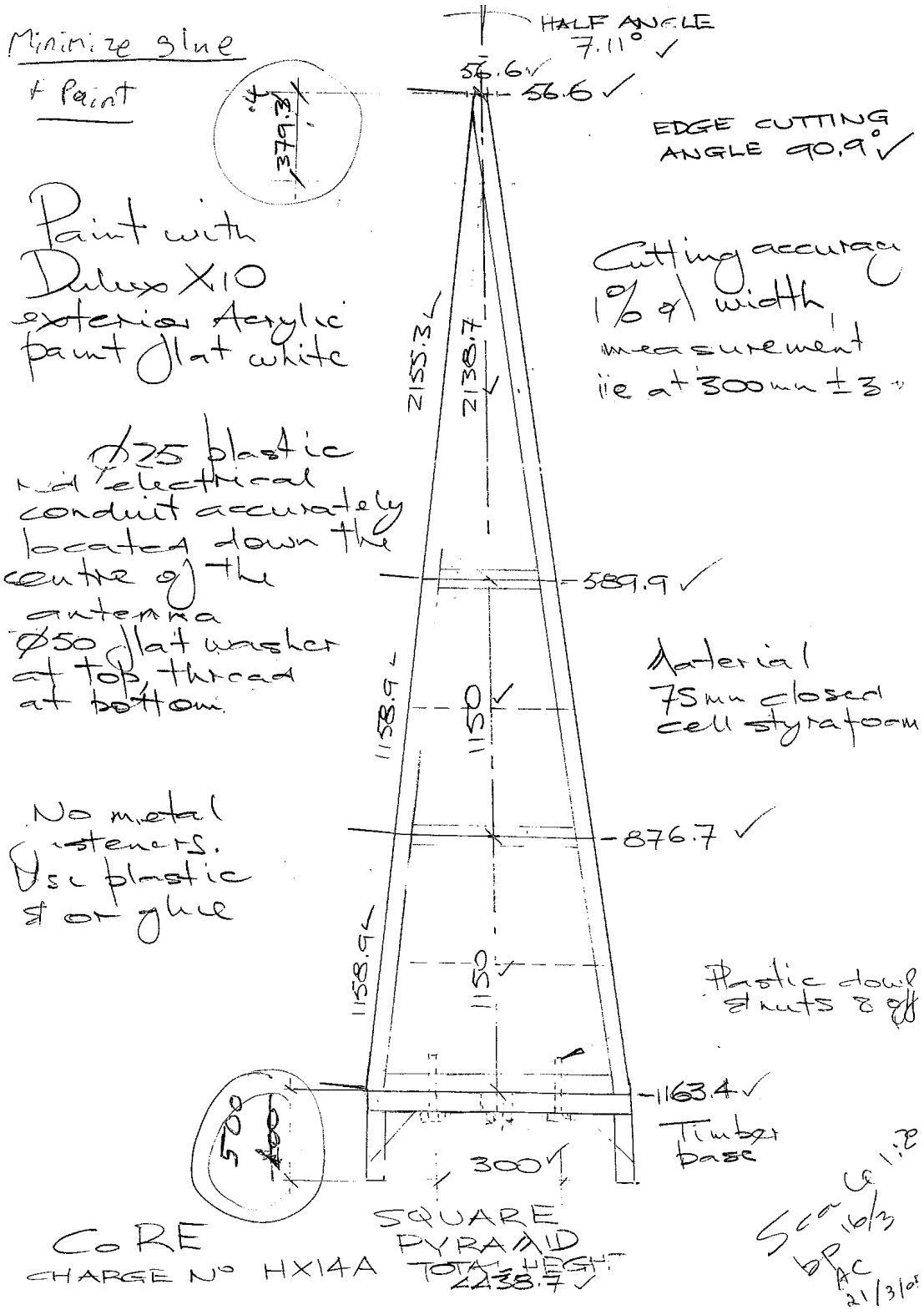
Minimize glue & Paint
HALF ANGLE 7.11° ✓
56.6 ✓
56.6 ✓
EDGE CUTTING ANGLE 90.9° ✓
379.3 ✓
Paint with Dulux X10 exterior Acrylic paint flat white
Cutting accuracy 1% of width, measurement ie at 300mm ± 3
2155.3 ✓
2138.7 ✓
Ø25 plastic mid electrical conduit accurately located down the centre of the antenna
Ø50 flat washer at top, thread at bottom
589.9 ✓
Material 75mm closed cell styrafoam
1158.9 ✓
150 ✓
No metal fasteners. Use plastic & or glue
876.7 ✓
1158.9 ✓
150 ✓
Plastic dowel & nuts & glue
1163.4 ✓
Timber base
500
400
300 ✓
SQUARE PYRAMID
TOTAL HEIGHT 2238.7 ✓
CORE
CHARGE Nº HX14A
Scale 1:2
16/3
bPAC 21/3/01

Appendix B

CORRELATOR FILE FORMAT

Tab. B.1: CoRE correlator binary data file format.

name	c type	description
sequence	int	spectrum sequence number: should increase by one per spectrum unless there are data transfer losses
time_s	u_long	time since 1 January 1970 00:00:00 in seconds
time_us	u_long	microseconds past the second
error	int	error word &0x3 - FFT overflow count 1 $\equiv \geq$ 2 FFT overflows 2 $\equiv \geq$ 4 FFT overflows 3 $\equiv \geq$ 4095 FFT overflows &0x12 - premultiplication upshift saturation count 1 $\equiv \geq$ 2 upshift overflows 2 $\equiv \geq$ 4 upshift overflows 3 $\equiv \geq$ 4095 upshift overflows
airtemp	signed char	air temperature near S5 board ($^{\circ}C$)
boardtemp	signed char	S5 board temperature ($^{\circ}C$)
v1ktemp	signed char	temperature of XC2V1000 FPGA ($^{\circ}C$)
v4ktemp	signed char	temperature of XC2V4000 FPGA ($^{\circ}C$)
auto_a	u_long[2047]	autocorrelations of channel A
auto_b	u_long[2047]	autocorrelations of channel B
cross_ab_r	long[2047]	real part of cross correlation
cross_ab_i	long[2047]	imaginary part of cross correlation

Appendix C

DATA REJECTION

C.1 Data Rejection Algorithm for This Work

1. *Dropout Rejection* - The band average autocorrelation over the band 155 MHz to 190 MHz, which was predominantly RFI free, was used to assess sampler and correlator performance. It was found that the band average autocorrelation gave a smooth time series for one correlator channel, but there were intermittent dropouts on the other channel. Further, there was an initial time constant when the calibration noise source was toggled. The first 9 spectra were rejected to avoid the steeper part of this step response. A linear function was fit to the remaining 91 points in the band average time series and points deviating from this fit by more than 4σ were rejected. This fitting and outlier removal was looped over 8 times. Any 100 spectrum correlator file that had more than 25% of its spectra rejected as dropouts was removed from analysis.

2. *Peak RFI Rejection* - Entire spectra were rejected if the autocorrelation in any channel exceeded average noise power by more than 10 dB. This limits the interference to noise power ratio to $a < 0.01$ and maintains a 56 dB dynamic range to clipping distortion as determined in §6.2.2.

3. *Averaging* - Dropout rejection flags for the autocorrelation spectra of the two receiver chains were OR'ed to generate dropout rejection flags for the cross-correlations. Cross-correlations that were not rejected were averaged over each correlator file at this stage.

4. *Band Average Time Domain RFI Rejection* - A 15^{th} order polynomial was fit to the time series of the 155 MHz to 190 MHz band average cross-correlation spectra generated in step (3). Next, a 12^{th} order polynomial was fit ignoring the 10 largest outliers from the previous fit. Complete 100 spectra correlator files were rejected and ignored when residuals of the second fit exceeded 4σ.

5. *Frequency Domain RFI Rejection* - A 15^{th} order polynomial was fit to the standard deviation spectrum of the remaining cross-correlation spectra. The polynomial was then refitted with the largest residual from the previous fit excluded. This process was repeated 6 times starting with a 15^{th} order polynomial fit and removing channels with residuals greater than 3σ each time. The order of the polynomial was increased by 6 at each step.

6. *Individual Channel Time Domain RFI Rejection* - A 5^{th} order polynomial was fit to the cross-correlation time series for each channel. Any time point that deviated from the polynomial fit by more than 10σ was excluded and then a new polynomial of one higher order was fit. This process was repeated up to a 13^{th} order polynomial. In the end, any channel that had at least one time point that deviated from the final polynomial fit by more than 10σ was rejected.

7. *Manual RFI Rejection* - The remaining cross-correlation data were overlayed and frequencies containing RFI were noted and manually rejected.

C.2 Kurtosis Based Data Rejection for Future Work

It may be better to reject poor data based on Kurtosis which measures the shape of a statistical distribution. It equals three for Gaussian noise, is lower for CW interference, and higher for pulsed sinusoids. The Kurtosis statistic of the random voltage v is defined by the ratio of its fourth central moment to the square of its second central moment (which is the variance)

$$K = \frac{m_4}{m_2^2}. \tag{C.1}$$

The n^{th} central moment of v is defined by

$$m_n = \langle (v - \langle v \rangle)^n \rangle . \tag{C.2}$$

Data rejection algorithms for radiometric data based on Kurtosis are unbiased (De Roo et al., 2007) as the Kurtosis statistic is independent of $\langle v^2 \rangle$ for a Gaussian distribution (D'Agostino and Stephens, 1986). Kurtosis can detect weak and intermittent interference that is hard to detect with an algorithm such as that proposed above that relies on detecting peaks in otherwise smooth spectra and time series.

The Kurtosis statistic can be written as a function of the first four moments about the origin

$$K = \frac{\langle v^4 \rangle - 4 \langle v^3 \rangle \langle v \rangle + 6 \langle v^2 \rangle \langle v \rangle^2 - 3 \langle v \rangle^4}{\left(\langle v^2 \rangle - \langle v \rangle^2 \right)^2}. \tag{C.3}$$

The correlator might be modified to accumulate $\langle v \rangle$, $\langle v^3 \rangle$ and $\langle v^4 \rangle$ required for Kurtosis calculation in addition to $\langle v^2 \rangle$ which is already accumulated for radiometry[1].

[1] It is possible to exclude $\langle v^3 \rangle$ at the expense of increasing variance in the Kurtosis estimate if there is a DC offset at the ADC input (De Roo, 2008).

BIBLIOGRAPHY

J. S. Bagla. Cosmological N-Body simulation: Techniques, Scope and Status. *Current Science*, 88:1088–1100, April 2005.

C. A. Balanis. *Antenna Theory*. Wiley, 2004.

M. L. Balogh, I. G. McCarthy, R. G. Bower, and V. R. Eke. Testing cold dark matter with the hierarchical build-up of stellar light. *Monthly Notices of the Royal Astronomical Society*, 385:1003–1014, April 2008. doi: 10.1111/j.1365-2966.2008.12903.x.

R. Barkana. Separating out the Alcock-Paczyński effect on 21-cm fluctuations. *Monthly Notices of the Royal Astronomical Society*, 372:259–264, October 2006. doi: 10.1111/j.1365-2966.2006.10882.x.

R. Barkana, Z. Haiman, and J. P. Ostriker. Constraints on Warm Dark Matter from Cosmological Reionization. *The Astrophysical Journal*, 558:482–496, September 2001. doi: 10.1086/322393.

D. G. Barnes, L. Staveley-Smith, W. J. G. de Blok, T. Oosterloo, I. M. Stewart, A. E. Wright, G. D. Banks, R. Bhathal, P. J. Boyce, M. R. Calabretta, M. J. Disney, M. J. Drinkwater, R. D. Ekers, K. C. Freeman, B. K. Gibson, A. J. Green, R. F. Haynes, P. te Lintel Hekkert, P. A. Henning, H. Jerjen, S. Juraszek, M. J. Kesteven, V. A. Kilborn, P. M. Knezek, B. Koribalski, R. C. Kraan-Korteweg, D. F. Malin, M. Marquarding, R. F. Minchin, J. R. Mould, R. M. Price, M. E. Putman, S. D. Ryder, E. M. Sadler, A. Schröder, F. Stootman, R. L. Webster, W. E. Wilson, and T. Ye. The Hi Parkes All Sky Survey: southern observations, calibration and robust imaging. *Monthly Notices of the Royal Astronomical Society*, 322:486–498, April 2001.

D. H. O. Bebbington. A radio search for primordial pancakes. *Monthly Notices of the Royal Astronomical Society*, 218:577–585, February 1986.

R. H. Becker, X. Fan, R. L. White, M. A. Strauss, V. K. Narayanan, R. H. Lupton, J. E. Gunn, J. Annis, N. A. Bahcall, J. Brinkmann, A. J. Connolly, I. Csabai, P. C. Czarapata, M. Doi, T. M. Heckman, G. S. Hennessy, Ž. Ivezić, G. R. Knapp, D. Q. Lamb, T. A. McKay, J. A. Munn, T. Nash, R. Nichol, J. R. Pier, G. T. Richards, D. P. Schneider, C. Stoughton, A. S. Szalay, A. R. Thakar, and D. G. York. Evidence for Reionization at z˜6: Detection of a Gunn-Peterson Trough in a z=6.28 Quasar. *Astronomical Journal*, 122:2850–2857, December 2001. doi: 10.1086/324231.

E. Bedrosian and S. O. Rice. The output properties of volterra systems (nonlinear systems with memory) driven by harmonic and gaussian inputs. *Proceedings of the IEEE*, 59(12):1688–1707, December 1971. ISSN 0018-9219.

J. S. Bendat. *Nonlinear System Analysis and Identification from Random Data*. Wiley, 1990.

W.R. Bennett. Response of a linear rectifier to signal noise. *The Journal of the Acoustical Society of America*, 15(3):164–172, 1944.

E. Bertschinger. Simulations of Structure Formation in the Universe. *Annual Review of Astronomy and Astrophysics*, 36:599–654, 1998. doi: 10.1146/annurev.astro.36.1.599.

S. Bharadwaj and S. S. Ali. The cosmic microwave background radiation fluctuations from HI perturbations prior to reionization. *Monthly Notices of the Royal Astronomical Society*, 352:142–146, July 2004. doi: 10.1111/j.1365-2966.2004.07907.x.

S. Bharadwaj and Sk. S. Ali. On using visibility correlations to probe the hi distribution from the dark ages to the present epoch - i. formalism and the expected signal. *Monthly Notices of the Royal Astronomical Society*, 356(4):1519–1528, February 2005.

S. Bharadwaj and S. K. Pandey. Probing non-Gaussian features in the HI distribution at the epoch of re-ionization. *Monthly Notices of the Royal Astronomical Society*, 358:968–976, April 2005. doi: 10.1111/j.1365-2966.2005.08836.x.

S. Bharadwaj and P. S. Srikant. HI Fluctuations at Large Redshifts: III - Simulating the Signal Expected at GMRT. *Journal of Astrophysics and Astronomy*, 25:67–+, March 2004.

S. Bharadwaj, B. B. Nath, and S. K. Sethi. Using HI to Probe Large Scale Structures at z ˜ 3. *Journal of Astrophysics and Astronomy*, 22:21–+, March 2001.

L. Blitz, D. N. Spergel, P. J. Teuben, D. Hartmann, and W. B. Burton. High-Velocity Clouds: Building Blocks of the Local Group. *The Astrophysical Journal*, 514:818–843, April 1999. doi: 10.1086/306963.

P. Bode, J. P. Ostriker, and N. Turok. Halo Formation in Warm Dark Matter Models. *The Astrophysical Journal*, 556:93–107, July 2001. doi: 10.1086/321541.

J. R. Bond, S. Cole, G. Efstathiou, and N. Kaiser. Excursion set mass functions for hierarchical Gaussian fluctuations. *The Astrophysical Journal*, 379:440–460, October 1991. doi: 10.1086/170520.

J. D. Bowman, A. E. E. Rogers, and J. N. Hewitt. Toward Empirical Constraints on the Global Redshifted 21 cm Brightness Temperature During the Epoch of Reionization. *ArXiv e-prints*, 710, October 2007.

A. H. Bridle. The spectrum of the radio background between 13 and 404 MHz. *Monthly Notices of the Royal Astronomical Society*, 136:219–+, 1967.

J. S. Bullock, A. V. Kravtsov, and D. H. Weinberg. Hierarchical Galaxy Formation and Substructure in the Galaxy's Stellar Halo. *The Astrophysical Journal*, 548: 33–46, February 2001. doi: 10.1086/318681.

E. F. Bunn and M. White. The 4 Year COBE Normalization and Large-Scale Structure. *The Astrophysical Journal*, 480:6–+, May 1997. doi: 10.1086/303955.

G.J. Burke and A.J. Poggio. *Numerical Electromagnetics Code (NEC) - Method of Moments*. Lawrence Livermore Laboritory, January 1981.

J. J. Bussgang. *Nonlinear Systems*, chapter Cross-correlation functions of amplitude distorted Gaussian inputs. Dowden, Hutchinson and Ross, 1975.

S. M. Carroll, W. H. Press, and E. L. Turner. The cosmological constant. *Annual Review of Astronomy and Astrophysics*, 30:499–542, 1992. doi: 10.1146/annurev.aa.30.090192.002435.

R. Cen. The Universe Was Reionized Twice. *The Astrophysical Journal*, 591:12–37, July 2003. doi: 10.1086/375217.

J. Cherry. Distortion analysis of weakly nonlinear filters using volterra series. Master's thesis, Department of Electronics, Carleton University, 1994.

A. P. Chippendale, M. Storey, and P. J. Hall. Low frequency array rfi site report: Mileura, western australia. Report to lofar isc, CSIRO Australia Telescope National Facility, 2003.

J. Chluba, J. A. Rubiño-Martín, and R. A. Sunyaev. Cosmological hydrogen recombination: populations of the high-level substates. *Monthly Notices of the Royal Astronomical Society*, 374:1310–1320, February 2007. doi: 10.1111/j.1365-2966.2006.11239.x.

T. R. Choudhury and A. Ferrara. Experimental constraints on self-consistent reionization models. *Monthly Notices of the Royal Astronomical Society*, 361: 577–594, August 2005. doi: 10.1111/j.1365-2966.2005.09196.x. URL `http://adsabs.harvard.edu/abs/2005MNRAS.361..577C`.

T. R. Choudhury and A. Ferrara. Physics of Cosmic Reionization. *ArXiv Astrophysics e-prints*, March 2006.

B. Ciardi and A. Ferrara. The First Cosmic Structures and Their Effects. *Space Science Reviews*, 116:625–705, February 2005. doi: 10.1007/s11214-005-3592-0. URL `http://adsabs.harvard.edu/abs/2005SSRv..116..625C`.

T. A. Clark, L. W. Brown, and J. K. Alexander. Spectrum of the Extra-galactic Background Radiation at Low Radio Frequencies. *Nature*, 228:847–849, November 1970. doi: 10.1038/228847a0.

D. Clowe, M. Bradač, A. H. Gonzalez, M. Markevitch, S. W. Randall, C. Jones, and D. Zaritsky. A Direct Empirical Proof of the Existence of Dark Matter. *Astrophysical Journal Letters*, 648:L109–L113, September 2006. doi: 10.1086/508162.

A. Coc, E. Vangioni-Flam, P. Descouvemount, A. Adahchour, and C. Angulo. Updated big bang nucleosynthesis compared with wilkinson microwave anisotropy probe observations and the abundance of light elements. *The Astrophysical Journal*, 600:544–552, January 2004.

S. Cole, W. J. Percival, J. A. Peacock, P. Norberg, C. M. Baugh, C. S. Frenk, I. Baldry, J. Bland-Hawthorn, T. Bridges, R. Cannon, M. Colless, C. Collins, W. Couch, N. J. G. Cross, G. Dalton, V. R. Eke, R. De Propris, S. P. Driver, G. Efstathiou, R. S. Ellis, K. Glazebrook, C. Jackson, A. Jenkins, O. Lahav, I. Lewis, S. Lumsden, S. Maddox, D. Madgwick, B. A. Peterson, W. Sutherland, and K. Taylor. The 2dF Galaxy Redshift Survey: power-spectrum analysis of the final data set and cosmological implications. *Monthly Notices of the Royal Astronomical Society*, 362:505–534, September 2005. doi: 10.1111/j.1365-2966.2005.09318.x.

S. Colombi, S. Dodelson, and L. M. Widrow. Large-Scale Structure Tests of Warm Dark Matter. *The Astrophysical Journal*, 458:1–+, February 1996. doi: 10.1086/176788.

R. E. Crochiere and L. R. Rabiner. *Multirate digital signal processing*. Prentice-Hall, Englewood Cliffs, N. J., 1983.

R. B. D'Agostino and M. A. Stephens. *Goodness-of-Fit Techniques*. Marcel Dekker, 1986.

D. J. Daniels. *Ground Penetrating Radar*. The Institution of Engineering and Technology, 2004.

D. Dardari. Joint clip and quantization effects characterization in OFDM receivers. *Circuits and Systems I: Regular Papers, IEEE Transactions on [Circuits and Systems I: Fundamental Theory and Applications, IEEE Transactions on]*, 53(8): 1741–1748, August 2006. ISSN 1549-8328. doi: 10.1109/TCSI.2006.875170.

K. K. Datta, S. Bharadwaj, and T. R. Choudhury. Detecting ionized bubbles in redshifted 21-cm maps. *Monthly Notices of the Royal Astronomical Society*, 382: 809–818, December 2007a. doi: 10.1111/j.1365-2966.2007.12421.x.

K. K. Datta, T. R. Choudhury, and S. Bharadwaj. The multifrequency angular power spectrum of the epoch of reionization 21-cm signal. *Monthly Notices of the Royal Astronomical Society*, 378:119–128, June 2007b. doi: 10.1111/j.1365-2966.2007.11747.x.

R. D. Davies, A. Pedlar, and I. F. Mirabel. A search for neutral hydrogen in primordial protoclusters at Z = 3.33 and 4.92. *Monthly Notices of the Royal Astronomical Society*, 182:727–733, March 1978.

A. G. de Bruyn, M. H. Wieringa, P. Katgert, and R. Sancisi. A WSRT Search for HI at Z=3.35. 130:211–+, 1988.

R. D. De Roo. A simplified calculation of the kurtosis for RFI detection. In *Geoscience and Remote Sensing Symposium, 2008. IGARSS 2008. IEEE International*, volume 2, pages 327–330, Boston, MA, USA, July 2008. doi: 10.1109/IGARSS.2008.4778994.

R. D. De Roo, S. Misra, and C. S. Ruf. Sensitivity of the kurtosis statistic as a detector of pulsed sinusoidal RFI. *IEEE Transactions on Geoscience and Remote Sensing*, 45:1938–1946, July 2007. ISSN 0196-2892. doi: 10.1109/TGRS.2006.888101.

R. DuHamel and D. Isbell. Broadband logarithmically periodic antenna structures. In *IRE International Convention Record*, volume 5, pages 119–128, March 1957.

J. Dunkley, E. Komatsu, M. R. Nolta, D. N. Spergel, D. Larson, G. Hinshaw, L. Page, C. L. Bennett, B. Gold, N. Jarosik, J. L. Weiland, M. Halpern, R. S. Hill, A. Kogut, M. Limon, S. S. Meyer, G. S. Tucker, E. Wollack, and E. L. Wright. Five-Year Wilkinson Microwave Anisotropy Probe (WMAP) Observations: Likelihoods and Parameters from the WMAP data. *ArXiv e-prints*, 803, March 2008.

J. Dyson. The unidirectional equiangular spiral antenna. *Antennas and Propagation, IEEE Transactions on*, 7(4):329 – 334, Oct 1959.

J. Dyson. The characteristics and design of the conical log-spiral antenna. *Antennas and Propagation, IEEE Transactions on*, 13(4):488 – 499, Jul 1965.

G. Efstathiou, C. S. Frenk, S. D. M. White, and M. Davis. Gravitational clustering from scale-free initial conditions. *Monthly Notices of the Royal Astronomical Society*, 235:715–748, December 1988.

D. J. Eisenstein and W. Hu. Baryonic Features in the Matter Transfer Function. *The Astrophysical Journal*, 496:605–+, March 1998. doi: 10.1086/305424.

V. R. Eke, S. Cole, and C. S. Frenk. Cluster evolution as a diagnostic for Omega. *Monthly Notices of the Royal Astronomical Society*, 282:263–280, September 1996.

R. F. Emerson. Biplex pipelined fft. The Deep Space Network Progress Report 42-34, NASA, 1976.

N. Y. Ermolova. Spectral analysis of nonlinear amplifier based on the complex gain-taylor series expansion. *IEEE Communications Letters*, 5(12):465–467, December 2001. ISSN 1089-7798. doi: 10.1109/4234.974487.

X. Fan, C. L. Carilli, and B. Keating. Observational Constraints on Cosmic Reionization. *Annual Review of Astronomy and Astrophysics*, 44:415–462, September 2006a. doi: 10.1146/annurev.astro.44.051905.092514.

X. Fan, M. A. Strauss, R. H. Becker, R. L. White, J. E. Gunn, G. R. Knapp, G. T. Richards, D. P. Schneider, J. Brinkmann, and M. Fukugita. Constraining the Evolution of the Ionizing Background and the Epoch of Reionization with z˜6 Quasars. II. A Sample of 19 Quasars. *Astronomical Journal*, 132:117–136, July 2006b. doi: 10.1086/504836.

G. B. Field. Excitation of the hydrogen 21-cm line. *Proceedings of the IRE*, 46: 240–250, January 1958.

G. B. Field. An attempt to observe neutral hydrogen between the galaxies. *The Astrophysical Journal*, 129:525, May 1959.

R. H. Frater, J. W. Brooks, and J. B. Whiteoak. The australia telescope. *Journal of Electrical And Electronics Engineering Australia*, 12(2):103–112, June 1992.

M. Fukigita and M. Kawasaki. Primordial helium abundance: A reanalysis of the Izotov-Thuan spectroscopic sample. *The Astrophysical Journal*, 646(2):691–695, August 2006.

S. R. Furlanetto. The global 21-centimeter background from high redshifts. *Monthly Notices of the Royal Astronomical Society*, 371:867–878, September 2006. doi: 10.1111/j.1365-2966.2006.10725.x.

S. R. Furlanetto, M. Zaldarriaga, and L. Hernquist. Statistical Probes of Reionization with 21 Centimeter Tomography. *The Astrophysical Journal*, 613:16–22, September 2004. doi: 10.1086/423028.

S. R. Furlanetto, S. P. Oh, and F. H. Briggs. Cosmology at low frequencies: The 21 cm transition and the high-redshift Universe. *Physics Reports*, 433:181–301, October 2006. doi: 10.1016/j.physrep.2006.08.002.

Galassi et al. *GNU Scientific Library Reference Manual*. 3 edition, January 2009.

N. Y. Gnedin. Reionization, Sloan, and WMAP: Is the Picture Consistent? *The Astrophysical Journal*, 610:9–13, July 2004. doi: 10.1086/421450.

N. Y. Gnedin and X. Fan. Cosmic Reionization Redux. *The Astrophysical Journal*, 648:1–6, September 2006. doi: 10.1086/505790.

N. Y. Gnedin, A. Ferrara, and E. G. Zweibel. Generation of the Primordial Magnetic Fields during Cosmological Reionization. *The Astrophysical Journal*, 539:505–516, August 2000. doi: 10.1086/309272.

G. A. Gray and G. W. Zeoli. Quantization and saturation noise due to analog-to-digital conversion. *IEEE Transactions on Aerospace and Electronic Systems*, 7 (1):222–223, January 1971. ISSN 0018-9251. doi: 10.1109/TAES.1971.310274.

F. W. Grover. *Inductance Calculations*. Dover, 1946.

J. E. Gunn and B. A. Peterson. On the Density of Neutral Hydrogen in Intergalactic Space. *The Astrophysical Journal*, 142:1633–1641, November 1965. doi: 10.1086/148444.

Z. Haiman and R. Cen. Constraining Reionization with the Evolution of the Luminosity Function of Lyα Emitting Galaxies. *The Astrophysical Journal*, 623: 627–631, April 2005. doi: 10.1086/428645.

Z. Haiman and G. P. Holder. The Reionization History at High Redshifts. I. Physical Models and New Constraints from Cosmic Microwave Background Polarization. *The Astrophysical Journal*, 595:1–12, September 2003. doi: 10.1086/377337.

E. Hardy and L. Noreau. A VLA search for cosmological H I at Z = 3.3. *Astronomical Journal*, 94:1469–1475, December 1987. doi: 10.1086/114579.

A. I. Harris. Spectroscopy with multichannel correlation radiometers. *Review of Scientific Instruments*, 76:4503–+, May 2005. doi: 10.1063/1.1898643.

C. G. T. Haslam, U. Klein, C. J. Salter, H. Stoffel, W. E. Wilson, M. N. Cleary, D. J. Cooke, and P. Thomasson. A 408 MHz all-sky continuum survey. I - Observations at southern declinations and for the North Polar region. *Astronomy and Astrophysics*, 100:209–219, July 1981.

C. G. T. Haslam, C. J. Salter, H. Stoffel, and W. E. Wilson. 408 MHz all-sky map. *Astronomy Data Image Library*, December 1995. URL `http://adsabs.harvard.edu/abs/1995ADIL...CH...01H`.

G. Hinshaw, M. R. Nolta, C. L. Bennett, R. Bean, O. Doré, M. R. Greason, M. Halpern, R. S. Hill, N. Jarosik, A. Kogut, E. Komatsu, M. Limon, N. Odegard, S. S. Meyer, L. Page, H. V. Peiris, D. N. Spergel, G. S. Tucker, L. Verde, J. L. Weiland, E. Wollack, and E. L. Wright. Three-Year Wilkinson Microwave Anisotropy Probe (WMAP) Observations: Temperature Analysis. *Astrophysical Journal Supplement*, 170:288–334, June 2007. doi: 10.1086/513698.

G. Hinshaw, J. L. Weiland, R. S. Hill, N. Odegard, D. Larson, C. L. Bennett, J. Dunkley, B. Gold, M. R. Greason, N. Jarosik, E. Komatsu, M. R. Nolta, L. Page, D. N. Spergel, E. Wollack, M. Halpern, A. Kogut, M. Limon, S. S. Meyer, G. S. Tucker, and E. L. Wright. Five-Year Wilkinson Microwave Anisotropy Probe Observations: Data Processing, Sky Maps, and Basic Results. *Astrophysical Journal Supplement*, 180:225–245, February 2009. doi: 10.1088/0067-0049/180/2/225.

C. J. Hogan and M. J. Rees. Spectral appearance of non-uniform gas at high Z. *Monthly Notices of the Royal Astronomical Society*, 188:791–798, September 1979.

D. H. Jones, W. Saunders, M. Colless, M. A. Read, Q. A. Parker, F. G. Watson, L. A. Campbell, D. Burkey, T. Mauch, L. Moore, M. Hartley, P. Cass, D. James, K. Russell, K. Fiegert, J. Dawe, J. Huchra, T. Jarrett, O. Lahav, J. Lucey, G. A. Mamon, D. Proust, E. M. Sadler, and K.-i. Wakamatsu. The 6dF Galaxy

Survey: samples, observational techniques and the first data release. *Monthly Notices of the Royal Astronomical Society*, 355:747–763, December 2004. doi: 10.1111/j.1365-2966.2004.08353.x.

E.-J. Kim, A. V. Olinto, and R. Rosner. Generation of Density Perturbations by Primordial Magnetic Fields. *The Astrophysical Journal*, 468:28–+, September 1996. doi: 10.1086/177667.

A. Klypin, A. V. Kravtsov, O. Valenzuela, and F. Prada. Where Are the Missing Galactic Satellites? *The Astrophysical Journal*, 522:82–92, September 1999. doi: 10.1086/307643.

J. P. Kneller and G. Steigman. BBN for pedestrians. *New Journal of Physics*, 6: 117–+, September 2004. doi: 10.1088/1367-2630/6/1/117.

E. Komatsu, J. Dunkley, M. R. Nolta, C. L. Bennett, B. Gold, G. Hinshaw, N. Jarosik, D. Larson, M. Limon, L. Page, D. N. Spergel, M. Halpern, R. S. Hill, A. Kogut, S. S. Meyer, G. S. Tucker, J. L. Weiland, E. Wollack, and E. L. Wright. Five-Year Wilkinson Microwave Anisotropy Probe Observations: Cosmological Interpretation. *Astrophysical Journal Supplement*, 180:330–376, February 2009. doi: 10.1088/0067-0049/180/2/330.

J. D. Kraus and R. J. Marhefka. *Antennas for All Applications*. McGraw Hill, 2002.

T. Kudoh, S. Basu, Y. Ogata, and T. Yabe. Three-dimensional simulations of molecular cloud fragmentation regulated by magnetic fields and ambipolar diffusion. *Monthly Notices of the Royal Astronomical Society*, 380:499–505, September 2007. doi: 10.1111/j.1365-2966.2007.12119.x.

J. A. Reeds M. H. Wright Lagarias, J.C. and P. E. Wright. Convergence properties of the nelder-mead simplex method in low dimensions. *SIAM Journal of Optimization*, 9(1):112–147, 1998.

D. L. Lager and R. J. Lytle. Fortran subroutines for the numerical evaluation of sommerfeld integrals unter anderem. Technical Report UCRL-73217, Lawrence Livermore Laboratory, CA, May 1975.

Xin Li, Peng Li, Yang Xu, R. Dimaggio, and L. Pileggi. A frequency separation macromodel for system-level simulation of RF circuits. In *Design Automation Conference, 2003. Proceedings of the ASP-DAC 2003. Asia and South Pacific*, pages 891–896, January 2003.

H. Liao, R. Wang, R. Chandra, and W. Dai. S-parameter based macro model of distributed-lumped networks using pade approximation. In *Circuits and Systems, 1993., ISCAS '93, 1993 IEEE International Symposium on*, pages 2319–2322, Chicago, IL, May 1993. doi: 10.1109/ISCAS.1993.394227.

A. V. Macciò, B. Moore, J. Stadel, and D. Potter. Dark Satellites and Cosmic Reionization. *ArXiv Astrophysics e-prints*, September 2006.

C. J. MacTavish, P. A. R. Ade, J. J. Bock, J. R. Bond, J. Borrill, A. Boscaleri, P. Cabella, C. R. Contaldi, B. P. Crill, P. de Bernardis, G. De Gasperis, A. de Oliveira-Costa, G. De Troia, G. di Stefano, E. Hivon, A. H. Jaffe, W. C. Jones, T. S. Kisner, A. E. Lange, A. M. Lewis, S. Masi, P. D. Mauskopf, A. Melchiorri, T. E. Montroy, P. Natoli, C. B. Netterfield, E. Pascale, F. Piacentini, D. Pogosyan, G. Polenta, S. Prunet, S. Ricciardi, G. Romeo, J. E. Ruhl, P. Santini, M. Tegmark, M. Veneziani, and N. Vittorio. Cosmological Parameters from the 2003 Flight of BOOMERANG. *The Astrophysical Journal*, 647:799–812, August 2006. doi: 10.1086/505558.

P. Madau, A. Meiksin, and M. J. Rees. 21 centimeter tomography of the intergalactic medium at high redshift. *The Astrophysical Journal*, 475:429–444, February 1997.

M. Mapelli, A. Ferrara, and E. Pierpaoli. Impact of dark matter decays and annihilations on reionization. *Monthly Notices of the Royal Astronomical Society*, 369:1719–1724, July 2006. doi: 10.1111/j.1365-2966.2006.10408.x.

J. C. Mather, D. J. Fixsen, R. A. Shafer, C. Mosier, and D. T. Wilkinson. Calibator design for the COBE far-infrared absolute spectrophotometer (FIRAS). *The Astrophysical Journal*, 512:511–520, February 1999.

M. Matsumoto and T. Nishimura. Mersenne twister: A 623-dimensionally equidistributed uniform pseudorandom number generator. *ACM Transactions on Modeling and Computer Simulation*, 8(1):3–30, January 1998.

P. E. Mayes. Frequency-independent antennas and broad-band derivatives thereof. *Proceedings of the IEEE*, 80(1):103–112, January 1992. ISSN 0018-9219. doi: 10.1109/5.119570.

J. McFadden. The correlation function of a sine wave plus noise after extreme clippings. *IRE Transactions on Information Theory*, 2(2):82–83, 1956.

S. S. McGaugh and W. J. G. de Blok. Testing the Dark Matter Hypothesis with Low Surface Brightness Galaxies and Other Evidence. *The Astrophysical Journal*, 499:41–+, May 1998.

J. Miralda-Escudé, M. Haehnelt, and M. J. Rees. Reionization of the Inhomogeneous Universe. *The Astrophysical Journal*, 530:1–16, February 2000. doi: 10.1086/308330.

O. D. Miranda, M. Opher, and R. Opher. Seed magnetic Fields Generated by Primordial Supernova Explosions. *Monthly Notices of the Royal Astronomical Society*, 301:547–550, December 1998.

J. Mock. JFFT. verilog & perl sourcecode, 2004. URL `http://www.mock.com/galfa/jfft/`.

B. Moore, S. Ghigna, F. Governato, G. Lake, T. Quinn, J. Stadel, and P. Tozzi. Dark Matter Substructure within Galactic Halos. *Astrophysical Journal Letters*, 524:L19–L22, October 1999. doi: 10.1086/312287.

M. F. Morales and J. Hewitt. Toward Epoch of Reionization Measurements with Wide-Field Radio Observations. *The Astrophysical Journal*, 615:7–18, November 2004. doi: 10.1086/424437.

M. F. Morales, J. D. Bowman, and J. N. Hewitt. Improving Foreground Subtraction in Statistical Observations of 21 cm Emission from the Epoch of Reionization. *The Astrophysical Journal*, 648:767–773, September 2006. doi: 10.1086/506135.

L. Noreau and E. Hardy. A VLA search for cosmological H I at Z = 3.3. II - New observations of three fields. *Astronomical Journal*, 96:1845–1849, December 1988. doi: 10.1086/114930.

V. Ossenkopf. The stability of spectroscopic instruments: a unified Allan variance computation scheme. *Astronomy and Astrophysics*, 479:915–926, March 2008. doi: 10.1051/0004-6361:20079188.

T. Padmanabhan. *Structure Formation in the Universe*. Cambridge University Press, 1993.

L. Page, G. Hinshaw, E. Komatsu, M. R. Nolta, D. N. Spergel, C. L. Bennett, C. Barnes, R. Bean, O. Doré, J. Dunkley, M. Halpern, R. S. Hill, N. Jarosik, A. Kogut, M. Limon, S. S. Meyer, N. Odegard, H. V. Peiris, G. S. Tucker, L. Verde, J. L. Weiland, E. Wollack, and E. L. Wright. Three-Year Wilkinson Microwave Anisotropy Probe (WMAP) Observations: Polarization Analysis. *Astrophysical Journal Supplement*, 170:335–376, June 2007. doi: 10.1086/513699.

B. E. J. Pagel, E. A. Simonson, R. J. Terlevich, and M. G. Edmunds. The primordial helium abundance from observations of extragalactic HII regions. *Monthly Notices of the Royal Astronomical Society*, 255:325–345, March 1992.

A. Parsons, D. Werthimer, J. Mock, and M. Dexter. The SERENDIP V spectrometer. Poster, 2004. URL `http://seti.berkeley.edu/casper/papers/2004-07-10\_Iceland\_SV\_poster.pdf`.

A. H. Pawlik, J. Schaye, and E. van Scherpenzeel. Keeping the Universe ionized: photoheating and the clumping factor of the high-redshift intergalactic medium. *MNRAS*, pages 307–+, March 2009. doi: 10.1111/j.1365-2966.2009.14486.x.

J. A. Peacock. *Cosmological Physics*. Cambridge University Press, 1999.

J. A. Peacock, S. Cole, P. Norberg, C. M. Baugh, J. Bland-Hawthorn, T. Bridges, R. D. Cannon, M. Colless, C. Collins, W. Couch, G. Dalton, K. Deeley, R. De Propris, S. P. Driver, G. Efstathiou, R. S. Ellis, C. S. Frenk, K. Glazebrook, C. Jackson, O. Lahav, I. Lewis, S. Lumsden, S. Maddox, W. J. Percival, B. A.

Peterson, I. Price, W. Sutherland, and K. Taylor. A measurement of the cosmological mass density from clustering in the 2dF Galaxy Redshift Survey. *Nature*, 410:169–173, March 2001.

P. J. E. Peebles. Recombination of the primeval plasma. *The Astrophysical Journal*, 153:1–11, July 1968.

P. J. E. Peebles. *Principles of Physical Cosmology*. Princeton Series in Physics. Princeton University Press, 1993.

U.-L. Pen, L. Staveley-Smith, J. Peterson, and T.-C. Chang. First Detection of Cosmic Structure in the 21-cm Intensity Field. *ArXiv e-prints*, 802, February 2008.

W. J. Percival, S. Cole, D. J. Eisenstein, R. C. Nichol, J. A. Peacock, A. C. Pope, and A. S. Szalay. Measuring the Baryon Acoustic Oscillation scale using the Sloan Digital Sky Survey and 2dF Galaxy Redshift Survey. *Monthly Notices of the Royal Astronomical Society*, 381:1053–1066, November 2007. doi: 10.1111/j.1365-2966.2007.12268.x.

S. Perlmutter, G. Aldering, G. Goldhaber, R. A. Knop, P. Nugent, P. G. Castro, S. Deustua, S. Fabbro, A. Goobar, D. E. Groom, I. M. Hook, A. G. Kim, M. Y. Kim, J. C. Lee, N. J. Nunes, R. Pain, C. R. Pennypacker, R. Quimby, C. Lidman, R. S. Ellis, M. Irwin, R. G. McMahon, P. Ruiz-Lapuente, N. Walton, B. Schaefer, B. J. Boyle, A. V. Filippenko, T. Matheson, A. S. Fruchter, N. Panagia, H. J. M. Newberg, W. J. Couch, and The Supernova Cosmology Project. Measurements of Omega and Lambda from 42 High-Redshift Supernovae. *The Astrophysical Journal*, 517:565–586, June 1999. doi: 10.1086/307221.

E. Polisensky. LFmap: A low frequency sky map generating program. LWA Memo 111, Naval Research Laboratory, September 2007.

David M. Pozar. *Microwave Engineering*. Wiley, 2 edition, 1998.

W. H. Press and P. Schechter. Formation of Galaxies and Clusters of Galaxies by Self-Similar Gravitational Condensation. *The Astrophysical Journal*, 187:425–438, February 1974. URL `http://adsabs.harvard.edu/abs/1974ApJ...187..425P`.

M. J. Rees and M. Reinhardt. Some Remarks on Intergalactic Magnetic Fields. *Astronomy and Astrophysics*, 19:189–+, July 1972.

A. G. Riess, L.-G. Strolger, J. Tonry, S. Casertano, H. C. Ferguson, B. Mobasher, P. Challis, A. V. Filippenko, S. Jha, W. Li, R. Chornock, R. P. Kirshner, B. Leibundgut, M. Dickinson, M. Livio, M. Giavalisco, C. C. Steidel, T. Benítez, and Z. Tsvetanov. Type Ia Supernova Discoveries at z ¿ 1 from the Hubble Space Telescope: Evidence for Past Deceleration and Constraints on Dark Energy Evolution. *The Astrophysical Journal*, 607:665–687, June 2004. doi: 10.1086/383612.

K. R. Rohlfs and T. L. Wilson. *Tools of Radio Astronomy*. Astronomy and Astrophysics Library. Springer, fourth edition, 2006.

D. A. Roshi, S. K. Sethi, U.-L. Pen, J. Peterson, R. Subrahmanyan, T.-C. Chang, C. Hirata, J. Roy, and Y. Gupta. HI signal from the epoch of reionization: A pilot observation with the GMRT. *Long Wavelength Astrophysics, 26th meeting of the IAU, Joint Discussion 12, 21 August 2006, Prague, Czech Republic, JD12, #50*, 12, August 2006.

V. H. Rumsey. Frequency independent antennas. In *IRE International Convention Record*, volume 5, pages 114–118, March 1957.

V. H. Rumsey. *Frequency independent antennas*. Academic, 1966.

G. B. Rybicki and I. P. dell'Antonio. The time development of a resonance line in the expanding universe. *The Astrophysical Journal*, 427:603–617, June 1994. doi: 10.1086/174170.

M. N. Saha. Ionisation in the solar chromosphere. *Philosophical Magazine*, 40:472, October 1920.

S. Saiyad Ali, S. Bharadwaj, and S. K. Pandey. Probing the bispectrum at high redshifts using 21-cm HI observations. *Monthly Notices of the Royal Astronomical Society*, 366:213–218, February 2006. doi: 10.1111/j.1365-2966.2005.09847.x.

A. Saleh. Frequency-independent and frequency-dependent nonlinear models of TWT amplifiers. *Communications, IEEE Transactions on [legacy, pre - 1988]*, 29(11):1715–1720, November 1981. ISSN 0096-2244.

Martin Schetzen. *The Volterra and Wiener Theories of Nonlinear Systems*. Robert E. Krieger Publishing Company, Malabar, Florida, 1989.

D. Scott. Recfast.for v1.4. FORTRAN sourcecode, February 2008. URL `http://www.astro.ubc.ca/people/scott/recfast.html`.

D. Scott and M. J. Rees. The 21-cm line at high redshift: a diagnostic for the origin of large scale structure. *Monthly Notices of the Royal Astronomical Society*, 247: 510–+, December 1990.

S. Seager, D. D. Sasselov, and D. Scott. A new calculation of the recombination epoch. *The Astrophysical Journal*, 523(1):L1–L5, September 1999.

U. Seljak and M. Zaldarriaga. A Line-of-Sight Integration Approach to Cosmic Microwave Background Anisotropies. *The Astrophysical Journal*, 469:437–+, October 1996. doi: 10.1086/177793.

J. A. Sellwood and A. Kosowsky. Does Dark Matter Exist? In J. E. Hibbard, M. Rupen, and J. H. van Gorkom, editors, *Gas and Galaxy Evolution*, volume 240 of *Astronomical Society of the Pacific Conference Series*, pages 311–+, 2001.

S. K. Sethi. HI signal from re-ionization epoch. *Monthly Notices of the Royal Astronomical Society*, 363:818–830, November 2005. doi: 10.1111/j.1365-2966.2005.09485.x.

S. K. Sethi and K. Subramanian. Primordial magnetic fields in the post-recombination era and early reionization. *Monthly Notices of the Royal Astronomical Society*, 356:778–788, January 2005. doi: 10.1111/j.1365-2966.2004.08520.x.

C. E. Shannon. A mathematical theory of communication. *The Bell System Technical Journal*, 27:379–423, 623–656, July, October 1948.

P. R. Shapiro and M. L. Giroux. Cosmological H II regions and the photoionization of the intergalactic medium. *Astrophysical Journal Letters*, 321:L107–L112, October 1987. doi: 10.1086/185015.

P. A. Shaver, R. A. Windhorst, P. Madau, and A. G. de Bruyn. Can the reionization epoch be detected as a global signature in the cosmic background? *Astronomy and Astrophysics*, 345:380–390, 1999.

R. K. Sheth and G. Tormen. Large-scale bias and the peak background split. *Monthly Notices of the Royal Astronomical Society*, 308:119–126, September 1999.

R. K. Sheth and G. Tormen. An excursion set model of hierarchical clustering: ellipsoidal collapse and the moving barrier. *Monthly Notices of the Royal Astronomical Society*, 329:61–75, January 2002. doi: 10.1046/j.1365-8711.2002.04950.x. URL `http://adsabs.harvard.edu/abs/2002MNRAS.329...61S`.

G. Sironi. The spectrum of the galactic non-thermal background radiation-1. Observations at 151-5 and 408 MHz. *Monthly Notices of the Royal Astronomical Society*, 166:345–354, February 1974.

D. N. Spergel and P. J. Steinhardt. Observational Evidence for Self-Interacting Cold Dark Matter. *Physical Review Letters*, 84:3760–3763, April 2000.

D. N. Spergel, L. Verde, H. V. Peiris, E. Komatsu, M. R. Nolta, C. L. Bennett, M. Halpern, G. Hinshaw, N. Jarosik, A. Kogut, M. Limon, S. S. Meyer, L. Page, G. S. Tucker, J. L. Weiland, E. Wollack, and E. L. Wright. First-Year Wilkinson Microwave Anisotropy Probe (WMAP) Observations: Determination of Cosmological Parameters. *Astrophysical Journal Supplement*, 148:175–194, September 2003. doi: 10.1086/377226.

D. N. Spergel, R. Bean, O. Doré, M. R. Nolta, C. L. Bennett, J. Dunkley, G. Hinshaw, N. Jarosik, E. Komatsu, L. Page, H. V. Peiris, L. Verde, M. Halpern, R. S. Hill, A. Kogut, M. Limon, S. S. Meyer, N. Odegard, G. S. Tucker, J. L. Weiland, E. Wollack, and E. L. Wright. Three-Year Wilkinson Microwave Anisotropy Probe (WMAP) Observations: Implications for Cosmology. *Astrophysical Journal Supplement*, 170:377–408, June 2007. doi: 10.1086/513700.

G. Steigman. Primordial Nucleosynthesis:. Successes and Challenges. *International Journal of Modern Physics E*, 15:1–35, 2006. doi: 10.1142/S0218301306004028.

P. A. Strittmatter. Gravitational collapse in the presence of a magnetic field. *Monthly Notices of the Royal Astronomical Society*, 132:359–+, 1966.

R. Subrahmanyan and K. R. Anantharamaiah. A search for protoclusters at Z = 3.3. *Journal of Astrophysics and Astronomy*, 11:221–235, June 1990.

R. A. Sunyaev and Y. B. Zeldovich. Formation of Clusters of Galaxies; Protocluster Fragmentation and Intergalactic Gas Heating. *Astronomy and Astrophysics*, 20: 189–+, August 1972.

G. Swarup. Giant meter-wavelength radio telescope - a proposal. Proposal, Radio Astonomy Centre, Tata Institute of Fundamental Research, Ootacamund, India, 1984.

G. Swarup and R. Subrahmanyan. Search for proto-clusters at meter wavelengths. In A. Hewitt, G. Burbidge, and L. Z. Fang, editors, *Observational Cosmology*, volume 124 of *IAU Symposium*, pages 441–444, 1987.

H. Tashiro and N. Sugiyama. Early reionization with primordial magnetic fields. *Monthly Notices of the Royal Astronomical Society*, 368:965–970, May 2006. doi: 10.1111/j.1365-2966.2006.10178.x.

M. Tegmark, M. R. Blanton, M. A. Strauss, F. Hoyle, D. Schlegel, R. Scoccimarro, M. S. Vogeley, D. H. Weinberg, I. Zehavi, A. Berlind, T. Budavari, A. Connolly, D. J. Eisenstein, D. Finkbeiner, J. A. Frieman, J. E. Gunn, A. J. S. Hamilton, L. Hui, B. Jain, D. Johnston, S. Kent, H. Lin, R. Nakajima, R. C. Nichol, J. P. Ostriker, A. Pope, R. Scranton, U. Seljak, R. K. Sheth, A. Stebbins, A. S. Szalay, I. Szapudi, L. Verde, Y. Xu, J. Annis, N. A. Bahcall, J. Brinkmann, S. Burles, F. J. Castander, I. Csabai, J. Loveday, M. Doi, M. Fukugita, J. R. I. Gott, G. Hennessy, D. W. Hogg, Ž. Ivezić, G. R. Knapp, D. Q. Lamb, B. C. Lee, R. H. Lupton, T. A. McKay, P. Kunszt, J. A. Munn, L. O'Connell, J. Peoples, J. R. Pier, M. Richmond, C. Rockosi, D. P. Schneider, C. Stoughton, D. L. Tucker, D. E. Vanden Berk, B. Yanny, and D. G. York. The Three-Dimensional Power Spectrum of Galaxies from the Sloan Digital Sky Survey. *The Astrophysical Journal*, 606:702–740, May 2004. doi: 10.1086/382125.

J. M. Uson, D. S. Bagri, and T. J. Cornwell. A search for redshifted neutral hydrogen from protoclusters of galaxies. *Astrophysical Journal Letters*, 377:L65–L68, August 1991. doi: 10.1086/186118.

J. H. van Vleck. The spectrum of clipped noise. Radio Research Lab 51, Harvard University, 1943.

J. H. van Vleck and D. Middleton. The spectrum of clipped noise. *Proceedings of the IEEE*, 54(1):2–19, 1966.

P. Wambacq, P. Dobrovolny, S. Donnay, M. Engels, and I. Bolsens. Compact modeling of nonlinear distortion in analog communicationcircuits. In *Design, Automation and Test in Europe Conference and Exhibition 2000. Proceedings*, pages 350–354, Paris, France, 2000. doi: 10.1109/DATE.2000.840295.

X. Wang, M. Tegmark, M. G. Santos, and L. Knox. 21 cm Tomography with Foregrounds. *The Astrophysical Journal*, 650:529–537, October 2006. doi: 10.1086/506597.

I. Wasserman. On the origins of galaxies, galactic angular momenta, and galactic magnetic fields. *The Astrophysical Journal*, 224:337–343, September 1978. doi: 10.1086/156381.

Eric W. Weisstein. "standard deviation distribution." from *MathWorld*–a wolfram web resource, 2009. URL `http://mathworld.wolfram.com/StandardDeviationDistribution.html`.

T. Westmeier, R. Braun, C. Brüns, J. Kerp, and D. A. Thilker. The relics of galaxy evolution: High-velocity clouds around the Andromeda Galaxy. *New Astronomy Review*, 51:108–112, February 2007. doi: 10.1016/j.newar.2006.11.002.

B. Widrow. *A study of rough amplitude quantization by means of Nyquist sampling theory*. PhD thesis, Department of Electrical Engineering, MIT, 1956.

B. Widrow, I. Kollar, and Ming-Chang Liu. Statistical theory of quantization. *IEEE Transactions on Instrumentation and Measurement*, 45(2):353–361, April 1996. ISSN 0018-9456. doi: 10.1109/19.492748.

M. H. Wieringa, A. G. de Bruyn, and P. Katgert. A Westerbork search for high redshift H I. *Astronomy and Astrophysics*, 256:331–342, March 1992.

W. Y. Wong, A. Moss, and D. Scott. How well do we understand cosmological recombination? *ArXiv e-prints*, 711, November 2007.

J. S. B. Wyithe and A. Loeb. A characteristic size of ˜10Mpc for the ionized bubbles at the end of cosmic reionization. *Nature*, 432:194–196, November 2004a. doi: 10.1038/nature03033.

J. S. B. Wyithe and A. Loeb. A large neutral fraction of cosmic hydrogen a billion years after the Big Bang. *NAT*, 427:815–817, February 2004b.

J. S. B. Wyithe, A. Loeb, and D. G. Barnes. Prospects for Redshifted 21 cm Observations of Quasar H II Regions. *The Astrophysical Journal*, 634:715–727, November 2005. doi: 10.1086/497160.

Q. Yu and Y. Lu. The Strömgren Sphere, the Environment, and the Reionization in the Local Universe of the Highest Redshift QSOs. *The Astrophysical Journal*, 620:31–43, February 2005. doi: 10.1086/426905.

M. Zaldarriaga, S. R. Furlanetto, and L. Hernquist. 21 Centimeter Fluctuations from Cosmic Gas at High Redshifts. *The Astrophysical Journal*, 608:622–635, June 2004. doi: 10.1086/386327.

Y. B. Zel'Dovich. Gravitational instability: An approximate theory for large density perturbations. *Astronomy and Astrophysics*, 5:84–89, March 1970.

Y. B. Zeldovich, V. G. Kurt, and R. A. Sunyaev. Recombination of hydrogen in the hot model of the universe. *Soviet Physics - JETP (Journal of Experimental and Theoretical Physics)*, 55(1):278–286, January 1969.

Q. Zhang, B. Suki, D. Westwick, and K. Lutchen. Factors affecting volterra kernel estimation: Emphasis on lung tissue viscoelasticity. *Annals of Biomedical Engineering*, 26:103–116, 1998.